

Dissertation
submitted to the
Combined Faculty of Mathematics, Engineering and Natural Sciences
of Heidelberg University, Germany
for the degree of
Doctor of Natural Sciences

Put forward by
Dane Marvin Späth
born in: Blaubeuren, Germany
Oral examination: June 11, 2025

A Critical Appraisal of Planets Orbiting Giant Stars

Referees:

PD Dr. Sabine Reffert
Prof. Dr. Laura Kreidberg

Dane Marvin Späth

A Critical Appraisal of Planets Orbiting Giant Stars

Ruprecht-Karls-Universität Heidelberg, March 31, 2025

Reviewers: PD Dr. Sabine Reffert

Prof. Dr. Laura Kreidberg

Supervisors: PD Dr. Sabine Reffert

Prof. Dr. Andreas Quirrenbach

Prof. Dr. Laura Kreidberg

Ruprecht-Karls-Universität Heidelberg

Extrasolar Planet Research Group

Landessternwarte Königstuhl

Zentrum für Astronomie

Königstuhl 12

69117 Heidelberg

Abstract

Giant stars provide a unique opportunity to study planets around intermediate-mass stars through radial velocity surveys and examine the impact of stellar evolution on planetary systems. Despite their growing numbers, few planets have been found with very short or long orbital periods. Furthermore, detections around luminous giants are debated as intrinsic mechanisms can mimic planetary signals. In this thesis, I rule out two transiting planet candidates from TESS via spectroscopic follow-up. To address the planet controversy surrounding luminous giants, I develop the simulation tool `pyoscillot`, showing that the radial velocities and activity indicators of the false-positive planet host NGC 4349 No. 127 can be reproduced by a non-radial oscillation model. I further combine data from the Lick, SONG, and CARMENES spectrographs to analyze ten planet candidates with intermediate orbital periods. I find that testing an extensive baseline of radial velocities for consistency with Keplerian orbits is crucial to rule out or confirm planets around luminous giants. While the signals of seven stars are intrinsically induced, I identify a long-period planet candidate orbiting HIP 64823. Finally, I present first results of the new échelle spectrograph mounted at the Waltz telescope at Landessternwarte, Heidelberg, demonstrating its potential for detecting planets around giants.

Zusammenfassung

Riesensterne bieten die Möglichkeit, Planetensysteme um Sterne mittlerer Massen mittels der Radialgeschwindigkeitsmethode zu finden und den Einfluss der stellaren Entwicklung zu untersuchen. Trotz ihrer zunehmenden Anzahl sind nur wenige Planeten mit sehr kurzen oder langen Umlaufperioden bekannt. Darüber hinaus werden Planetenentdeckungen um sehr leuchtkräftige Riesen kritisch diskutiert, da intrinsische Prozesse Planetensignale in Radialgeschwindigkeitsdaten imitieren können. In dieser Arbeit widerlege ich zwei durch TESS gefundene Transit-Planetenkandidaten mittels Radialgeschwindigkeitsmessungen. Um die Planetenkontroverse um leuchtkräftige Riesen zu untersuchen, entwickle ich die Simulationssoftware `pyoscillot`. Ich zeige, dass ein Modell einer nicht-radialen Oszillation die Radialgeschwindigkeiten und Aktivitätsindizes des widerlegten Planetensystems um NGC 4349 No. 127 erklären kann. Anschließend analysiere ich zehn Planetenkandidaten mit mittleren Umlaufperioden durch eine Kombination von Daten der Lick, SONG und CARMENES Spektrographen. Ich zeige, dass ein präzises Testen einer langen Zeitserie von Radialgeschwindigkeiten auf Übereinstimmung mit Kepler-Orbits die wichtigste Methode ist, um Planeten um leuchtkräftige Riesen zu bestätigen oder zu widerlegen. Die Radialgeschwindigkeitssignale von sieben Sternen werden intrinsisch verursacht. Dagegen finde ich einen vielversprechenden, langperiodischen Planetenkandidaten um HIP 64823. Zuletzt präsentiere ich erste Ergebnisse des neuen Échelle Spektrographen am Waltz Teleskop der Landessternwarte Heidelberg, die zeigen, dass das Instrument bereit und in der Lage ist, Planeten um Riesensterne zu entdecken.

Für Mama

Acknowledgements

The work that constitutes this thesis could not have begun, let alone been completed, without the encouragement and support of many more people than I could possibly thank here. I would like to extend my heartfelt thanks to all of you!

Above all, I would like to express my deepest gratitude to my supervisor, Sabine Reffert, for the incredible support over the years and for always being available. Her guidance in discussing and solving both big and small challenges, as well as resolving some emotional crises, has been absolutely invaluable. *Thank you so much, Sabine!* I would also like to thank Laura Kreidberg for the always helpful input during IMPRS committee meetings that offered new perspectives to solve seemingly intractable problems, and for taking the time to be the second referee for this thesis. I am further sincerely thankful to my second supervisor, Andreas Quirrenbach, for the always very helpful discussions, the valuable feedback, and the support throughout the years. Moreover, I would like to thank Joachim Wambsganß and Matthias Bartelmann for joining the thesis defense committee.

I am further deeply grateful to Sabine Reffert, Adrian Kaminski, and Paul Heeren for proofreading chapters of this thesis and for numerous discussions, as well as to Trifon Trifonov, Emily Hunt, Alex Golovin, Sepideh Sadegi, Jonas Kemmer, Hans-Günter Ludwig, and Stephan Stock for the support in different aspects of the analysis. I also thank Davide Gandolfi for the help in reducing FIES data. I would further like to thank the whole Waltz team for the joint effort, especially Julian Stürmer for the support with the technical aspects (secretly he has always been happy to leave his desk for a while to play around with the spectrograph). A special mention is also well deserved by Marcelo Tala Pinto and Paul Heeren, whose tireless work in previous years was vital to get to us to where we are today. A heartfelt thank you is also more than due to the LSW workshop, namely Lutz Geuer, Markus Zuber, Lars Ulrich, Edwin Lutz, and Jochen Tietz, as well as to Stefan and Thomas Zinser for always being a swift help at the Waltz. I am also happy to have shared many observation nights with numerous companions. Special thanks go to Vivek Reddy Pininti and Daniel Götz for the most enduring support! I would also like to thank the LSW IT team, Ingo, Florian, Monika, and Philipp, for the support! Sincere thanks are also due to Ditta Müller-Wolkenstein for the administrative help.

Further, I would like to take the time to thank the "Exploring the Diversity of Extrasolar Planets" priority program of the DFG for the financial support. A special thank you shall also be extended to the program's outreach team for giving me the incredible opportunity to learn and take part in numerous outreach activities and for sharing some very fun and productive meetings!

Of course, there are many more friends and colleagues, whose support lies above all in providing the fun that makes it all worthwhile! I would like to thank all the members of the LSW, for the welcoming atmosphere on top of the hill, the S.M.A.R.T. team, Emily, Sepideh,

Theodora, and Philipp, for the joint solving of puzzles, both literally and figuratively, the forest walks, and the overall help in structuring and organizing much of this work, as well as Nina and Chris for the many fun lunch meetings! I am also more than thankful to the Mahlzeit crew, for the cherished breaks and the new perspectives they offered, the SV Wacker, the TVE, especially Markus for the joint rides home, and all my childhood friends for sharing this journey with me and for sticking by me through it all!

Lastly and most importantly, I would like to thank my family for everything they have done for me and given to me throughout my life. I am deeply grateful to my father Roland for planting the seeds of scientific curiosity in me as a child, for many a *lecture* (even though they repeated a few times), and for giving me the unshakable belief that I am capable of writing this thesis. I would also like to extend my gratitude to his wife Ingrid for the encouragement and support in times of grief. From the bottom of my heart, I would like to thank my mum Andrea for much more than could ever be expressed in words. Thank you for always encouraging and believing in me, giving me the strength to go through my life! And thank you for teaching me what really matters in the end. You have been pivotal in encouraging me to pursue this thesis, and although you would not see its completion, I know that you would have been very proud! *Danke Mama!* I am further more than grateful for the support of my sister Jacqueline for always having been at my side and going through the toughest of times together! Finishing this thesis would not have been possible without you!

Finally, I would like to express my deepest gratitude to my girlfriend Christina for having made every step along this journey together. Thank you for laughing and crying together, for your encouragement, for putting things into perspective, and, sometimes, for putting up with the craziness. You have earned more than a fair share of this! I am so looking forward to our next journey together!

To all of you, thank you!

Contents

Abstract	I
Acknowledgements	V
List of Tables	XIII
List of Figures	XVII
1 Introduction	1
1.1 Exoplanets - A human perspective	1
1.2 Planets around giant stars	3
1.3 The effect of stellar evolution on planetary systems	5
1.4 Planet occurrence rate around giant stars	8
1.5 The Lick RV survey	9
1.6 The radial velocity method applied to giant stars	12
1.6.1 p-mode oscillations	14
1.6.2 The iodine cell method	15
1.6.3 Activity indicators	15
1.7 The transit method applied to giant stars	19
1.8 The astrometric method applied to giant stars	21
1.9 The planet controversy around luminous giants	23
1.10 Possible intrinsic origins of RV variations of giants	26
1.10.1 Oscillatory convective modes and non-radial oscillations	26
1.10.2 Convective processes and magnetic activity	28
1.11 Goal and structure of this thesis	29
2 Radial velocity non-detections of <i>Gaia</i> astrometric and TESS transiting candidates	31
2.1 Non-Confirmation of the Astrometric Binary Candidate HD 113283	31
2.1.1 Introduction	31
2.1.2 Results	32
2.1.3 Discussion	32
2.2 Radial velocity non-detections of two evolved TESS Objects of Interest	34
2.2.1 Motivation and target selection	34

2.2.2	Stellar properties	35
2.2.3	Transit and radial velocity data	36
2.2.4	Discussion of TOI 1489	38
2.2.5	Discussion of TOI 1684	40
2.2.6	Conclusions	45
3	Simulating non-radial oscillations of evolved stars	47
3.1	General simulation paradigm	47
3.1.1	Representation in spherical coordinates	47
3.1.2	Implementation of non-radial oscillations	48
3.1.3	Line-of-sight projection	50
3.1.4	Temperature fluctuations	51
3.1.5	Stellar rotation	53
3.2	Computation of high-resolution spectra	53
3.2.1	PHOENIX - The underlying model spectra	54
3.2.2	Temperature interpolation	55
3.2.3	Velocity shift	55
3.2.4	Spectrum integration	56
3.2.5	Adjusting the resolution	56
3.2.6	Synthesizing instrument specific spectra	57
3.2.7	Data reduction	58
3.3	Optional Effects	60
3.3.1	Convection - Macroturbulence	60
3.3.2	Line asymmetries due to convective blueshift	61
3.3.3	Center-to-limb variations	65
3.4	Testing the simulation results	67
3.4.1	Line bisector variations	67
3.4.2	The base model	68
3.4.3	The effect of the chromatic limb-darkening correction	71
3.4.4	The influence of the parameters for $l = 1, m = 1$ modes	73
4	Non-radial oscillations mimicking a brown dwarf orbiting the cluster giant NGC 4349 No. 127	79
4.1	Introduction	79
4.2	Observations and stellar parameters	82
4.2.1	Stellar parameters	82
4.2.2	Data	83
4.3	Simulations	85
4.3.1	Description of non-radial oscillations	86
4.3.2	Calculation of the synthetic spectrum	87
4.4	Results	90

4.4.1	Confirmation of the intrinsic nature of the RV variations	90
4.4.2	Correlations between the activity indicators and the RVs	92
4.4.3	Simulation of a dipole, retrograde ($l = 1, m = 1$) oscillation mode	96
4.4.4	Comparison between the data and the oscillation model	98
4.4.5	Cross-correlation profiles	100
4.4.6	Photometric variations	101
4.5	Other oscillation modes	103
4.5.1	$l=1$ modes	103
4.5.2	Higher-order l -modes	108
4.6	Discussion	110
4.6.1	Oscillatory convective modes	111
4.6.2	Magnetic activity	114
4.7	Summary	115

5 Distinguishing planets from intrinsically induced radial velocity signals in evolved stars 117

5.1	Introduction	117
5.2	Sample and stellar parameters	120
5.3	Observations	122
5.3.1	Lick observations	122
5.3.2	Lick $H\alpha$ index	123
5.3.3	SONG observations	123
5.3.4	CARMENES observations	124
5.4	Results	126
5.4.1	Radial velocity time series and Keplerian fits	126
5.4.2	Radial velocity residual analysis	128
5.4.3	Infrared test	131
5.4.4	Analysis of the activity indicator time series	134
5.5	Combined results for individual stars	140
5.5.1	HIP 7607	140
5.5.2	HIP 7884	142
5.5.3	HIP 16335	143
5.5.4	HIP 38253	144
5.5.5	HIP 46390	145
5.5.6	HIP 47959	146
5.5.7	HIP 64823	146
5.5.8	HIP 73620	147
5.5.9	HIP 75458	148
5.5.10	HIP 84671	149
5.5.11	HIP 88048	150
5.5.12	HIP 89826	150

5.5.13	Summary of the results	151
5.6	The long-period planet candidate HIP 64823	152
5.6.1	Radial velocity modeling	152
5.6.2	Stacked Bayesian GLS analysis	154
5.7	Discussion	157
5.8	Summary	162
6	The Waltz radial velocity survey: Steps toward routine observations	165
6.1	Motivation and survey goals	165
6.2	Instrument overview	166
6.2.1	The Waltz telescope and dome	166
6.2.2	Frontend	167
6.2.3	Spectrograph	168
6.2.4	Additional components and infrastructure	170
6.3	Improvements to the Waltz infrastructure	171
6.3.1	Miscellaneous improvements	171
6.3.2	Realignment of the telescope and spectrograph	173
6.3.3	Relocation of the PMT	175
6.4	The CTI effect	178
6.4.1	Characterization	178
6.4.2	Correcting the CTI effect	182
6.4.3	Rotation of the CCD	185
6.5	First on-sky tests of the Waltz RV survey	187
6.5.1	Formal RV uncertainties	187
6.5.2	Short-term RV stability	188
6.5.3	Long-term RV stability	190
6.5.4	Testing the RVs on an established planet host	191
6.6	Outlook and future plans	192
7	Conclusions	195
7.1	Summary of the results	195
7.2	Future of planet detections orbiting giants	197
7.2.1	Short-period planets	197
7.2.2	The planet controversy around luminous giants	198
7.2.3	Long-period planets and planets in binary systems	201
7.3	Final remarks	202
	Personal bibliography	203
	Bibliography	205
	Software acknowledgements	217

Data acknowledgements	219
Abbreviations and acronyms	221
A Appendix to Chapter 2	223
A.1 FEROS RVs for HD 113283	223
A.2 FIES RVs for TOI 1489	224
A.3 FIES RVs for TOI 1684	225
B Appendix to Chapter 4	226
B.1 Linear correlation between $H\alpha$ and RV	226
B.2 Discussion of the ASAS-3 photometry	226
B.3 Oscillation modes with $m = l$	230
B.4 Oscillation modes with $m = -l$	231
B.5 HARPS data set	232
C Appendix to Chapter 5	233
C.1 Priors used for the Keplerian modeling	233
C.2 Corner plot of the joint 1P+GP model for HIP 64823	234

List of Tables

2.1	Stellar parameters derived by <i>SPOG+</i>	35
3.1	Parameters used for the base oscillation model	69
4.1	Stellar parameters of NGC 4349 No. 127	84
4.2	Parameters used for the retrograde dipole oscillation model	98
5.1	Stellar parameters derived by Stock et al. (2018)	120
5.2	Number of spectra collected per instrument	127
5.3	Keplerian parameters obtained through nested sampling.	130
5.4	Results of the 1P+GP nested sampling modeling.	154
A.1	FEROS RVs for HD 113283	223
A.2	FIES RVs for TOI 1489	224
A.3	FIES RVs for TOI 1684	225
B.1	HARPS RVs and activity indicators for NGC 4349 No. 127	232
C.1	Priors used for the Keplerian models	233
C.2	Priors used for the modeling of HIP 64823	233

List of Figures

1.1	The pale blue dot revisited. Credit: NASA/JPL-Caltech	1
1.2	Masses and periods of known planets orbiting giants and other stars	4
1.3	Simulations of a $1 M_{\text{Jup}}$ planet's orbit around a $1.5 M_{\odot}$ star during the RGB evolution. Credit: Villaver et al. (2014)	7
1.4	Planet occurrence rate as a function of host mass and metallicity. Credit: Wolthoff et al. (2022)	9
1.5	Planet occurrence rate as a function of orbital period. Credit: Wolthoff et al. (2022)	10
1.6	Histograms of the stellar parameters for the Lick sample	11
1.7	Spectral region around the Ca II H and K lines. Credit: Schröder et al. (2009)	16
1.8	Illustration of the CCF and activity indicators. Credit: Lafarga et al. (2020) .	18
1.9	Illustration of the chromatic index. Credit: Zechmeister et al. (2018)	19
1.10	RV variations of γ Dra. Credit: Hatzes et al. (2018)	24
1.11	Period-luminosity plot of variable giants in the LMC	27
2.1	Analysis of the FEROS RVs and <i>Gaia</i> DR3 scanning law for HD 113283	33
2.2	<i>Gaia</i> DR3 color-magnitude diagram highlighting TOI 1684 and TOI 1489	36
2.3	TESS transit analysis for TOI 1489	39
2.4	FIES RV analysis for TOI 1489	40
2.5	BLS periodograms for TOI 1489	41
2.6	Combined BLS periodogram for TOI 1489	41
2.7	TESS transit analysis for TOI 1684	42
2.8	FIES RV analysis for TOI 1684	44
3.1	Temporal snapshot of an $l = 1, m = 1$ non-radial oscillation mode	52
3.2	Test of the <code>pyoscillot</code> resolution adjustment	57
3.3	Example of a simulated, extracted HARPS spectrum	59
3.4	PHOENIX spectrum broadened by a macroturbulent kernel	61
3.5	Continuum normalization for a PHOENIX spectrum	62
3.6	Measured mean bisector of a normalized PHOENIX spectrum	63
3.7	CCF and bisector simulations for a Sun-like and an evolved star	64
3.8	Limb-darkening intensity as a function of μ at three different wavelengths .	67
3.9	Simulated bisector variations	68

3.10	Simulation of an $l = 1, m = 1$ oscillation mode for three different instruments	70
3.11	Comparison between models including and excluding the limb-darkening correction	72
3.12	Difference in the RV amplitudes per order between the limb-darkening uncorrected and corrected oscillation modes	73
3.13	Change of the amplitude, phase, and offset for the RVs and activity indicator time series as a function of the oscillation parameters	75
3.14	Change of the amplitude, phase, and offset for the RVs and activity indicator time series as a function of the stellar parameters	77
4.1	<i>Gaia</i> DR3 color-magnitude diagram for the open cluster NGC 4349	85
4.2	HARPS RVs for NGC 4349 No. 127	91
4.3	GLS periodograms of the HARPS RVs and activity indicators	93
4.4	Observed and simulated correlations between activity indicators and RVs	94
4.5	Observed and simulated RVs and activity indicators plotted against time	95
4.6	CCFs and bisector profiles for the observed and simulated spectra	97
4.7	RVs and activity indicators of dipole oscillation modes plotted against time	104
4.8	Correlation plots between activity indicators and RVs for modes with $l = 1$, $m = l$, and $m = -l$	105
4.9	Period-luminosity plot of giant stars with RV variations of intrinsic origins	111
5.1	Color-magnitude diagram based on <i>Gaia</i> DR3 photometry	121
5.2	Best Keplerian models for the 12 stars in the sample	129
5.3	MLPs of the RVs and the residuals after subtracting the best Keplerian model	132
5.4	Comparison of the semi-amplitudes between CARMENES VIS and NIR	134
5.5	Results of the linear correlation analysis	136
5.6	Maximum likelihood periodograms for six sample stars	138
5.7	Maximum likelihood periodograms for the remaining six stars	139
5.8	Results of the DBSCAN clustering algorithm	141
5.9	Model of a long-period planet and a short-period GP for HIP 64823	155
5.10	S-BGLS analysis for all 12 stars	156
5.11	Luminosity of the stars plotted against the RV period	160
5.12	Semi-amplitudes of intrinsically RV-variable stars plotted against luminosity	162
6.1	The Waltz telescope peering into the evening sky. Credit: Moritz Kirschner	167
6.2	Model of the Waltz frontend. Credit: Heeren (2021) and Marcelo Tala Pinto	168
6.3	Model of the Waltz spectrograph. Credit: Heeren (2021)	169
6.4	The spare Waltz science fiber imaged by the FN system	174
6.5	The fiber aligned behind the pinhole	174
6.6	S/N per square root of exposure time as a function of V magnitude	175
6.7	Setup of the new PMT location	176
6.8	PMT measurements of the dark level and of a faint star	177

6.9	S/N at 5528 Å as a function of the accumulated PMT counts	178
6.10	The CTI effect visualized using warm pixels in a dark frame	179
6.11	Binned count ratios of warm pixels as a function of CCD columns and rows .	181
6.12	Mean shape of 9928 rows containing warm pixels	183
6.13	Pixel count ratios after applying the CTI correction by Vakhidov (2024) . . .	184
6.14	Preliminary CTI correction test for Aldebaran	185
6.15	RV vs. $(S/N)^2$ for the vertical and horizontal CCD orientations	186
6.16	RV uncertainties σ_{RV} as a function of S/N	187
6.17	Test of the short-term stability	189
6.18	Long-term Waltz RV time series for σ Dra	190
6.19	Waltz RVs for ι Dra	192
6.20	Lick RVs for three long-period candidates	193
6.21	The Waltz telescope monitored in infrared light	194
7.1	Preliminary correlation analysis for NGC 2423 No. 3	199
7.2	RV models for HIP 64823 and a planet candidate in a binary system	201
B.1	Correlation between $H\alpha$ indicator and RV for NGC 4349 No. 127	226
B.2	Observed and simulated photometry for NGC 4349 No. 127	227
B.3	GLS periodogram of the ASAS-3 V-band photometry for NGC 4349 No. 127 .	229
B.4	RVs and activity indicators for modes with $m = l$ plotted against time	230
B.5	RVs and activity indicators for modes with $m = -l$ plotted against time . . .	231
C.1	Corner plot of the joint 1P+GP model for HIP 64283	234

Introduction

” *The more I look at things, I cannot get rid of the feeling that existence is quite weird! When you consider man as a little germ that lives on an unimportant rock ball that revolves around an insignificant star on the outer edges of one of the smaller galaxies. What a put-down that was! But on the other hand - if you think about that for a few minutes - I am absolutely amazed to discover myself on this rock ball rotating around a spherical fire. It's a very odd situation!*

— **Alan Watts**

British “philosophical entertainer” (1915 - 1973)

1.1 Exoplanets - A human perspective



Fig. 1.1.: “A mote of dust suspended in a sunbeam”- Carl Sagan, Pale Blue Dot, 1994.
Credit: NASA/JPL-Caltech

It was February 14, 1990, when NASA’s Voyager 1 spacecraft was rotated to take a final look at its home planet. What resulted is one of the most iconic images in the history of space exploration, one that would be translated into poetic words by famous astronomer Carl Sagan (see Fig. 1.1). This picture shows our home, our “pale blue dot”, covering

only a fraction of a pixel in a stream of reflected sunlight, seemingly questioning the relevance of our doings on a cosmic scale. In the words of Prof. Sagan: “Our posturings, our imagined self-importance, the delusion that we have some privileged position in the universe are challenged by this point of pale light.”

Throughout history, humanity has wondered about the Universe and our place within it. And throughout the millennia, our perspectives have changed dramatically. For nearly 1500 years, dating back to Ptolemy’s *Almagest*, the dominating astronomical world view was the geocentric model, until the works by Polish astronomer Nicolaus Copernicus placed the Sun instead of the Earth into the center of the Universe. In the centuries that followed, our central place on the cosmic stage was further diminished as advances in observational astronomy revealed the vast expanse of our own Milky Way, let alone the distances to other galaxies.

It is thus, perhaps, not surprising that astronomers in the Renaissance, such as Christiaan Huygens, already speculated about the existence of planets orbiting other stars than our Sun. In consequence, already in 1855 the first recorded claim of an exoplanet orbiting the binary star 70 Ophiuchi was made by Capt. W. S. Jacob ([Luther, 1855](#)). Although a false alarm, this was a first step in the hunt for exoplanets, which would finally be successful in 1992, when [Wolszczan & Frail \(1992\)](#) discovered two planets orbiting the pulsar PSR1257+12, succeeded by the first discovery of an exoplanet orbiting a main-sequence star by [Mayor & Queloz \(1995\)](#). These finally revealed that our “pale blue dot” is but one of likely billions of planets within the Milky Way.

In the years that followed, immense progress was made as the field advanced beyond the mere discovery of planets to exploring their compositions, atmospheres, formation, and evolution. This progress is deeply rooted in humanity’s enduring curiosity about the origin and fate of our own home planet. And thus, it is not surprising that we wonder what the future might keep in store for our Earth and the solar system, as the Sun will inevitably evolve off the main-sequence and become a red giant star in a few billion years.

This fate is still a matter of debate (see, e.g., [Sackmann et al. 1993](#); [Schröder & Smith 2008](#); [Veras 2016](#)) as assumptions included in the prediction models, such as the solar mass loss or the strength of tides, critically influence the outcome ([Veras, 2016](#)). A critical input into such models, thus, can be derived by detecting and exploring the planet population around stars that have already undergone this evolution. By comparison with exoplanet systems around stars with similar properties on the main-sequence, the effect of the stellar evolution on the systems can be analyzed (e.g., [Villaver & Livio 2009](#); [Kunitomo et al. 2011](#); [Villaver et al. 2014](#)). At the same time, giant stars also offer a unique opportunity to search for planetary systems around more massive stars, which are inaccessible to the most successful exoplanet detection method at intermediate periods, the radial velocity (RV) method (see [Sect. 1.6](#)), during their main-sequence stage. Thus, they allow for the study

of the differences in planetary systems around stars of various stellar masses, which can be an important independent constraint on planet formation theory (e.g., Currie 2009).

Naturally, answering these research questions relies on a sample of confirmed planets orbiting giant stars that should be as large, unbiased, and reliable as possible. These giants, however, present their unique challenges when studied using the RV method. They are known for short-term RV jitter, caused by p-mode oscillations (see Sect. 1.6.1), which complicates the detection of low-mass planets. More concerning is the recent discovery that several previously confirmed planets are actually misidentified stellar signals of uncertain origin (see Sect. 1.9). Finally, the sample of known planets orbiting giants is still relatively small at short ($P \lesssim 100$ d) and long orbital periods ($P \gtrsim 5$ yr), due to selection effects, intrinsic biases of the detection methods, and baseline limits of observing programs. This thesis aims to contribute toward expanding the number of planets orbiting giants at short and long orbital periods, while, at the same time, aiming to enhance our understanding of the intrinsic processes that can mimic planets at intermediate periods.

1.2 Planets around giant stars

The first exoplanet orbiting a giant was arguably detected even before the first planet orbiting a main-sequence star. Hatzes & Cochran (1993) studied the RV variations of the three giant stars Arcturus, Aldebaran, and Pollux, finding long-period RV variations for each, with those of Pollux being later attributed to a planetary companion (Hatzes et al., 2006; Reffert et al., 2006) (Note the discussion on Aldebaran and Pollux in Sects. 1.9 and 1.10.2). Nevertheless, it took some more years, until the first planets orbiting stars that had already evolved off the main-sequence were unanimously confirmed. These were orbiting the subgiant ϵ Ret (Butler et al., 2001), and the K giant ι Dra (Frink et al., 2002). In the following, I focus only on evolved stars that have already left the subgiant branch and started to ascend the red giant branch (RGB) or have evolved even further.

In consequence, a number of RV surveys began to target giant stars (Setiawan et al., 2003b; Sato et al., 2003; Hatzes et al., 2005; Niedzielski et al., 2007; Lovis & Mayor, 2007; Johnson et al., 2007; Han et al., 2010; Jones et al., 2011; Wittenmyer et al., 2011; Niedzielski et al., 2015). These also include the Lick RV survey of giant stars (Frink et al., 2001), within the context of which this thesis is situated and which is explored in more detail in Sect. 1.5. These surveys, as well as individual detections from other programs, have yielded over 150 planets orbiting giant stars so far.

In Fig. 1.2, I plot the masses and orbital periods of known planets color-coded by the employed detection method.¹ I overplot, as red star symbols, the planets known to orbit

¹Data from <https://exoplanetarchive.ipac.caltech.edu/>

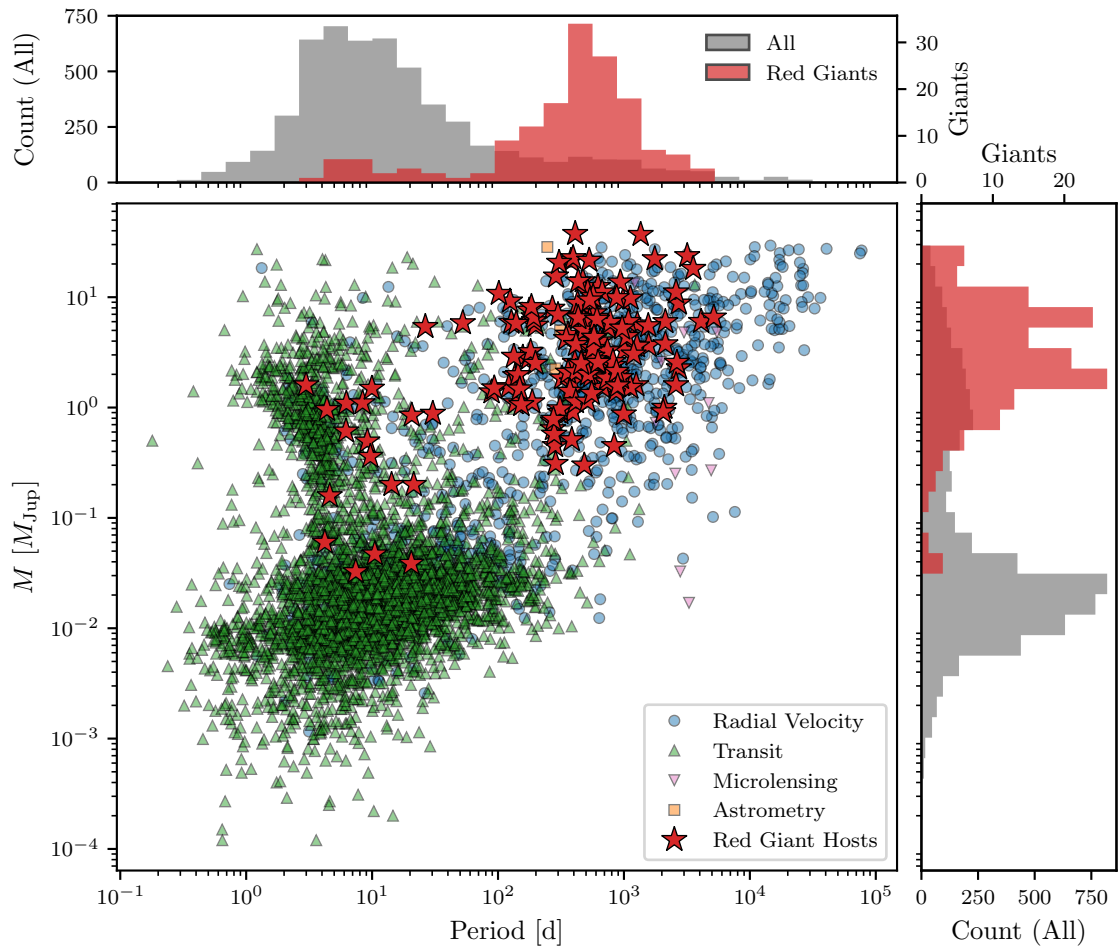


Fig. 1.2.: Masses and periods of known planets orbiting giants and other stars. Top: Histogram of the planetary periods. Note the separate y-axis for the planets orbiting giants. Right: Histogram of the planetary masses. Note that the minimum masses $m_p \sin i$ are plotted for planets detected via the RV method.

giants.² In the top and right panels, I show histograms of the planetary periods and masses, respectively. I note that minimum masses were used for the planets detected solely via the RV method (see Sect. 1.6). For that reason, and due to the varying quality and reliability of online catalogs, such data should not be used for rigorous statistical analyses. Nevertheless, they serve well to yield a first impression of the planet population known around giants.

As can be seen, these planets are typically giant planets with, on average, comparably long orbital periods, which were mostly detected via the RV method. Only few have been found using the transit method (see Sect. 1.7), which is far more successful for main-sequence stars, heavily biasing these planets toward short orbital periods. In fact,

²Data from <https://www.lsw.uni-heidelberg.de/users/sreffert/giantplanets/giantplanets.php> and supplemented by the transiting planets listed in Sect. 1.7.

for a long time no planets with orbits smaller than $a \lesssim 0.7$ AU were found around giants (see, e.g., [Sato et al. 2008](#)), a fact that triggered several studies targeting the orbital evolution of planets during the stellar evolution ([Villaver & Livio, 2009](#); [Kunitomo et al., 2011](#); [Villaver et al., 2014](#)). On the other end of the period distribution, no planets with orbital periods $P \gtrsim 14.2$ yr (only somewhat longer than the orbital period of Jupiter) are yet known, with the record holder being HD 154391 b ([Xiao et al., 2024](#)). The only exception is the long-period brown-dwarf companion present in the ι Dra system, whose orbital parameters are, however, yet weakly constrained ([Hill et al., 2021](#)). While this can certainly be attributed to observational biases, it shows that a large part of the parameter space is yet to be explored.

1.3 The effect of stellar evolution on planetary systems

As briefly touched upon in [Sect. 1.1](#), the fate of the Earth during the evolution of the Sun up the RGB is still not entirely solved ([Veras, 2016](#)). [Schröder & Smith \(2008\)](#) conclude that the chances of Earth avoiding engulfment as the Sun reaches its maximum extent at the tip of the RGB are small. However, if all the uncertainties in the model assumptions aligned favorably, there would still be a small chance of the Earth avoiding this fate. Existing planetary systems around RGB and horizontal branch (HB) stars can yield important observational constraints to such models. It is thus worth to briefly review the effects at play during the stellar evolution. I refer to the excellent review articles by [Veras \(2016\)](#) and [Mustill \(2024\)](#) for more detailed reading. These give also a concise overview of the relevant processes of stellar evolution itself.

The main factor influencing the architecture of planetary systems during the stellar evolution is the balance between the mass loss of the host star and the effect of tides ([Villaver & Livio, 2009](#); [Villaver et al., 2014](#); [Mustill, 2024](#)). In principle, also the planet's mass changes due to material accretion or the evaporation of surface and atmospheric components as temperatures rise. This change of the planetary mass is, however, found to be negligible compared to the change of the host mass ([Villaver & Livio, 2009](#)). A further contribution is given by the gravitational and frictional drag due to the interaction between the planet and the material expelled from the giant. [Villaver & Livio \(2009\)](#) and [Villaver et al. \(2014\)](#), however, also found this to be negligible prior to engulfment.

The mass loss of a star ascending the RGB is significant and much larger than during the main-sequence phase. [Mustill \(2024\)](#), for instance, gives typical mass loss rates of $10^{-14} M_{\odot} \text{yr}^{-1}$ during the main-sequence phase, which can increase up to $10^{-7} M_{\odot} \text{yr}^{-1}$ at the tip of the RGB, with mass loss rates increasing for more massive stars. The host's mass loss, if assumed to be isotropic and occurring on timescales much longer than the orbital period (i.e., adiabatic mass loss), conserves the inclination, eccentricity, and longitude of

periastron of the planetary orbit. Thus, due to the conservation of angular momentum, the orbital distance between planet and star increases (Veras et al., 2011; Mustill, 2024). If the orbital period is comparable to the mass-loss timescale (the non-adiabatic regime, Veras et al. 2011), for instance, for very long-period planets, the orbital elements can be disrupted substantially and bodies can become unbound (Veras et al., 2011; Mustill, 2024).

Tidal forces, on the other hand, have the opposite effect. The relevant tidal mechanism, commonly known as equilibrium tide or stellar tide, leads to a distortion of the spherical shape of the giant star due to the gravitational force exerted by the planetary body (Mustill, 2024). The resulting shape of the star follows the equipotential contours in a rotating reference frame. That is, there are two bulges, one pointing toward the planet and one pointing away from it (Mustill, 2024). Due to the finite response time of the fluid comprising the star, and as giants typically rotate slower than the orbital period of the planet (if close enough for tidal forces to be significant), this bulge lags behind the planet. Thus, the gravitational force between the bulge and the planet transfers angular momentum from the planet's orbital motion onto the stellar rotation, speeding up the latter while slowing down the former. As a result, the planet spirals inward. The stellar tides also dampen the eccentricity of planetary orbits on similar timescales as the dampening of the orbital distance (Mustill & Villaver, 2012). While, in principle, the planetary body can also experience tides, the stellar tides are found to be dominating during the giant branch stages (Mustill & Villaver, 2012; Villaver et al., 2014; Veras, 2016).

Thus, the fate of a planetary system is determined by the balance between the stellar mass loss, which leads to orbital expansion, and the stellar tides, which typically lead to orbital decay (Villaver et al., 2014). Detailed modeling critically depends on assumptions of stellar evolution, mass loss, and tidal theory. Figure 1.3 shows a simulation by Villaver et al. (2014) of a $1 M_{\text{Jup}}$ planet at different initial orbital distances from a $1.5 M_{\odot}$ star as the latter evolves along the RGB. For smaller initial separations (red), the tidal forces dominate over the orbital expansion due to the stellar mass loss and the planet is engulfed. Beyond the black, dotted line, which indicates the distance from the star at which tidal effects start to become negligible, the orbits expand and survive the tip of the RGB. In the intermediate regime (between the solid and dotted black lines) planets spiral inward but avoid engulfment. It is further noteworthy, that engulfment occurs only in a very short timespan ($\delta T \sim 50 \text{ Myr}$) close to the tip of the RGB, and that beyond a certain orbital distance, planetary systems are influenced comparably little by their host's evolution.

Villaver & Livio (2009) and Villaver et al. (2014) found that more massive planets have a higher chance of being engulfed, which follows naturally as the strength of the stellar tides depends on the planetary mass. In contrast, when focusing on stars with masses $1.5 M_{\odot} \leq M_{\star} \leq 2.0 M_{\odot}$, Villaver et al. (2014) show that the mass of the stars has a

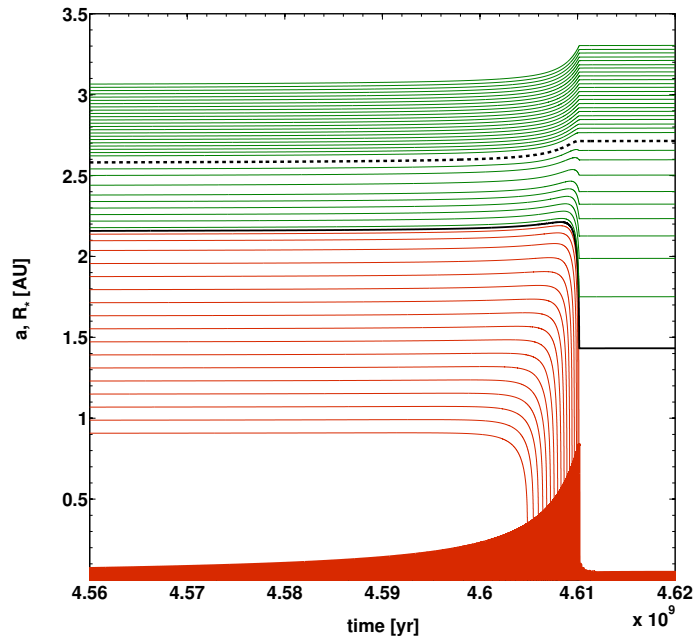


Fig. 1.3.: Simulations of a $1 M_{\text{Jup}}$ planet’s orbit, with varying initial separations, around a $1.5 M_{\odot}$ star during the RGB evolution. The red area indicates the stellar radius. Green lines represent configurations that avoid engulfment, while red configurations are engulfed. The solid black line indicates the minimum distance at which engulfment is avoided, while the dotted black line encodes the orbital distance beyond which tides play an insignificant role. Credit: Villaver et al. (2014), © AAS. Reproduced with permission.

comparably small influence on the outcome of the planetary system, only leading to a minor decrease of the likelihood of being engulfed for more massive stars.

This, however, changes drastically when extending the analysis to higher stellar masses. Villaver & Livio (2009) and Kunitomo et al. (2011) find that planets orbiting stars more massive than about $M \gtrsim 2 M_{\odot}$ can survive at initial separations much closer to the star compared to lower-mass stars. This can easily be understood, as more massive stars do not experience a Helium-flash and thus reach a much smaller maximum radius at the tip of the RGB. Thus, for higher-mass stars, planets can survive further inward and the distance to which stellar tides influence the planets is much reduced.

A further implication that can be derived from models, such as presented in Fig. 1.3, is the expected population of planets orbiting lower-mass, horizontal branch giants. In this specific model, the innermost region of the orbital plane would be cleared from planets after the RGB tip. However, several initially further out planets would have moved inward due to the stellar tides, coming as close to the star as $a \sim 1.5$ AU. Indeed, the planet orbits around the HB stars according to these models would be expected to have a rather distinctive distribution of orbital periods, different from the initial distribution on the

main-sequence. Naturally, a large sample of planets detected around HB stars with similar properties would provide an important test of these models. [Kunitomo et al. \(2011\)](#) compared their predictions of HB systems with the real systems known at the time and conclude that the real systems are found only at larger orbital distances than would be allowed by tidal theory. They suggest that the primordial population of giant planets orbiting more massive stars is likely fundamentally different, such as suggested by [Currie \(2009\)](#). See also the discussion by [Reffert et al. \(2015\)](#).

Finally, [Villaver et al. \(2014\)](#) made the interesting observation that stellar tides should not lead to rapid engulfment of planets with orbital distance $0.08 \text{ AU} < a < 0.5 \text{ AU}$ until the later stages of the RGB (see again [Fig. 1.3](#)). Thus, the lack of these planets from the earlier RV surveys cannot be explained by tidal theory alone and encourages searches for planets occupying this parameter space ([Veras, 2016](#)). [Sect. 1.7](#) and [Chapt. 2](#) touch upon whether the transit method can contribute toward enhancing the number of close-in planets.

1.4 Planet occurrence rate around giant stars

One of the most important reasons to specifically target evolved stars in planet searches is that they allow the study of stars more massive than about $1.5 M_{\odot}$ in RV surveys. The RV method is not sensitive to these stars while on the main-sequence due to few spectral lines and high rotation velocities (discussed in more detail in [Sect. 1.6](#)). The most comprehensive study has recently been conducted by [Wolthoff et al. \(2022\)](#), combining the planet detections from three large RV surveys. [Fig. 1.4](#) presents their giant planet occurrence rate as a function of the stellar mass (left) and as a function of the host metallicity (right). They find the occurrence rate to peak at $1.68 M_{\odot}$, which is consistent with the earlier studies by [Reffert et al. \(2015\)](#) and [Jones et al. \(2016\)](#). All three studies find no planets at masses $M > 3 M_{\odot}$, which is consistent with the predictions by planet formation theory (e.g., [Kennedy & Kenyon 2008, 2009](#); [Currie 2009](#)), as higher mass stars are predicted and observed to disperse their planet forming disks more quickly ([Burkert & Ida, 2007](#); [Ribas et al., 2015](#); [Gaidos et al., 2025](#)).

[Wolthoff et al. \(2022\)](#) also confirm a positive correlation between the occurrence rate of giant planets and the host metallicity ([Fig. 1.4](#), right), which had previously been reported ([Reffert et al., 2015](#); [Jones et al., 2016](#); [Ghezzi et al., 2018](#)). They find the dependence to be somewhat reduced compared to the well-established correlation found for main-sequence stars (e.g., [Fischer & Valenti 2005](#); [Udry & Santos 2007](#)), which might be explained by a suggested connection between orbital period and host metallicity ([Jenkins et al., 2017](#); [Petigura et al., 2018](#)) that could lead to an enhanced engulfment of planets in metal-rich systems. The giant planet-metallicity correlation is an important condition to

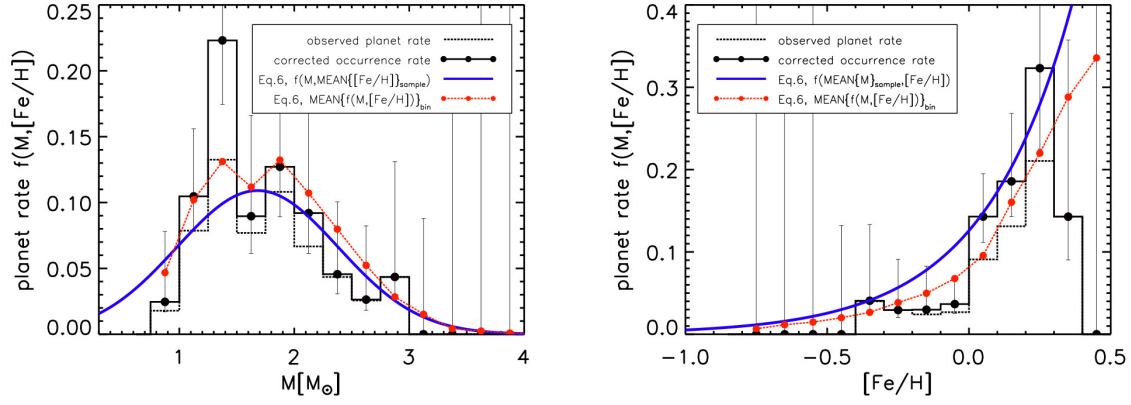


Fig. 1.4.: Planet occurrence rate as a function of host mass (left) and of host metallicity (right). Dotted bins indicate the occurrence rates of detected planets, while solid bins show these rates corrected for survey completeness. Overplotted in blue is a fit of the occurrence rate, modeled as an exponential distribution in metallicity and a Gaussian distribution in mass (their Eq. 6). The red dots indicate the expected occurrence rate for the actual stars located in each bin within the sample. Credit: [Wolthoff et al. \(2022\)](#). Reproduced with permission from Astronomy & Astrophysics, © ESO.

be explained by planet formation theory (e.g., [Johnson & Li 2012](#); [Maldonado et al. 2019, 2025](#)).

[Fig. 1.5](#), adopted from [Wolthoff et al. \(2022\)](#), further shows the giant planet occurrence rate as a function of orbital period. As can be seen, the relation peaks at around $P \sim 700$ d, at shorter periods than found for main-sequence stars ([Fernandes et al., 2019](#)). This is contrary to the expectations, as the snow lines for more massive stars should be located further out ([Wolthoff et al., 2022](#)). This discrepancy cannot yet be resolved.

Overall, they find the giant planet occurrence rate for giant stars to be $10.7_{-1.6}^{+2.2}$ %. The occurrence rate is slightly enhanced for stars yet ascending the RGB ($14.2_{-2.7}^{+4.1}$ %) compared to stars on the HB ($6.6_{-1.3}^{+2.0}$ %). In principle, this would be consistent with the general expectation from the stellar evolution, as planets would most likely be engulfed close to the tip of the RGB (see [Sect. 1.3](#)). However, at least for the Lick sample, most detected planets are too distant from the stars to have been affected strongly by their hosts' evolution ([Reffert et al., 2015](#)). Instead, [Wolthoff et al. \(2022\)](#) argue that the difference in the occurrence rates can be accounted for by different mass distributions among the stellar hosts on the RGB and HB and can thus not be seen as evidence of planet engulfment.

1.5 The Lick RV survey

The Lick RV survey, which is of special interest within the context of this thesis, was a long-term monitoring campaign of 373 G and K giant stars. It was started in 1999

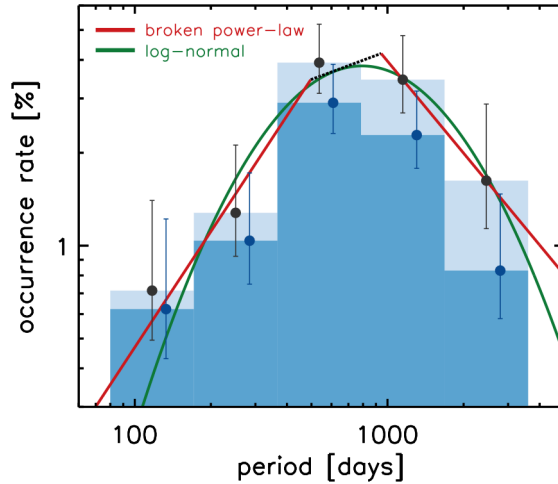


Fig. 1.5.: Planet occurrence rate as a function of orbital period. The dark blue histogram portrays the occurrence rate of detected planets, while the light blue bins show the occurrence rates corrected for survey completeness. A broken power-law (red) and log-normal (green) distribution have been fitted to the corrected occurrence rates. Credit: [Wolthoff et al. \(2022\)](#). Reproduced with permission from Astronomy & Astrophysics, © ESO.

using the Hamilton Spectrograph ([Vogt, 1987](#)) mounted at the 60 cm Coudé Auxiliary Telescope (CAT) located at UCO/*Lick* in California, USA. The survey originally comprised 86 K giants selected from the HIPPARCOS catalog ([ESA, 1997](#)) to be photometrically stable and to be single stars ([Frink et al., 2001](#)). These stars were originally searched for binary companions in order to serve as astrometrically stable grid stars for NASA’s Space Interferometry Mission (SIM) ([NASA, 1999](#)), which was, however, canceled. The sample was extended in 2000 and 2004 by 96 and 194 stars, respectively, relaxing the constraints on photometric stability and including G and K giants of bluer colors ([Reffert et al., 2015](#)). Nevertheless, the photometric variability still remained below 0.01 mag. Three stars were excluded due to being visual binaries ([Reffert et al., 2015](#)). All stars are very bright with V magnitudes ranging from $V = -0.05$ mag (Arcturus) to $V = 6.0$ mag.

The stellar parameters for all but one star in the sample were derived consistently by [Stock et al. \(2018\)](#) using Bayesian inference on a grid of PARSEC stellar evolutionary models ([Bressan et al., 2012](#)). [Stock et al. \(2018\)](#) find 70 out of the 372 stars to be most likely located on the RGB, with the remaining 302 stars situated on the HB. Figure 1.6 shows a histogram of the masses, radii, and luminosities of the sample stars, differentiating between RGB stars (red) and HB stars (blue). The HB sample is somewhat more massive than the RGB sample, with mean mass $\overline{M}_* = 2.4 M_\odot$, compared to $\overline{M}_* = 1.3 M_\odot$ for the RGB sample. One can further observe that a sizable fraction of the stars have relatively large radii ($R \gtrsim 20 R_\odot$) and high luminosities ($L \gtrsim 100 L_\odot$), which is of relevance due to the planet controversy discussed for such stars in [Sect. 1.9](#).

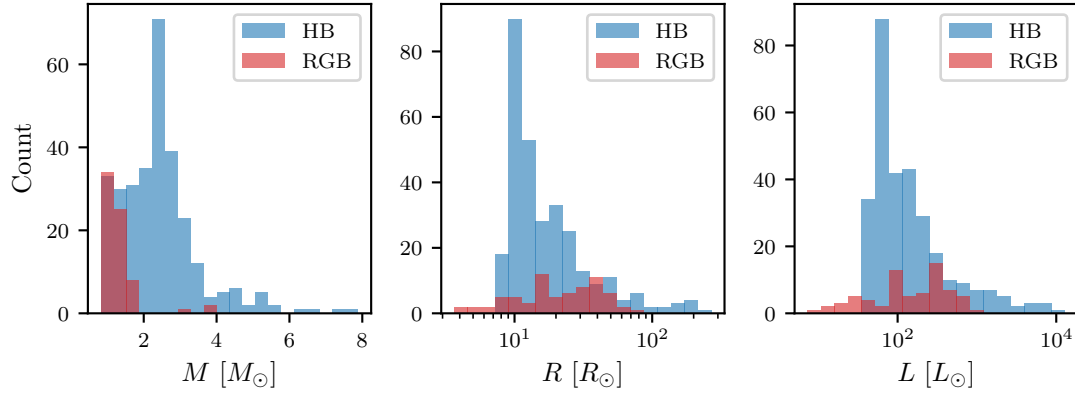


Fig. 1.6.: Histograms (Mass, Radius, Luminosity) of the stellar parameters derived by [Stock et al. \(2018\)](#) for 372 stars in the Lick sample.

Using the Hamilton spectrograph with $R \sim 50000$, the Lick RV survey employed the iodine cell technique (see [Sect. 1.6.2](#)) to achieve a typical RV precision $\sigma_{\text{RV}} \sim 5 - 8 \text{ m s}^{-1}$ ([Reffert et al., 2015](#)). It came to its unfortunate preliminary end in 2011 as the iodine cell was damaged by a heater malfunction ([Fischer et al., 2013](#)). Over its twelve years, nearly 14 000 RV measurements were taken. For the most interesting stars, observations were scheduled with about a monthly cadence, while for other stars the cadences were as infrequent as about one observation per year.

The survey detected the first planet orbiting a giant star, namely ι Dra b ([Frink et al., 2002](#)). Further 17 planets (including brown dwarfs) in 14 stellar systems were found among stars present in the Lick sample ([Hatzes et al., 2006](#); [Reffert et al., 2006](#); [Sato et al., 2007](#); [Liu et al., 2008](#); [Schwab, 2010](#); [Wittenmyer et al., 2011](#); [Mitchell et al., 2013](#); [Trifonov et al., 2014](#); [Lee et al., 2014](#); [Ortiz et al., 2016](#); [Takarada et al., 2018](#); [Quirrenbach et al., 2019](#); [Luque et al., 2019](#); [Tala Pinto et al., 2020](#); [Teng et al., 2023a](#)). I note that these include the planet published to orbit HIP 16335 ([Lee et al., 2014](#)), which is discussed in [Chapt. 5](#). A recent overview of most systems can be found in [Wolthoff et al. \(2022\)](#).

The survey further comprises around 20 stars which are classified as planet candidates ([Reffert et al., 2015](#)). These are stars that show (semi-) periodic RV variations but with larger-than-expected RV jitter or otherwise challenging RV curves. Several systems also host planetary candidates and additional large-amplitude, long-term RV variations, likely due to stellar companions. Lastly, there is a number of stars showing long-term trends (linear, quadratic, or resembling partially sampled sinusoids), which could be indicative of long-period planetary or brown-dwarf companions.

After the conclusion of the Lick survey, it was decided to build a new échelle spectrograph to be mounted at the 72 cm Waltz telescope at Landessternwarte (LSW), Heidelberg, to continue the survey ([Tala et al., 2016](#)). In the meantime, select stars were monitored using

CRIRES (Kaeufl et al., 2004; Mitchell et al., 2013; Trifonov et al., 2014, 2015; Ortiz et al., 2016), the Hertzprung/SONG spectrograph on Tenerife, Spain (Grundahl et al., 2007; Andersen et al., 2014; Grundahl et al., 2017; Fredslund Andersen et al., 2019; Heeren et al., 2021), as well the CARMENES spectrograph at Calar Alto, Spain (Quirrenbach et al., 2014).

This thesis aims to analyze many of the planet candidates, which remained inconclusive after the end of the Lick survey. For this purpose, I combine Lick data with spectra taken by SONG and CARMENES in [Chapt. 5](#). I further aim to enable continued long-term monitoring of the entire sample using the Waltz telescope. While the whole sample will be targeted, a special emphasis will be put on planet candidates, stars with long-term trends, and planet candidates in binary systems. The steps toward enabling these observations, as well as first on-sky tests of the Waltz telescope, are detailed in [Chapt. 6](#).

1.6 The radial velocity method applied to giant stars

The fundamental idea of the radial velocity method is to measure a star’s reflex motion along the line of sight induced by the presence of an orbital companion. This can be achieved by the means of high-resolution spectroscopy, making use of the Doppler effect. That is, measuring the periodic shift in wavelength of the stellar spectral lines as the star is moving toward (negative RV) and away from (positive RV) the observer along its orbit around center of mass of the star-planet system.

The change of the RVs as a function of time can be described using Keplerian orbits, which are explored in detail, for instance, in [Murray & Correia \(2010\)](#), [Perryman \(2018\)](#), or [Trifonov \(2024\)](#). The semi-amplitude K_\star of the host star’s RV curve, can be expressed using typical quantities as ([Lovis, 2010](#))

$$K_\star = \frac{28.4329 \text{ m s}^{-1}}{\sqrt{1 - e^2}} \frac{m_p \sin i}{M_{\text{Jup}}} \left(\frac{m_\star + m_p}{M_\odot} \right)^{-\frac{2}{3}} \left(\frac{P}{1 \text{ yr}} \right)^{-\frac{1}{3}}. \quad (1.1)$$

Here, m_\star and m_p describe the masses of star and planet, respectively, while P and e represent the period and eccentricity of the orbit. As can further be seen from [Eq. 1.1](#), the RV method is fundamentally limited to measuring a planet’s “minimum mass” $m_p \sin i$, with i being the unknown inclination angle, since only the projected velocities along the line of sight can be measured ([Lovis, 2010](#)). This degeneracy can only be lifted by combining the RV method with additional information, such as that provided by the transit (see [Sect. 1.7](#)) or astrometric methods (see [Sect. 1.8](#)). Using [Eq. 1.1](#), one can see that a Jupiter-like exoplanet orbiting a Sun-like star on a circular orbit with $P = 1 \text{ yr}$ induces a periodic RV variation of semi-amplitude $K_\star = 28.4329 \text{ m s}^{-1}$, which reduces to merely $K_\star \sim 9 \text{ cm s}^{-1}$ for an Earth-analog.

Achieving such precision in the RVs is challenging and depends on the properties of the spectrograph and the targeted star. The RV precision is proportional to (Hatzes, 2019)

$$\sigma_{\text{RV}} \propto (\text{S/N})^{-1} R^{-1.2} \Delta\lambda^{-1/2} f(v \sin i) f(\text{Spec.type}), \quad (1.2)$$

where S/N is the spectrum's signal-to-noise ratio, R and $\Delta\lambda$ are the instrument's resolving power and wavelength coverage, and $f(v \sin i)$ and $f(\text{Spec.type})$ are functions encoding the dependence of the RV precision on the projected rotation velocity and spectral type of the star, respectively. The former can be fit by (Hatzes, 2019)

$$f(v \sin i) \propto 0.62 + (0.21 \log R - 0.86) \cdot v \sin i + (0.0026 \log R - 0.0103) \cdot (v \sin i)^2, \quad (1.3)$$

which for fast rotators ($v \sin i > 10 \text{ km s}^{-1}$) scales roughly as $f(v_{\text{rot}}) \propto (v \sin i)^{1.3}$. The spectral type of the star, and thus its effective temperature, influences the RV precision roughly as $f(\text{Spec.type}) \sim 0.16 \exp(1.79 \frac{T_{\text{eff}}}{5000 \text{ K}})$ for $T_{\text{eff}} > 5000 \text{ K}$ (Hatzes, 2019), encoding the number of spectral lines. From these scaling relations, one can deduce why targeting giant stars is the only means to achieve high enough RV precision to detect exoplanets for stars more massive than about $1.5 M_{\odot}$. Their progenitors on the main-sequence, which are of spectral types F5 or earlier, have high surface temperatures and are fast rotators, which quickly suppresses the achievable RV precision (Sato et al., 2003; Galland et al., 2005; Johnson et al., 2007; Lagrange et al., 2009; Assef et al., 2009; Trifonov, 2024).

From Eq. 1.2, one can also infer the need for a high spectral resolving power R . Typically, cross-dispersed échelle spectrographs with $R \gtrsim 50000$ are employed (see Eversberg & Vollmann 2015 for a thorough introduction), which allow for a compact design at high resolving powers. State-of-the-art spectrographs, such as HARPS (Mayor et al., 2003), CARMENES (Quirrenbach et al., 2014), or ESPRESSO (Pepe et al., 2021) utilize simultaneous calibration sources such as Thorium-Argon (ThAr) lamps, Fabry-Pérot etalons (see, e.g., Coffinet et al. 2019; Schäfer et al. 2018; Pepe et al. 2021; Bauer et al. 2015), or laser frequency combs (Reichert et al., 1999; Udem et al., 2002; Pepe et al., 2021; Schmidt & Bouchy, 2024) to achieve a precise wavelength calibration. However, such instruments need to be in extremely stable environmental conditions in terms of ambient temperature and pressure and are typically enclosed in vacuum chambers to avoid thermal drifts. While relatively costly, RV precision $\sigma_{\text{RV}} < 1 \text{ m s}^{-1}$ can be achieved, with ESPRESSO even aiming for a long-term RV precision $\sigma_{\text{RV}} \sim 10 \text{ cm s}^{-1}$ (Pepe et al., 2021).

These instruments further have the important advantage of obtaining stable instrumental profiles (IPs) (Perryman, 2018; Hatzes, 2019), which allow for studying more subtle changes of, for instance, the shapes of spectral lines, which can otherwise be dominated by instrumental effects. This allows the reliable determination of additional metrics sensitive to various types of intrinsic processes in stars (see Sect. 1.6.3). Such intrinsic variations also become the main concern when searching for true Earth-analogs orbiting

main-sequence stars (Fischer et al., 2016; Perryman, 2018). Such stars have RV “jitter” of the order of 1 m s^{-1} caused by the granulation, short-term activity variations, star spots, long-term magnetic cycles, and short-term p-mode oscillations (Perryman, 2018).

1.6.1 p-mode oscillations

In convective atmospheres of lower-mass ($M \lesssim 2 M_{\odot}$, Hekker 2013) main-sequence stars, subgiants, or giant stars, turbulent convective motions can excite standing waves (Bedding & Kjeldsen, 2003). These oscillations are intrinsically damped but get stochastically excited by the convective motions and are called p-modes, as pressure is the restoring force (Christensen-Dalsgaard, 2005; Hekker & Mazumdar, 2013). Typically, many oscillation modes, both radial and non-radial ones, are excited (Bedding & Kjeldsen, 2003; Hekker & Mazumdar, 2013). A thorough introduction into the basics of stellar oscillations can be found in review articles or textbooks such as Kurtz (2006) or Aerts (2021).

As the oscillations for all stars with convective zones are excited by very similar physics and have similar properties, these oscillations are also referred to as “solar-like oscillations”. For the Sun, these p-modes have a typical period of roughly five minutes and a peak RV amplitude of about 23 cm s^{-1} (Hatzes, 2019). Analyzing the p-mode oscillations using power spectra of photometric or RV data sets reveals a distinctive pattern (e.g., Bedding & Kjeldsen 2003), which can be used to determine fundamental solar (or stellar) properties and further, more advanced physics (see, e.g., the overview by Aerts 2021). For stars other than the Sun, Kjeldsen & Bedding (1995) proposed scaling relations to derive the period of maximum power, as well as the typical RV amplitude:

$$P_{\text{max}} = \frac{(R/R_{\odot})^2 \sqrt{T_{\text{eff}}/5777 \text{ K}}}{M/M_{\odot}} \cdot 5.46 \text{ min} \quad (1.4)$$

$$v_{\text{osc}} = \frac{L/L_{\odot}}{M/M_{\odot}} \cdot (0.234 \pm 0.014) \text{ m s}^{-1} \quad (1.5)$$

Thus, for giant stars, the typical periods of the oscillations are hours to days with RV amplitudes ranging from a few m s^{-1} to several tens of m s^{-1} . For the typically low observing cadences of RV planet surveys, the p-mode oscillations effectively present a white noise component in the data. For the Lick giants, Hekker et al. (2006) found typical amplitudes in the range $10 - 20 \text{ m s}^{-1}$ for the most stable stars in the sample. Frink et al. (2001) showed that this RV jitter increases for stars with redder colors, while Hekker et al. (2008) correlated the RV jitter with the surface gravity of the stars, $\log g$, showing that lower surface gravities strongly enhance the jitter amplitudes. I note that the non-radial p-mode oscillations for giant stars can couple to g-mode oscillations (gravity as the restoring force) in the core, resulting in so-called mixed modes (e.g., Hekker & Mazumdar 2013).

1.6.2 The iodine cell method

As a consequence of the sizable RV jitter, the costly process of obtaining an RV precision $\sigma_{\text{RV}} < 1 \text{ m s}^{-1}$ is less critical when targeting giants. Instead, many surveys employ the iodine cell method pioneered by [Campbell & Walker \(1979\)](#) (using hydrogen fluoride), [Cochran & Hatzes \(1990\)](#), [Marcy & Butler \(1992\)](#), [Valenti et al. \(1995\)](#), and [Butler et al. \(1996\)](#). In this method, a glass tube filled with I_2 gas heated to $T \sim 50^\circ\text{C}$ is placed into the light path, which leaves a dense forest of fine iodine absorption lines imprinted on the spectrum. The iodine lines are most prevalent in the wavelength regime $5000 \text{ \AA} - 6000 \text{ \AA}$. The shift in wavelength $\Delta\lambda$ is then determined by dividing the spectrum in many small chunks and forward modeling each chunk using a high S/N template observation T_\star , which was deconvolved from the instrumental profile beforehand, and a high-resolution laboratory spectrum of the iodine gas T_{I_2} following ([Butler et al., 1996](#))

$$I_{\text{obs}} = k \cdot [T_{I_2}(\lambda) \cdot T_\star(\lambda + \Delta\lambda)] * \text{LSF}. \quad (1.6)$$

Here, the latter term encapsulates the modeling of the line spread function (LSF) of the spectrograph, while k describes the model of the continuum within the chunk. Using this setup, a traditional RV precision $\sigma_{\text{RV}} \sim 3 \text{ m s}^{-1}$ has been achievable ([Valenti et al., 1995](#); [Butler et al., 1996](#)), while updated spectrograph designs as in HIRES/Keck ([Vogt et al., 1994](#); [Butler et al., 2017](#)) or SONG ([Andersen et al., 2014](#)) even reach RV precision at the 1 m s^{-1} level. The iodine cell method was also employed at the Hamilton/Lick spectrograph (see [Sect. 1.5](#)) and is used at the Waltz telescope (see [Chapt. 6](#)). The iodine cell method is thus perfectly capable of searching for massive planetary companions orbiting giants. The use of stabilized spectrographs for more detailed analyses of the stellar spectral properties targeting intrinsic variations is explored in [Chapts. 4 and 5](#).

1.6.3 Activity indicators

Over the years, a range of additional metrics have been developed that are sensitive to intrinsically induced RV variations. That is, RV variations that are not caused by a planet but are instead mimicked by phenomena occurring in the star. As most of these metrics have been developed in the context of RV surveys targeting main-sequence stars, for which magnetic activity (e.g., spots, plages) is typically the main concern, these are commonly referred to as “activity indicators”. How sensitive these are for other types of phenomena, such as long-period stellar oscillations, is discussed in [Chapts. 3, 4, and 5](#).

To test whether a RV signal is intrinsically induced, it is common to search for variations of these indicators at similar periods as the RVs, or to search for correlations between these metrics and the RVs. If any such variations or correlations are present, it is typically

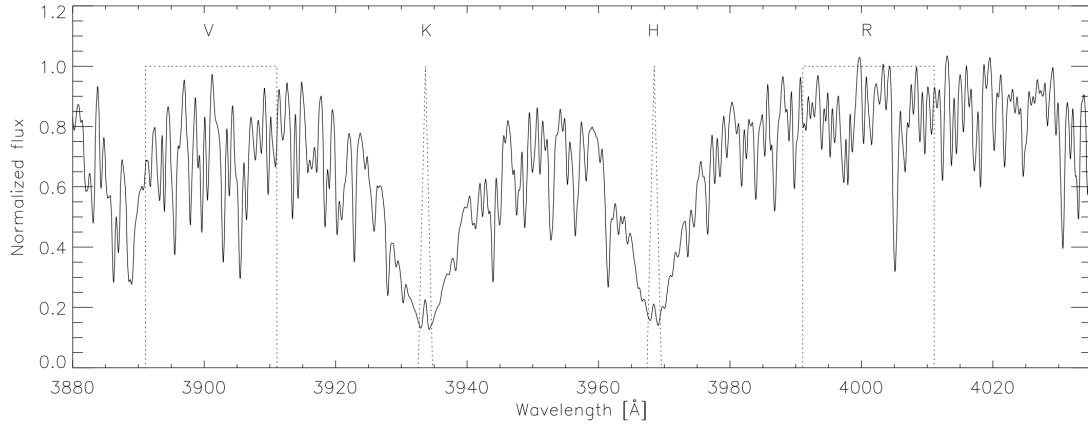


Fig. 1.7.: Spectral region around the Ca II H and K lines for the F-type star HD 48676. A reversal due to chromospheric emission can be observed in the line cores. The regions used to compute the Mt. Wilson S-Index (Eq. 1.7) are marked as dotted areas. Credit: Schröder et al. (2009). Reproduced with permission from Astronomy & Astrophysics, © ESO.

regarded as a strong sign against a planetary origin of the RV variations (Hatzes, 2019). A straight-forward metric is the comparison of the RVs with simultaneous photometry (Hatzes, 2019). Most other metrics are typically secondary information that can be derived from high-resolution spectra.

Individual spectral lines

The traditional activity indicators target variations in prominent spectral lines, such as the Ca II H and K lines (3933.7 Å and 3968.5 Å) or the H α line (6562.8 Å). In cool stars, the cores of these lines are formed in the stellar chromosphere (Hatzes, 2019). Magnetic activity can lead to chromospheric heating and plagues, which both lead to emission in these lines. For very active stars that can be observed as a line inversion in the core of the line, while for less active stars this typically only leads to a filling of the spectral line, decreasing its depth (Hatzes, 2019; Gomes da Silva et al., 2011). Figure 1.7 (Schröder et al., 2009) shows the spectral region surrounding the Ca II H and K lines for the F-type main-sequence star HD 48676. In the cores of the spectral lines, one can observe a reversal.

One commonly used metric to quantify this line inversion is the Mt. Wilson S-index (Vaughan et al., 1978; Baliunas et al., 1995). It calculates the flux ratio between the cores of the H and K lines, F_H and F_K , and two adjacent continuum regions, F_V and F_R (see Fig. 1.7), as (Baliunas et al., 1995; Schröder et al., 2009; Hatzes, 2019):

$$S = \alpha \frac{F_H + F_K}{F_V + F_R}. \quad (1.7)$$

Here, α is a calibration factor. While the absolute value of S can give a measurement of the overall magnetic activity, in the context of RV surveys the temporal variations of S are typically most relevant (Hatzes, 2019). Similar metrics target other spectral lines, such as the H α line (Kürster et al., 2003; Bonfils et al., 2007; Boisse et al., 2009), the Ca II infrared triplet (IRT), the Na I D lines (Gomes da Silva et al., 2011; Zechmeister et al., 2018), or the He I D3 triplet (Boisse et al., 2009; Gomes da Silva et al., 2011). In context of the CARMENES survey targeting M dwarfs (Ribas et al., 2023), also the TiO bands proved to be sensitive to activity (Schöfer et al., 2019). For the Lick sample, Staudt (2020) has developed a metric for the variations of the H α line.

Variations of the spectral line shapes

Other metrics try to quantify variations of the shapes of spectral lines. Such metrics can be derived either from individual lines or from averaged line profiles, such as available as a natural by-product when reducing the RVs using a cross-correlation function (CCF) with a line mask (e.g., Baranne et al. 1996; Lafarga et al. 2020). These metrics include measurements of line bisectors (e.g., Dravins 1987; Gray & Nagel 1989; Queloz et al. 2001), or the width or depth of spectral lines (e.g., Lafarga et al. 2020).

Figure 1.8 (Lafarga et al., 2020) illustrates a common set of metrics that can be derived from the CCF. These are its full width at half maximum (FWHM) and depth (contrast), typically derived by fitting a Gaussian profile. Zechmeister et al. (2018) proposes to quantify the second moment of the line shapes without the use of a CCF via the differential linewidth (dLW). The dLW correlates with the FWHM and the contrast (Zechmeister et al., 2018; Jeffers et al., 2022).

Figure 1.8 further illustrates the CCF bisector (gray), for which a zoom-in is shown in the right panel. Lafarga et al. (2020), following Queloz et al. (2001), defines the BIS as the difference between the average RV in the top (90 – 60%) and bottom (40 – 10%) (shaded areas) parts of the CCF ($BIS = \overline{RV}_{top} - \overline{RV}_{bot}$). Several other, similar metrics exist to quantify variations of the line bisectors (e.g., Hatzes 1996; Gray 1997; Boisse et al. 2011; Figueira et al. 2013). The sensitivity of bisector measurements, however, depends on the quality of the spectra, and loses sensitivity at low rotation velocities (e.g., Saar & Donahue 1997; Saar et al. 1998; Santos et al. 2003).

Such metrics also rely on the stability of the spectrograph, as variations of the LSF can dominate over spectral line variations of stellar origin. Although attempted in the past (e.g., Reffert et al. 2006), these are typically not derived from non-stabilized spectrographs.

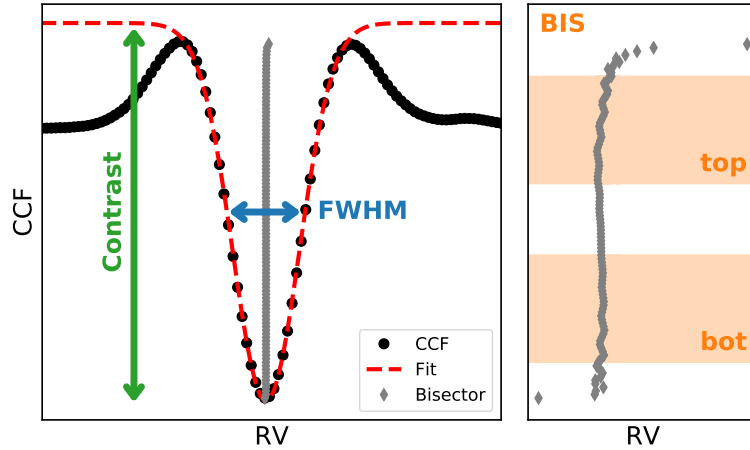


Fig. 1.8.: Illustration of the CCF and its associated activity indicators targeting the width (FWHM), depth (Contrast), and bisector (BIS). Right: Zoom-in on the bisector to illustrate the two regions used to compute the velocity difference. Credit: Lafarga et al. (2020). Reproduced with permission from Astronomy & Astrophysics, © ESO.

Analyzing the chromatic behavior of the RVs

If RV periodicity is caused by a planet, one would expect a consistent RV amplitude to be measured across all wavelength regimes. Spectrographs that do not employ an iodine cell, typically measure the RVs independently in each spectral order and average these order RVs to derive a more precise measurement (e.g., Zechmeister et al. 2018). As each spectral order covers a different wavelength range, a high enough precision on the individual order RVs allows for measuring trends with wavelength, such as illustrated in Fig. 1.9.

Zechmeister et al. (2018) defines the chromatic index (CRX, labeled as β in Fig. 1.9) as the slope of the RVs per order o as a function of their central wavelength λ_o as

$$v(o) = v + \text{CRX} \cdot \ln \frac{\lambda_o}{\lambda_v}. \quad (1.8)$$

Here, λ_v is the wavelength at which the function is equal to the averaged RV. The CRX is measured in units of $\text{m s}^{-1} \text{Np}^{-1}$ (Zechmeister et al., 2018). Implementing a similar metric for the reduction of iodine cell spectra was attempted by Heeren et al. (2023), however, the results need further improvement and testing. One problem in such spectrographs is the limited wavelength range used to determine the RVs (about 5000 – 6200 Å) compared to stabilized spectrographs (see, e.g., Fig. 1.9 for the visual channel of CARMENES).

Another way to check for any chromatic behavior of the RVs is to compare the amplitudes measured in spectrographs that cover different wavelength regimes, for instance the optical and the near-infrared. This is made possible by spectrographs such as CARMENES, CRIRES (Kaeufl et al., 2004), or CRIRES+ (Dorn et al., 2023). Such tests have been

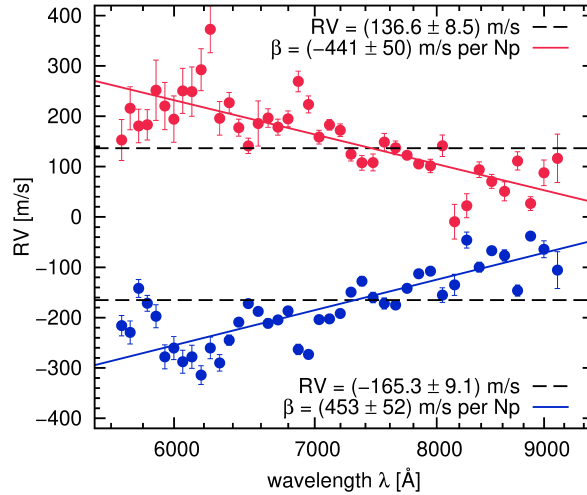


Fig. 1.9.: RVs measured for individual orders plotted against the central wavelength of the orders. Two different spectra, measured at different epochs (red, blue), are shown. Trends following Eq. 1.8 were fitted to the data. Their slopes β (referred to as CRX in the main text) and averaged RVs are listed. Credit: Zechmeister et al. (2018). Reproduced with permission from Astronomy & Astrophysics, © ESO.

successfully conducted for main-sequence stars (e.g, Huélamo et al. 2008) and giants (Mitchell et al., 2013; Trifonov et al., 2014, 2015; Ortiz et al., 2016).

1.7 The transit method applied to giant stars

While the RV method is sensitive to the minimum mass of exoplanets, the transit method targets their radii. The fundamental idea is very simple. If the orbital plane of the planetary system and the line of sight align favorably, then the planet will periodically block a part of the light emitted by the stellar disk and thus reduce the star’s observed brightness. If monitored at high temporal cadence, a transit light curve can be observed. The relative depth of the transit $\frac{\Delta F}{F}$ can be estimated from the radii of the planet R_p and the star R_\star as (see, e.g., Haswell 2010)

$$\frac{\Delta F}{F} = \left(\frac{R_p}{R_\star} \right)^2. \quad (1.9)$$

Thanks to its advantage of being applicable to whole fields of the night sky, enabling the monitoring of thousands of stars simultaneously, the transit method has been the most successful exoplanet detection technique yielding over 74% of all detected exoplanets, with the most prominent space-borne missions such as *Kepler* (Borucki et al., 2010), K2 (Howell et al., 2014), and TESS (Ricker et al., 2015) accounting for nearly 90% of all confirmed transiting planets.³ Naturally, the full potential of the transiting technique is

³https://exoplanetarchive.ipac.caltech.edu/docs/counts_detail.html

only unlocked when being combined with subsequent RV measurements which can yield the planet's true mass (as the inclination i can be constrained) and thus its density. For more in-depth introductions to the transiting method, I refer to textbooks such as [Haswell \(2010\)](#), [Perryman \(2018\)](#), or [Deeg & Alonso \(2018\)](#).

The early results of the RV studies targeting giant stars revealed a distinctive lack of close-in planets ([Johnson et al., 2007](#); [Sato et al., 2008](#)), despite the RV method's intrinsic bias to detect such planets and despite the fact that these were commonly found around main-sequence stars (see, e.g., [Mayor & Queloz 1995](#); [Charbonneau et al. 2000](#)). It was thus suspected that such planets could be very rare around giants, either due to planet engulfment during the stellar evolution ([Sato et al., 2008](#); [Villaver & Livio, 2009](#); [Villaver et al., 2014](#)) or due to primordial differences, as the giant stars are on average more massive than known main-sequence host stars, which is linked to a faster gas dissipation within the protoplanetary disks and thus a halt of planet migration ([Burkert & Ida, 2007](#); [Currie, 2009](#); [Ribas et al., 2015](#); [Gaidos et al., 2025](#)).

The transit method is further more challenging to apply to giant stars, as the transit depth is strongly decreased by larger stellar radii (Eq. 1.9), while transit durations increase (see, e.g., Eq. 14 in [Winn 2010](#)). These long transit durations largely disabled early ground based surveys from detecting transiting planets around giants as these complicate the data reduction of photometric time series, which typically involve the removal of systematic trends in the data ([Assef et al., 2009](#)). The much longer timescales of the p-mode oscillations, especially for rather evolved giants, also pose a challenge to light curve extraction pipelines developed for space-borne missions, as longer-period stellar variations can be misidentified as instrumental systematics (e.g., [North et al. 2017](#)). Furthermore, as giants typically show larger intrinsic photometric variability (e.g., [Aigrain et al. 2009](#); [North et al. 2017](#)) they were actively removed from the initial target sample of the *Kepler* mission ([Batalha et al., 2010](#); [Brown et al., 2011](#); [Grunblatt, 2024](#)). Nevertheless, due to lucky oversights, as well as the later K2 and TESS missions, which also allowed for monitoring giants, a few transiting planets orbiting giants could be confirmed.

An attempt at a (likely non-exhaustive) summary of the transiting planets orbiting giant stars - selected via $\log(g) \lesssim 3.5$ - reveals 16 planets orbiting 14 stars, which could be classified as being at least in the early stages of the RGB. These include: Kepler-56 b and c ([Huber et al., 2013](#); [Steffen et al., 2013](#)), Kepler-91 b ([Lillo-Box et al., 2014](#)), Kepler-391 b and c ([Rowe et al., 2014](#)), Kepler-432 b ([Ortiz et al., 2015](#); [Ciceri et al., 2015](#); [Quinn et al., 2015](#)), K2-97 b ([Grunblatt et al., 2016](#)), K2-39 b ([Van Eylen et al., 2016](#)), K2-132 b ([Grunblatt et al., 2017](#); [Jones et al., 2018](#)) TOI-197 b ([Huber et al., 2019](#)), TOI-2337 b, TOI-2669 b ([Grunblatt et al., 2022](#)), TIC 365102760 b ([Grunblatt et al., 2024](#)), TOI 4377 b, TOI 4551 b ([Pereira et al., 2023](#)), and TOI 7047 b ([Saunders et al., 2025](#)). I note that an exact determination is somewhat subjective, as nearly all the systems are only starting to ascend up the RGB or are still in the transition region between the subgiant branch and

the RGB. Many more systems can be found orbiting subgiants. A recent overview is also presented by [Grunblatt \(2024\)](#).

In contrast to the early findings by RV studies, [Grunblatt et al. \(2019\)](#) and [Temmink & Snellen \(2023\)](#) find similar, or even tentatively enhanced, occurrence rates of hot Jupiters orbiting giant stars compared to those orbiting main-sequence stars. [Grunblatt \(2024\)](#) argues that the initial lack of close-in planets in RV surveys might be a consequence of the selection of more evolved stars, as well as due to observational biases (e.g., the observation cadences) making short-period planets more difficult to discern from the intrinsic p-mode jitter. Nevertheless, the small absolute number of transiting planets around giants, especially those that have already evolved significantly up the RGB, calls for an increased number of detections to allow detailed studies of the effect of stellar evolution on close-in planetary systems. Increasing this number is attempted in [Chapt. 2](#).

1.8 The astrometric method applied to giant stars

The final exoplanet detection method of interest within this thesis is the astrometric method. At the moment, only five planets are listed in the NASA exoplanet archive, which have been found using astrometry. However, this number is predicted to increase drastically with the upcoming publication of the fourth data release (DR4) of the *Gaia* ([Gaia Collaboration et al., 2016](#)) spacecraft anticipated for 2026, as well as its fifth and final release (DR5) toward the end of the decade.⁴ [Perryman et al. \(2014\)](#) estimates up to 70 000 planet detections with a *Gaia* baseline of 10 years, which it completed before being shutdown in January 2025. Already after the release of *Gaia* DR3 ([Gaia Collaboration et al., 2023](#)), the first confirmed planets, and a number of yet unconfirmed candidates have been published ([Holl et al., 2023](#); [Sozzetti et al., 2023](#); [Stefánsson et al., 2025](#)).

The astrometric method relies on measuring the reflex motion of a host star due to the orbit of its planetary companion as projected onto the tangential plane of sky. Detailed introductions into the method can be found in textbooks such as [Perryman \(2018\)](#) or [Quirrenbach \(2010\)](#). Here, I focus on its application on giant stars. The apparent astrometric signature of the photocenter of a star-planet system with orbital period P can be approximated as ([Quirrenbach, 2010](#)):

$$\theta = 954 \mu\text{as} \cdot \frac{m_p}{M_{\text{Jup}}} \left(\frac{M_\star}{M_\odot} \right)^{-2/3} \left(\frac{P}{\text{yr}} \right)^{2/3} \left(\frac{d}{\text{pc}} \right)^{-1}, \quad (1.10)$$

assuming $M_\star \gg m_p$ and a circular orbit. Here, d is the distance to the star. Opposite to the RV method (and the transit method due to smaller transit probabilities), the astrometric

⁴<https://www.cosmos.esa.int/web/gaia/release>

method is thus more sensitive to larger orbital separations. However, the astrometric signal also decreases with distance. The latter is also the reason why planetary detections around giant stars will be much less common than around main-sequence stars, as there are few giants at close distances. Within 25 pc, for instance, the ratio is about 250:1 (Golovin et al., 2023). Perryman et al. (2014) estimates only about 400 planet detections orbiting giants from *Gaia*, albeit using relatively crude assumptions on their planet population.

Intrinsic variability in giant stars, such as caused by star spots, p-mode oscillations, non-radial oscillations, or granulation, can further lead to intrinsic noise in the determined position of the photocenter (e.g., Quirrenbach 2010). Svensson & Ludwig (2005) and Ludwig (2006) studied the photocentric variations caused by the granulation pattern and find it to scale as g^{-1} . For a giant star, with, for instance, $\log g = 2.0$, the photocentric displacement would be of the order $\frac{100 \mu\text{as}}{d[\text{pc}]}$. Similarly, Eriksson & Lindegren (2007) estimated the expected photocentric jitter for K and G giants due to photometric spots and other photometric variations in the range $\frac{50-500 \mu\text{as}}{d[\text{pc}]}$. This would likely disallow the detection of rocky planets orbiting giants. The signals of Jupiter-mass companions, however, can be significantly larger, depending on the orbital period.

Gaia DR5 is expected to achieve a parallax precision of $\sigma_{\varpi} \approx 7 \mu\text{as}$ for stars with $G = 13 \text{ mag}$.⁵ The astrometric precision for stars with $3 \text{ mag} \leq G < 13 \text{ mag}$ is challenging to establish due to unresolved calibration issues for very bright stars. Indeed, for *Gaia* DR3 the formal uncertainties are much exceeded by the actual astrometric jitter measured for very bright stars (e.g., Kiefer et al. 2021; Lindegren et al. 2021). For current data releases, the parallax uncertainties for bright stars are furthermore known to be underestimated (e.g., El-Badry et al. 2021). It is unknown whether future data releases can resolve the issues to some extent.

Feng (2024), following Perryman et al. (2014), summarizes the detection threshold for an astrometric signal as $5 < \text{S/N} = \frac{\theta}{3.2 \cdot \sigma_{\varpi}}$, in which the factor 3.2 quantifies further instrumental or systematic uncertainties. Assuming optimistically that the best *Gaia* precision can also be reached for bright stars in future releases, one can estimate that for the 318 stars in the Lick sample with $G > 3 \text{ mag}$, *Gaia* would be able to detect Jupiter-like companions in $P = 10 \text{ yr}$ orbits for about 10 stars, using the stellar masses derived by Stock et al. (2018) and distances derived from HIPPARCOS parallaxes (ESA, 1997). This number increases to 287, when considering a brown dwarf mass ($m_p = 13 M_{\text{Jup}}$), with the median astrometric signal being $\theta \sim 370 \mu\text{as}$. While detecting lower-mass companions might seem too optimistic if the *Gaia* calibration for very bright stars cannot be improved significantly, detecting potential brown dwarfs might be possible. I stress that I simply estimate the number of stars for which the signals of such orbital companions could be observable by *Gaia*, specifically not making assumptions on the planet occurrence rates.

⁵<https://www.cosmos.esa.int/web/gaia/science-performance>

Estimating the intrinsic photocentric jitter contributions from the granulation and photometric variations (spots, p-mode oscillations) at $\frac{100 \mu\text{as}}{d[\text{pc}]}$ each and adding these to the error budget in quadrature, does not significantly alter these estimations. While the astrometric signature would increase for further out planets, these would also extend past the *Gaia* baseline of 10.5 years, making the reconstruction of the orbits more challenging, albeit not impossible if a suitable fraction was observed. Combination of *Gaia* and HIPPARCOS epoch astrometry could in such cases be promising. However, the HIPPARCOS astrometric data has significantly larger uncertainties (van Leeuwen, 2007), such that the combination of both time series is likely only helpful for systems with large astrometric signatures. Systematic differences in the reference frames would further need to be accounted for.

However, even if astrometric orbits cannot be fully reconstructed, they can still yield upper limits of the true masses of planets detected via the RV method (e.g., Frink et al. 2002; Reffert & Quirrenbach 2011) or help to constrain RV orbital solutions (e.g., Reffert & Quirrenbach 2006). Furthermore, constraints derived by the proper motion anomaly between HIPPARCOS and *Gaia* measurements (Kervella et al., 2019, 2022) can help to determine the inclination or the argument of periastron for systems detected via other methods. Nevertheless, in order to conduct such studies, the characteristics of the *Gaia* spacecraft, its data, and possible instrumental errors sources must be well understood. The detection of a spurious astrometric detection by *Gaia* is discussed in Chapt. 2.

1.9 The planet controversy around luminous giants

Predating the first confirmation of a planet orbiting a giant, intrinsic sources of observed RV variations, such as star spots, radial, or non-radial oscillations, which could explain long-period RV variations of giants, have been discussed (Hatzes & Cochran, 1993, 1996, 1998a,b). A few years later, the existence of planets orbiting giants was firmly established, for instance, due to RV signals with high eccentricities that are hard to be mimicked by intrinsic variations (e.g., Frink et al. 2002), or due to the lack of variations in commonly used activity indicators such as line bisectors (e.g., Setiawan et al. 2003a). This led to a steady increase of planetary detections orbiting giants using the RV method.

However, Hatzes et al. (2018) present RV variations of the very luminous giant γ Dra ($L = 510 \pm 51 L_{\odot}$, $R = 49.03 \pm 2.52 R_{\odot}$, Hatzes et al. 2018; Mozurkewich et al. 2003; Koleva & Vazdekis 2012), shown in Fig. 1.10. Overplotted is a one-planet Keplerian model, with amplitude $K = (148.4 \pm 4.1) \text{ m s}^{-1}$, which fits the measurements well between 2003 and 2011 (upper panel). However, between 2011 and 2014, the signal amplitude drops significantly, reemerging in 2014 but with a clear phase shift. Hatzes et al. (2018) also find evidence of a sinusoidal modulation of K with period $P \sim 10.6 \text{ yr}$. The authors attempt to model the observed RVs using a two-planet model but find a low probability ($P \lesssim 2\%$) of

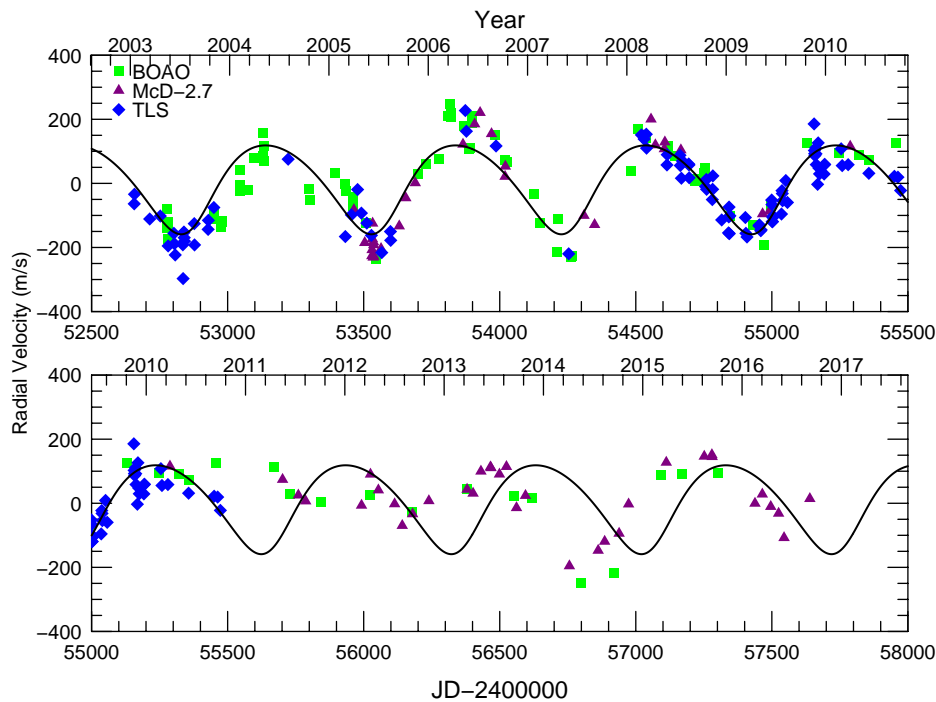


Fig. 1.10.: RV variations of γ Dra. A one-planet Keplerian fit is overplotted. Clear deviations from the model can be seen for the more recent data. Credit: [Hatzes et al. \(2018\)](#), © AAS. Reproduced with permission.

the system being stable, and thus favor an intrinsic origin of the large-amplitude variation. However, they cannot find any strong evidence of intrinsic variations present in the line bisectors, photometric data, or variations of the Ca II K line.

Similarly, [Reichert et al. \(2019\)](#) discuss the bright giant Aldebaran, which has similar stellar properties to γ Dra ($L = 402^{+11}_{-10} L_{\odot}$, $R = 44.01^{+0.74}_{-0.71} R_{\odot}$, [Stock et al. 2018](#)) and had previously been thought to host a massive exoplanet ([Hatzes et al., 2015](#)). Combining data from the Lick RV survey (see [Sect. 1.5](#)) with the RVs published by [Hatzes et al. \(2015\)](#), they also find clear phase shifts when attempting to model the RVs using a single planetary companion, while including a second orbital companion would make the system unstable. [Reichert et al. \(2019\)](#) further show that the growth of the Lomb-Scargle power, i.e., the power of a Lomb-Scargle periodogram at the RV period ([Lomb, 1976](#); [Scargle, 1982](#)), of the real data does not increase linearly as expected from simulations but drops significantly after about 300 RV measurements. Akin to γ Dra, Aldebaran does not show periodic variations close to the main RV period in HIPPARCOS photometry, or in time series targeting the depth of Ca lines or the H α line ([Hatzes et al., 2015](#)).

Further luminous giants have been found with similar behavior. These include 42 Dra (Döllinger et al., 2009; Döllinger & Hartmann, 2021), Sanders 364 (Brucalassi et al., 2017; Zhou et al., 2023), for which multiperiodic RV behavior has been noticed, HD 135438 (Lee et al., 2023), and ϵ Cyg (Heeren et al., 2021). The latter, however, is an eccentric binary system with additional shorter-term RV variations at a period $P = 291$ d. Similar to γ Dra and Aldebaran, the RVs also show a clear phase shift. Heeren et al. (2021), however, consider the heartbeat phenomenon as the origin (see, e.g., Thompson et al. 2012), which would not be applicable to single stars. ϵ Cyg might thus present a different type of intrinsic variation. Teng et al. (2023b) present the two cases of 41 Lyn and 14 And, for which line bisector variations can be found at similar periods to the RVs. However, these periods also match closely with $P = \frac{1}{2}$ yr, which suggests an instrumental origin.

The above planetary systems have largely been refuted based on inconsistencies in the RVs, such as phase shifts or amplitude changes. As most of the RV measurements in these reference have been acquired using the iodine cell technique (see Sect. 1.6.2), a relatively small number of activity indicators are available. In contrast, Delgado Mena et al. (2018) study the RV variations and a number of activity indicators acquired with HARPS (Mayor et al., 2003) for three giants located in open clusters. Two of the stars, NGC 2423 No. 3 and NGC 4349 No. 127, were published to host massive planetary or brown-dwarf companions by Lovis & Mayor (2007). Nevertheless, a reanalysis of the HARPS data set reveals that the shapes of spectral lines, as measured by the BIS or the FWHM of the CCF (see Sect. 1.6.3), vary at the same period as the RVs or show correlations with the RVs. For NGC 4349 No. 127, also tentative variations of the depth of the $H\alpha$ line at the RV period are observed. Jointly, these are interpreted as conclusive evidence against the existence of the orbital companions.

These findings are affirmed by Delgado Mena et al. (2023), who also add NGC 2345 No. 50 and NGC 3532 No. 670 to the list of luminous giants, which show long-period ($P \gtrsim 2$ yr), large-amplitude ($K \gtrsim 200$ m s⁻¹) RV periodicity, accompanied by variations in the activity indicators that argue against orbital companions. Interestingly, Delgado Mena et al. (2023) find the $H\alpha$ indicator, generally regarded to be most sensitive to chromospheric activity (see Sect. 1.6.3), to be the most decisive indicator jointly with the FWHM of the CCF. Nonetheless, they conclude that a combination of a long time series of RVs, a reliable set of activity indicators, and additional information, such as photometric data, are needed to decisively rule out or confirm planets orbiting luminous giants.

To draw an intermediate summary, it appears that there exists a class of quite luminous giants (typically $L \gtrsim 100 L_{\odot}$) that show long-term RV variations, with periods typically on the order of several hundred days, which can appear coherent on timescales similar to ten years and thus mimic planets convincingly. None of the stars were found to have obvious photometric variations in the available data sets that would match the periods of the RVs. For some stars, activity indicators from HARPS helped to rule out planetary companions,

for other stars such indicators were either not available or not conclusive against planets. Thus, the full picture remains quite ambiguous. Döllinger & Hartmann (2021) find that all four doubtful planet detections analyzed in their sample (γ Dra, Aldebaran, 42 Dra, and HD 122430, Setiawan 2003; Soto et al. 2015) have radii $R > 21 R_{\odot}$. They also find that most published planets orbiting giants with radii exceeding this threshold have periods $300 \text{ d} < P < 800 \text{ d}$, a region which they share with the four doubtful planets, thus suggesting that more false positives might be present among the published companions.

1.10 Possible intrinsic origins of RV variations of giants

1.10.1 Oscillatory convective modes and non-radial oscillations

To resolve the mysterious RV variations of γ Dra, Hatzes et al. (2018) propose that the phenomenon might be linked to so-called oscillatory convective modes, which have been developed by Saio et al. (2015) to explain the photometric variability of luminous giant stars showing long secondary periods (LSPs, see discussion below). These oscillatory convective modes are theorized to be dipole ($l = 1$, with l describing the number of angular nodes on the stellar surface) non-radial g^{-} (gravity) modes which could become oscillatory in non-adiabatic conditions that are present in the envelopes of very luminous giants (Saio et al., 2015; Takayama & Ita, 2020). Hatzes et al. (2018) and Reichert et al. (2019) show that their models, as plotted on a period-luminosity plot, would cross the region, in which γ Dra and Aldebaran are situated.

To illustrate that, I plot in Fig. 1.11, the periods and luminosities of photometrically variable giants in the Large Magellanic Cloud (LMC) as published in the OGLE-III catalog (Soszyński et al., 2009). I use the infrared flux method (Blackwell & Lynas-Gray, 1994) to convert K band magnitudes into luminosities. Giants identified as “OGLE small-amplitude red giants” are shown in orange, while Mira-like and semi-regular variables are plotted in red (see Soszyński et al. 2009). For stars that show LSPs, the secondary period is plotted in blue. One can observe separate sequences of stars which are labeled following Wood et al. (1999) and Soszyński et al. (2021). Overplotted in shades of pink are models of oscillatory convective modes for different stellar masses by Saio et al. (2015) with mixing-length parameter $\alpha = 1.2$. These can be seen to reproduce similar period-luminosity relations to the stars present on sequence D. Based on the ideas of Hatzes et al. (2018) and Reichert et al. (2019), I further plot the giant stars mimicking planets (discussed in Sect. 1.9) as purple star symbols. As discussed by the two publications, several of the stars can be observed to potentially coincide with an extrapolation of the models by Saio et al. (2015). Other stars, however, can be seen to be at significantly lower luminosities. It remains very uncertain whether such modes could be excited in these stars.

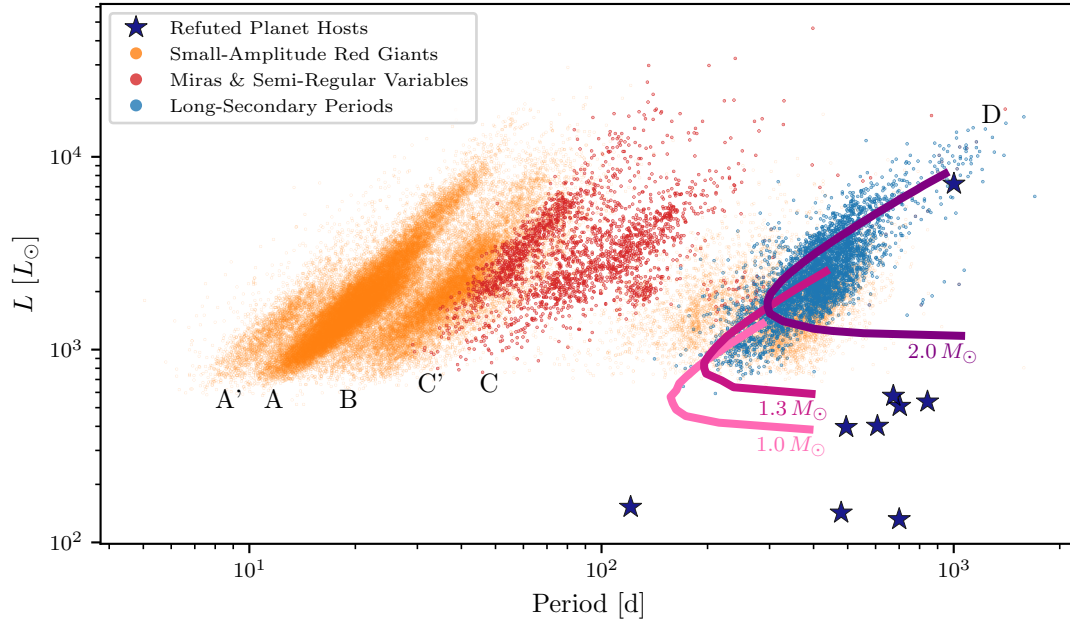


Fig. 1.11.: Period-luminosity plot of variable giants in the LMC from the OGLE-III catalog (Soszyński et al., 2009). OGLE small-amplitude red giants are shown in orange, while Mira-like variables and semi-regular variables are shown in red. Long-secondary periods on sequence D are shown in blue. The well-established period-luminosity sequences are labeled. The discussed false-positive planet hosts (Sect. 1.9) are plotted as purple star symbols, while three models of oscillatory convective modes for different stellar masses (Saio et al., 2015) are shown in pink.

Long predating the publication of oscillatory convective modes, Hatzes (1996) presented simulations showing that non-radial oscillations can produce sinusoidal RV variations in giant stars, which, however, would be accompanied by variations of the bisectors, making it possible to detect such oscillations. Radial pulsations, on the other hand, can be ruled out due to the long RV periods (Hatzes & Cochran, 1993; Cox et al., 1972; Hatzes et al., 2018; Reichert et al., 2019). Thus, regardless of whether such non-radial oscillations are oscillatory convective modes or are driven by another mechanism, they remain a promising candidate for explaining the planet controversy surrounding luminous giants. In Chapt. 3, I introduce the fundamentals of non-radial oscillations and develop a simulation tool, which is applied to a known false-positive planet host in Chapt. 4.

Discussion on the origin of long secondary periods

In general, the predictions by Saio et al. (2015) are debated as the origin of the LSPs. The idea that sequence D might be explained by non-radial g^- modes can be traced back to Wood et al. (1999) and Wood (2000), although ultimately dismissed in these publications.

It is partially based on the fact that Mira-like variables are located on sequence C and pulsate radially in the fundamental mode, while sequences B and A correspond to its overtones. It is also sequence B on which the primary period of most LSPs is located (Wood et al., 1999; Nicholls et al., 2009). Thus, radial pulsations as the origin of sequence D can be ruled out, leaving non-radial oscillations as one alternative (Wood, 2000). The models by Saio et al. (2015) have been used by Takayama & Ita (2020) to predict variations of the luminosities, effective temperatures, and radii, which match the observations. Takayama (2023) also found period modulations in some sequence D stars, which could be explained by oscillatory convective modes.

As an alternative, Wood et al. (1999) and Wood (2000) proposed that sequence D might be caused by a stellar companion within a large dust cloud that periodically eclipses the primary. This is supported by the finding that sequence D stars show excess flux in the mid-infrared (IR), which is interpreted as the consequence of stellar mass ejection settling in a disk (Wood & Nicholls, 2009). On the other hand, Hinkle et al. (2002) and Nicholls et al. (2009) found problems in this binary hypothesis when analyzing a sample of sequence D stars using RVs. Nevertheless, a very strong argument for the binary scenario is given by Soszyński et al. (2021), who find secondary eclipses in mid-IR photometry that are attributed to the primary stars eclipsing the low-mass stellar or brown-dwarf companions in their dusty clouds. Goldberg et al. (2024) also discuss oscillatory convective modes as a potential origin of the LSP observed for Betelgeuse. However, they conclude that the underlying model assumptions by Saio et al. (2015), non-adiabatic radiative transport in the outermost layers and mixing-length parameter $\alpha = 1.2$, do not accurately represent the conditions in supergiants. The necessity of a subsolar value of the mixing-length parameter to match the models of oscillatory convective modes to sequence D was already mentioned by Saio et al. (2015).

Thus, whether oscillatory convective modes can be excited and whether these are causing the LSPs is still a matter of debate. Whether these would be applicable to the less luminous stars among the curious RV-variable stars that mimic planets may further be debated.

1.10.2 Convective processes and magnetic activity

Motivated by the fact that variations of the $H\alpha$ line seem to accompany non-planetary RV variations, Delgado Mena et al. (2018, 2023) propose that, instead of non-radial oscillations, magnetic activity could be the origin. On the main-sequence, especially for low-mass stars, magnetic fields on the stellar surface lead to phenomena such as cool spots or hot plages that can lead to sizable RV variations (e.g., Hatzes 2002; Desort et al. 2007; Boisse et al. 2009; Hatzes 2019; Baroch et al. 2020; Ruh et al. 2024).

The magnetic fields on giant stars are comparably poorly understood but generally found to be weaker than those found for late main-sequence stars (e.g., [Berdyugina 2008](#); [Aurière et al. 2009, 2015](#)). However, it has to be noted that recently strong magnetic fields in the cores of giants have been found using *Kepler* data ([Li et al., 2022](#); [Deheuvels et al., 2023](#); [Li et al., 2023](#)). Nevertheless, cool spots which could produce RV variations are inherently linked to photometric variations, which were not observed for the giants whose planetary systems are at question. This finding argues against such spots ([Reffert et al., 2015](#); [Reichert et al., 2019](#)).

To mitigate this issue, [Delgado Mena et al. \(2023\)](#), as well as private communications within the reference, propose that for giant stars with weak magnetic fields, the RV variations would not be caused by cool spots but instead by velocity structures that could locally suppress convection. These could lead to velocity variations without photometric variations. In this regard, the bright giant Pollux is noteworthy, which has been published to host a planet by [Hatzes et al. \(2006\)](#) and [Reffert et al. \(2006\)](#). On the other hand, in a series of publications, [Aurière et al. \(2009, 2013, 2021\)](#) find a weak magnetic surface field on Pollux that varies with a period ($P \sim 660$ d), similar to the orbital period of the planet ($P \sim 590$ d). Whether this can be seen as evidence against the planet will have to be further scrutinized. Interestingly, [Amard et al. \(2024\)](#) present simulations showing that the magnetic field strength of Pollux is coupled to the scale of the convective motions, providing a potential link to the suggestion by [Delgado Mena et al. \(2023\)](#).

[Rolo et al. \(2024\)](#) further analyze a sample of variable giants, including the stars presented in [Delgado Mena et al. \(2023\)](#), and find a connection between enhanced levels of variations in activity indicators and enhanced Lithium contents in the stellar spectrum. Such an enhanced Lithium abundance is generally regarded as being connected to higher levels of chromospheric and thus likely magnetic activity ([Snedden et al., 2022](#)).

Overall, magnetic activity as manifested through variable levels of convection can be regarded as a viable alternative to explain the planet controversy. Nevertheless, both the theoretical and observational sides are still poorly explored. To contribute to the observational basis, I investigate in [Chapt. 5](#) a sample of RV-variable giant stars to determine whether traces of chromospheric activity can be found.

1.11 Goal and structure of this thesis

The overall goal of this thesis is to enhance the statistical sample and improve the reliability of the planet population orbiting giant stars. Specifically, I aim to:

- I. Increase the number of known planets with short orbital periods ($P \lesssim 100$ d).

- II. Enhance our understanding of the intrinsic phenomena that can mimic planet at intermediate periods ($100 \text{ d} < P \lesssim 5 \text{ yr}$).
- III. Enable future studies searching for the long-period planet population ($P \gtrsim 5 \text{ yr}$).

In light of Goal I, I present in [Chapt. 2](#) the (unsuccessful) RV follow-up of two evolved transiting candidates identified with TESS. I further discuss the RV non-detection of a main-sequence binary candidate identified by *Gaia*, which can contribute to an improved filtering of the *Gaia* astrometric solution in preparation for upcoming data releases.

To achieve Goal II, I present in [Chapt. 3](#) the fundamentals of the newly developed simulation tool `pyoscillot`, designed to predict the observational fingerprints of non-radial oscillations in spectroscopic data. I give a thorough introduction of its underlying principles, and discuss the general influence of the oscillation parameters on the observables.

I apply these findings in [Chapt. 4](#) to HARPS data of the known false-positive evolved planet host NGC 4349 No. 127, showing that a dipole non-radial oscillation can explain the variations of the RVs, the activity indicators, and their correlations.

In [Chapt. 5](#), I combine 25 years of RV data from Lick, SONG, and CARMENES for ten planet candidates, aiming to rule out or confirm planets, and search for indications of non-radial oscillations or chromospheric activity. One star, HIP 64823, remains a promising candidate to host a long-period planet. The other stars indicate that an extensive time series of RV measurements remains the most critical diagnostic tool to test the reliability of planet detections.

To enable such long-term RV monitoring, as well as to achieve Goal III, I present the final steps to enable routine science observations with the Waltz telescope in [Chapt. 6](#). I present first on-sky tests of the instrument's performance, and its short- and long-term stability.

I conclude in [Chapt. 7](#) with a summary of the results, combining the findings of this thesis, and highlighting future steps to study the planet population orbiting giant stars.

Radial velocity non-detections of *Gaia* astrometric and TESS transiting candidates

In this chapter, I summarize independent RV follow-up campaigns targeting a *Gaia* astrometric binary candidate orbiting a main-sequence star (Sect. 2.1) and two TESS planet candidates orbiting evolved stars (Sect. 2.2).

2.1 Non-Confirmation of the Astrometric Binary Candidate HD 113283

Details of authorship: The contents of this section have been published almost identically as a *Research Note of the American Astronomical Society* (Spaeth et al., 2023),¹ jointly with Sabine Reffert, Trifon Trifonov, and Alex Golovin. The analysis, figures, and text have been contributed by me, with valuable suggestions both scientifically and in terms of the presentation of the results by my co-authors. Figure 2.1 has been rescaled to fit into the format of this chapter. The identified false-positive binary candidate HD 113283, was later independently recognized as having a spurious astrometric solution by the *Gaia* team.² The case can contribute toward an improved filtering process of *Gaia* astrometric candidates in light of the upcoming *Gaia* DR4.

2.1.1 Introduction

Among the products of *Gaia* DR3 (Gaia Collaboration et al., 2016, 2023) are 169,227 non-single stars with solutions by the astrometric pipeline presented in Halbwachs et al. (2022) and by the refined 'exoplanet pipeline' (Holl et al., 2022b). The latter is run on 'stochastic' sources labeled as 'OrbitalAlternative*' and on 19,845 preselected stars labeled as 'OrbitalTargetedSearch*' within the `nss_two_body_orbit` table.

¹Licensed under CC BY 4.0 (<https://creativecommons.org/licenses/by/4.0/>).

²<https://www.cosmos.esa.int/web/gaia/dr3-known-issues>

The 533 stars with solutions in the 'OrbitalTargetedSearch*' sample include the nearby and bright ($\varpi = (40.476 \pm 0.015)$ mas, $G = (6.9540 \pm 0.0028)$ mag, [Gaia Collaboration et al. 2023](#)) G5 dwarf HD 113283 (= HIP 64690 = GJ 11909 = *Gaia* DR3 5765846127180770432). The astrometric two-body solution has period $P = (20.025 \pm 0.013)$ d, eccentricity $e = 0.737 \pm 0.097$, and significance $a_0/\sigma_{a_0} = 4.705$ ([Holl et al., 2022b](#)).

2.1.2 Results

Using `nsstools`³ ([Halbwachs et al., 2022](#)) we converted the Thiele-Innes coefficients to Campbell elements ($a_0 = (0.84 \pm 0.18)$ mas, $i = 54.8^\circ \pm 4.3^\circ$, $\omega = 77.1^\circ \pm 6.5^\circ$, $\Omega = 168.0^\circ \pm 6.5^\circ$). Using

$$f_{\mathcal{M}} = \frac{(m_2 \sin i)^3}{(m_1 + m_2)^2} = \frac{(2\pi)^2 (a_1 \sin i)^3}{GP^2} \quad (2.1)$$

we derive the mass function $f_{\mathcal{M}} = 0.0016 M_{\odot}$ assuming equality between the semi-major axes of photocenter and host star, $a_0 = a_1$. The host mass $m_1 = 0.9 M_{\odot}$ ([Mortier et al., 2013a](#)) yields a companion mass $m_2 > 0.15 M_{\odot}$, which is a lower limit due to the stellar companion's non-negligible luminous contribution. Therefore, radial velocity (RV) variations with semi-amplitude $K_1 > 13.5 \text{ km s}^{-1}$ are expected.

To confirm the astrometric candidate, fifteen spectra were taken using FEROS ([Kaufer et al., 1999](#)) mounted on the MPG/ESO 2.2-meter telescope in La Silla. The spectra were extracted using CERES⁴ ([Brahm et al., 2017](#)) and reduced using both CERES and SERVAL ([Zechmeister et al., 2018](#)).⁵ Both results, with the respective means subtracted ($\overline{RV}_{\text{CERES}} = (-4.789 \pm 0.002) \text{ km s}^{-1}$), are presented in [Fig. 2.1](#) (top) along with the GLS periodograms (middle) ([Zechmeister & Kürster, 2009](#)). The CERES and SERVAL results have standard deviations of 7.2 m s^{-1} and 7.4 m s^{-1} respectively and no significant periodicity. Therefore, the RV data indicate that the *Gaia* two-body solution is spurious.

2.1.3 Discussion

The solution's significance $a_0/\sigma_{a_0} = 4.705$ is on the lower end of the distribution of the 'OrbitalTargetedSearch*' sample ([Holl et al., 2022b](#)) and would be discarded for the 'OrbitalAlternative*' sample and in the standard astrometric pipeline ([Halbwachs et al., 2022](#)), which uses a selection criterion $a_0/\sigma_{a_0} > 158/\sqrt{P[\text{d}]}$ (≈ 35.3 for HD 113283). More stringent selection criteria would result in a cleaner 'OrbitalTargetedSearch*' final sample.

³<https://gitlab.obspm.fr/Gaia/nsstools>

⁴<https://github.com/rabrahm/ceres>

⁵<https://github.com/mzechmeister/serval>

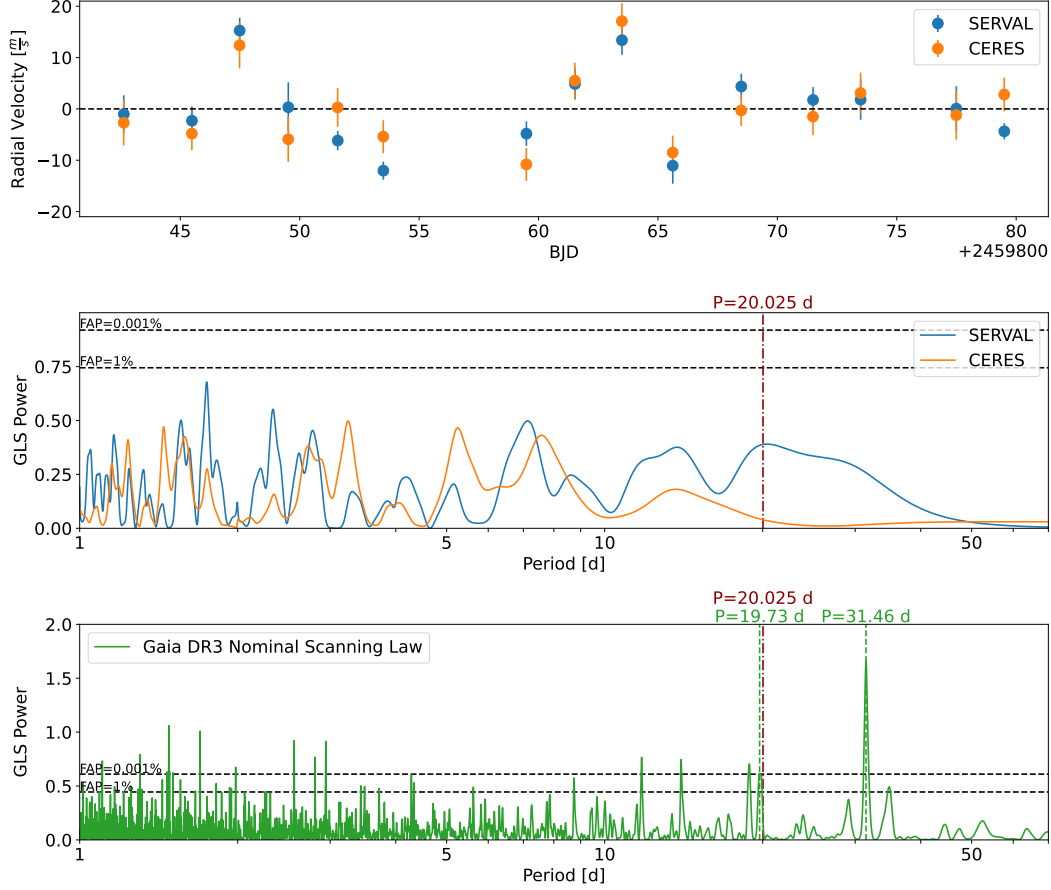


Fig. 2.1.: Top: FEROS RVs reduced by CERES (orange) and SERVAl (blue) with standard deviations of $\sigma = 7.2 \text{ m s}^{-1}$ and $\sigma = 7.4 \text{ m s}^{-1}$ respectively. Middle: GLS periodograms computed for the two RV time series. No significant power can be observed at the 20.025 d period (red, dash-dotted). Bottom: GLS periodogram of the star’s observation times according to the *Gaia* DR3 nominal scanning law with a significant peak at $P = 19.73 \text{ d}$ (green, dashed).

Furthermore, we calculated the semi-major axis of the apparent orbit $\tilde{a}_0 \approx 498 \mu\text{as}$ following [Appourchaux et al. \(2015\)](#). Comparing this to the one-body *Gaia* solution (astrometric_excess_noise = $122.86 \mu\text{as}$), it is apparent that the astrometric signature of the two-body solution is much larger than expected. After the two-body solution by [Holl et al. \(2022b\)](#) is subtracted, an excess noise (astrometric_jitter in the nss_two_body_orbit table) of $113.24 \mu\text{as}$ remains, a reduction of merely $9.62 \mu\text{as}$, which further indicates a discrepancy between the one- and two-body solutions. By comparison, the validated sources in [Holl et al. \(2022b\)](#) show much larger reductions of the excess noise.

[Holl et al. \(2022a\)](#) show that spurious solutions caused by *Gaia*’s scan angle and scanning law cluster at periods following $365.25/P [\text{d}] = m \cdot 5.8 + n$, where m and n are the

number of cycles per precession period (~ 63.0 d) and per year, respectively. Fig. 2.1 (bottom) shows a GLS periodogram of the star’s observation times according to the *Gaia* DR3 nominal scanning law calculated using the `scanninglaw` package (Green, 2018).⁶ A significant peak at $P = 19.73$ d close to the 20.025 d period is apparent, which is likely linked to an overdensity of spurious solutions at $P = 19.9$ d ($m = 3, n = 1$). This finding casts serious doubts on the nature of the *Gaia* solution. One can also identify a strong peak at 31.46 d which coincides with the second harmonic of the precession period ($m = 2, n = 0$). Holl et al. (2022a) propose that most spurious solutions are caused by optical pairs with fixed orientation and separation < 0.5 as (background stars or long-period binaries). Archival images reveal no background objects in the immediate vicinity of HD 113283. RV variations at a long orbital period remain possible when including three archival spectra, however, no significant proper motion anomaly based on Hipparcos and *Gaia* EDR3 astrometry was detected (Kervella et al., 2022).

In any case, HD 113283 advocates for a more stringent filtering of the *Gaia* two-body solutions.

2.2 Radial velocity non-detections of two evolved TESS Objects of Interest

2.2.1 Motivation and target selection

As discussed in the Sect. 1.7, transiting planets orbiting giants are still rare. Confirmation of such systems can, however, provide valuable insights into the tidal effects that affect planetary systems at various stages of the stellar evolution (see, e.g., Grunblatt 2024). Furthermore, by increasing the number of confirmed short-period planets orbiting evolved stars, earlier occurrence rate studies (Grunblatt et al., 2019; Temmink & Snellen, 2023) could be greatly enhanced to allow a more comprehensive comparison to main-sequence hosts. Our goal, thus, was to contribute toward this progress by successive RV follow-up of transiting candidates identified by TESS (Ricker et al., 2015) in the northern sky.

As a starting point, I screened all public TESS Objects of Interest (TOIs) available from Cycle 2, the first TESS observation sequence in the northern hemisphere. I crossmatched the public TOIs with the *Gaia* DR2 (Gaia Collaboration et al., 2016, 2018) and Starhorse (Anders et al., 2019) catalogs to derive stellar parameters. I excluded main-sequence stars by selecting only stars with surface gravities $\log(g) < 3.8$, aided by the *Gaia* DR2 color-magnitude diagram. To ensure reasonable time demands for 2.5-meter-class telescopes, I further restricted the stars to be brighter than TESS magnitude $T < 9$ mag based on the

⁶<https://github.com/Gaiaverse/scanninglaw>

Tab. 2.1.: Stellar parameters derived by *SPOG+*.

TOI	ID	SpT	ES	M M_{\odot}	R R_{\odot}	L L_{\odot}	$\log(g)$ cm s^{-2}	T_{eff} K	[Fe/H]
1489	BD+61 1660	K0	HB	$1.92^{+0.08}_{-0.03}$	$8.34^{+0.08}_{-0.04}$	$40.41^{+0.11}_{-0.08}$	$2.89^{+0.01}_{-0.01}$	5044^{+11}_{-16}	$-0.12^{+0.22}_{-0.09}$
1684	HIP 20334	G5	RGB	$1.00^{+0.08}_{-0.05}$	$3.01^{+0.03}_{-0.10}$	$4.78^{+0.03}_{-0.34}$	$3.48^{+0.04}_{-0.03}$	4915^{+14}_{-17}	$-0.14^{+0.09}_{-0.18}$

Notes. “ES” denotes the determined evolutionary stage which, for both stars, was found with a high probability. The metallicities [Fe/H] were taken from the literature (Anders et al., 2022; Bochanski et al., 2018).

TESS Input Catalog (TIC) (Stassun et al., 2018), which left 15 TOIs. Several of these were flagged as potential false positives based on public information available through the website of the Exoplanet Follow-up Observing Program (ExoFOP).⁷

I selected the two most promising candidates based on their transit light curves and stellar properties, favoring lower luminosity giants with bluer colors to decrease the influence of the stellar RV jitter. I further searched for indications of contaminating sources based on the TESS target pixel files, or indications of stellar variability based on *Gaia* flags. For ideal target selection, I further took into account observational constraints given by the choice of the FIES spectrograph mounted at the Nordic Optical Telescope on La Palma. This left the transiting candidates TOI 1489 and TOI 1684, for which observation time was successfully granted in semesters 2021B, 2022A, and 2022B.

2.2.2 Stellar properties

I derived the stellar parameters based on a Bayesian inference on PARSEC evolutionary tracks (Bressan et al., 2012) using *SPOG+* (Stock et al., 2018).⁸ I used *G*-band magnitudes, $G - RP$ colors, and parallaxes from *Gaia* DR3 (Gaia Collaboration et al., 2016, 2023), as well as extinction values given in the Starhorse catalog (Anders et al., 2022). For TOI 1489, I further adopted the metallicity as determined in the Starhorse catalog, while for TOI 1684 I used the metallicity given by Bochanski et al. (2018). The stellar parameters determined by *SPOG+* are given in Table 2.1. For both stars, the determined stellar parameters are consistent within the errorbars with the Starhorse catalog.

Figure 2.2 shows a *Gaia* DR3 color-magnitude diagram. The locations of TOI 1489 and TOI 1684 are shown as cyan and orange stars, respectively. To provide a visual reference, I overplot the fifth catalog of nearby stars (CNS5, Golovin et al. 2023) in blue and confirmed evolved planet hosts in red.⁹ I further plot three PARSEC evolutionary tracks for different stellar masses. TOI 1684 can be found in the transition between the subgiant and the

⁷<https://exofop.ipac.caltech.edu/>

⁸<https://github.com/StephanStock/SPOG>

⁹<https://www.lsw.uni-heidelberg.de/users/sreffert/giantplanets/giantplanets.php>

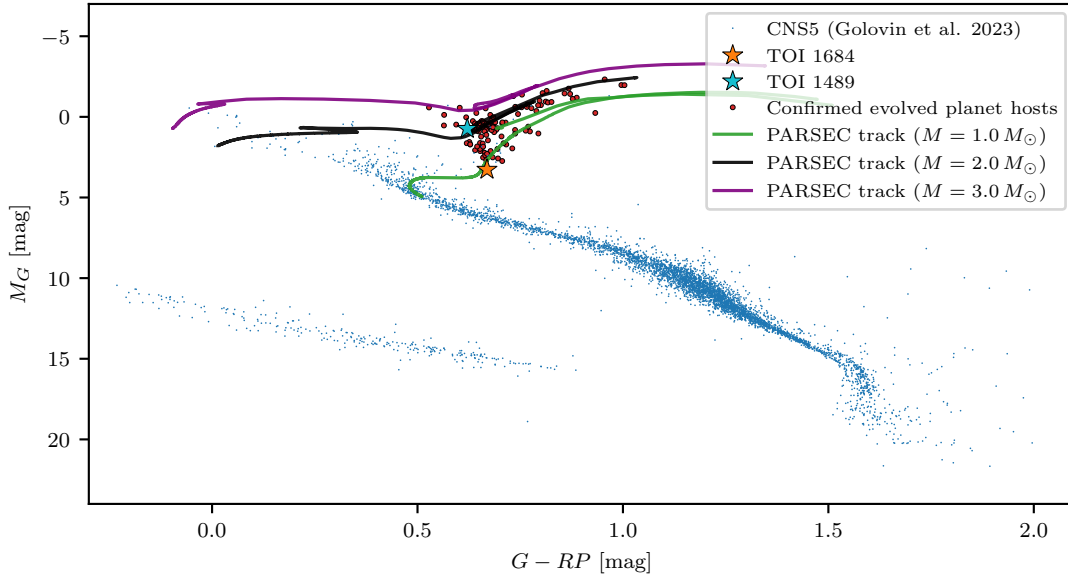


Fig. 2.2.: *Gaia* DR3 color-magnitude diagram highlighting the positions of TOI 1684 (orange) and TOI 1489 (cyan). For visual reference, I overplot the fifth catalog of nearby stars (CNS5, Golovin et al. 2023), as well as confirmed evolved planet hosts for which *Gaia* or HIPPARCOS data is available. I further plot three evolutionary tracks for $1 M_\odot$ (green), $2 M_\odot$ (black), and $3 M_\odot$ (purple) taken from PARSEC (Bressan et al., 2012).

early red giant branch as expected for a star of mass $M \sim 1 M_\odot$. TOI 1489 coincides well with the red clump expected for an evolved star of mass $M \sim 2 M_\odot$.

2.2.3 Transit and radial velocity data

Both targets discussed in this analysis are transiting planet candidates identified by the Transiting Exoplanet Survey Satellite (TESS, Ricker et al. 2015), a space-born, (nearly) all-sky, photometric mission launched by NASA in 2018. TESS operates four independent wide-field cameras that scan a field of view of 24×24 deg each. The initial TESS mission monitored each hemisphere for one year, acquiring data for each sector for 27.4 d, before shifting its field of view eastward. As a result, targets near the ecliptic are present in only one sector per observation cycle per hemisphere, while targets near the ecliptic pole are part of the continuous viewing zone (Ricker et al., 2015). Due to constraints on data downlink, about 200 000 targets were pre-selected to be monitored using a two-minute cadence, while data for the whole sector was, initially, available using a 30-minute cadence in the Full Frame Images (FFIs). After the completion of its initial two-year mission, TESS is operated in the extended mission, acquiring data in cadences of 20 s and 120 s for selected targets, as well as FFIs with 10-minute cadence.

Two-minute (as well as 20-second) cadence data is processed by the Science Processing Operations Center (SPOC). The SPOC pipeline provides aperture photometry that was corrected for systematic errors and is described by [Jenkins et al. \(2016\)](#). These corrected photometric measurements are labeled Pre-search Data Conditioning Simple Aperture Photometry (PDCSAP) and are used in the analysis when available. The SPOC results are automatically screened for transiting candidates and, when alerted, vetted by the TESS Science Office at MIT, who release surviving transiting planet candidates as TOIs.¹⁰ These are announced via the Mikulski Archive for Space Telescopes (MAST)¹¹ and the ExoFOP. FFIs, on the other hand, are processed using the Quick Look Pipeline (QLP, [Huang et al. 2020](#)) and also made available at MAST. The pipeline performs a photometric extraction using different apertures and combines multiple sectors to conduct a search for transiting candidates. These are vetted by the TESS Science Office and alerted as TOIs.¹² The QLP and SPOC light curves are available through the `lightkurve` python package ([Lightkurve Collaboration et al., 2018](#)).

The RV follow-up was conducted using the FIES spectrograph ([Telting et al., 2014](#)) mounted at the 2.56 m Nordic Optical Telescope (NOT, [Djupvik & Andersen 2010](#)) located at the Roque de las Muchachos Observatory on La Palma, Spain. FIES is a fiber-fed, cross-dispersed échelle spectrograph in white-pupil design. We used the high-resolution mode which achieves typical resolving powers $R \sim 67\,000$, covering the wavelength range 370–730 nm. The stability of the instrument over time windows of several days to weeks was found to be on the order of 8 m s^{-1} ([Telting et al., 2014](#)). This is on a similar level to the short-term p-mode pulsations expected for typical giant stars ([Hekker et al., 2006](#)). To measure and correct these instrumental drifts, we acquired long ThAr calibration frames before and after each science observations as suggested by [Buchhave et al. \(2010\)](#).

The FIES observations were made available through open time proposals by the Opticon RadioNet Pilot in semesters 2021B, 2022A, and 2022B. Unfortunately, due to bad weather and the outbreak of the Cumbre Vieja volcano on La Palma, only six spectra were acquired for TOI 1684 in semester 2021B. The star was thus observed again in semester 2022B, acquiring another 34 spectra. Two of the latter spectra had to be discarded during the reduction process due to very low signal-to-noise ratios (S/N). TOI 1489 was observed in semester 2022A yielding 25 spectra.

The spectra have been reduced by Prof. Davide Gandolfi following the approach outlined in [Gandolfi et al. \(2015\)](#). The results are based on a multi-order cross-correlation using the spectrum with the highest S/N as reference. The RVs for TOI 1489 have mean uncertainties of $\bar{\sigma}_{\text{RV,error}} = 6.7 \text{ m s}^{-1}$, while the average RV uncertainties for the slightly brighter star TOI 1684 are $\bar{\sigma}_{\text{RV,error}} = 5.0 \text{ m s}^{-1}$. The nominal measurement uncertainties are perfectly

¹⁰<https://heasarc.gsfc.nasa.gov/docs/tess/the-tess-extended-mission.html>

¹¹<https://mast.stsci.edu/portal/Mashup/Clients/Mast/Portal.html>

¹²<https://tess.mit.edu/qlp/>

apt to detect gas giants in short orbits around evolved stars with RV jitter of similar magnitude. The RVs are tabulated in [Appendix A](#).

2.2.4 Discussion of TOI 1489

TOI 1489 (TIC 219751469) was not pre-selected for two-minute cadence observations. The transiting planet candidate was thus found in the FFIs by the QLP ([Huang et al., 2020](#)) combining TESS sectors 14 to 19. It was alerted as a transiting candidate of orbital period $P = 6.98301 \pm 0.00234$ d and radius $R \sim 1.2 R_{\text{Jup}}$. However, it was noted already in the observing notes provided by the ExoFOP, that the orbital period could be falsely identified and that some transits were found to be inconsistent between odd and even transits.¹³

While at first, such a short-period planet orbiting a star that has likely already left the RGB and entered the state of core Helium burning on the HB might seem unlikely, it is not entirely impossible given its stellar mass $M = 1.92_{-0.03}^{+0.08} M_{\odot}$. Its mass is close to the boundary at which stars do not experience a Helium flash at the tip of the RGB ($\sim 2 M_{\odot}$), especially when further considering the mass loss. Such stars reach a much smaller maximum radius at the tip of the RGB such that planets can survive closer to the star (see, e.g., [Villaver & Livio 2009](#)). The planet might also have experienced significant orbital decay.

At the time of writing the proposal for RV follow-up (August 2021), several additional sectors of FFI light curves were available. I thus reanalyzed the TESS data, searching for periodic signals using the Transit Least Squares (TLS, [Hippke & Heller 2019](#)) algorithm, which revealed a longer-period ($P = 12.13$ d) signal to be somewhat more significant than the reported $P = 6.98$ d period. I fitted the FFI light curves combining TESS sectors 13 to 26 as provided by the QLP using the fitting software `juliet` ([Espinoza et al., 2019](#)), which uses a dynamic nested sampling approach using `dynesty` ([Speagle, 2020](#)) and `batman` ([Kreidberg, 2015](#)) for calculating transit light curves.

The best transit fit can be seen in [Fig. 2.3](#) (left) and was found to have an orbital period $P = 12.13$ d. However, the transit is relatively shallow (as expected for the giant star) and noisy. The transit depth would be consistent with a planetary companion of radius $R \sim 0.96 R_{\text{Jup}}$, similar to, but somewhat smaller than, the planetary candidate reported by the ExoFOP. I note that the transit duration $T_{\text{transit}} \sim 4.7$ h is shorter than would be expected for such a large star. I refrain from listing the full transit parameters due to the arguments against the planet hypothesis below.

Assuming a roughly Jovian mass for the planet, one would expect RV variations with a semi-amplitude $K \sim 50 \text{ m s}^{-1}$ for the longer period, while the shorter period $P = 6.98$ d

¹³<https://exofop.ipac.caltech.edu/tess/target.php?id=219751469>

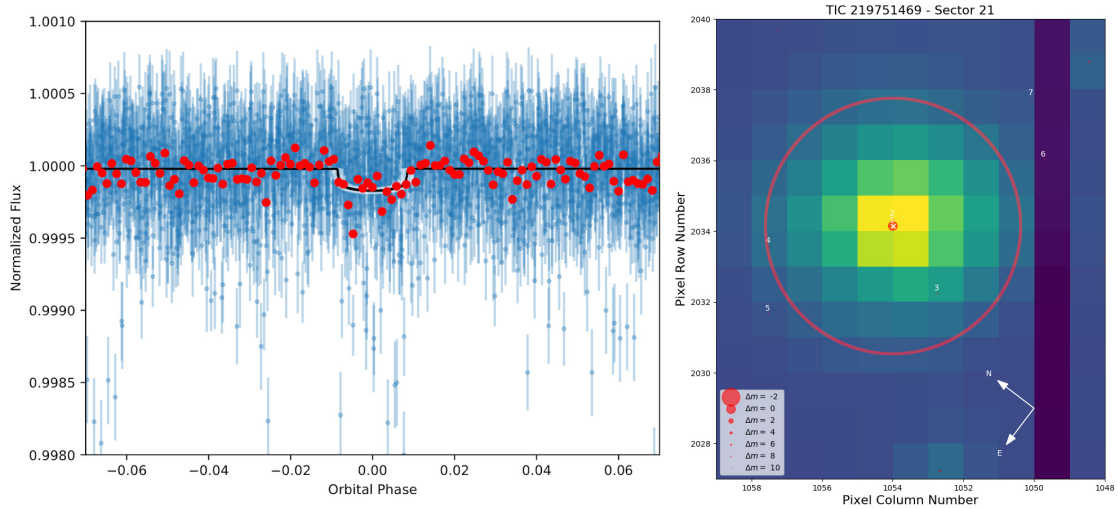


Fig. 2.3.: Transit analysis of the TESS FFI light curves for TOI 1489. Left: Transit fit using `juliet` combining TESS sectors 13 to 26. The phase folded TESS photometry, as provided by QLP, is shown in blue, with the binned fluxes shown in red. The best transit fit is shown in black and its uncertainties are shown in light blue. The best orbital period was determined to be at $P = 12.13$ d, rather than the reported $P = 6.98$ d. The phase is given as the fraction of the whole orbit. Right: TESS target pixel file in sector 21 computed by the `tpfplotter` tool. The 3.5 px aperture used by QLP is overplotted as a red circle. Three faint light sources (labeled 2, 3, and 4) can be seen in the aperture. Source 2 is likely a bound stellar companion to TOI 1489.

would lead to expected RV amplitudes $K \sim 60 \text{ m s}^{-1}$. We planned the RV follow-up observations such that both periods would be well sampled.

The right panel of Fig. 2.7 shows a cutout of the TESS target pixel files created using the `tpfplotter` (Aller et al., 2020). As can be seen, there are three faint sources within the aperture (3.5 px) used by the QLP. The closest source, labeled as number 2, was found to be a binary companion to TOI 1489 of mass $M = 0.44^{+0.23}_{-0.22} M_{\odot}$ separated by about 1640 AU from the giant (Behmard et al., 2022). However, due to the large separation, it cannot be responsible for the short-period transiting candidate. With a G -band magnitude difference of 8.5 mag (Behmard et al., 2022), it is likely to faint to have a large influence on the photometry. We also could not find any indications of large photometric variability in any of the three contaminating light sources in the *Gaia* catalog or the literature.

Overall, 25 FIES RVs have been acquired in semester 2022A. These are shown in Fig. 2.4 (left). As can be seen, there are no large RV variations present in the data set. The standard deviation of the RV measurements is $\sigma_{\text{RV}} = 7.9 \text{ m s}^{-1}$, much smaller than expected for the transiting planet candidate. The variations are roughly consistent with the p-mode jitter expected for this evolved star. In the right panel, I plot a Maximum Likelihood Periodogram (MLP, Zechmeister et al. 2019) of the RV measurements. I mark the two proposed planet periods in red and cyan. As can be seen, there is no significant periodicity

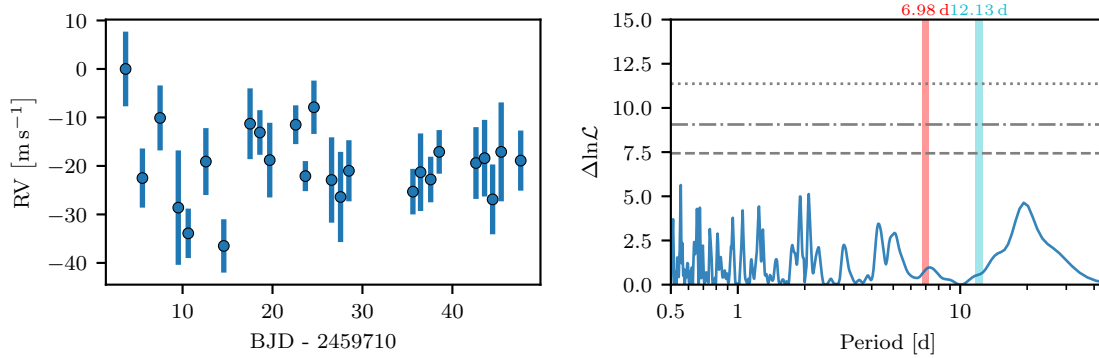


Fig. 2.4.: FIES RVs for TOI 1489. Left: The FIES RVs plotted against time. Right: MLP of the FIES RVs. The false alarm probabilities (FAPs) of 5%, 1%, and 0.1% are plotted as dashed, dash-dotted, and dotted gray lines, respectively. The two possible periods of the transiting candidate are highlighted in red and cyan.

at either candidate period or any other period. It can thus be concluded that the RV measurements refute the transiting planet candidate orbiting TOI 1489.

This is consistent with the updated findings by the TESS Follow-up Observing Program Working Group (TFOPWG), who classify TOI 1489 as a false alarm since 2023. Indeed, after the conclusion of the initial TESS mission, TOI 1489 was added to the two-minute cadence target list for the extended mission. Due to its high declination it was observed in numerous additional sectors with shorter cadence. As was noted by the TFOPWG, the planet period does not show up consistently in more recent TESS data. I plot a BLS periodogram search (Kovács et al., 2016) in each individual two-minute-cadence sector in Fig. 2.5. Solely TESS sector 21, which was already part of the original mission, shows a peak close to the reported $P = 6.98$ d period. This peak is not apparent in more recent sectors. The longer-period peak is also not visible in any sector other than sector 51.

In Fig. 2.6, I combine the individual sectors into a single BLS periodogram search. I mark the two candidate periods in red and cyan. While peaks can be observed at both periods, they do not dominate the periodogram compared to other peaks in the vicinity. Thus, it can be concluded that the transit signal was likely a misidentified signal caused by intrinsic variability. The transiting planet candidate orbiting TOI 1489 was thus a false alarm.

2.2.5 Discussion of TOI 1684

Analysis of the transit and radial velocity data

TOI 1684 (TIC 85031598, HIP 20334) was alerted as a transiting candidate after the TESS observations in sector 19 using SPOC two-minute cadence data. It was alerted as a planet

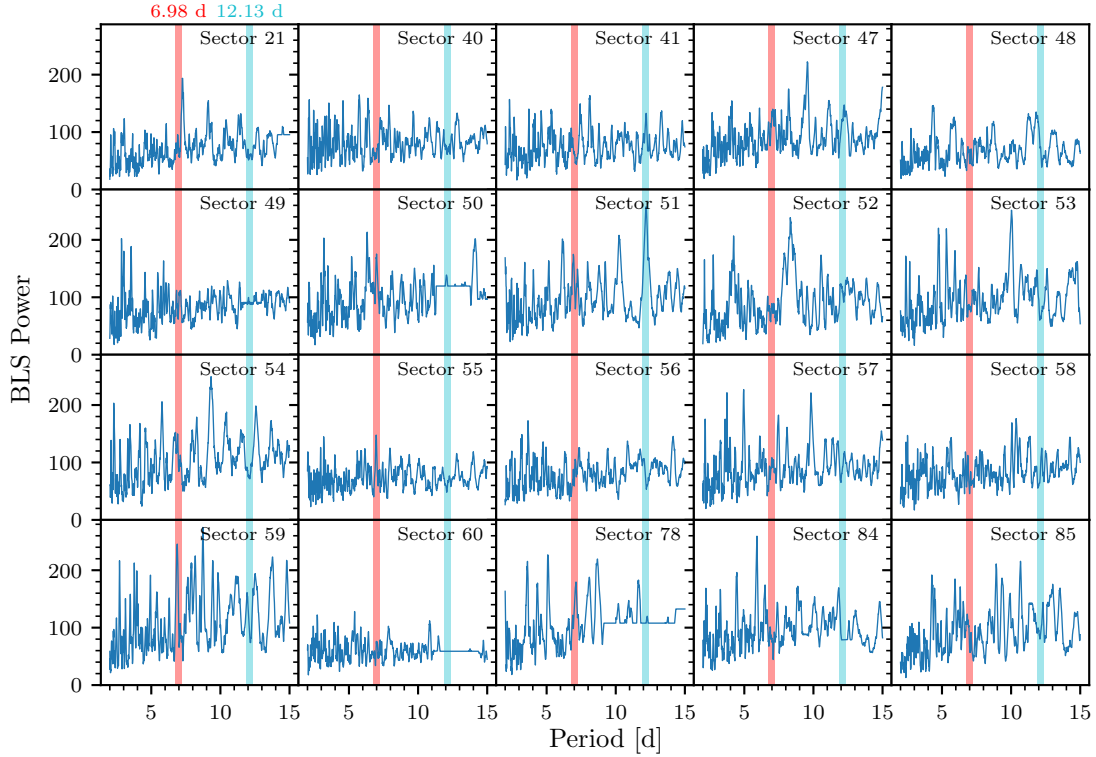


Fig. 2.5.: BLS periodograms for TOI 1489 for all two-minute cadence TESS sectors. The candidate periods of $P = 6.98$ d and $P = 12.13$ d are marked in red and cyan, respectively. A slightly dominant peak close to the reported TOI period is only visible in sector 21. The strongest indication of periodicity at $P = 12.13$ d is merely apparent in sector 51. All other sectors show no indication of significant periodicity at either period.

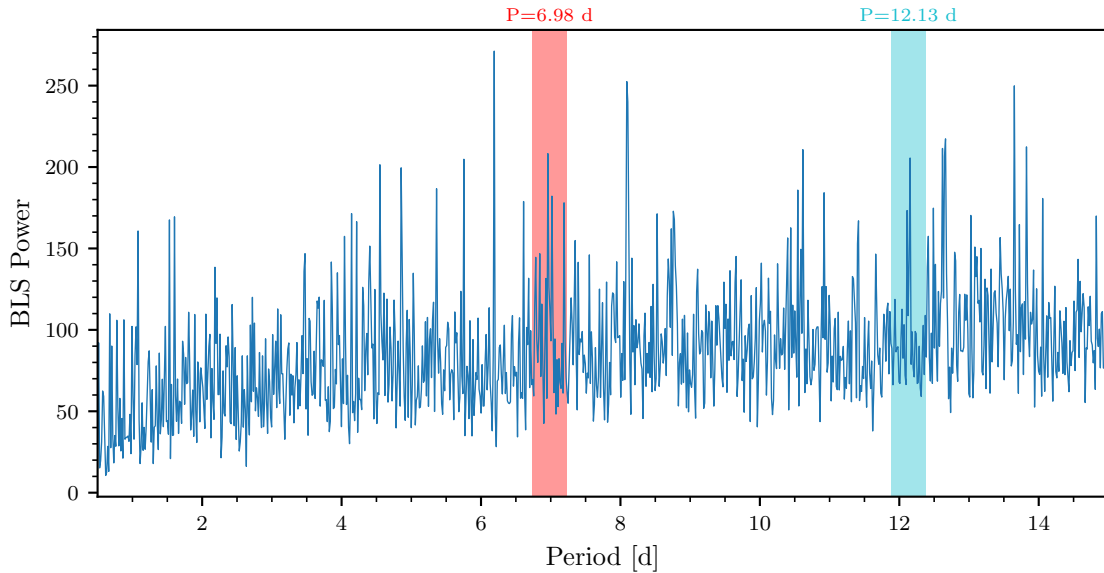


Fig. 2.6.: BLS periodogram combining all two-minute cadence TESS sectors for TOI 1489. The two candidate periods are marked in red and cyan.

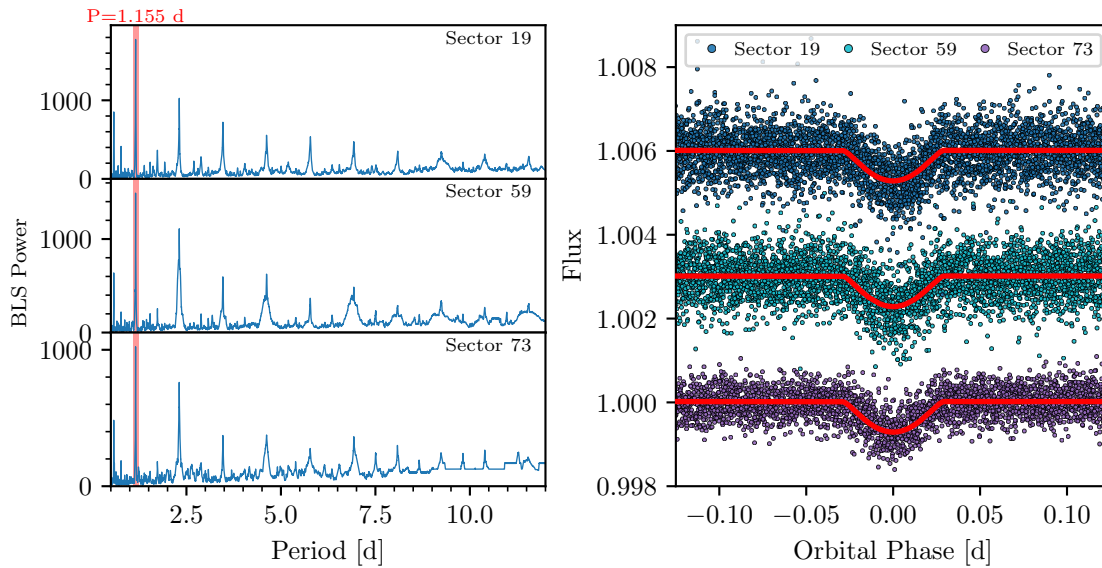


Fig. 2.7.: TESS transit analysis for TOI 1684. Left: BLS periodograms for the three TESS sectors using SPOC two-minute cadence photometry. Right: Phase folded transit curves of the three sectors. Offsets were applied to sectors 19 and 59. The best transit model derived via a nested sampling using `juliet` is overlotted in red.

candidate of radius $R \sim 9.4 R_{\oplus}$, in a $P = 1.155$ d orbit by the ExoFOP.¹⁴ It was noted that the transit is slightly V-shaped but remained a planet candidate. The star was further observed in sectors 59 and 73 in the extended TESS mission.

In Fig. 2.7 (left), I show the BLS periodogram search performed independently (due to the long gaps between the sectors) using the PDCSAP flux for each sector. I mark the reported planet candidate period $P = 1.155$ d in red. It is clearly apparent in all three sectors. One can also observe its harmonics at longer periods. The normalized PDCSAP flux from each sector, phase folded to the transit period, is plotted in the right panel. I apply offsets to sectors 19 and 59 for visual clarity. As can be seen, the transit signal is consistently present in all three TESS sectors. Overplotted in red is the best transit model obtained by performing a nested sampling of the parameter posterior distributions using `juliet`, combining the photometry from the three TESS sectors and the RVs obtained from the FIES observations (see below). While providing a visually convincing fit to the transit data, several irregularities were noted during the fitting process.

During initial tests using only the transit data and different priors, it was noticed that the transit is modelled with a large impact parameter $b \sim 1$, indicating that the transit is only grazing the stellar disk. Consequently, several of the parameter posteriors distribution, for instance for the limb-darkening parameters, are broad and weakly constrained by the fit. Additionally, fitting for the stellar density lead to inconsistent estimates compared to the

¹⁴<https://exofop.ipac.caltech.edu/tess/target.php?id=85031598>

calculated density of the giant $\rho \sim 51.6 \text{ kg m}^{-3}$. Finally, including a freely fitted dilution parameter D in the transit model, resulted in $D \sim 0.25$, indicating that the transit model is influenced by a diluting light source. All of these initial findings already cast doubts on the reliability of the transit model. These are further discussed below.

Nevertheless, to test the consistency between the TESS photometry and the RVs, I performed a joint modeling of both data sets using constrained, normal priors on the orbital period P and time of mid-transit T_0 motivated by the BLS search. I further used a Gaussian prior on the stellar density $\rho [\text{kg m}^{-3}] \sim \mathcal{N}(50, 10)$ and a fixed eccentricity $e = 0$ motivated by the short orbital period. I otherwise used wide, uniform priors. As already mentioned, the best transit model is shown as red lines in Fig. 2.7 (right). The posterior distribution of the impact parameter b is consistent with unity, indicating a grazing transit. Again, due to the problems with the planet hypothesis listed in the following, I refrain from listing the full transit parameters of the fit.

The problems in finding a well-defined transit model detailed above, are reinforced by the analysis of the FIES RVs in Fig. 2.8. The left panel portrays the MLP of the 32 FIES RVs taken in 2022. I exclude the six measurements taken in 2021 in this plot, as the long time gap between the observation campaigns leads to strong aliasing which complicates the analysis. I mark the period of the transit signal as the red shaded region. There is no significant periodicity at the transit period or any other period in the vicinity. The right panel of Fig. 2.8 shows the FIES RV measurements phase folded to the joint `juliet` model. I mark the data stemming from 2021 as red squares. However, the data from 2021 and 2022 were used as one data set during the modeling.

The best Keplerian model derived from the joint `juliet` model is plotted in red. The posterior distribution of the semi-amplitude K is consistent with zero within 2σ . Its most likely value $K = 0.49^{+0.89}_{-0.48} \text{ m s}^{-1}$ was adopted from the maximum of the posterior distribution. The uncertainties are estimated by calculating the region containing 68.27% of the samples. The Keplerian models consistent with this confidence region are shown in red in Fig. 2.8 (right). The errorbars represent the instrumental uncertainties, the model estimates an independent jitter component of $\sigma_{\text{RV}} = 5.9^{+1.4}_{-1.1} \text{ m s}^{-1}$ as expected due to p-mode pulsations for a mildly evolved star. The joint transit-RV model can thus not find a significant periodic variation in the RVs at the period of the transit.

Nevertheless, one can estimate whether a transiting planet could still be consistent with the data. Assuming first that the grazing transit model ($b \sim 1$) correctly describes a transiting object orbiting the giant star, leads to a planet-to-star radius ratio $p = 0.039 \pm 0.002$, and thus a radius of the transiting object of $R_p = 1.17^{+0.06}_{-0.07} R_{\text{Jup}}$. Müller et al. (2024) analyzes the relation between the masses and radii of transiting planets. From their Fig. 1, one can roughly estimate a lower mass limit of $M_p \sim 55 M_{\oplus}$ for a very inflated planet of that radius. However, even for this lower mass estimate, one would expect RV variations with a semi-amplitude $K \sim 33.5 \text{ m s}^{-1}$, inconsistent with the derived amplitude range.

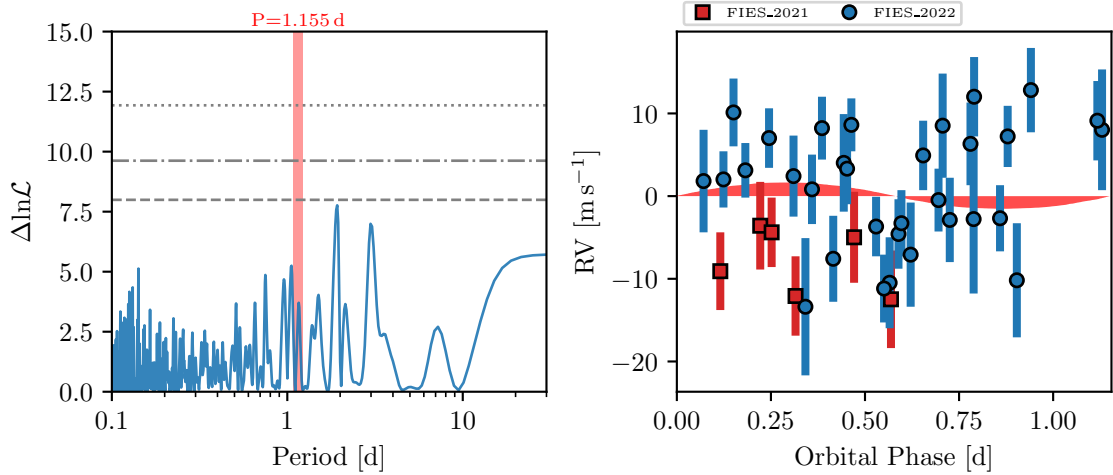


Fig. 2.8.: FIES RV analysis for TOI 1684. Left: MLP of the RVs taken in 2022. The transit candidate period $P = 1.155$ d is marked in red. The FAPs of 5% (dashed), 1% (dash-dotted), and 0.1% (dotted) are plotted as gray horizontal lines. Right: The whole data set phase folded to the best orbital fit at the transit period. The 1- σ region of possible Keplerian models is plotted in red.

If one, for the sake of the argument, assumes that the grazing transit is incorrect and derives the planetary radius directly from the transit depth, one can estimate a planetary radius $R_p \sim 8.9_{-0.3}^{+0.1} R_\oplus$, for which planetary masses as low as $M_p \sim 11 M_\oplus$ can be found in Müller et al. (2024) within the 3- σ region of possible radii. From the juliet fit, the largest possible semi-amplitude in a 3- σ region is $K \sim 4.2 \text{ m s}^{-1}$, which would correspond to a planet mass of $M_p \sim 6.9 M_\oplus$. This most extreme scenario would correspond to an extremely low planet density of $\rho_p \sim 0.075 \text{ g cm}^{-3}$, an unrealistic value even for very inflated hot Jupiters (see also Fig. 2 of Müller et al. 2024). At the small planetary masses required here, such low densities can be ruled out. I conclude that the RVs exclude the possibility that a planet orbiting the giant star can explain the observed transit signal.

Discussion of alternative explanations

The most likely explanation for TOI 1684 was proposed by Zhang et al. (2022) in a poster contribution to the *American Astronomical Society Meeting*. They claim to have detected a K dwarf companion to TOI 1684 using Keck/NIRC2 AO imaging. The stellar companion is reported to be about 4 mag fainter than the giant star and separated by about 6.5 AU in an inclined orbit with $i \sim 45^\circ$. The transiting signal is presumed to originate from the secondary source instead of the primary.

The star can indeed be found to be a convincing binary system candidate based on a significant ($S/N > 200$) HIPPARCOS-Gaia DR3 proper motion anomaly (Kervella et al., 2022) and its presence among the stars with an additional acceleration in the astrometric

solution of *Gaia* DR3 (Halbwachs et al., 2022; Gaia Collaboration et al., 2016, 2023). The secondary component is, however, not resolved in *Gaia* DR3.

Surprisingly, I do not find a large offset between the RV data sets taken in 2021 and 2022. However, thanks to additional HIRES RV measurements (Vogt et al., 1994) that span a significantly longer baseline and have been provided by J. Zhang (priv. comm., 2025), I could confirm that the FIES RVs were, by chance, sampled at either side of the RV maximum of a long-period binary orbit.

Naturally, the orbit of this long-period stellar companion cannot cause the 1.155 d signal. However, using the Keck Planet Imager and Characterizer (KPIC) (Delorme et al., 2021), J. Zhang (priv. comm, 2025) obtained two RV data points of the K dwarf revealing an RV difference larger than 10 km s^{-1} , confirming the origin of the transit signal to be a stellar companion eclipsing the K dwarf. These results will be published in an upcoming article (Zhang et al., in prep.). These findings are also consistent with the assessment by Prša et al. (2022), which include the star in a list of eclipsing binaries due to phase inconsistencies between the primary and secondary eclipses, indicating an eccentric orbit.¹⁵

Assuming the reported magnitude difference of 4 mag and estimating the radius of the K dwarf at $R \sim 0.8 R_{\odot}$, one can estimate the radius of the transiting companion to be $R_c > 0.14 R_{\odot}$, placing it likely into the M dwarf regime. Thus, TOI 1684 is likely located in a hierarchical triple star system with a red giant primary orbited by an eclipsing binary pair consisting of two dwarf stars with spectral types K and M.

2.2.6 Conclusions

I conclude that both transiting planet candidates are false positives. While TOI 1489 was a false alarm, TOI 1684 was found to be in a hierarchical triple star system.

The field as a whole has made large progress in confirming transiting planets orbiting subgiants and giants (Saunders et al., 2022; Grunblatt et al., 2022, 2023, 2024; Pereira et al., 2023; Saunders et al., 2024, 2025; Chontos et al., 2024), further strengthening the findings by Grunblatt et al. (2019) and Temmink & Snellen (2023), that hot Jupiters are as common around mildly evolved stars, as they are around main-sequence stars. Recent findings even suggest the existence of two distinct classes of hot giant planets around subgiants, indicating independent formation scenarios (Chontos et al., 2024). Grunblatt et al. (2023) find that longer-period transiting planets tend to have larger eccentricities, which challenges current theories of star-planet interactions during the stellar evolution (see Sect. 1.3) and provides a link to planet-planet interactions playing an additional role. Other systems allow for constraining the timescales of planet inflation during the

¹⁵Their live results can be seen at <https://tessebs.villanova.edu/85031598.1>

post-main-sequence stage of their host stars (Saunders et al., 2022) and for studying the timescales of the stripping of planetary atmospheres (Grunblatt et al., 2024). In any case, the transiting planet population orbiting post-main-sequence stars proves to be a laboratory to study the influence of host stars on their planetary companions.

Simulating non-radial oscillations of evolved stars

In Sect. 1.9, I introduce the planet controversy surrounding luminous giants. These stars show (semi-) periodic RV variations which mimic orbital companions but are originating intrinsically. Radial pulsations can be ruled as the origin as the periods are longer than the fundamental mode (Hatzes & Cochran, 1993; Cox et al., 1972; Hatzes et al., 2018; Reichert et al., 2019). Star spots are unlikely (e.g., Reffert et al. 2015) as no photometric variations are detected. Non-radial oscillations remain a promising explanation (Hatzes et al., 2018) and may be linked to oscillatory convective modes (Saio et al., 2015).

Hatzes (1996) showed that non-radial oscillations can cause sinusoidal RV variations, which, however, would also have an effect on the spectral line shapes and bisectors. Since then, the available activity indicators have evolved significantly with the advent of new spectrographs and reduction pipelines. However, so far there are no published attempts to simulate the signatures of non-radial oscillations in modern activity indicators.

In this Chapter, I present the `pyoscillot`¹ simulation suite, developed to simulate HARPS (Mayor et al., 2003) and CARMENES (Quirrenbach et al., 2014) spectra, aiming study the relations between RVs and activity indicators for non-radial oscillations. It is inspired by the work of Hatzes (1996), but also draws inspiration from codes such as SOAP (Boisse et al., 2011), StarSim (Herrero et al., 2016), SOAP-GPU (Zhao & Dumusque, 2023), and the works by Kochukhov (2004) and Baroch et al. (2020). Most of these, however, target the effect of star spots. Here, I give an introduction to the code and provide general insights into the oscillation parameters. The simulations are applied to the known false-positive planet host NGC 4349 No. 127 (Delgado Mena et al., 2018, 2023) in Chapt. 4.

3.1 General simulation paradigm

3.1.1 Representation in spherical coordinates

At its core, `pyoscillot` studies the effect of surface phenomena by mapping physical properties, such as effective temperature or velocity, onto a unit sphere represented in

¹<https://github.com/DaneSpaeth/pyoscillot>

spherical coordinates. The sphere consists of $N_{\text{sph}} \times N_{\text{sph}}$ grid points sampled uniformly for the two angles θ and ϕ . N_{sph} is typically selected to be 1000 but does not yet define the resolution N_{grid} at which the stellar disk is sampled at a later stage.

I follow the ISO convention, defining θ as the polar angle (or colatitude) measured from the polar axis (z-axis) of the sphere and ranging from 0 to π , and ϕ as the azimuthal angle measured from the positive y-axis, ranging from 0 to 2π . In this initial coordinate frame, the z-axis is chosen to always coincide with the symmetry axis of both the oscillation and the rotation. A set of physical properties, such as the ones stemming from a non-radial oscillation, can be defined for each position (θ, ϕ) on the surface.

3.1.2 Implementation of non-radial oscillations

Although, oscillations of stars are fundamentally 3D phenomena, their observational effects are dominated by the outer layers of the photosphere. For this reason, and since studying the underlying physical processes causing the oscillations is beyond the scope of this work, a simple model of non-radial oscillations at the stellar “surface” was chosen.

For a spherically symmetric star, under the assumption of hydrostatic equilibrium and small perturbations of the spherical symmetry, the solutions of the equations of motion have displacements (Kurtz, 2006; Aerts, 2021)

$$\xi_r(r, \theta, \phi, t) = a(r)Y_l^m(\theta, \phi) \exp(i2\pi\nu t) \quad (3.1)$$

$$\xi_\theta(r, \theta, \phi, t) = b(r) \frac{\partial Y_l^m(\theta, \phi)}{\partial \theta} \exp(i2\pi\nu t) \quad (3.2)$$

$$\xi_\phi(r, \theta, \phi, t) = \frac{b(r)}{\sin \theta} \frac{\partial Y_l^m(\theta, \phi)}{\partial \phi} \exp(i2\pi\nu t). \quad (3.3)$$

Here, $a(r)$ and $b(r)$ are the amplitudes of the radial and horizontal components, respectively. ν is the oscillation frequency and $Y_l^m(\theta, \phi)$ are the spherical harmonics:

$$Y_l^m(\theta, \phi) = \sqrt{\frac{2l+1}{4\pi} \frac{(l-m)!}{(l+m)!}} P_l^m(\cos \theta) \exp(im\phi). \quad (3.4)$$

$P_l^m(\cos \theta)$ are the Legendre Polynomials defined as

$$P_l^m(\cos \theta) = \frac{(-1)^m}{2^l l!} (1 - \cos^2 \theta)^{\frac{m}{2}} \frac{d^{l+m}}{d \cos^{l+m} \theta} (\cos^2 \theta - 1)^l. \quad (3.5)$$

l describes the number of angular nodes on the surface, while m defines the number of nodal lines which run through the oscillation pole, with $-l \leq m \leq l$.

When neglecting perturbations of the gravitational potential, the so-called Cowling approximation (Cowling, 1941), the displacement amplitude in the horizontal direction $b(r)$ at the stellar surface can be expressed as a function of the displacement in the radial direction $a(r)$, introducing the factor (Kochukhov, 2004; Aerts, 2021)

$$K \equiv \frac{a(r)}{b(r)} = \frac{GM_\star}{(2\pi\nu)^2 R_\star^3}. \quad (3.6)$$

Here, M_\star and R_\star are the mass and radius of the star, respectively, and G is the gravitational constant. The approximation is strictly only valid for modes of high radial order n and high degree l . It is typically small (~ 0.001) for high-order p-modes, such as the ones present in the Sun, but relatively large (10 – 1000) for high-order g-modes (Aerts, 2021). Within `pyoscillot`, the relation $b(r) = K \cdot a(r)$ is adopted, leaving K as an input parameter.

In the context of false-positive planet detections around giants, the velocity amplitudes are relatively small. For simplicity, I therefore neglect geometrical distortions and keep the stellar radius at unity ($r = 1$) during the oscillation. The simulations can therefore be visualized as mapping the oscillation components onto the unit sphere. The velocity components of the oscillation are determined by calculating the temporal derivative (Schrijvers et al., 1997; Kochukhov, 2004) of the displacement vectors resulting in

$$v_r = \frac{\partial \xi_r}{\partial t} = i2\pi\nu \cdot \frac{a}{C} Y_l^m(\theta, \phi) \exp(i2\pi\nu t) \quad (3.7)$$

$$v_\theta = \frac{\partial \xi_\theta}{\partial t} = i2\pi\nu \cdot \frac{Ka}{C} \frac{\partial Y_l^m(\theta, \phi)}{\partial \theta} \exp(i2\pi\nu t) \quad (3.8)$$

$$v_\phi = \frac{\partial \xi_\phi}{\partial t} = i2\pi\nu \cdot \frac{Ka}{C \sin \theta} \frac{\partial Y_l^m(\theta, \phi)}{\partial \phi} \exp(i2\pi\nu t). \quad (3.9)$$

Within `pyoscillot`, I define $v_{\text{osc}} = 2\pi\nu a/C$ as the velocity amplitude in the radial direction. Consequently, $K \cdot v_{\text{osc}}$ is the velocity amplitude in θ and ϕ direction. Since spherical harmonics are normalized to fulfill the condition

$$\int |Y_l^m|^2 d\Omega = 1, \quad (3.10)$$

I introduce the normalization factor $C = \max(\text{Re}(iY_l^m(\theta, \phi)))$ for $m \neq 0$, and $C = \max(\text{Re}(Y_l^m(\theta, \phi)))$ for $m = 0$, such that v_{osc} can be regarded as the amplitude of the radial component at the position of maximum variation on the stellar surface.

The partial derivatives of the spherical harmonics can be expressed as²

$$\frac{\partial Y_l^m(\theta, \phi)}{\partial \theta} = \frac{m}{\tan \theta} Y_l^m(\theta, \phi) + \sqrt{(l-m)(l+m+1)} \exp(-i\phi) Y_l^{m+1}(\theta, \phi) \quad (3.11)$$

$$\frac{\partial Y_l^m(\theta, \phi)}{\partial \phi} = im Y_l^m(\theta, \phi). \quad (3.12)$$

²See e.g. <https://functions.wolfram.com/PDF/SphericalHarmonicY.pdf>

The local velocity vector on the simulated stellar surface is then given by the real part of the velocity components multiplied with their respective unit vectors (Kochukhov, 2004)

$$\mathbf{v}_{osc} = \text{Re}(v_r) \cdot \hat{\mathbf{r}} + \text{Re}(v_\theta) \cdot \hat{\boldsymbol{\theta}} + \text{Re}(v_\phi) \cdot \hat{\boldsymbol{\phi}}. \quad (3.13)$$

3.1.3 Line-of-sight projection

To mimic the process of spectrum acquisition, the coordinates on the unit sphere and their associated physical properties need to be projected onto a 2D plane. First, an inclination angle i is chosen, which is defined as the angle between the symmetry axis of the oscillation (the z-axis) and the line of sight. To account for this viewing position, the reference frame is rotated via an Euler's rotation by $(90^\circ - i)$ around the x-axis.

In principle, another azimuthal rotation of the observing position around the z-axis could be added. However, for simplicity I choose to avoid this second rotation. For single modes, this second rotation is either irrelevant (in case of rotationally symmetric modes) or degenerate with an arbitrary temporal phase shift. I therefore absorb this rotation into the temporal phase shift applied to the oscillation components. I note that this additional rotation of the reference frame could become relevant in more complex scenarios, when combining multiple modes with different periods and phase relations.

The observer is chosen to be located at infinite distance on the y' -axis in the rotated reference frame. Thus, the unit vector along the line of sight in the original, unprimed coordinate system is defined by

$$\hat{\mathbf{u}}_{\text{LoS}} = \begin{bmatrix} 0 \\ -\cos(90^\circ - i) \\ \sin(90^\circ - i) \end{bmatrix}. \quad (3.14)$$

Opposite to scalar quantities (e.g., effective temperature), vector quantities (such \mathbf{v}_{osc}) are projected onto the line of sight by calculating the scalar product with $\hat{\mathbf{u}}_{\text{LoS}}$. The sign of the projection operation was selected such that a positive amplitude along the radial direction (i.e., an outward oscillation) leads to a negative projected value, consistent with the RV definition. Only grid points on the hemisphere facing the observer are projected.

Finally, the projected values are linearly interpolated onto a regularly sampled 2D grid with $N_{\text{grid}} \times N_{\text{grid}}$ positions (along the x' and z' -axis). The sampled positions can be regarded as the center points of cells covering the projected stellar disk with uniform areas. For cell center points that fall outside the original cloud of projected points, the linear interpolation is replaced by a nearest neighbor interpolation to ensure physically plausible values at the stellar edge.

Figure 3.1 illustrates the coordinate frame and the projection process. In the top row, I plot the three velocity components of a non-radial oscillation on the unit sphere, which further define the original, unprimed cartesian coordinate system. The color-coding portrays the amplitude of each velocity component at each position on the stellar sphere. The sphere is here seen from an arbitrary observing position. The second row then represents the view of the upper panels from a specific observing position. I here choose an inclination angle $i = 90^\circ$, such that the observer is on the original y-axis, and the x' - and z' -axes correspond to the original x- and z-axes. The bottom row portrays the result of the projection process, by performing a scalar product with \hat{u}_{LoS} .

It is evident (e.g. from the r -component) that I chose the sign of the projection such that a positive oscillation amplitude (outward oscillation) corresponds to a negative RV. One furthermore can observe that the projected velocities depend on the unit vectors of the individual velocity components. While the projected r -component is dominated by the central part of the stellar disk, the projected ϕ - and θ -components are strongest toward the limb. One can also observe how the signs of the projected θ and ϕ velocity components are flipped due to the changing orientation of their unit vectors across the stellar disk.

For each cell i in the 2D coordinate frame, a geometric weight w_i is computed by calculating the percentage of the cell's area covered by the stellar disk. This weight is later used during the spectrum combination. To compute the local, combined oscillation velocity $v_{\text{osc},i}$, all three velocity components are projected onto the line of sight and summed up. Within `pyoscillot`, the user can add an unlimited amount of oscillation modes with the different parameters ($l, m, P_{\text{osc}}, v_{\text{osc}}, K, \delta T_{\text{eff}}, \psi_T$). The contributions of all modes are summed up. No interaction between the modes is calculated. It is therefore left for the user to provide physically plausible parameters.

3.1.4 Temperature fluctuations

The density and pressure variations associated with non-radial oscillations lead to temperature variations within the stellar interior and the stellar atmosphere. In adiabatic conditions, [Buta & Smith \(1979\)](#) showed that the temperature variations are proportional to the relative radial displacement ([Townsend, 1997](#)). [Dupret et al. \(2002\)](#) and [De Ridder et al. \(2002\)](#) showed that, assuming non-adiabatic conditions, the local variations of effective temperature can be phase shifted with respect to the radial displacement:

$$\frac{\delta T_{\text{eff}}}{T_{\text{eff}}} = f_T \frac{\xi_r}{R} \exp(i\psi_T), \quad (3.15)$$

with the scaling factor f_T , the relative radial displacement $\frac{\xi_r}{R}$, and the phase shift ψ_T . Within `pyoscillot`, I follow this approach defining δT_{eff} as the amplitude of the local

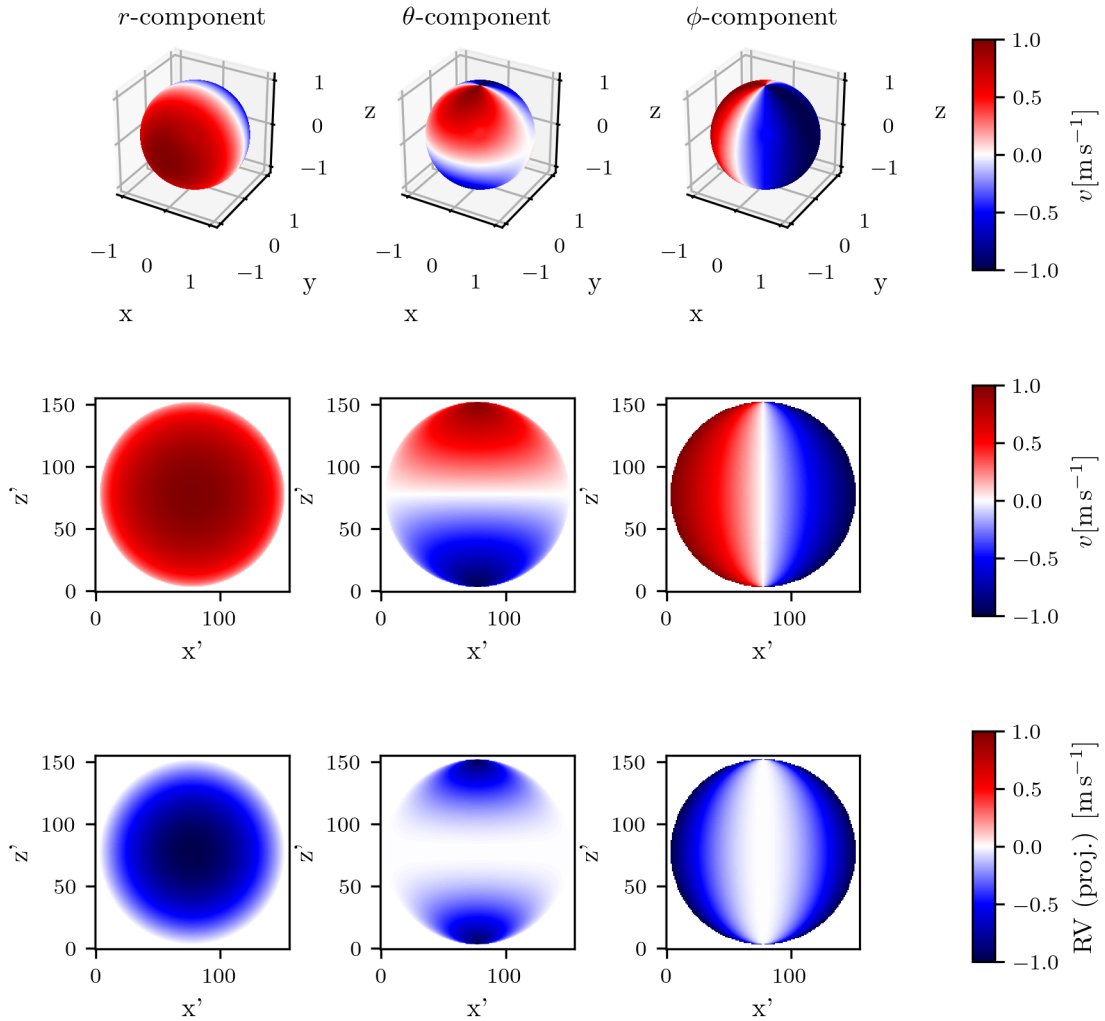


Fig. 3.1.: Temporal snapshot of a non-radial oscillation with mode $(l = 1, m = 1)$, $v_{\text{osc}} = 1 \text{ m s}^{-1}$ and $K = 1$. Top row: r , θ , and ϕ components plotted on top of the 3D spherical model. Middle row: Components projected onto the 2D plane with inclination 90° (without projection onto the line of sight). Bottom row: Line of sight projection of the components. As one can see, for a positive amplitude v_{osc} pointed toward the observer, a negative RV is resulting to conform with the standard definition. One can further observe that for both the θ and ϕ components, the contribution is strongest at the limbs. Furthermore, due to the changing orientation of the unit vectors across the visible stellar disk, the sign of the projected oscillation velocity is flipped when the unit vectors point away from the observer.

effective temperature variation. To enhance the physical meaning of the δT_{eff} parameter, I normalize the amplitude at the point of maximum radial displacement to unity, defining δT_{eff} as the maximum temperature variation on the simulated stellar surface. Thus, the local effective temperature for each grid point can be calculated as

$$T_{\text{eff,local}} = T_{\text{eff}} + \delta T_{\text{eff}} \operatorname{Re} \left(\frac{Y_l^m(\theta, \phi)}{\max(\operatorname{Re}(Y_l^m(\theta, \phi)))} \exp(i(2\pi\nu t + \psi_T)) \right). \quad (3.16)$$

As the effective temperature is a scalar quantity, no scalar product with the line of sight has to be computed during the projection onto the 2D plane.

3.1.5 Stellar rotation

Next to the oscillation velocity field, the stellar rotation plays an important role to model stellar spectra. Within `pyoscillot`, the rotation axis always coincides with the z-axis and therefore with the symmetry axis of the oscillation. The rotation vector is

$$\mathbf{v}_{\text{rot}} = v_{\text{rot}} \sin(\theta) \cdot \hat{\phi}. \quad (3.17)$$

Here, v_{rot} is the user defined rotation velocity in m s^{-1} . Its sign is defined such, that a positive v_{rot} yields a rotation of the star in positive ϕ direction. Negative values of v_{rot} are allowed and lead to rotation in the opposite direction. With this definition and the positive exponent in the $\exp(i2\pi\nu t)$ term in Eq. 3.2, positive m correspond to retrograde modes for $v_{\text{rot}} > 0$, consistent with the definition by [Hatzes \(1996\)](#) and [Kurtz \(2006\)](#), but opposite to, for instance, [Aerts \(2021\)](#).

Same as the oscillation velocity vector, the rotation velocity vector is projected onto the line of sight. The total velocity of each projected area on the 2D plane is the sum of the projected oscillation and rotation velocities.

3.2 Computation of high-resolution spectra

The goal of `pyoscillot` is to provide observables that can be compared to observations. The common observables available in the context of planet detections around giant stars are time series of high-resolution spectra (apt for measuring RVs) or photometry in various photometric filters. This section discusses the calculation of high-resolution spectra in isolation of additional, optional effects which are discussed in [Sect. 3.3](#).

To create a time series of spectra, `pyoscillot` first performs the above calculation of the oscillation velocities for one or multiple oscillation modes with user-defined parameters (l , m , P_{osc} , v_{osc} , K , δT_{eff} , ψ_T , v_{rot}) at user-defined epochs. These can either be provided or be calculated by `pyoscillot` automatically. `Pyoscillot` is parallelized, as each epoch is simulated independently, allowing the execution on multiple cores.

3.2.1 PHOENIX - The underlying model spectra

As the underlying model spectra, I use the high-resolution spectra of the PHOENIX library³ published by [Husser et al. \(2013\)](#). These were synthesized from a grid of model atmospheres calculated using PHOENIX ([Hauschildt & Baron, 1999](#)) in spherical mode. They are available on a grid ranging from $2300 \text{ K} \leq T_{\text{eff}} \leq 12\,000 \text{ K}$ (in 100 K and 200 K steps), $0.0 \leq \log g \leq 6.0$ (in steps of 0.5), $-4.0 \leq [\text{Fe}/\text{H}] \leq +1.0$ (in steps of 1.0 or 2.0 for low metallicities), and $-0.2 \leq [\alpha/\text{Fe}] \leq +1.2$ (in steps of 0.2). The spectra are sampled with a sampling rate $\frac{\lambda}{\Delta\lambda} = R \sim 500\,000$. However, they were not convolved with any kernel ([Husser, 2012](#)), i.e., it should solely be regarded as the sampling rate of the spectra. The stellar spectra were broadened to account for the effect of microturbulence according to scaling relations based on the convective motion in the model atmospheres. The employed microturbulences are available in the FITS headers of the PHOENIX spectra.

As a base, I use the PHOENIX spectrum for the user defined parameters (T_{eff} , $\log g$, and $[\text{Fe}/\text{H}]$). To minimize the influence of interpolation errors, I restrict the base parameters of a star to lie exactly on a PHOENIX grid point. I further select $[\alpha/\text{Fe}] = 0.0$ for all simulated stars. `Pyoscillot` downloads the respective PHOENIX spectrum automatically and saves it for future use, if not yet available in a pre-defined directory. To save computational power, the spectra are cut according to the user defined parameters λ_{min} and λ_{max} for each simulation run. The spectra are used with the original, physical PHOENIX continuum.

I note that the employed PHOENIX spectra are already disk-integrated spectra. Ideally, one would like to use a synthetic spectrum calculated from a model atmosphere for a specific observing angle $\mu = \cos \gamma$, with γ being the angle between the surface normal and the line of sight. Such spectra are available from the Göttingen PHOENIX spectral library (these are named “specific intensity spectra”). Unfortunately, these are only available with a resolving power $R \sim 10\,000$, too low to allow the calculation of high-resolution spectra for spectrographs like HARPS and CARMENES. Thus, I resort to the full, disk-integrated spectra offered by the PHOENIX “HiRes” mode. If higher-resolution, line-of-sight specific spectra were to become available in the future, these could easily be implemented within `pyoscillot`, likely improving the overall accuracy of the simulations.

³<https://phoenix.astro.physik.uni-goettingen.de/>

3.2.2 Temperature interpolation

To account for the variations of the effective temperature, a suitable interpolation between the spectra of the PHOENIX grid is necessary. Husser et al. (2013) advocates a point-wise cubic spline interpolation. Inspired by Husser (2012) and Husser et al. (2016), I use a cubic spline interpolation in one dimension following Press et al. (2007)

$$F(\lambda) = AF_j(\lambda) + BF_{j+1}(\lambda) + CF_j(\lambda)'' + DF_{j+1}(\lambda)'' \quad (3.18)$$

Here, $F(\lambda)$ is the flux at wavelength λ at a temperature T_{eff} , to which shall be interpolated to. $F_j(\lambda)$ and $F_{j+1}(\lambda)$ are the neighboring grid points with corresponding temperature $T_{\text{eff},j}$ and $T_{\text{eff},j+1}$, respectively. The coefficients A, B, C, and D are given by

$$A = \frac{T_{\text{eff},j+1} - T_{\text{eff}}}{T_{\text{eff},j+1} - T_{\text{eff},j}} \quad (3.19)$$

$$B = 1 - A = \frac{T_{\text{eff}} - T_{\text{eff},j}}{T_{\text{eff},j+1} - T_{\text{eff},j}} \quad (3.20)$$

$$C = \frac{1}{6}(A^3 - A)(T_{\text{eff},j+1} - T_{\text{eff},j})^2 \quad (3.21)$$

$$D = \frac{1}{6}(B^3 - B)(T_{\text{eff},j+1} - T_{\text{eff},j})^2. \quad (3.22)$$

The interpolation merely depends on the temperature and flux at the two neighboring grid points, as well as the second derivative with respect to T_{eff} . I adopted the implementation of the second derivatives from the `spexxy` framework.⁴ The interpolated PHOENIX spectra were precomputed in 0.1 K steps.

In the context of small-amplitude non-radial oscillations, the main varying parameter (apart from the velocity) is the local effective temperature. The variations of the surface gravity can be expected to be much smaller. De Ridder et al. (2002), for example, found variations of $\log(g)$ below 0.01 dex for large effective temperature variations of the order of 500 K to 1300 K. Since the PHOENIX grid is comparably coarse in $\log(g)$ with steps of 0.5 dex, I avoid an interpolation in $\log(g)$. The same is true for the metallicity $[\text{Fe}/\text{H}]$, which can be expected to be relatively constant during an oscillation cycle.

3.2.3 Velocity shift

For each grid cell, the temperature-adjusted spectra are next shifted according to the combined projected velocity of rotation and oscillation. Within `pyoscillot`, this shift is implemented by first oversampling the PHOENIX spectra at equidistant 0.001 Å steps, shifting the wavelength array following the relativistic Doppler shift, and performing a

⁴<https://github.com/thusser/spexxy>

cubic spline interpolation back onto the original wavelength grid. This allows for a simple addition of all spectra during the spectrum combination process.

3.2.4 Spectrum integration

With the temperature-adjusted and shifted spectra for each cell i on the 2D stellar disk, the disk integrated spectrum $I_{\text{integrated}}(\lambda)$ for each epoch can be computed as the sum of all local spectra $I_i(T_{\text{eff},i}, v_i, \lambda)$ multiplied by the weight w_i , which is unity for cells completely covered by the stellar disk, 0 for cells outside the disk, and proportional to the area covered by the disk for edge cells. The final spectrum is then given by

$$I_{\text{integrated}}(\lambda) = \frac{1}{\sum_i w_i} \sum_i I_i(T_{\text{eff},i}, v_i, \lambda) \cdot w_i. \quad (3.23)$$

I divide by the sum of all weights to maintain a reasonable normalization of the combined spectrum. I note again that the local spectra still maintain the original, PHOENIX continuum, albeit interpolated to the local effective temperature. Thus, the spectra are implicitly weighted by intensity during the spectrum combination. A further intensity weighting according to the optional effect of limb darkening is described in [Sect. 3.3.3](#).

3.2.5 Adjusting the resolution

Since the goal of `pyoscillot` is to provide spectra that can be compared to real spectra, the simulation has to mimic the acquisition process of a spectrograph. Within this context, these are HARPS ([Mayor et al., 2003](#)) and both channels of the CARMENES spectrograph ([Quirrenbach et al., 2014](#)). The most important step is to adjust the spectra according to the instruments' resolving powers.

At this point, the combined spectra are still in the natural PHOENIX wavelength sampling which was selected to coincide with a resolving power of $R \sim 500\,000$. As briefly mentioned, these are theoretical spectra which were not convolved with any kernel ([Husser, 2012](#)). To match the final spectra to the resolving power of the instruments, the spectra are first split into the individual spectral orders following a wavelength grid taken from a real observation. The order spectra are next smoothed with a Gaussian profile.

The necessary standard deviation of the Gaussian profile can be calculated via

$$R_{\text{inst}} = \frac{\lambda}{\text{FWHM}} = \frac{\lambda}{2\sqrt{2 \ln 2} \sigma_{\text{inst}}}, \quad (3.24)$$

in which σ_{inst} is the standard deviation for the smoothing kernel in wavelength space. Since the width of the smoothing kernel is wavelength dependent, `pyoscillot` performs

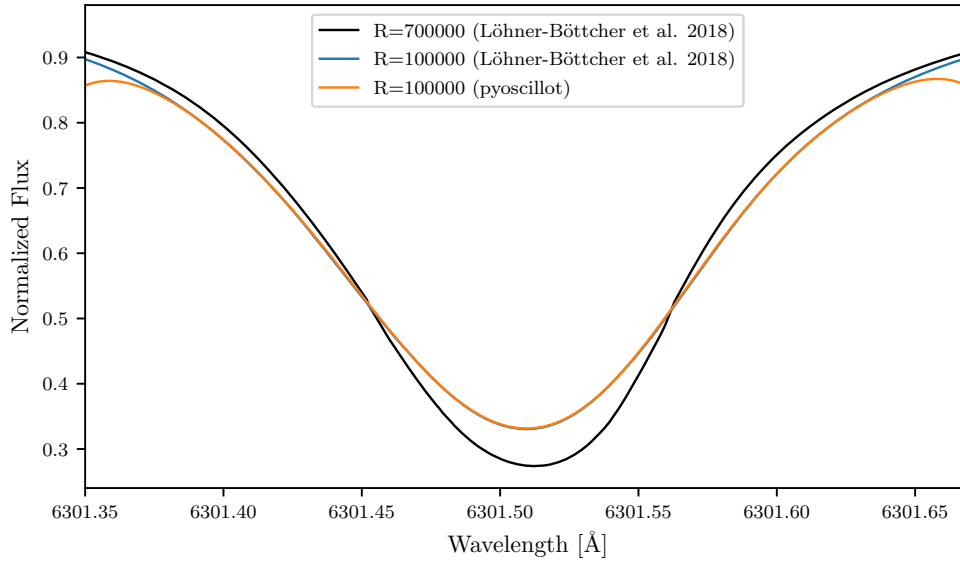


Fig. 3.2.: Test of the `pyoscillot` resolution adjustment. The $R = 700\,000$ line profile of the Fe I 6301.5008 Å was extracted from Löhner-Böttcher et al. (2018) (their Fig. 12). Afterwards the resolving power was adjusted to $R = 100\,000$ (orange). For comparison the $R = 100\,000$ result by (Löhner-Böttcher et al., 2018) is plotted in blue.

the smoothing per wavelength grid point. The resolving powers are: HARPS: $R = 115\,000$ Mayor et al. 2003, CARMENES-VIS: $R = 94\,600$, CARMENES-NIR: $R = 80\,400$ ⁵. `Pyoscillot` assumes a constant resolving power over the whole wavelength range.

To test the resolution adjustment, I compared the results with the resolution change by Löhner-Böttcher et al. (2018). Figure. 3.2 shows their $R = 700\,000$ line profile (black), which was smoothed to $R = 100\,000$ by `pyoscillot` (orange). Within the relevant line center, the `pyoscillot` result matches very well with the published $R = 100\,000$ result (blue, Löhner-Böttcher et al. 2018). I note that the smoothed model deviates from the published model at the edges as no data was available outside the plotted wavelength regime, thus leading to a fringing effect. For full simulations, this effect is taken care of by using a wavelength padding of 100 Å adjacent to both ends of the spectral range.

3.2.6 Synthesizing instrument specific spectra

To be able to use the standard reduction pipelines to acquire the observables from the synthetic spectra, it is necessary to mimic the data products available from observations. To achieve this, `pyoscillot` takes a real observation from each instrument as a reference. This real spectrum is an extracted spectrum created by the standard extraction pipelines

⁵<https://carmenes.caha.es/ext/instrument/index.html>

(HARPS DRS for HARPS, CARACAL for CARMENES). For HARPS, these are labeled “*_e2ds_A.fits”, while for CARMENES these are labeled “*_vis_A.fits” or “*_nir_A.fits” for the visual and near-infrared channels, respectively. From this reference observation, the calibrated wavelength grid per spectral order is extracted. For the simulations presented in [Spaeth et al. \(2024\) \(Chapt. 4\)](#), an observation of NGC 4349 No. 127 was used.

For each spectral order, `pyoscillot` selects the corresponding cutout of the simulated spectrum (after the spectrum combination) padded by 100 \AA . After the resolution adjustment with the instrument’s resolving power, the simulated spectrum is then rebinned into the wavelength “pixels”. I tested both a rebinning and an interpolation onto the reference wavelength grid and found negligible differences. However, rebinning mimics the acquisition process of a real CCD more closely. The simulated, physical flux values are further converted to count values by normalizing to the mean count value of the respective order of the real, reference observation. This conversion was mainly implemented to allow the subsequent reduction pipeline to work with similar quantities as for real observations. However, tests revealed that it is of negligible importance.

Ideally, one would further convert the energy flux of the simulated spectra to a photon flux, which more accurately follows the acquisition process of a CCD. I tested this conversion and found negligible differences. As there are additional effects of a real CCD, such as the wavelength-dependent quantum efficiency, which are challenging to model accurately, it was decided to use the original energy flux for the results in [Spaeth et al. \(2024\)](#) (see [Chapt. 4](#)). The conversion to photon flux can be switched on for testing.

In the case of HARPS spectra, the extracted spectra still contain the blaze continuum. As the reduction pipelines for HARPS are tuned to remove that continuum, I multiply the simulated spectra with a measured HARPS blaze function for each order. The blaze function is extracted from the “*_blaze_A.fits” file associated with the reference spectrum.

The resulting arrays of spectra per order are finally saved in FITS files adapted from the reference observation. Several header keywords are adjusted. These include the time of observation, the exposure time, and the barycentric correction which is set to zero. [Figure 3.3](#) shows an example of a simulated HARPS spectrum.

3.2.7 Data reduction

Finally, the simulated instrument-specific spectra can be reduced to obtain the observables, that is the RVs and the activity indicators. To acquire a full set of the latter, I employ two separate reduction pipelines. I first reduce the spectra using the least-square fitting pipeline `SERVAL` ([Zechmeister et al., 2018](#)). `SERVAL` was initially designed for the CARMENES spectrograph but was also tested on HARPS data, for which it can produce more precise RVs than the standard HARPS pipeline ([Trifonov et al., 2020](#)). `SERVAL` determines the

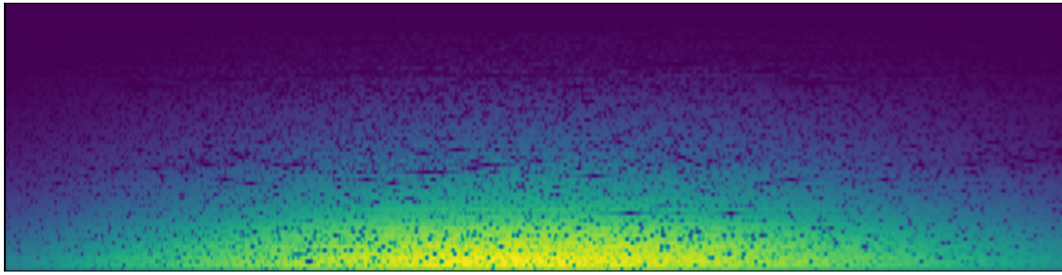


Fig. 3.3.: Example of a simulated, extracted HARPS spectrum. Each row corresponds to one spectral order. Wavelength increases top to bottom and left to right.

RVs by first creating a high S/N template by shifting and co-adding all available spectra. Afterwards the RVs are determined through least-squares fitting. SERVAL provides the activity indicators CRX and dLW (see Sect. 1.6.3) and several line indices, including the $H\alpha$ indicator. These line indicators, however, are mostly sensitive to chromospheric activity which is not simulated. These are thus not used for simulated spectra.

To stay close to the real observations, I use the standard parameters for all instruments, as published in the gitHub repository of the SERVAL pipeline.⁶ No telluric masking is employed for the simulated reduction. I further use the barycentric correction saved in the FITS headers, which were set to zero during the spectrum creation. The template used during the SERVAL reduction is created from the simulated spectra.

Another set of activity indicators is available by reducing the spectra using the RACCOON pipeline (Lafarga et al., 2020).⁷ Similar to SERVAL, RACCOON was also developed for CARMENES but can equally be applied to HARPS. It uses a weighted binary mask to compute a cross-correlation function (CCF) for each spectral order. These CCFs are averaged to provide the final results. RACCOON derives the RVs, the FWHM and contrast of the CCF, as well as the BIS (see Sect. 1.6.3). Again, I use the standard settings for all instruments, not masking regions which would be affected by tellurics. The weighted binary mask can be created from a SERVAL template via routines provided by RACCOON. For the reduction results presented in Spaeth et al. (2024), this mask was created from the real template of the observations of NGC 4349 No. 127.

Finally, the synthetic spectra can also be used to estimate photometric variations. For a simple estimate, the simulated spectra are multiplied with the normalized V-band filter curve⁸ and integrated.

⁶<https://github.com/mzechmeister/serval>

⁷<https://github.com/mlafarga/raccoon>

⁸<http://spiff.rit.edu/classes/phys440/lectures/filters/bess-v.pass>

3.3 Optional Effects

There are several additional effects that can influence the observed spectra and the derived observables. These can be selected by the user and are detailed in this section.

3.3.1 Convection - Macroturbulence

The photospheres of cool stars dominantly transport energy via convection (Murdin, 2001). These convective motions affect the shapes of spectral lines (Gray, 2021). Motivated by observations and simulations, the change of the width of spectral lines due to this convective motion, is typically separated into the contributions of micro- and macroturbulence. For the former, the turbulent elements are much smaller than the optical depth. The effect can therefore be accounted for in the radiative transport calculations when computing model spectra and is included in the PHOENIX spectral database (Husser et al., 2013). The latter, however, occurs on spatial scales much larger than the optical depth and must therefore be included after a stellar spectrum is synthesized from a model atmosphere. The effect of this macroturbulence is sometimes referred to as the “first signature of granulation” and generally manifests itself as a broadening of spectral lines (Gray, 2021).

Within `pyoscillot`, I adopt the simple isotropic model of macroturbulence, which can yield reasonable results as long as no physical meaning is attributed to the macroturbulent velocity parameter ζ (Gray, 2021). I note that I refer to ζ as v_{macro} when discussing it as the input variable for the simulations. The PHOENIX spectra (after being interpolated to a local temperature) are broadened by a Gaussian kernel to account for the macroturbulent velocity v_{macro} , converted to a wavelength change. Although in velocity space the width of the kernel is constant across the spectrum, its width in wavelength space is not.

The Gaussian broadening kernel in wavelength space is therefore expressed in terms of its FWHM, converted to $\sigma_{\lambda} = \frac{FWHM_{\lambda}}{2\sqrt{2\log 2}}$, and subsequently converted into the sampling space of the PHOENIX wavelength grid. This procedure is performed for each position in the wavelength grid and yields a local broadening kernel for each position. The actual broadening operation, performed for each wavelength position, is then simply the sum of the product of all flux values and the local broadening kernel. This operation has to be performed in a wavelength range that is much smaller than the whole PHOENIX range, but large enough that the Gaussian kernel has dropped sufficiently.

Overall, the above procedure yields a fast implementation of a convolution with a non-constant kernel. As there are small jumps at fixed wavelength positions in the sampling rate of the PHOENIX spectra, `pyoscillot` locally interpolates over the jumps to be able to calculate the product of the broadening kernel and the flux values with a fixed sampling rate. Figure 3.4 shows the effect of the macroturbulent broadening with $v_{\text{macro}} = 5000 \text{ m s}^{-1}$

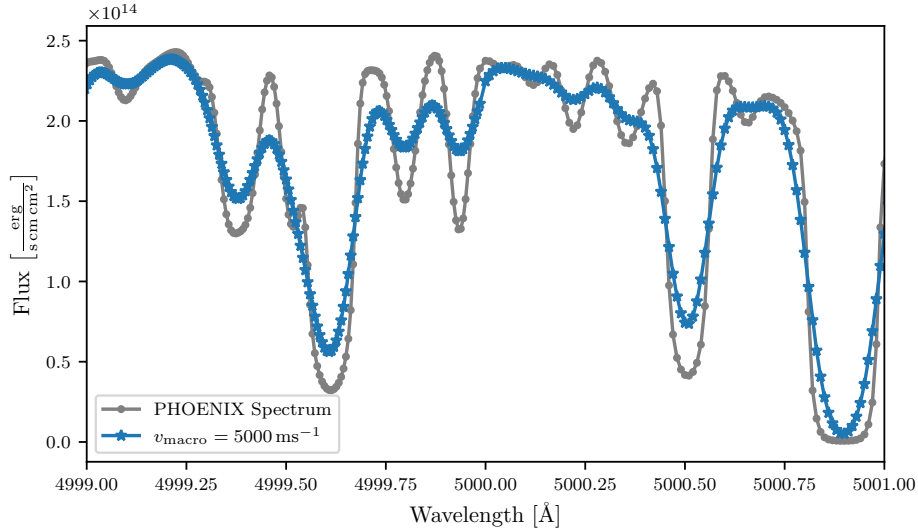


Fig. 3.4.: PHOENIX spectrum (gray) broadened by a macroturbulent kernel with $v_{\text{macro}} = 5000 \text{ m s}^{-1}$ (blue). I note the change of sampling at $\lambda = 5000 \text{ \AA}$ present in the original PHOENIX spectrum. A linear interpolation to allow the broadening operation at the adjacent pixels is applied. Only a small cutout is presented for visual clarity.

for a small 2 \AA cutout of a PHOENIX spectrum. The effect of the macroturbulence on the observables of a non-radial oscillation are studied in Sect. 3.4.4.

3.3.2 Line asymmetries due to convective blueshift

Convection also introduces asymmetries in spectral lines. The granulation pattern on the surface of cool stars consists of granules and intergranular lanes. In the granules, the hot and buoyant gas rises toward the surface. There, the gas cools and sinks back toward deeper layers in the intergranular lanes. The light emitted from the granules is therefore blueshifted, while light stemming from the intergranular lanes is redshifted (Gray, 2021). The combined spectral line, resulting from the contributions of both the granules and the lanes, is thus distorted in its symmetry. As the granulation pattern is spatially dominated by the granules, in which the gas is furthermore hotter, the overall line shape is mainly influenced by the granules. The contribution of the lanes mostly leads to a suppression of the red wing of the spectral line (Gray, 2021). In practice, there is an additional depth (and thus velocity) dependence, further complicating the exact distortion of the line shapes. The overall effect is often referred to as the “second signature of granulation” and can be tracked using line bisectors (Gray, 2021). When targeting individual spectral lines, it typically leads to a "C" shaped bisector for stars below the granulation boundary (Gray, 2005). To test whether the distorted line profiles influence the observables of non-radial oscillations, an approximation of the effect was implemented.

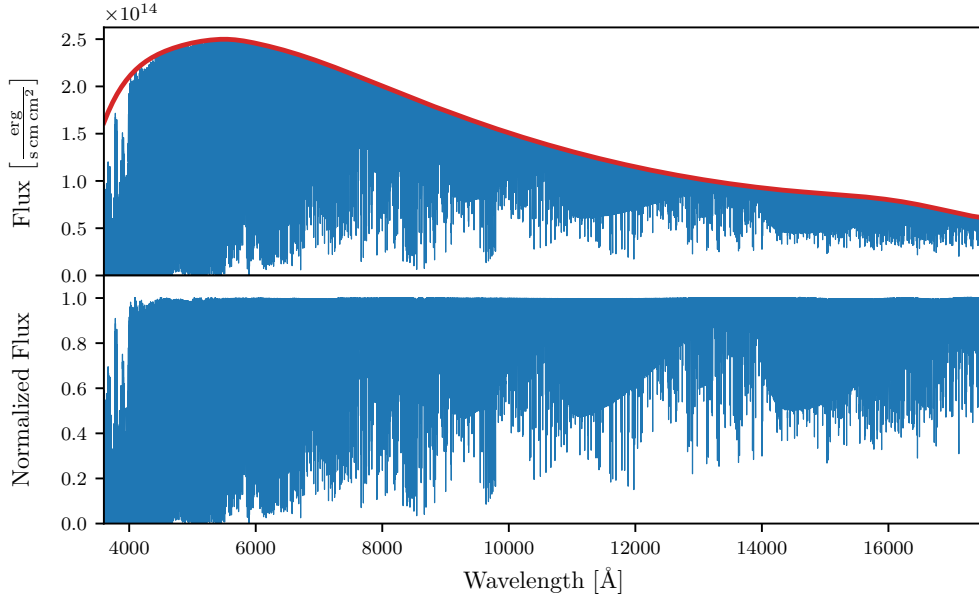


Fig. 3.5.: Continuum normalization for a PHOENIX spectrum with $T_{\text{eff}} = 4500$ K, $\log g = 2.0$, and $[\text{Fe}/\text{H}] = 0.0$. Top: The raw PHOENIX spectrum (blue) and its estimated continuum (red). Bottom: The normalized PHOENIX spectrum.

I follow the approach by [Zhao & Dumusque \(2023\)](#), who present a similar simulation code (SOAP-GPU) developed to study the effect of surface spots on main-sequence stars. In order to include a convective blueshift model into the PHOENIX spectra, these first have to be normalized and their intrinsic bisectors have to be removed ([Zhao & Dumusque, 2023](#)). These bisectors cannot accurately describe convective processes since the PHOENIX spectra are synthesized from 1D atmospheric models.

Normalizing stellar spectra over a large wavelength range in the presence of absorption is challenging, especially for comparably cool stars ([Gray, 2021](#)). `Pyoscillot` computes a normalization using RASSINE ([Cretignier et al., 2020](#)). The normalization was precomputed in steps of 0.1 K for the desired PHOENIX grid range. It was performed from 3550 Å to 17 550 Å to cover all three implemented instruments. For cool stars, the continuum is affected unequally by absorption over this wavelength range, particularly at the Balmer jump near $\lambda \sim 3645$ Å. As a result, finding a set of RASSINE parameters for the entire wavelength regime proved to be challenging. The normalization is therefore performed in three separate regions, optimizing the parameters in each, and calculating a smooth transition in between. With this approach, a satisfying and reliable normalization was found for all cool stars of relevance. Figure 3.5 shows an example of a continuum normalization.

Next, the intrinsic bisector of the normalized PHOENIX spectrum has to be measured and removed. Following [Zhao & Dumusque \(2023\)](#), I measure the bisectors of five Fe I lines (5250.2084 Å, 5250.6453 Å, 5434.5232 Å, 6173.3344 Å, 6301.5008 Å) of the normalized PHOENIX spectrum, calculate the mean bisector in predefined depth bins, and fit

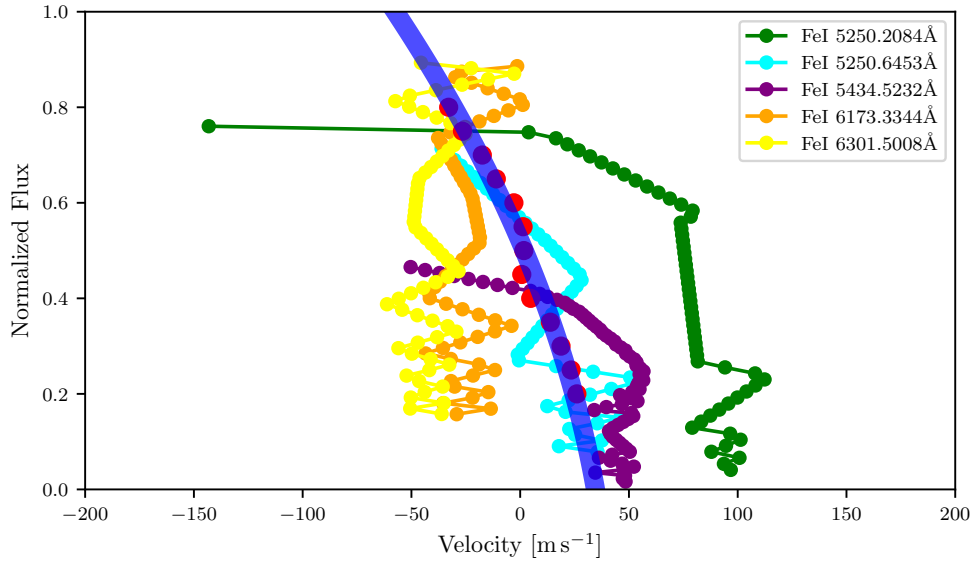


Fig. 3.6.: Measured mean bisector of a normalized PHOENIX spectrum. The bisectors of the five Fe I lines were averaged (red points) and fitted with a second order polynomial (blue).

the mean bisector with a second order polynomial. The measured bisector model is then removed from the PHOENIX spectra. Figure 3.6 shows an example of a fit result.

Finally, the wavelength shifts from a bisector model taken from the literature are calculated from the bisector-removed, normalized spectrum and applied to the bisector-removed, unnormalized spectrum, which is then used for the subsequent calculations. The bisector shapes are best studied for the Sun, for which [Löhner-Böttcher et al. \(2019\)](#) measured bisector models resolved at different observation angles μ . These μ -dependent bisectors can be used if the user selects to simulate a Sun-like bisector.

Unfortunately, such disk-resolved measurements are only available for the Sun. Since the main purpose of `pyoscillot` is to study evolved stars, such models cannot be used. Instead, I use the bisector models of the giant stars presented by [Gray \(2005\)](#). Although these are disk-averaged bisectors, I decided to use the models for all angles μ within `pyoscillot`. Additional bisector models, also simulated ones, can easily be added into `pyoscillot`.

To measure the bisectors of the individual lines of real stars, very high S/N measurements using high-resolution spectrographs are necessary ([Hatzes, 1996](#)). As the typical spectra acquired for RV determination have insufficient S/N for this purpose (and `pyoscillot` is primarily intended to mimic such observations), I focus on the most common observable targeting the shape of spectral lines in context of exoplanet surveys, which is the CCF.

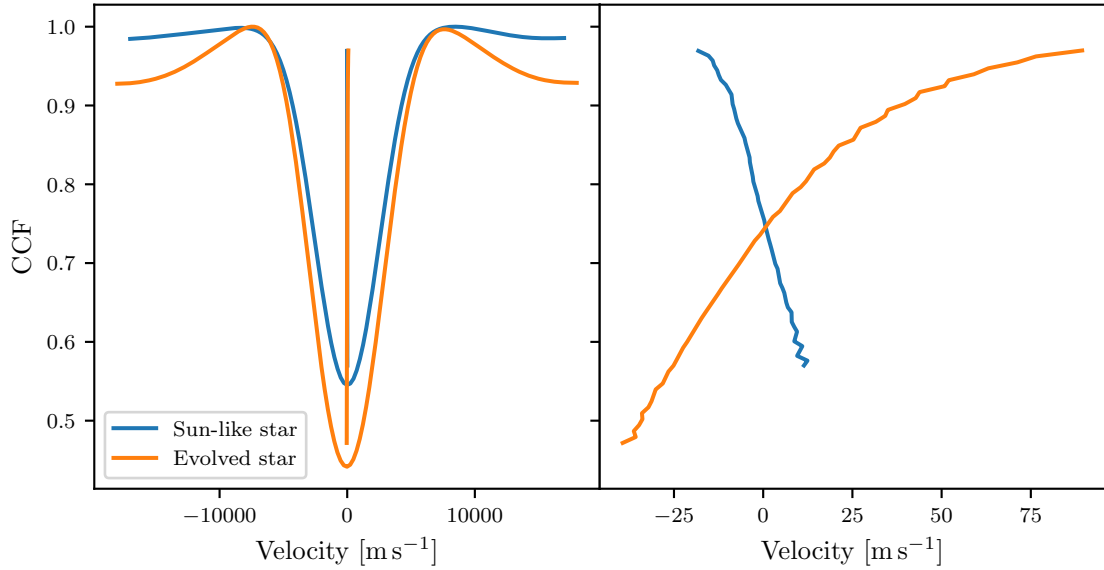


Fig. 3.7.: Simulated CCFs and bisectors for a Sun-like (blue) and a giant (orange). The right panel shows a zoom-in on the bisectors. The CCF bisector shapes for the Sun and evolved stars as presented by [Dall et al. \(2006\)](#) (their Fig. 2) can be generally reproduced.

To test the bisector models, I simulated a Sun-like bisector model ($T_{\text{eff}} = 5800 \text{ K}$, $\log g = 4.5$, $[\text{Fe}/\text{H}] = 0$) and an evolved bisector model ($T_{\text{eff}} = 4500 \text{ K}$, $\log g = 2.0$, $[\text{Fe}/\text{H}] = 0$) using the bisector of Arcturus by [Gray \(2005\)](#), without adding any oscillation and without including the effects of limb darkening and macroturbulence. Both were modeled with $v_{\text{rot}} = 1750 \text{ m s}^{-1}$ observed at inclination $i = 90^\circ$. The CCFs were computed using RACCOON. The resulting CCFs and the measured bisectors are shown in [Fig. 3.7](#) for the Sun-like model (blue) and the evolved model (orange), respectively. Similar HARPS measurements for evolved and main-sequence stars, including the Sun, were presented by [Dall et al. \(2006\)](#) (their Fig. 2). The simplified `pyoscillot` implementation reproduces the observed behavior of a general left-leaning bisector for main-sequence stars with right-leaning bisectors for evolved stars. As in [Dall et al. \(2006\)](#), the span of the evolved bisector is generally larger than for the Sun-like case, although the velocity span of the simulated Sun-like bisector ($\sim 35 \text{ m s}^{-1}$) is somewhat smaller than the observed span ($\sim 50 \text{ m s}^{-1}$). Such differences are expected since the CCF and bisector shape critically depend on stellar and instrumental properties and the exact mask used for the CCF, as discussed by [Dall et al. \(2006\)](#). Furthermore, I used a different reduction pipeline (RACCOON). In general, the `pyoscillot` results are consistent with the observations.

In [Fig. 4.6](#) in [Spaeth et al. \(2024\)](#) (Chapt. 4), we compare the simulated bisectors with the observations for NGC 4349 No. 127. Best accordance was found with the bisector model for the giant star β Boo taken from [Gray \(2005\)](#). While the general bisector trend is reproduced, not all influences on the CCF can be modelled accurately. An exact comparison between simulated and observed bisectors should thus be treated carefully. It was further

found that the influence of the bisectors is negligible on the RVs and the activity indicators, and serves mainly to give an absolute offset for the BIS, as might be expected.

I note that there is an additional effect, referred to as the “third signature of granulation”, which is not included in `pyoscillot`. That is, the overall net blueshift of each spectral line due to the dominating contribution by the blueshifted emission of the granules. This net blueshift is furthermore dependent on the line depth, as shallower lines are typically formed deeper into the stellar atmosphere, and thus show larger line shifts (Gray, 2021; Liebing et al., 2021, 2023). However, such a depth dependent shift of spectral lines is challenging to apply to the available PHOENIX spectra. Moreover, since the granulation is not coupled to the oscillations within `pyoscillot`, this shift of the spectral lines would stay constant over the oscillation cycle and thus play an insignificant role on the observables. The same argument applies if one would, for simplicity, use a constant convective blueshift, regardless of the depth of a line. Thus, this correction was omitted. I note that the correction might become relevant, if one were to accurately use the information that the spectra at the limb of the star are formed higher in the stellar photosphere, and accurately model the velocity distribution (and its projection) of the convective process. However, since the PHOENIX spectra are only available as disk-integrated spectra (see discussion in Sect. 3.2.1), and the 3D velocity distributions of the convection are not readily available for giant stars, such a correction is beyond the current scope of this work.

3.3.3 Center-to-limb variations

When viewing a spatially resolved stellar disk, such as the surface of our Sun, an observer sees the integrated emission along the line of sight for each surface element. Due to the opacity of the gas, this emission is modulated by the optical depth τ . The optical depth is defined such, that after the emitted light of lower stellar layers has passed through one optical depth, its intensity has dropped by a factor $\frac{1}{e}$. It is therefore the approximate depth to which the emitted light probes the stellar photosphere (Gray, 2021).

From geometric considerations, one can easily see that an observed ray emitted from the same depth at the limb of the star has a longer optical path through the photosphere, compared to a ray emitted in the center. Thus, at $\tau = 1$, the emission from the limb probes a higher atmospheric layer compared to the emission from the disk center. As the temperature within the stellar atmosphere (to first order) increases with depth, it can be understood that the black-body emission is reduced at the limb, an effect widely known as limb darkening or center-to-limb variation.

The center-to-limb variations depend on wavelength, an effect best studied for the Sun. [Hestroffer & Magnan \(1998\)](#) described the intensity profile as a function of μ as

$$I(\mu, \lambda) = 1 - u(1 - \mu^{\alpha(\lambda)}), \quad (3.25)$$

and fit data provided by [Pierce & Slaughter \(1977\)](#) and [Neckel & Labs \(1994\)](#). They determined the center-of-limb variations of the Sun to be best described using $u = 1$ and a wavelength dependent $\alpha \sim -0.023 + 0.292\lambda^{-1}$ for $1099 \text{ nm} \gtrsim \lambda \gtrsim 416 \text{ nm}$ and $\alpha \sim -0.507 + 0.441\lambda^{-1}$ for $303.3 \text{ nm} \lesssim \lambda \lesssim 357 \text{ nm}$. Between 357 nm and 416 nm the relation was not fitted due to discontinuities caused by the Balmer jump at $\lambda \sim 365 \text{ nm}$ and the $\text{H}\epsilon$ line at $\lambda \sim 390 \text{ nm}$ ([Hestroffer & Magnan, 1998](#)).

This simple relation has proven to provide accurate results in agreement with recent observations ([Thuillier et al., 2011](#); [Lamy et al., 2015](#)). Although this relation was calibrated for the Sun, it has the advantage of encapsulating a wavelength dependence, which is especially important in context of the RV measurements. It is thus preferred over limb-darkening models more applicable to giant stars that are calibrated only in singular photometric filters. Using wavelength dependent models for evolved stars would be ideal, but these were not available in the literature.

The three instruments HARPS, CARMENES-VIS, and CARMENES-NIR, which are currently implemented in `pyoscillot`, cover the wavelength ranges $378 \text{ nm} - 691 \text{ nm}$ ⁹ ([Mayor et al., 2003](#)), $520 \text{ nm} - 960 \text{ nm}$, and $960 \text{ nm} - 1710 \text{ nm}$ ¹⁰ ([Quirrenbach et al., 2014](#)), respectively. While the implementation for the visual CARMENES channel is straightforward, as it covers the complete wavelength range, extrapolation is required for the other two instruments. However, examining Fig. 3 of [Hestroffer & Magnan \(1998\)](#), which shows α being well described by the above relation down to wavelengths $\lambda \sim 385 \text{ nm}$, it seems plausible to do so for the HARPS spectrograph, since only a small fraction of the spectrum remains outside this range. I further adopt an extrapolation for the NIR arm of CARMENES.

As the PHOENIX spectra are disk-integrated, they include a limb-darkening relation stemming from the underlying model atmosphere. This limb-darkening relation is unfortunately not known. I thus divide PHOENIX spectra by a disk-averaged relation following Equation 3.25. Afterwards, I multiply the local spectra for each cell at its respective angle μ with the local intensity correction. The final, disk-integrated spectra thus include the wavelength- and μ -dependence of the limb-darkening effect.

In [Fig. 3.8](#), I plot the limb-darkening profile over the stellar disk as a function of μ . I choose three wavelengths, which lie at the center of the respective instruments. From these differing profiles one can deduce that during the spectrum combination process, different parts of the stellar disk will carry differing weights in different instruments.

⁹<https://www.eso.org/sci/facilities/lasilla/instruments/harps/overview.html>

¹⁰<https://carmenes.caha.es/ext/instrument/index.html>

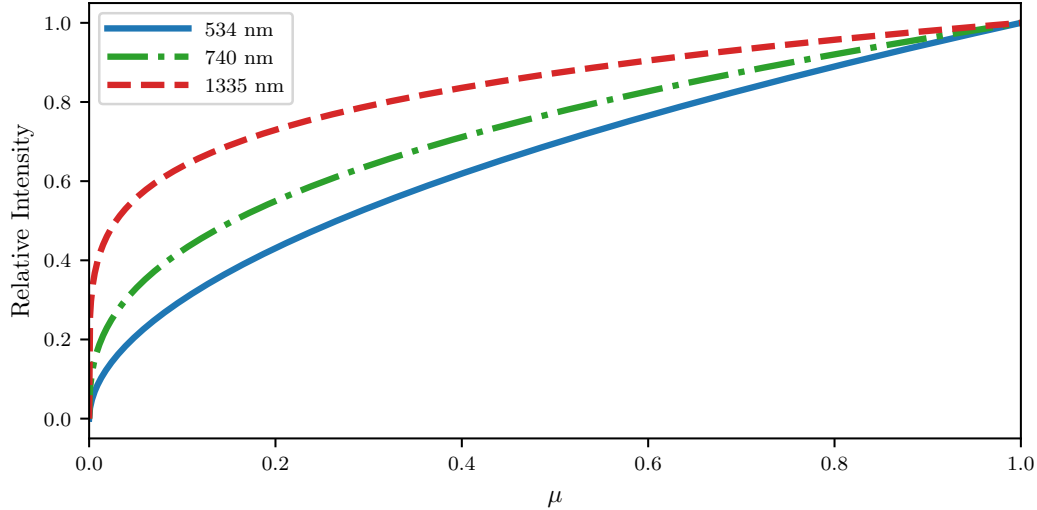


Fig. 3.8.: Relative limb-darkening intensity as a function of μ at three different wavelengths, chosen to roughly coincide with the central wavelengths of HARPS (blue, solid), CARMENES-VIS (green, dash-dotted), and CARMENES-NIR (red, dashed).

That is to say, the contribution of the cells at the limb of the stellar disk is reduced to a larger extent in the HARPS spectrograph than in spectrographs at longer wavelengths. These differing contributions by different parts of the stellar disk can lead to slight phase differences between different instruments, which are discussed in Sect. 3.4.2. The effect of the limb darkening on the oscillation models is examined in Sect. 3.4.3.

3.4 Testing the simulation results

3.4.1 Line bisector variations

The `pyoscillot` simulations of non-radial oscillations are inspired by similar simulations by Hatzes (1996). The author, therein, predicted distinctive bisector variations of individual spectral lines for different oscillation modes. These serve as a first test to validate the `pyoscillot` implementation of non-radial oscillations.

Figure 3.9 presents the line bisectors measured for an unblended, strong absorption line at $\lambda = 6254.29 \text{ \AA}$ for three different oscillations modes at three different phases of the oscillation. I use the same settings as in Hatzes (1996) and a base PHOENIX spectrum for a star with parameters $T_{\text{eff}} = 4500 \text{ K}$, $\log g = 2$, and $[\text{Fe}/\text{H}] = 0.0$. The latter were not specified by Hatzes (1996). I exclude any additional effects and do not smooth the spectra to any specific resolving power.

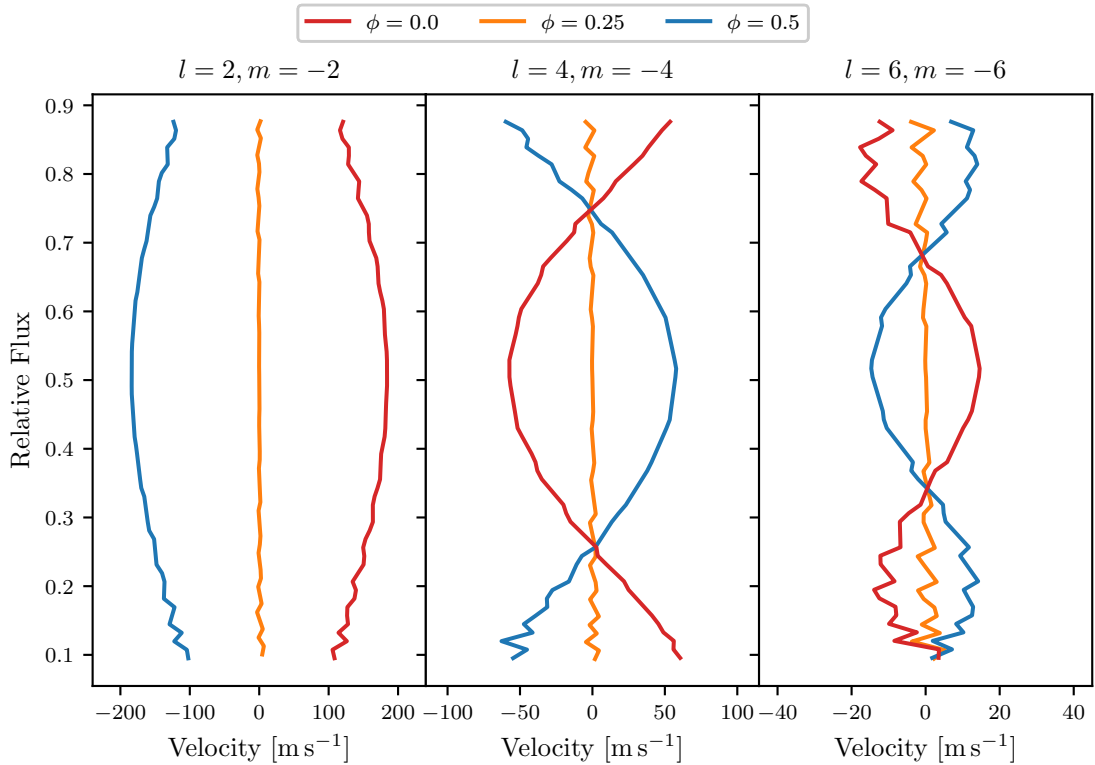


Fig. 3.9.: Simulated bisector variations measured for a spectral line at $\lambda = 6254.29 \text{ \AA}$ for $l = 2, m = -2$ (left), $l = 4, m = -4$ (middle), and $l = 6, m = -6$ (right).

As can be seen, the line bisectors for the three oscillations modes follow a distinctive pattern, with the number of intersection points increasing for larger l , while the velocity span decreases. These findings are consistent with the findings by [Hatzes \(1996\)](#). I note that there are slight differences between the absolute `pyoscillot` bisector velocity spans and the ones presented by [Hatzes \(1996\)](#). However, given the differing underlying model spectra (with likely different microturbulent broadening), such differences are to be expected. In general, the `pyoscillot` simulations seem to provide consistent results with the literature.

3.4.2 The base model

Next, I examine the basic behavior of a retrograde, dipole ($l = 1, m = 1$) non-radial oscillation. The parameters for the oscillation model are inspired by the findings for NGC 4349 No. 127. It is discussed in more detail in [Spaeth et al. \(2024\)](#) and [Chapt. 4](#). Here, it serves to give a first overview of the observable effects of the oscillation. The simulation parameters are summarized in [Table 3.1](#). I include the effects of limb darkening and the bisector correction for the convective blueshift. I simulate 40 data points for

Tab. 3.1.: Parameters used for the base oscillation model.

Parameter	Value
T_{eff}	4500 K
$\log(g)$	2.0
[Fe/H]	0.0
l	1
m	1
P	674.0 d
v_{osc}	0.30 ms^{-1}
K	1856
v_{rot}	1700 ms^{-1}
v_{macro}	4822 ms^{-1}
δT_{eff}	2.5 K
ψ_T	0°
i	90°
N_{grid}	150×150
limb darkening	on
bisector model	β Boo

the three instruments HARPS, CARMENES-VIS, and CARMENES-NIR. Due to the high K factor, the oscillation is dominated by the horizontal (θ , ϕ) components.

In Fig. 3.10, I present the simulation results, showing the change of the RVs and differences from the mean for the activity indicators. I fit sinusoids that follow the data points closely, which are left out for visual clarity. First, it is evident that the non-radial oscillation leads to sinusoidal variations of the RVs. This variation could be mistaken for an exoplanet in context of RV surveys. One can observe that the RV amplitudes in all three instruments are relatively similar, although slight differences exist.

The amplitudes increase slightly when measured in spectrographs at longer wavelengths. This effect can easily be understood in context of the limb-darkening correction, that is discussed more closely in Sect. 3.4.3. It implies that testing the infrared RVs for consistency with the visual RVs (see, e.g., Trifonov et al. 2014) is theoretically promising, but rather unfeasible in practice given the intrinsic jitter of the very bright giant stars of interest. This statement remains valid, as long as the influence of the temperature variations is small compared to the influence of the chromatic limb-darkening correction.

Opposite to a planet signal, for which the activity indicators should not show any periodicity at the orbital period, the simulation of a non-radial oscillation leads to periodic variations in the indicators. The amplitudes of the signals in the activity indicators and their phase relations with the RVs are studied in more detail in Spaeth et al. (2024) (Chapt. 4). This basic finding implies that it is possible to detect such oscillations in the activity indicators and use these to confirm or reject planets. However, great care has to be taken when trying

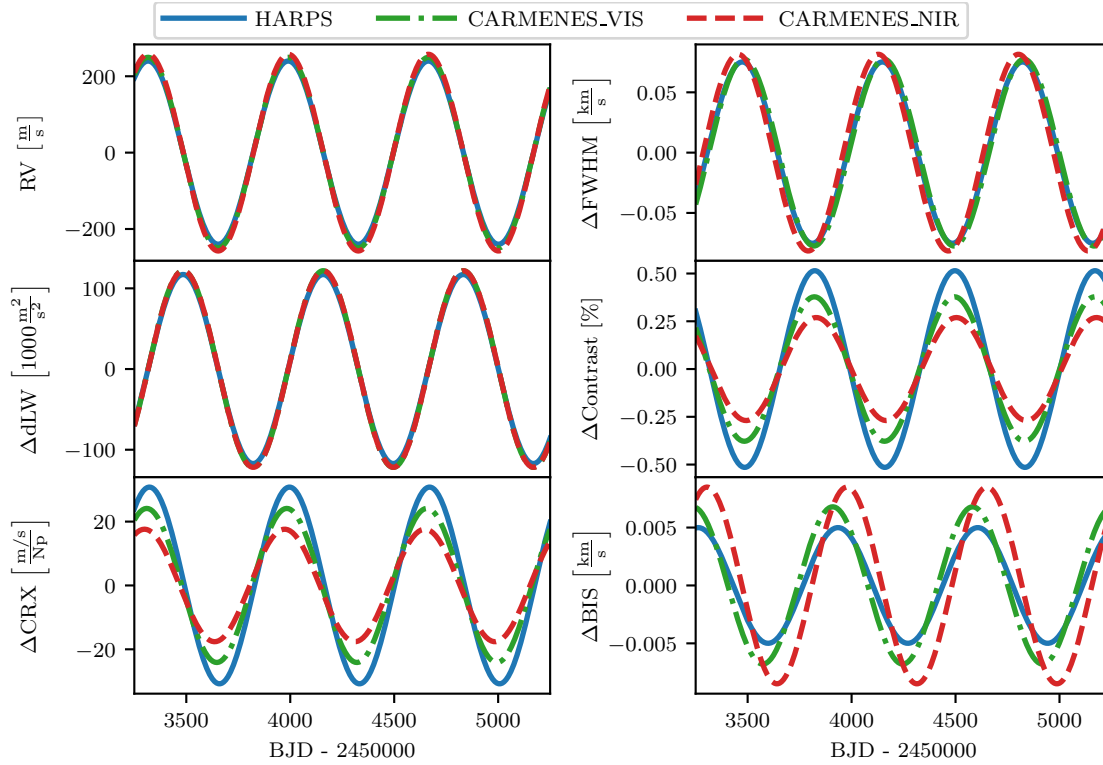


Fig. 3.10.: Simulation of a $l = 1, m = 1$ oscillation mode for HARPS (blue, solid), CARMENES-VIS (green, dash-dotted), and CARMENES-NIR (red, dashed).

to confirm a planetary origin of RV periodicity as a superposition of several oscillation modes and scatter in real data can obscure the variations. This is also discussed more closely in Spaeth et al. (2024) (Chapt. 4).

Comparing the periodic signals between the different instruments, one first observes that variations in the activity indicators can have large differences in their amplitudes. While the dLW and FWHM indicators are quite similar for all three instruments, the contrast of the CCF, the CRX, and the BIS deviate significantly. For the CRX, this drop of the variation’s amplitude can easily be deduced from the consideration that the limb darkening is dominating the CRX variation, as is examined more closely in Sect. 3.4.3. As the limb darkening generally becomes less pronounced toward longer wavelengths (see, e.g., Fig. 3.8), a decrease of the CRX amplitude follows naturally. Furthermore, also the contrast of the effective temperature variation decreases in the infrared and thus further decreases the CRX amplitude. However, this effect is of minor importance, as the CRX amplitude due to the temperature variation is comparably small.

The different amplitudes in the contrast of the CCF can be understood since the simulated spectrographs have different resolving powers, which smear out the underlying variations of the spectral lines. It is not entirely clear, why the BIS variations show the opposite behavior, that is, why the variations simulated for HARPS are smaller than those for the

NIR channel of CARMENES. It can likely be explained by the different sets of spectral lines that are used to measure the CCF for each of the simulated spectrographs. However, the differing strength of the limb darkening might also influence the variations, as different parts of the stellar disk have different weights in the spectrum combination due to the differing intensity profiles over the stellar disk, as evident from Fig. 3.8.

Looking at the phase relations, one can observe that the phases of the variations in the RVs and dLW are relatively similar between the different instruments. For the other four indicators, there are more apparent phase shifts, however, they generally remain small. They are largest for the BIS, which, in case of NGC 4349 No. 127 (Spaeth et al., 2024) is the least impactful indicator due to the slow rotation. Understanding these phase shifts is not straightforward as several factors come into play.

On the one hand, the influence of the temperature contrast becomes less relevant for longer wavelengths. As discussed in Sect. 3.4.3 and shown in Fig. 3.11, the interplay of temperature variations and limb darkening can lead to phase shifts in the activity indicators. Thus, a reduced influence of the temperature contrast can result in phase shifts. More important, however, is again the influence of the limb darkening itself. As apparent from Fig. 3.8 and Eq. 3.25, the intensity profile due to the limb darkening as a function of μ changes for different wavelengths. This intensity profile (as a function of wavelength) for a specific cell effectively acts as a weight relative to other cells. Thus, the relative weights of cells change between different instruments with different wavelength regimes. Consequently, the interplay between the projection of the oscillation's velocity components and differing weights can lead to small phase shifts in the indicators.

In general, one can see from this simple oscillation model that a non-radial oscillation can lead to significant and periodic RV variations, that are, however, accompanied by variations in the activity indicators. The amplitudes of the RVs are relatively similar in the three wavelength regimes considered here, while the amplitudes in the activity indicators can deviate significantly. The phase relations between the indicators and the RVs are generally similar, however, there are some small differences between the instruments.

3.4.3 The effect of the chromatic limb-darkening correction

To illustrate the effect of limb darkening on a non-radial oscillation model, I run the same simulation without the limb-darkening correction. Figure 3.11 compares the two oscillations models for the HARPS spectrograph. The original, limb-darkening corrected oscillation is portrayed in blue, while the uncorrected version is plotted in orange.

The RV amplitude is significantly suppressed by the limb darkening. This is due to the fact that the oscillation is dominated by its horizontal components (large K factor), which are strongest toward the limb. These are, however, also the cells that are most strongly

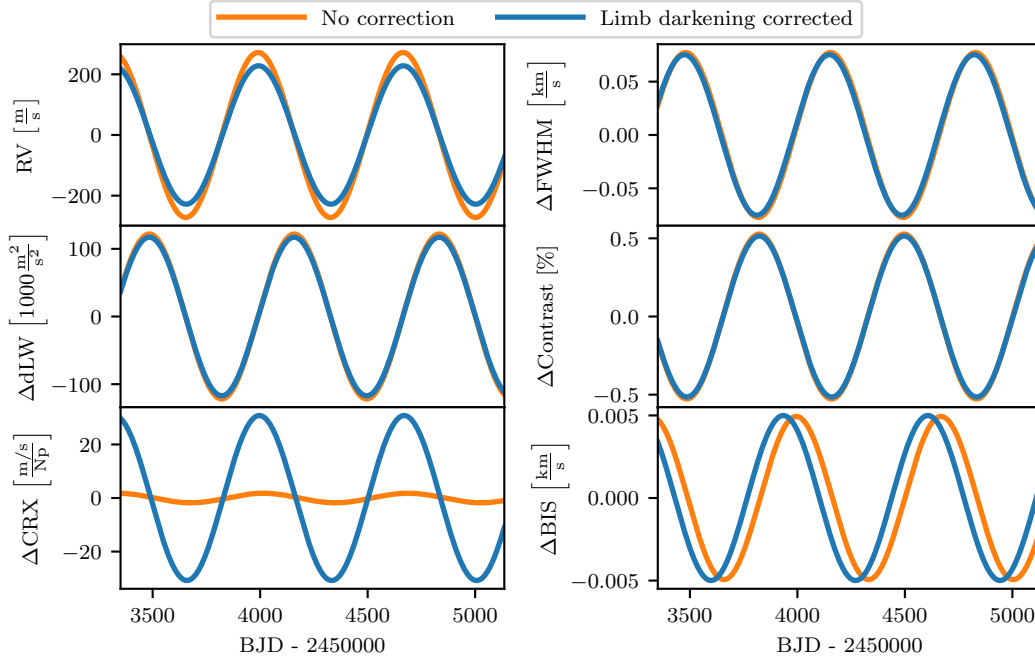


Fig. 3.11.: Comparison between models including (blue) and excluding (orange) the limb-darkening correction.

suppressed by the limb darkening. Opposite to the RVs, the dLW and the FWHM and contrast of the CCF are not strongly affected. For these, only marginal changes in the amplitudes and small phase shifts (in case of the FWHM) can be seen.

This phase shift is much more apparent for the BIS variations, while the amplitude of the BIS variation stays roughly constant. As discussed in Sect. 3.4.2, these phase shifts can again be understood as a consequence of the effective wavelength-dependent weights for the simulation cells that are introduced by the limb darkening correction. With differing weights, different cells will be most influential in determining the spectral line asymmetry in both simulations. As these cells are maximized at different oscillation phases (comparing the two simulations), phase shifts can emerge. I note that I removed the means from each time series. There can be significant offsets between the two models. For instance, the limb darkening also reduces the contribution of the rotational broadening which leads to a general decrease of the FWHM. In the context of RV surveys, however, the variations of the activity indicators, not their absolute values, are typically of main interest.

Finally, one can observe a strong change of the amplitude of the CRX variations. While the variations are comparably small when no limb darkening is included, its amplitude is much increased when including its effect. In the uncorrected case, these variations stem directly from the relatively small temperature variation ($\delta T_{\text{eff}} = 2.5 \text{ K}$). However, as the limb darkening according to Eq. 3.25 is wavelength-dependent, its reduction of the RV amplitude (top left) is stronger at the blue end of the spectrograph compared to the red

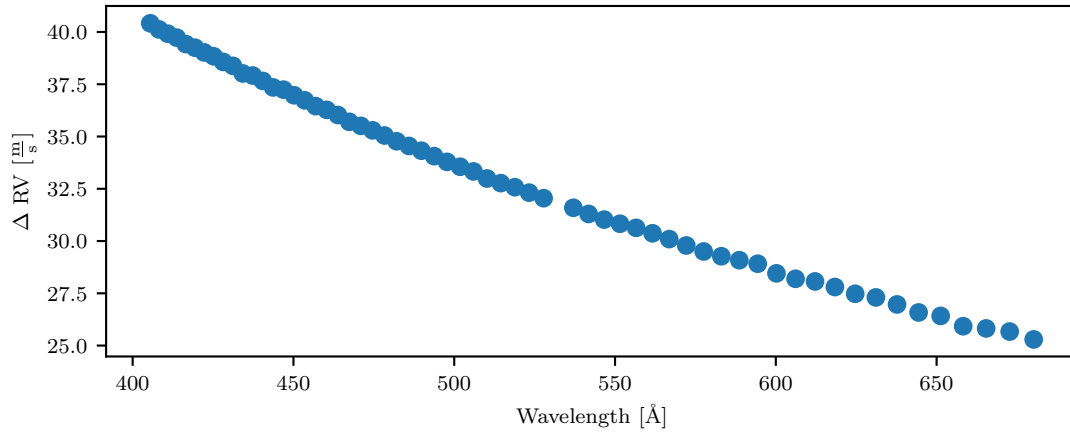


Fig. 3.12.: Difference in the RV amplitudes per order between the limb-darkening uncorrected and corrected models. The central wavelengths of the orders are plotted on the x-axis.

end. This chromatic behavior of the RVs manifests in variations of the CRX, which are roughly in phase with the RVs.

To illustrate this more closely, I plot in Fig. 3.12 the difference between the uncorrected and corrected RVs for each spectral order of the HARPS spectrograph against each order’s central wavelength. These were computed by fitting sinusoids to each order’s time series data. One can clearly observe that the difference in the RVs decreases toward longer wavelength (i.e., the RV amplitude becomes relatively larger at longer wavelengths for the limb-darkening corrected model). This effect dominates the CRX variation over the effect of the temperature variation and causes a positive correlation (chromaticity) between the CRX and the RVs. However, these relations can change for different oscillation modes, which is examined more closely in Spaeth et al. (2024) (Chapt. 4).

3.4.4 The influence of the parameters for $l = 1, m = 1$ modes

To conclude the general introduction to the `pyoscillot` simulation suite, I study the influence of the individual simulation parameters on the observables. I focus on simulations of isolated $l = 1, m = 1$ modes for HARPS. Other $l = 1$ modes and higher order l modes are examined more closely in Spaeth et al. (2024) (Chapt. 4). For all simulations, I use the above base simulation as a reference and change each parameter at a time. For each simulation, I fit a sinusoid with a fixed period to the resulting variations, and examine the changes of the amplitude, phases, and offsets of the variations. I note that for this particular test, the energy flux measurements were converted to photon fluxes. However, this was found to have negligible effect.

In Fig. 3.13, I study the influence of the oscillation parameters v_{osc} , K , δT_{eff} , and ψ_T (the phase of the temperature variation). In the left column, I plot the relative difference of the individual variation's amplitude A compared to the amplitude of the base model A_0 , same as the change of the offset O compared to the base offset O_0 in the right column. The middle panels portray the absolute changes of the phase ψ of each simulation's observables compared to the base model. I plot the RVs and the five activity indicators in different colors specified in the legend.

I omit plotting the RVs and dLW in the right column portraying the offset of the variations. That is because they both are relative to a specific template that is created from each time series. Thus, their absolute values (and thus the mean of their variation) holds little information. Furthermore, I plot the change of the offset of the CRX variation with a separate y-axis marked in red on the right side of the right column. This is due to the fact, that the original CRX offset of $O_0 \sim 2.52 \text{m s}^{-1} \text{Np}^{-1}$ is small, and thus small absolute changes quickly lead to large relative changes that visually dominate the more subtle relative differences of the other observables.

Examining Fig. 3.13, one can observe that by increasing either the oscillation's velocity amplitude v_{osc} (top row), or the K parameter (second row), the amplitude (left column) of all observables is linearly increasing. There are only slight differences in the individual slopes. Both v_{osc} and K have, perhaps unsurprisingly, the strongest influence on the RVs. Thus, when trying to model a real star, one should start out by finding appropriate parameters for both. I note that the choice of the K parameter can be motivated by physical constraints (see Eq. 3.6).

The fact that an increase of either v_{osc} or K also strongly increases the amplitudes in the activity indicators implies that a non-radial oscillation with a large RV amplitude (such as the case for NGC 4349 No. 127), is likely also much easier to detect in the activity indicators compared to RV signals with smaller amplitudes. However, also the rotation velocity can increase the amplitude in the indicators substantially (see below). These findings are of importance for the planet candidates discussed in Chapt. 5.

In the central column, one can observe the phase shifts associated with changing both parameters. These are generally small. The most pronounced phase shifts are apparent for the FWHM of the CCF, likely a consequence of the changing ratio between the velocity of the oscillation and the constant velocity of the rotation (also inversely apparent from Fig. 3.14).

Looking at the offset of the observables (right column), one notes that the CRX is most affected. However, as mentioned, this large relative change is partly due to the fact that the offset of the base model's CRX variation is comparably small. For the line shape indicators, FWHM and contrast of the CCF, one can see that an increase of the oscillation's velocity with high K factors slightly increases the average width of the spectral lines, and

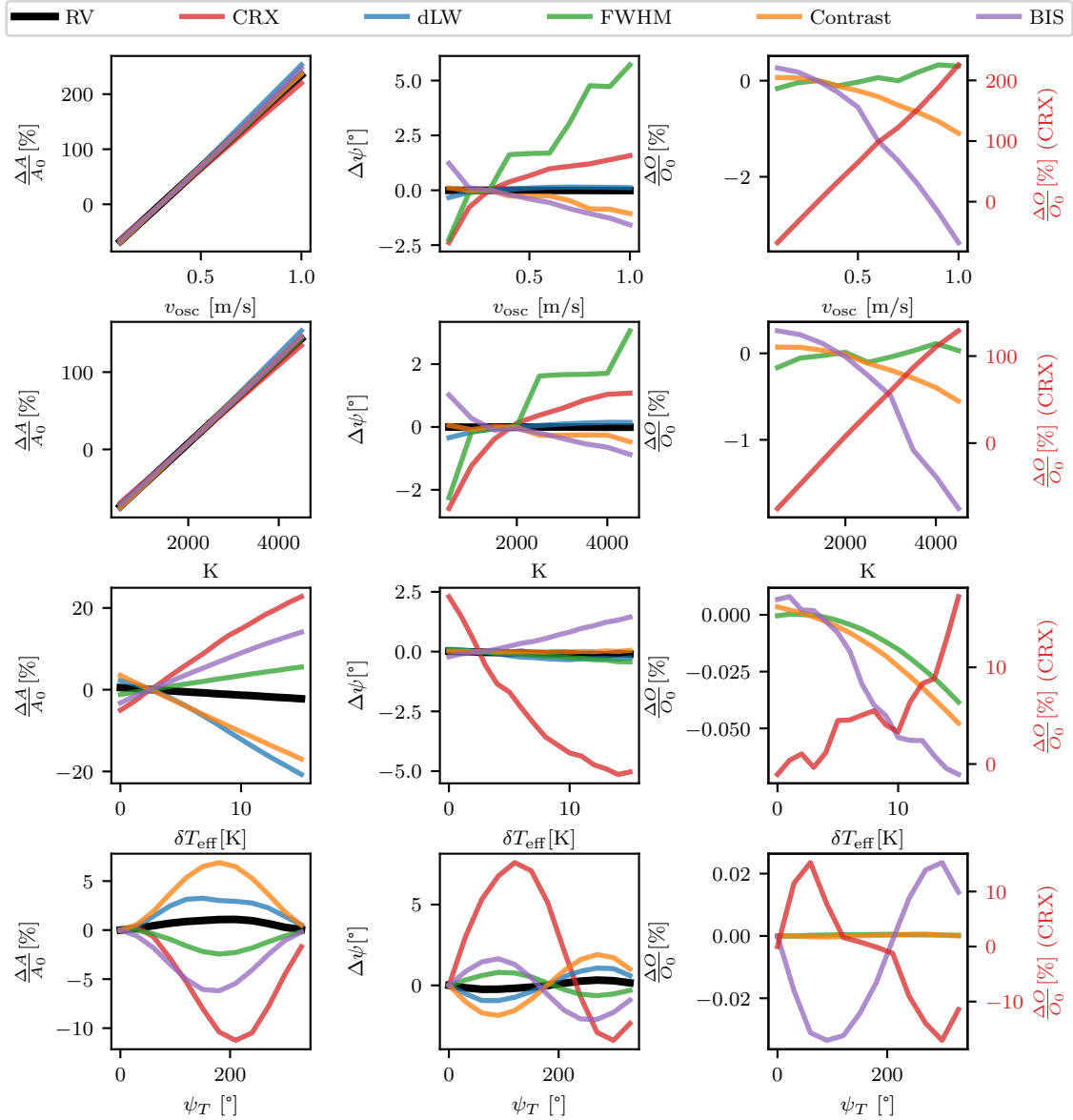


Fig. 3.13.: Change of the amplitude (left column), phase (middle column), and offset (right column) for the RVs and activity indicator time series as a function of the oscillation parameters. All changes are relative to the base model discussed above.

thus inversely decreases their contrast. However, the effect is much smaller than the effect of changing the rotational or macroturbulent broadening, as discussed below. For the BIS, there is further a noticeable overall decrease with increasing oscillation velocities. In other words, the general rightward leaning trend as depicted, for instance, in Figs. 3.7 and 4.6 is slightly straightened. With the typical scatter in real data, this effect would likely be too small to be noticeable for small rotation velocities.

Looking at the bottom two rows of Fig. 3.13, that summarize the effect of the temperature variations, both in terms of their amplitude δT_{eff} , and their phase ψ_T relative to the radial displacement, one can see that they have an effect on the amplitude (left column) of most observables. However, as the amplitude of the dLW variations can be rescaled with a multiplicative factor to match a real star (see Spaeth et al. 2024 or Chapt. 4), the strongest effect is seen on the CRX, followed by the contrast of the CCF. While the CRX variations slightly increase with increasing δT_{eff} , the contrast variations are slightly damped. However, I remind again that the limb darkening is dominating the CRX variation. The change would indeed be more apparent, if one were to disable its influence. The RV variation itself is affected comparably little. Phase shifts of the temperature variation (bottom left panel) also lead to a change of the amplitudes. However, these are generally only of the order of $\lesssim 5\%$ for most observables other than the CRX.

Interestingly, one can see that neither a change of δT_{eff} nor changes of the phase of the temperature variation ψ_T have strong effects on the phase of observables' variations. The strongest effect, as might be expected, can be seen for the CRX, which most directly measures the effects of the temperature contrast. However, even the CRX shows phase shifts $|\psi| \lesssim 7.5^\circ$. One can thus see, that the phase relations presented in Spaeth et al. (2024) (Chapt. 4) between the activity indicators and the RVs cannot be easily amended for an isolated $l = 1, m = 1$ oscillation mode. The changes of the offset of the variations (right column) are rather small for both parameters considered.

Turning to Fig. 3.14, in which more general parameters of the simulated star are examined, one can first observe the influence of the macroturbulent velocity v_{macro} (top row) and the rotation velocity v_{rot} (second row). Both, to first order, act to broaden all spectral lines, which is evident from the right column, as the FWHM of the CCF increases and the contrast of the CCF decreases with increasing velocities. Both also play a role for the variations' amplitudes. Interestingly, the macroturbulence most strongly reduces the amplitude of the contrast variations, followed by the FWHM and the dLW. This can likely be understood as an increase of the macroturbulent broadening will generally lead to more smoothed out spectral lines, such that the adjacent continuum affects the spectral lines more strongly, thus damping variations of their widths and depths.

Somewhat opposite to this, an increase of the rotation velocity, leads to a fairly strong increase of the amplitudes of the three observables. This can be understood, as, opposite to the macroturbulent broadening, which is implemented as a smoothing of the underlying PHOENIX spectra, the rotational broadening is implemented via its velocity contributions. Thus, one can intuitively imagine that a large rotation velocity combined with the oscillation velocity, leads to different parts of the spectral line profile to be most affected. For instance, if one considers a cell at the limb of the star with a given oscillation velocity, its velocity contribution will more directly influence the center of a spectral line in case of a low rotation velocity. For a large rotation velocity, the cell's velocity contribution will

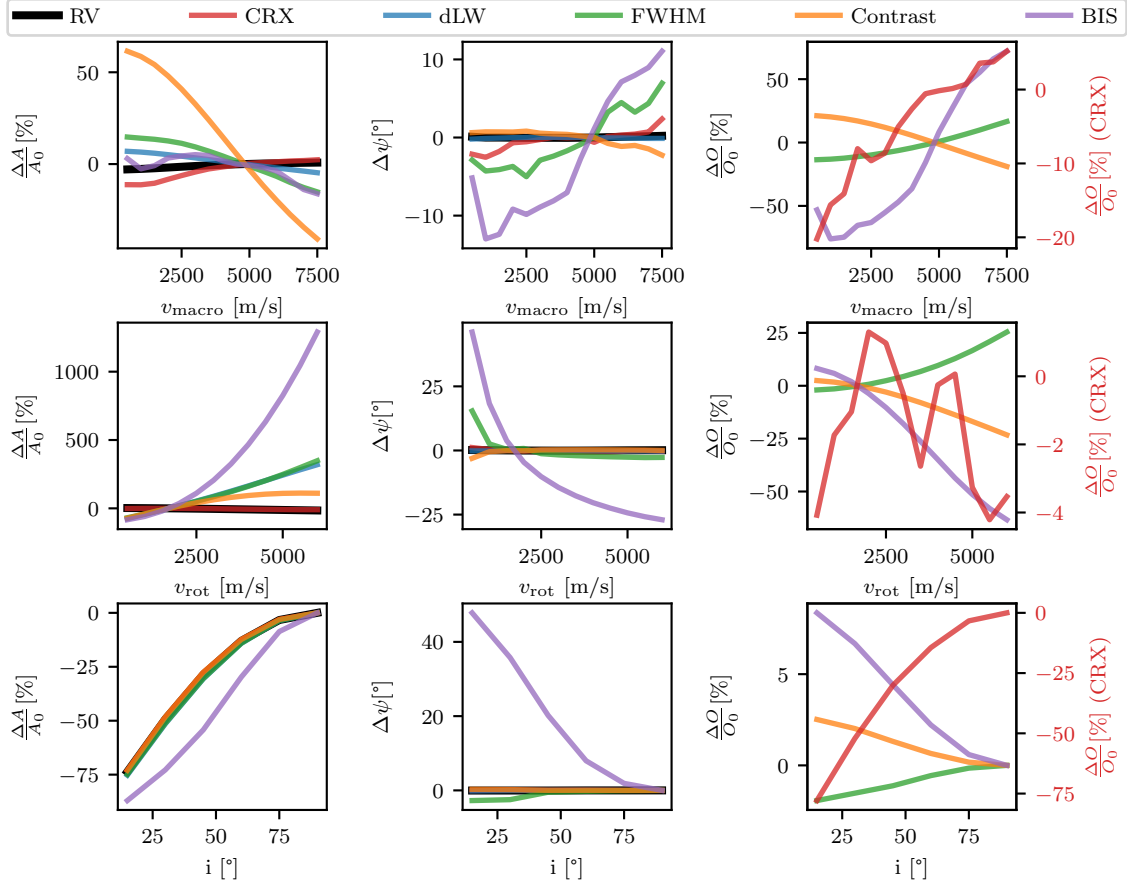


Fig. 3.14.: Change of the amplitude (left), phase (middle), and offset (right) for the RVs and activity indicator time series as a function of the stellar parameters. All changes are relative to base model discussed above.

be shifted toward the flank, which manifests in generally larger variations of the spectral line's FWHM, contrast, and dLW. Unsurprisingly, the BIS variations become much more pronounced for larger rotation velocities, which implies that the variations of the BIS, which were not detected for NGC 4349 No. 127 (Spaeth et al. 2024, Chapt. 4), would be much more apparent for stars with higher rotation velocities. This is also consistent with the general expectations (see Sect. 1.6.3). Lastly, for both the macroturbulence and the rotation, the resulting RV variations are relatively constant compared to the other parameters, although a slight increase is apparent with increasing v_{macro} , while the RV decreases with increasing v_{rot} .

I note that the phase shifts (center column) are generally small for all indicators except the BIS. For the BIS, these phase shifts, are likely again a consequence of the oscillation affecting different parts of the spectral lines for different v_{rot} (and also partly for different v_{macro}). The BIS indicator generally seems to be most sensitive to phase shifts in that regard. Along with the phase of the BIS variation, also the offset of its time series is most

strongly affected. For large v_{rot} , for instance, one can thus observe, that the bisectors are generally straightened up compared to Fig. 4.6 discussed in Chapt. 4, but have a much larger periodic variation from the mean position.

Finally, one can observe in the bottom row of Fig. 3.14, how the observables change for different inclination angles i . As expected for an $l = 1, m = 1$ mode, the amplitudes are maximized for $i = 90^\circ$ (equator-on) and drop significantly for smaller i . Interestingly, this drop in amplitude is again accompanied by a significant phase shift of the BIS variations, whose amplitude is, however, generally quite small for this simulation. The other indicators (except for the FWHM at small i) are not affected by strong phase shifts. As the rotation velocity is equally projected onto the line of sight, it is straightforward to see that the offset of the FWHM (bottom right panel) increases with inclination angle i , while the contrast of the CCF decreases. Likely due to this projection effect, one can observe a similar behavior for the BIS offset as shown when plotting it as a function of v_{rot} (middle right panel). Finally, I notice a relatively strong increase of the CRX offset, which is likely linked to the increasing, observed velocity amplitude as observed in Fig. 3.13.

To summarize, the strongest change of the RV amplitude is caused by the v_{osc} and K parameters, that also strongly influence the amplitudes of the variations of all activity indicators. Thus, detecting the variations in the activity indicators can be expected to be more feasible for RV-variable giants with larger amplitudes. The temperature variations most strongly influence the CRX, but also have an effect on other observables. Nevertheless, the effect of the limb darkening dominates the variations of the CRX. The macroturbulence and, even more importantly, the rotation have a strong effect on the amplitudes of the line shape indicator, FWHM, contrast, dLW, and BIS, while they affect the RVs to a much lesser extent. Finally, the phase relations between most indicators and the RVs are relatively stable for this $l = 1, m = 1$ oscillation mode. Only the BIS variations show larger phase deviations in specific scenarios. Thus, the observed phase relations for NGC 4349 No. 127 (Spaeth et al., 2024) are only marginally influenced by the choice of the parameters. Therefore, the amplitudes of the observed variations give the most crucial constraints on the simulation parameters.

In the next chapter, which is based on Spaeth et al. (2024), I combine the above findings and apply these to the known false-positive evolved planet host NGC 4349 No. 127. I further discuss different modes for $l = 1$ and higher-order modes.

Non-radial oscillations mimicking a brown dwarf orbiting the cluster giant NGC 4349 No. 127

Details of authorship: The contents of this chapter have been published almost identically as a journal article in *Astronomy & Astrophysics* (Spaeth et al., 2024),¹ jointly with my co-authors Sabine Reffert, Emily L. Hunt, Adrian Kaminski, and Andreas Quirrenbach. Figure 4.1 has been created by Emily L. Hunt. The other figures, the analysis, and the main body of text have been contributed by me. I acknowledge valuable input in the design of the analysis, the presentation of the results, and the final formulations by my co-authors, as well as the reviewer. The figures and tables have been slightly rescaled to fit into the format of the chapter. The appendix was moved to the [Appendix B](#).

4.1 Introduction

With the advent of large-scale transit surveys such as *Kepler* (Borucki et al., 2010), K2 (Howell et al., 2014), and TESS (Ricker et al., 2015), the number of known exoplanets has increased drastically to over 5600 confirmed planets to date.² Despite this immense wealth of newly discovered planets, less than 200 of these have been found orbiting evolved stars.³ Due to intrinsic biases of the transit surveys, the majority of planets orbiting giant stars have been found using the radial velocity (RV) method.

Targeting giant stars in RV surveys offers important additions to surveys targeting main-sequence stars. Specifically, it allows the detection of planets around the evolved counterparts of stars more massive than about $1.5 M_{\odot}$ (Reffert et al., 2015), which are increasingly inaccessible to RV measurements during their main-sequence phase, due to high effective temperatures and rotation rates (Sato et al., 2003; Galland et al., 2005; Johnson et al., 2007; Lagrange et al., 2009; Assef et al., 2009). Furthermore, analyzing the planet population in later evolutionary stages allows studies of the effect of stellar evolution on planetary

¹Licensed under CC BY 4.0 (<https://creativecommons.org/licenses/by/4.0/>).

²<https://exoplanetarchive.ipac.caltech.edu/> (June 2024)

³<https://www.lsw.uni-heidelberg.de/users/sreffert/giantplanets/giantplanets.php>

systems. Therefore, detecting a statistically meaningful sample of planets around giant stars is crucial in order to capture a full picture of the general planet population. For simplicity, we also refer to low-mass brown dwarfs ($M \lesssim 30M_{\text{Jup}}$) as planets within this work.

However, detecting planets orbiting giants using the RV method has its own challenges. First, most giant stars are known to undergo short-term, stochastically driven p-mode oscillations, called solar-like oscillations. For giants, these typically occur on timescales of hours to days and lead to RV jitter on the order of $\sim 10 \text{ m s}^{-1}$ to $\sim 20 \text{ m s}^{-1}$, even for giant stars considered to be relatively stable (Kjeldsen & Bedding, 1995; Hekker et al., 2006, 2008). This intrinsic noise can often be overcome with sufficient statistics, but limits the detectable orbital companions to those with rather high masses (typically Jovian or higher).

Less understood, and therefore more challenging, is the recent discovery of several giant stars showing long-term, periodic RV variations, some of which were already attributed to planets or brown dwarfs, yet were later shown to be incompatible with orbital companions. These include γ Dra (Hatzes et al., 2018), Aldebaran (Reichert et al., 2019), ϵ Cyg (Heeren et al., 2021), 42 Dra (Döllinger & Hartmann, 2021), Sanders 364⁴ (Zhou et al., 2023), 41 Lyn, 14 And (both Teng et al. 2023b), and the cluster giants NGC 2423 No. 3, NGC 2345 No. 50, NGC 3532 No. 670, and NGC 4349 No. 127⁵ (Delgado Mena et al., 2018, 2023). Döllinger & Hartmann (2021) show that doubtful planet detections around giant stars mostly accumulate at periods between 300 d and 800 d and around stars with radii $R > 21 R_{\odot}$, pointing at a common origin of these RV variations.

Wolthoff et al. (2022) present the planet occurrence rate around evolved stars as a function of the orbital period, which follows a broken power law relation peaking at $P \sim 720$ d, very close to the periods of the identified false positive detections. If a significant number of as-yet-unidentified false positives contaminate the comparably small sample of planets around giants, significant implications on the planet occurrence rate and its interpretation are to be expected (Wolthoff et al., 2022).

Moreover, as the phenomenon is still poorly understood and can mimic planets quite convincingly in RV data, it is often impracticable to unambiguously confirm new planets around giant stars (see, e.g., Tala Pinto et al. 2020; Niedzielski et al. 2021; Jeong et al. 2022; Teng et al. 2022; Zhou et al. 2023). This is due to the fact that it is not yet clear which observables are the most decisive diagnostics to separate intrinsic signals from orbital companions for giants. This problem is made even worse by the varying availability, in data sets from different spectrographs, of spectral diagnostics targeting such intrinsic variations. These are commonly referred to as activity indicators, and we adopt this term even though we do not (mainly) target magnetic activity in this work.

⁴SIMBAD identifier: BD+12 1917

⁵SIMBAD identifiers: NGC 2423 3, NGC 2345 50, HD 96789, and NGC 4349 127

So far, several intrinsic origins have been discussed. Radial oscillations can usually be ruled out due to the long-period nature of the suspected signals, which appear at periods much longer than the fundamental radial mode (Hatzes & Cochran, 1993; Cox et al., 1972; Hatzes et al., 2018; Reichert et al., 2019). In the binary system ϵ Cyg, the heartbeat phenomenon was considered (Heeren et al., 2021); however, it is not applicable to single stars. Magnetic surface structures, such as cool spots, can in most cases equally be ruled out, as they should manifest themselves in much larger photometric variations than were reported for the above stars (Reichert et al., 2019; Heeren et al., 2021). Delgado Mena et al. (2023) (and references therein) propose magnetic plagues or other magnetic structures that locally reduce convection and could cause RV variations without associated photometric variations. However, the magnetic fields on the surface of most giant stars are still not well understood (see, e.g., Aurière et al. 2011, 2013, 2015; Konstantinova-Antova et al. 2024, for notable exceptions).

Non-radial oscillations, on the other hand, can cause large amplitude RV variations at long periods (Hatzes, 1996; Hatzes & Cochran, 1999). Hatzes et al. (2018) link the aforementioned phenomenon of false positive planet detections to oscillatory convective modes presented by Saio et al. (2015). These modes were proposed as the origin for the sequence D of the long secondary periods (LSPs) observed for variable bright giant stars (Wood et al., 1999; Wood, 2000). These are dipole ($l = 1$) g^- -modes that become oscillatory in the non-adiabatic conditions present in the envelopes of luminous ($\log L/L_{\odot} \gtrsim 3$) giant stars (Takayama & Ita, 2020). Reichert et al. (2019) build on this argument, showing in their Fig. 8 that both γ Dra and Aldebaran fall into a region in the period-luminosity diagram in which an extrapolation of the models by Saio et al. (2015) could potentially explain the observed variations. Nevertheless, no satisfying attempt to apply models of non-radial oscillations to the observables of a known false positive evolved planet host has been published to date.

In this work we reexamine the RV variations of the cluster giant NGC 4349 No. 127, previously thought to host a brown dwarf companion in a $P = 677.8$ d orbit originally published by Lovis & Mayor (2007). However, Delgado Mena et al. (2018) show that, while the RV signal is stable in HARPS (High Accuracy Radial velocity Planet Searcher) spectra, variations of the full width at half maximum (FWHM) of the cross-correlation function (CCF) and the $H\alpha$ index at the orbital period are present. The authors therefore refute the companion's existence, favoring rotational modulation of magnetic activity as the most likely alternative, while not ruling out non-radial oscillations. Delgado Mena et al. (2023) affirm these findings by presenting 11 additional RV measurements.

Here, we present a reanalysis of the HARPS data set adding measurements of the chromatic index (CRX) and differential line width (dLW) variations by using the SERVAl (Zechmeister et al., 2018) pipeline, as well as the contrast of the CCF by using the RACCOON (Lafarga et al., 2020) reduction software. We reveal a linear correlation between the RV, on the one

hand, and the CRX and the $H\alpha$ indicator, on the other hand, respectively. We further show that the dLW, the FWHM of the CCF, and the contrast of the CCF each correlate with the RV in a “closed-loop” relation. We additionally present simulations of the observational effects of non-radial oscillations that can closely reproduce the periods and amplitudes of the activity indicator variations, as well as the phase differences with the RV.

This paper is structured as follows. In Sect. 4.2 we give an overview of the stellar parameters, observations, and data reduction. In Sect. 4.3 we present the `pyoscillot` simulation suite developed to simulate the effect of non-radial oscillations on HARPS spectra. We present newly detected correlations between the activity indicators and the RVs in Sect. 4.4, and show that they are consistent with a retrograde, dipole, non-radial oscillation model. In Sect. 4.5 we present general observational properties of different oscillation modes. We discuss our non-radial oscillation model in the context of oscillatory convective modes in Sect. 4.6, before summarizing our findings in Sect. 4.7.

4.2 Observations and stellar parameters

4.2.1 Stellar parameters

NGC 4349 No. 127 is the most evolved star of the open cluster NGC 4349 (Delgado Mena et al., 2018), located at a distance $d = 1788.9 \pm 2.9$ pc (Hunt & Reffert, 2023), with an estimated age of around 300 Myr (Holanda et al., 2022; Tsantaki et al., 2023; Hunt & Reffert, 2023). The stellar parameters vary considerably between different studies and are summarized in Table 4.1.

In Fig. 4.1, we plot a color-magnitude diagram based on *Gaia* DR3 photometry (Gaia Collaboration et al., 2016, 2023), highlighting the position of NGC 4349 No. 127 as the orange star marker. The membership list and isochrone fit were taken from Hunt & Reffert (2023). The star’s exact evolutionary state is ambiguous between the first or second ascent on the red giant branch (RGB), as was discussed in the literature (Delgado Mena et al., 2016; Tsantaki et al., 2023). One reason for this ambiguity is the differential extinction $0.57^{+0.30}_{-0.31}$ mag in the V band present in the cluster (Hunt & Reffert, 2023), which is also evident from the spread at the turn-off of the main sequence in Fig. 4.1. This complicates the determination of a specific extinction value for NGC 4349 No. 127, adding uncertainty to its intrinsic photometry. The difficulty in determining an accurate extinction value could also (partially) explain the variability of the stellar parameters summarized in Table 4.1.

We also tested the stellar parameters using Bayesian inference based on *Gaia* DR3 parallaxes and photometry using SPOG+⁶ (Stock et al., 2018). We use extinction values taken

⁶<https://github.com/StephanStock/SPOG>

from the Starhorse catalog (Anders et al., 2022). The metallicity was taken from Tsantaki et al. (2023). The tool yields a probability of 99.1% for the star being on the horizontal branch (HB) or second ascent on the RGB. The stellar parameters derived by SPOG+ are listed in Table 4.1.

While the results for T_{eff} are roughly consistent with other determinations in the literature, SPOG+ estimates a significantly lower mass, radius, and luminosity. The age determination of the star $\tau = 930_{-330}^{+300}$ Myr also significantly deviates from the estimated age for the whole cluster from other studies. We assume that stellar parameters derived from spectroscopy or ones that take the whole cluster into account should generally be regarded as more accurate. SPOG+ is also quite sensitive to the choice of extinction values, which are difficult to determine. However, as masses of giant stars derived from evolutionary models are suspected to be overestimated (see, e.g., Lloyd 2011), we note this somewhat lower mass estimate, as well as the lower mass estimates by Anders et al. (2022) and Mortier et al. (2013b), and the general variability of the parameters in Table 4.1.

The star has furthermore been found to show enhanced Li abundance compared to other giant stars in the cluster and compared to field stars (Carlberg et al., 2016; Delgado Mena et al., 2016; Tsantaki et al., 2023), which was proposed to be caused by planet engulfment. However, Holanda et al. (2022) notes that the determined Li abundance is still below the traditional limit for Li-rich giant stars $\log \epsilon(\text{Li}) \geq 1.50$.

Given the precision of the results and favoring parameters derived by spectroscopy, we base our analysis and discussion on the stellar parameters derived by Tsantaki et al. (2023) and Delgado Mena et al. (2023). For the simulations presented in Sect. 4.4, we chose ($T_{\text{eff}} = 4500$ K, $\log g = 2.0$, $[\text{Fe}/\text{H}] = 0.0$) as the closest grid point of the PHOENIX spectral library. We refrain from interpolating the base spectrum of the simulations to the exact parameters due to the differences shown in the literature (Table 4.1) and to avoid interpolation errors. Using the relation by Hekker & Meléndez (2007), we determine the value of the macroturbulence to be $\zeta = 4822 \pm 39$ m s⁻¹ at this effective temperature.

4.2.2 Data

We downloaded 58 publicly available, extracted HARPS (Mayor et al., 2003) spectra from the ESO science archive⁷ for NGC 4349 No. 127. The spectra were taken between 2005 and 2022 and have signal-to-noise ratios (S/N) per extracted pixel between 25 and 62 (with one outlier at 14.7) at the peak of the blaze function of (physical) order 102, which is centered around 6000 Å. The data were taken as part of a long-term RV survey of intermediate-mass giant stars in open clusters and were originally published by Lovis & Mayor (2007) and Delgado Mena et al. (2018, 2023).

⁷<http://archive.eso.org/scienceportal/home>

Tab. 4.1.: Overview of the stellar parameters determined for NGC 4349 No. 127 in the literature.

M M_{\odot}	R R_{\odot}	L L_{\odot}	T_{eff} K	$\log g$ [cm s $^{-2}$]	[Fe/H] dex	ξ km s $^{-1}$	$v \sin i$ km s $^{-1}$	ζ km s $^{-1}$	A_V mag	Ref.
$2.20^{+0.38}_{-0.20}$	$23.3^{+0.9}_{-1.4}$	211^{+3}_{-4}	4566^{+123}_{-70}	$2.04^{+0.13}_{-0.06}$	-	-	-	-	$0.67^{+0.06}_{-0.07}$	SPOG+, 1 (phot)
$3.29^{+0.28}_{-0.56}$	-	-	-	-	-	-	-	-	$0.86^{+0.19}_{-0.15}$	2 (phot)
3.01 ± 0.24	-	-	4417 ± 12	1.78 ± 0.05	0.17 ± 0.02	-	-	-	1.16	3 (spec)
3.41 ± 0.27	-	-	4567 ± 31	1.83 ± 0.08	-	-	-	-	1.16	3 (phot)
-	38.0 ± 2.6	575.4	-	-	-	-	4.81	4.66	1.16	4, 3 (spec+phot)
-	-	-	4420 ± 70	1.70 ± 0.20	-0.13 ± 0.13	1.51 ± 0.07	4.20 ± 0.60	3.0	1.24 ± 0.06	5 (spec)
-	-	-	4597 ± 39	1.78 ± 0.09	-	-	-	-	1.24 ± 0.06	5 (phot)
$1.56^{+0.20}_{-0.36}$	-	-	4199^{+61}_{-57}	$1.43^{+0.01}_{-0.03}$	$-0.29^{+0.01}_{-0.11}$	-	-	-	$0.67^{+0.06}_{-0.07}$	6 (phot)
2.4	-	-	4370 ± 78	1.70 ± 0.22	-0.20 ± 0.11	1.70 ± 0.06	< 2	~ 5.0	0.90	7 (spec)
3.81 ± 0.23	37.0 ± 4.9	646^{+205}_{-156}	4503 ± 70	1.99 ± 0.19	-0.13 ± 0.04	1.77 ± 0.07	6.13	-	-	8 (spec+phot)
1.37 ± 0.37	-	-	4445 ± 87	1.64 ± 0.23	-0.25 ± 0.06	1.84 ± 0.08	-	-	-	9 (spec+phot)
3.77 ± 0.36	44.7 ± 2.5	774^{+467}_{-291}	4519 ± 100	1.92 ± 0.2	-0.21 ± 0.12	2.08 ± 0.20	-	-	1.08	10 (spec+phot)

Notes. Presented are mass M , radius R , luminosity L , effective temperature T_{eff} , surface gravity $\log g$, metallicity [Fe/H], microturbulent velocity ξ , rotational broadening $v \sin i$, macroturbulent velocity ζ , and the V-band extinction A_V used to determine the parameters. The values for reddening $E(B - V)$ given by Holanda et al. (2022) and Carlberg et al. (2016) were converted assuming $A_V = 3.1E(B - V)$.

(1) Stock et al. (2018); (2) Hunt & Reffert (2024); (3) Tsantaki et al. (2023); (4) Delgado Mena et al. (2023); (5) Holanda et al. (2022); (6) Anders et al. (2022); (7) Carlberg et al. (2016); (8) Delgado Mena et al. (2016); (9) Mortier et al. (2013b); (10) Ghezzi et al. (2010)

We reduced the spectra using the SERVAL pipeline (Zechmeister et al., 2018), which derives radial velocities via a least-squares optimization of the RV shift relative to a high signal-to-noise stellar template obtained by coadding the available observations. SERVAL was shown to produce slightly more precise RV results than the default HARPS data reduction software (DRS) (Trifonov et al., 2020). The SERVAL pipeline furthermore computes additional activity indicators, namely the CRX and the dLW (Zechmeister et al., 2018), which have proven to be effective indicators to detect activity for main-sequence dwarfs, especially in context of the CARMENES (Calar Alto high-Resolution search for M dwarfs with Exoearths with Near-infrared and optical Echelle Spectrographs) survey (Quirrenbach et al., 2014). It moreover calculates several line indices, of which the $H\alpha$ index will be used within this work.

We furthermore utilized the RACCOON reduction software (Lafarga et al., 2020) to obtain radial velocities using a CCF with a weighted binary mask. The mask was created from the SERVAL template via the routines provided by the RACCOON software. It furthermore provides three activity indicators targeting the contrast and FWHM of the CCF and calculates the Bisector Inverse Slope (BIS) (Lafarga et al., 2020). We prefer the RACCOON pipeline over the default HARPS DRS, since the latter is not publicly available and can therefore not be used to reduce the simulated data presented in Sect. 4.4. The results of the RACCOON pipeline are generally in good agreement with the HARPS DRS results, but yield somewhat higher RV uncertainties compared to HARPS DRS and SERVAL (see Table B.1).

We separated the spectra taken before (46 spectra) and after (12 spectra) 2 June 2015, to account for the HARPS fiber change.⁸ We did not separate the spectra further, accounting

⁸<https://www.eso.org/sci/facilities/lasilla/instruments/harps/news.html>

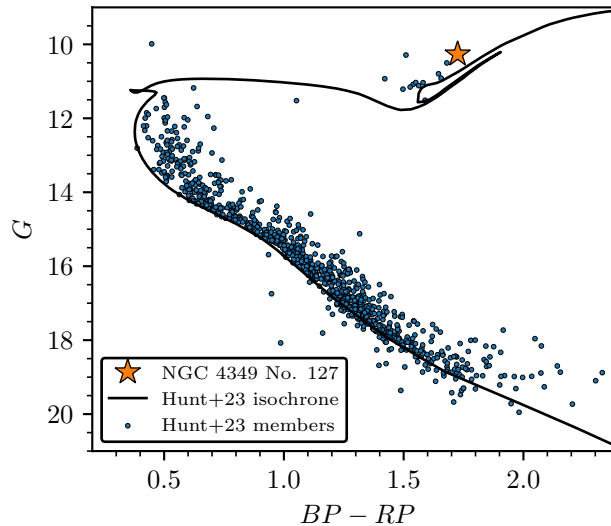


Fig. 4.1.: Color-magnitude diagram for the open cluster NGC 4349 based on *Gaia* DR3 photometry. The membership list and isochrone fit were taken from [Hunt & Reffert \(2023\)](#). NGC 4349 No. 127 is the most evolved star of the cluster, indicated by the orange star marker. Its evolutionary state is ambiguous between the first or second ascent on the RGB.

for the HARPS warm-up on 23 March 2020, as only three spectra were taken after this date. We treated the two subsets as separate RV time series, allowing for a relative offset.

We restricted the analysis of the activity indicators to the 46 spectra acquired before the HARPS fiber exchange, as we noted significant offsets of the activity indicators by analyzing the activity time series of quiet stars using the HARPS RVBANK ([Trifonov et al., 2020](#)) (see also Appendix A of [Delgado Mena et al. 2023](#)). As these offsets are (to our knowledge) poorly understood and constrained, we decided to focus merely on the spectra acquired prior to the fiber change. Both the SERVAL and RACCOON RVs and activity indicators are listed in [Table B.1](#).

4.3 Simulations

To study whether non-radial oscillations could explain the variations of the radial velocities and the activity indicators, we simulate the observational effect of these on HARPS spectra. The simulations are part of the simulation suite `pyoscillot`.⁹

⁹<https://github.com/DaneSpaeth/pyoscillot>

4.3.1 Description of non-radial oscillations

We start out with a model of the stellar photosphere, using spherical coordinates (θ, ϕ) , with θ being the polar angle (or colatitude), measured from the oscillation pole and ranging from 0 to π , and ϕ being the azimuthal angle, ranging from 0 to 2π . Each of the grid points has a local effective temperature T_{eff} and a local oscillation velocity vector \mathbf{v}_{osc} defined by the three components (Kurtz, 2006; Hatzes, 1996; Schrijvers et al., 1997; Kochukhov, 2004)

$$v_r = \frac{\partial \xi_r}{\partial t} = i2\pi\nu \frac{a}{C} Y_l^m(\theta, \phi) \exp(i2\pi\nu t), \quad (4.1)$$

$$v_\theta = \frac{\partial \xi_\theta}{\partial t} = i2\pi\nu \frac{Ka}{C} \frac{\partial Y_l^m(\theta, \phi)}{\partial \theta} \exp(i2\pi\nu t), \quad (4.2)$$

$$v_\phi = \frac{\partial \xi_\phi}{\partial t} = i2\pi\nu \frac{Ka}{C \sin \theta} \frac{\partial Y_l^m(\theta, \phi)}{\partial \phi} \exp(i2\pi\nu t), \quad (4.3)$$

which are oriented in the directions of the local unit vectors of \mathbf{r} , θ , and ϕ , respectively. We use the real part of the velocity components to calculate the final local velocities. Here, ξ describes the local displacement vector, ν is the oscillation frequency, a is the displacement amplitude in the radial direction, K is the ratio between the radial and the horizontal displacement, and Y_l^m are the spherical harmonics defined as

$$Y_l^m(\theta, \phi) = \sqrt{\frac{2l+1}{4\pi} \frac{(l-m)!}{(l+m)!}} P_l^m(\cos \theta) \exp(im\phi). \quad (4.4)$$

Here we introduce the quantum numbers l and m . l is the number of line of nodes on the stellar surface, while m is the azimuthal order quantifying how many of these line of nodes run through the oscillation pole. It ranges from $-l \leq m \leq l$. $P_l^m(\cos \theta)$ are the Legendre Polynomials defined by

$$P_l^m(\cos \theta) = \frac{(-1)^m}{2^l l!} (1 - \cos^2 \theta)^{\frac{m}{2}} \frac{d^{l+m}}{d \cos^{l+m} \theta} (\cos^2 \theta - 1)^l. \quad (4.5)$$

Thus, the velocity amplitude in the radial direction is given by $v_{\text{osc}} = 2\pi\nu \frac{a}{C}$, and consequently $K \cdot v_{\text{osc}}$ is the velocity amplitude in the θ and ϕ directions. We introduce the normalization factor $C = \max(\text{Re}(iY_l^m(\theta, \phi)))$ for $m \neq 0$, and $C = \max(\text{Re}(Y_l^m(\theta, \phi)))$ for $m = 0$, such that v_{osc} can be regarded as the amplitude of the radial component at the position of maximum variation on the stellar surface, giving it a straight-forward interpretation. Both v_{osc} and K are input parameters to be defined by the user. In the Cowling approximation, neglecting perturbations of the gravitational potential, K can be expressed as (Aerts, 2021; Cowling, 1941)

$$K = \frac{GM_\star}{(2\pi\nu)^2 R_\star^3}. \quad (4.6)$$

Associated with the (physical) radial displacement are variations of the local effective temperature of a scale δT_{eff} and at a phase ψ_T . Assuming non-adiabatic conditions, we can express the local effective temperature as (Dupret et al., 2002; De Ridder et al., 2002)

$$T_{\text{eff,local}} = T_{\text{eff}} + \delta T_{\text{eff}} \operatorname{Re} \left(\frac{Y_l^m(\theta, \phi)}{\max(\operatorname{Re}(Y_l^m(\theta, \phi)))} \exp(i(2\pi\nu t + \psi_T)) \right), \quad (4.7)$$

defining δT_{eff} as the amplitude of the temperature variation at the position of maximum variation on the stellar surface. The scale of the temperature variation is not influenced by the choice of the oscillation velocity v_{osc} , such that a reasonable value for δT_{eff} has to be chosen by the user.

As the velocity components of interest are generally low, we neglect geometrical distortions of the stellar sphere and keep the stellar radius at unity at all times. Thus, the simulations can be visualized as mapping the oscillation's velocity components onto the unit sphere, neglecting the displacements of the individual positions. We further do not include surface-normal variations which were found to play a minor role on the variation of line widths by De Ridder et al. (2002). However, we note that Townsend (1997) advocates to include both surface-normal and surface-area variations to accurately reproduce photometric continuum variations.

4.3.2 Calculation of the synthetic spectrum

After choosing an inclination angle, defined as the angle between the polar axis of the oscillation and the line of sight, the velocity and temperature fields are projected onto a flat, uniformly spaced 2D grid of size $N_{\text{grid}} \times N_{\text{grid}}$, using triangulation and linear interpolation. The directional velocity components are further projected onto the line-of-sight vector, and can thereafter be summed up to yield the local combined oscillation velocity for each element on the grid.

We further add a projected rotational velocity for each position characterized by the (unprojected) rotational velocity v_{rot} . We fix the axis of rotation to coincide with the polar axis of the simulated star and thus with the symmetry axis of the oscillation. The summation of the projected, combined oscillation velocity and the projected rotational velocity yield the final, local velocities along the line of sight v_i for each position i . This local velocity will subsequently be used to Doppler shift the local spectra as detailed below.

The projected positions on the grid can be regarded as the center points of small surface areas with the same projected area. For cells at the limb of the star, a geometric weight w_i is calculated as these are only partially covering the stellar disk.

For each grid cell, a synthetic stellar spectrum is calculated by performing a cubic spline interpolation with respect to the local effective temperature $T_{\text{eff},i}$ within a grid of synthetic spectra taken from the PHOENIX spectral library¹⁰ (Husser et al., 2013). For computational speed, the cubic spline interpolation is performed in 0.1 K steps. For simplicity, we do not interpolate the spectra with respect to the surface gravity $\log g$ and the metallicity $[\text{Fe}/\text{H}]$. Both are fixed to the closest value for NGC 4349 No. 127, that is $\log g = 2.0$ and $[\text{Fe}/\text{H}] = 0.0$.

Ideally, one would like to use the specific intensity spectra available from the PHOENIX library, which were calculated for a model atmosphere under different observation angles $\mu = \cos \gamma$, with γ being the angle between the line of sight and the surface normal. However, these are only available with a sampling rate of 1.0 \AA , too low to simulate high-resolution échelle spectra. We are therefore forced to use the high-resolution spectra of the PHOENIX spectral library. As these are already disk-integrated spectra, the final simulated spectrum can only be regarded as a relatively crude approximation.

Implementation of the limb-darkening correction

Since we are interested in the observational effects of non-radial oscillations, which can be dominated by their horizontal components and thus strongest toward the limb of the stellar disk, we implement a wavelength-dependent limb-darkening correction. Hestroffer & Magnan (1998) fit the intensity profile of the solar disk as a function of μ and wavelength λ using data provided by Pierce & Slaughter (1977) and Neckel & Labs (1994) and provide the relation

$$I(\mu, \lambda) = 1 - u(1 - \mu^{\alpha(\lambda)}). \quad (4.8)$$

Hestroffer & Magnan (1998) use $u = 1$ and determine $\alpha \sim -0.023 + 0.292\lambda^{-1}$ for λ in units of μm and $416 \text{ nm} \lesssim \lambda \lesssim 1099 \text{ nm}$. Since the wavelength range of HARPS extends down to 378 nm at the blue end, we extrapolate the model, despite the discontinuity at $\lambda \sim 390 \text{ nm}$ discussed by Hestroffer & Magnan (1998).

As the underlying PHOENIX spectra are already disk-integrated and therefore include the effect of limb darkening, we first divide each local spectrum by the wavelength-dependent intensity profile for the mean angle $\bar{\mu}$. Next, the limb-darkening effect is added back into the models by multiplying with the respective intensity profile for each cell according to its local angle μ_i . By this approach, we add an implicit weight based on the intensity according to the angle μ_i during the spectrum combination process detailed below. Ideally, one would like to use μ and wavelength-dependent models for a star more similar to NGC 4349 No. 127, but such models are not available in the literature.

¹⁰<https://phoenix.astro.physik.uni-goettingen.de/>

We further include the effect of macroturbulent broadening by convolving the local spectra with a wavelength-dependent Gaussian kernel, specified by a user-defined macroturbulent velocity ζ . Microturbulent broadening has already been included during the synthesis of the base PHOENIX spectrum, albeit at a fixed value for each grid point within the PHOENIX library (Husser et al., 2013).

Implementation of the convective blueshift correction

We also include an estimation for the effect of convective blueshift on the spectral line bisectors, following the approach by Zhao & Dumusque (2023). As the PHOENIX spectral library is derived from 1D atmospheric models, they do not properly reproduce line bisector shapes (Zhao & Dumusque, 2023). The intrinsic bisectors of the PHOENIX spectra therefore have to be removed prior to adding in a more plausible bisector shape stemming from convective processes.

First, the PHOENIX spectra are normalized using RASSINE (Cretignier et al., 2020). Using the normalized spectra we first calculate the small wavelength shifts necessary to remove the intrinsic PHOENIX bisector by measuring the bisectors of five FeI lines (FeI 5250.2084 Å, FeI 5250.6453 Å, FeI 5434.5232 Å, FeI 6173.3344 Å, FeI 6301.5008 Å) and calculating the average. Next, the wavelength shifts from one of the giant stars presented by Gray (2005) are calculated using the bisector-removed, normalized spectra. Both the wavelength shifts are applied to each grid point in the unnormalized PHOENIX spectra. These are then used during the spectrum combination process. By testing all available bisectors, we found that the observed CCF bisectors are well reproduced using the bisector model of the giant star β Boo. While this procedure creates CCF bisectors quite similar to the observed ones, it has little effect on the observables presented in Sect. 4.4.

Combination of the local spectra

Finally, after including each of the effects on the local spectra (local temperature variation, limb darkening, convective blueshift), the individual spectra have to be Doppler-shifted before being summed to yield the disk-integrated spectrum.

To yield accurate Doppler shifts, we first oversample the wavelength grid at equidistant 0.001 Å steps and perform a cubic spline interpolation for the flux values at the oversampled grid points. After the spectra are Doppler-shifted according to the summed local velocities of oscillation and rotation v_i , the shifted flux values are then linearly interpolated back onto the original wavelength grid, which is common for all surface grid points. Finally, the spectra are summed, accounting for the reduced geometrical weights w_i for cells at the edge of the star, and divided by the sum of all geometrical weights to maintain

a reasonable normalization of the spectra. The final, disk-integrated spectrum can be expressed as

$$I_{\text{integrated}}(\lambda) = \frac{1}{\sum_i w_i} \sum_i I_i(T_{\text{eff},i}, v_i, \mu_i, \lambda) \cdot w_i. \quad (4.9)$$

Applying the above steps, we calculate synthetic stellar spectra including the effect of non-radial oscillations. The code is also able to study other effects such as star spots, which is however beyond the scope of this publication.

Conversion to simulated HARPS spectra

The combined spectrum is next smoothed with a Gaussian kernel to bring the spectrum to the required resolution for each spectrograph. For HARPS, $R = 115\,000$ (Mayor et al., 2003) is used (CARMENES VIS and NIR channels are also available). The smoothed spectra are then rebinned onto an extracted wavelength grid of a real HARPS observation of NGC 4349 No. 127. Conceptually, converting the combined spectrum from an energy flux to a photon flux would more closely mimic the acquisition process of a real CCD. However, tests revealed that the differences are negligible and we thus decided to omit the conversion for simplicity. Next, a measured blaze function is applied to each spectral order and the necessary FITS header keywords are altered to mimic a real observation. Finally, the spectrum is saved in the FITS format and the RVs can be reduced from the simulated, extracted spectra. The simulation is performed at user-defined epochs.

The final spectra are then reduced using the RACCOON and SERVAL pipelines – identical to the processing applied to real observations – yielding the simulated RVs and activity indicators. For the RACCOON pipeline, we use the weighted mask created from the real observations. For the SERVAL reduction, a new template is created for the simulation.

For the simulation results presented below, we performed the simulation with a grid of size 150×150 . This number was chosen for computational speed, but tests at higher resolutions revealed negligible differences.

4.4 Results

4.4.1 Confirmation of the intrinsic nature of the RV variations

From the 46 spectra acquired prior to the HARPS fiber change in 2015, two (BJD = 2454323.471811, BJD = 2454349.472032) were found to be strong outliers in the dLW time series. These have dLW = 96.6 and dLW = 96.4, respectively, while the dLW time

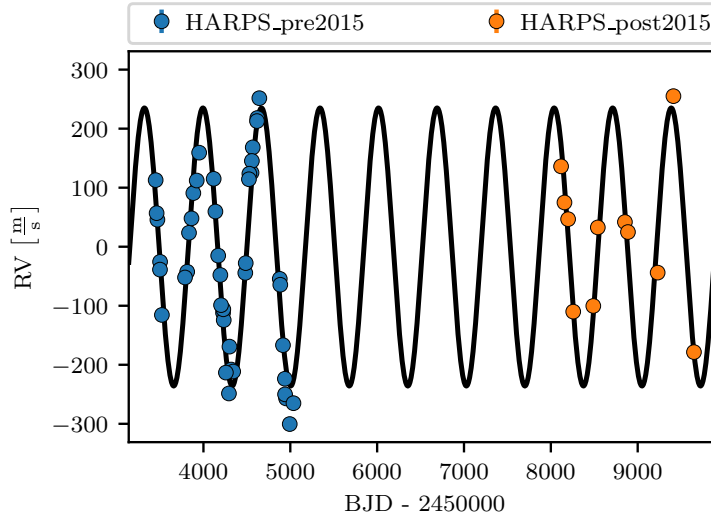


Fig. 4.2.: RVs reduced by SERVAL prior to (blue) and after (orange) the HARPS fiber change in 2015 plotted against time. The error bars are smaller than the size of the markers. A sinusoidal fit is plotted in black and reveals the RVs to be consistent with a long-lived, coherent signal that could (when examined in isolation to other diagnostics) be attributed to a brown dwarf orbiting the primary.

series for the other spectra varies between -21 and 24 . These two spectra were discarded from all time series. We note that the two data points do not have particularly low S/N and are not conspicuous in the RVs or any of the other activity indicators. It remains unclear, why the two spectra are strong outliers in only one indicator.

Another strong outlier (BJD = 2458849.842858) in the RV time series was removed from the 12 spectra acquired after 2015. Again, it remains uncertain why the spectrum deviates strongly in the RVs. It has sufficient S/N, albeit slightly below average.

The remaining 44 spectra taken before the fiber change and 11 spectra taken after the fiber change are plotted in Fig. 4.2 as blue and orange data points, respectively. We treated the two data sets independently and fitted for an offset. We plot a fitted sinusoid with period $P = 674.0 \pm 0.1$ d in black to illustrate that the RV signal is consistent with a periodic variation stable over at least fifteen years. This RV variation by itself could easily be attributed to an orbiting companion, which was however shown not to exist by Delgado Mena et al. (2018, 2023), based on significant periodicity of the FWHM of the CCF close to the proposed orbital period. Delgado Mena et al. (2018) further report periodicity of the $H\alpha$ index close to the orbital period but with a false alarm probability (FAP) less significant than 1.0%, which is further reduced in significance when including the spectra acquired after 2015 (Delgado Mena et al., 2023). Moreover, the authors find a weak but significant correlation between $H\alpha$ and RV.

With the additional activity indicators available through the SERVAL and RACCOON reductions, we can strengthen these findings. Figure 4.3 shows a generalized Lomb-

Scargle (GLS) periodogram (Zechmeister & Kürster, 2009) of the 44 spectra acquired prior to the HARPS fiber change and reveals that the RV periodicity in the pre 2015 data set (red dashed line) is accompanied by further significant peaks of the activity indicators close to the orbital period. Besides the FWHM, also the contrast of the CCF and the dLW of the SERVAL reduction show strong peaks more significant than the $FAP = 0.1\%$ level, which was determined via bootstrapping with 10 000 reshuffles. The peak in the contrast GLS is slightly offset at $P = 645.4$ d.

Both the $H\alpha$ - and the CRX-periodograms furthermore have peaks at the orbital period, or slightly offset in case of the CRX ($P = 645.4$ d). While both peaks are formally less significant than the $FAP = 5\%$ level, the fact that they appear very close to the RV period and are the largest peak in their respective periodograms is certainly not a coincidence and indicates a signal at the RV period in $H\alpha$ and CRX. Only the BIS periodogram is inconspicuous. Taken together, the additional spectral diagnostics strengthen the findings by Delgado Mena et al. (2018, 2023), rule out a physical companion, and thus confirm the intrinsic origin of the RV variations.

4.4.2 Correlations between the activity indicators and the RVs

To find an alternative explanation for the radial velocity variations, we searched for correlations between the activity indicators and the RVs. Figure 4.4 shows the CRX, dLW, contrast, and FWHM of the CCF plotted against the RV for the 44 HARPS spectra taken prior to the 2015 fiber exchange. For all indicators, we plot the absolute deviation from the mean value, which was determined by fitting sinusoids and determining the offset, to allow an easier comparison with the simulated variations.

All data points in Fig. 4.4 are color-coded with the RV period $P = 674.0$ d present in the full data set (including the spectra taken after 2015). It is evident from the top left panel that the CRX is positively correlated with the RV with a Pearson's r value $r = 0.54$ with p-value $p(r) = 0.015\%$. We fitted a linear relation using orthogonal distance regression and perform an F -test (Fisher, 1925) to validate the relation's significance against a constant model, resulting in a p-value $p(F\text{-test}) = 0.002\%$. Following Tal-Or et al. (2018) and Benjamin et al. (2018), we regard the correlation as significant. As Delgado Mena et al. (2023), we further note a significant positive correlation of the $H\alpha$ index with the RV with $r = 0.48$ and $p(F\text{-test}) = 0.2\%$ (shown in Fig. B.1).

Furthermore, we observe closed-loop correlations with the RV for the dLW, contrast, and FWHM of the CCF. That is, the activity indicators correlate elliptically with the RVs with each data point's position on the ellipse given by the phase of the variation, indicated by the color-coding. Such ellipses are effectively Lissajous curves resulting from sinusoidal variations at the same period but with different amplitudes and phase shifts close to $\frac{\pi}{2}$.

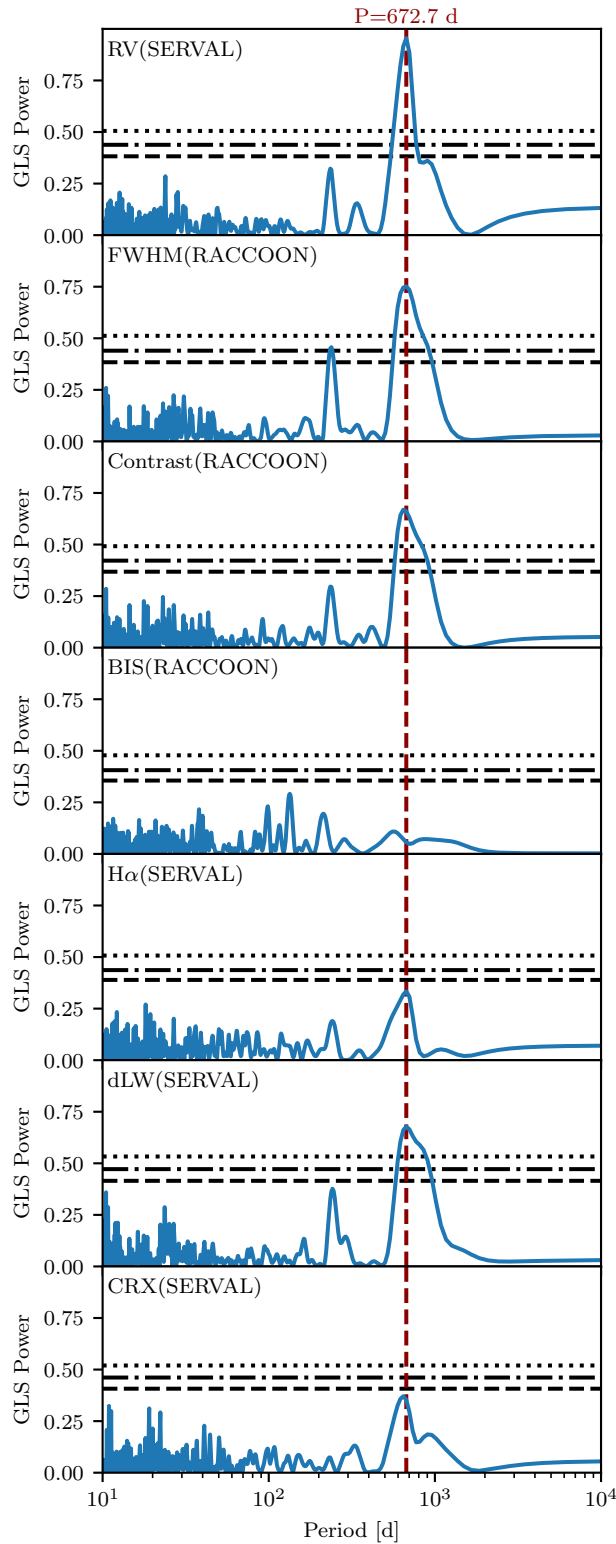


Fig. 4.3.: GLS periodograms of the RVs and activity indicators calculated for the 44 HARPS spectra acquired prior to the fiber change. The FAP of 5% (dashed line), 1% (dash-dotted line), and 0.1% (dotted line) were determined using a bootstrap with 10 000 reshuffles and are plotted for each panel. The strong RV periodicity at $P = 672.7$ d is accompanied by significant periodicity of the FWHM and contrast of the CCF and the dLW. The $H\alpha$ indicator of the SERVAL reduction and the CRX show peaks at or very close to the orbital period that, however, have FAP > 5%. The BIS is inconspicuous.

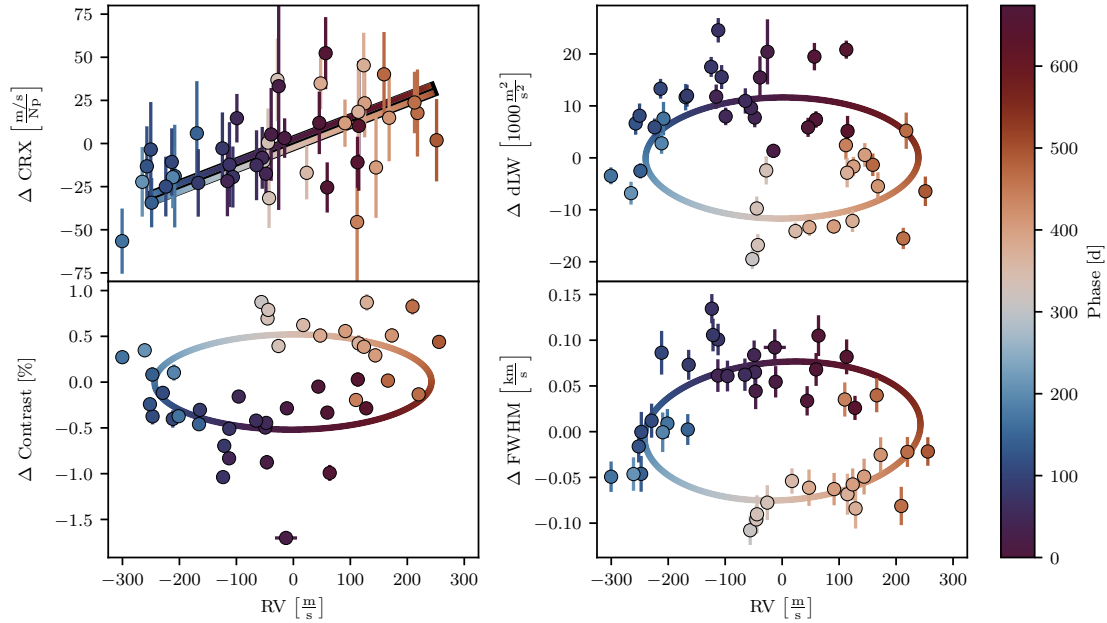


Fig. 4.4.: Observed (data points) and simulated (lines) correlations between the activity indicators and the RVs for 44 spectra taken prior to the HARPS fiber change. For each panel, the mean (RV and any of the indicators, respectively) was subtracted. Each data point is color-coded with the phase according to the best RV period $P = 674.0$ d. While the CRX (top left) shows a significant positive correlation with the RVs ($r=0.54$, $p(F\text{-test}) = 0.002\%$), dLW, FWHM, and contrast of the CCF are correlated with the RVs in a closed-loop behavior. We plot the linear (CRX) and elliptical fits (dLW, FWHM, contrast) to the simulated data points for the best model of a $l = 1, m = 1$ oscillation mode as solid lines applying the same color-coding. As a linear relationship is predicted between CRX and RV, we plot the ascending and descending phase relations on top of the black fit to the simulations. The simulated ellipses can closely reproduce the observed behavior including the amplitudes, phases, and directions of correlation.

The color-coding further reveals the direction of correlation, which is anti-clockwise for FWHM and dLW but clockwise for the contrast, which is to be expected as FWHM and contrast should be inversely dependent on each other. We note that the dLW measures a similar line variation as the FWHM and the contrast and should therefore not be regarded as an entirely independent indicator (Zechmeister et al., 2018; Jeffers et al., 2022). However, as the results stem from different reduction pipelines (RACCOON vs SERVAL) with different approaches to derive the RVs, it is reassuring that we find a similar behavior for both reductions.

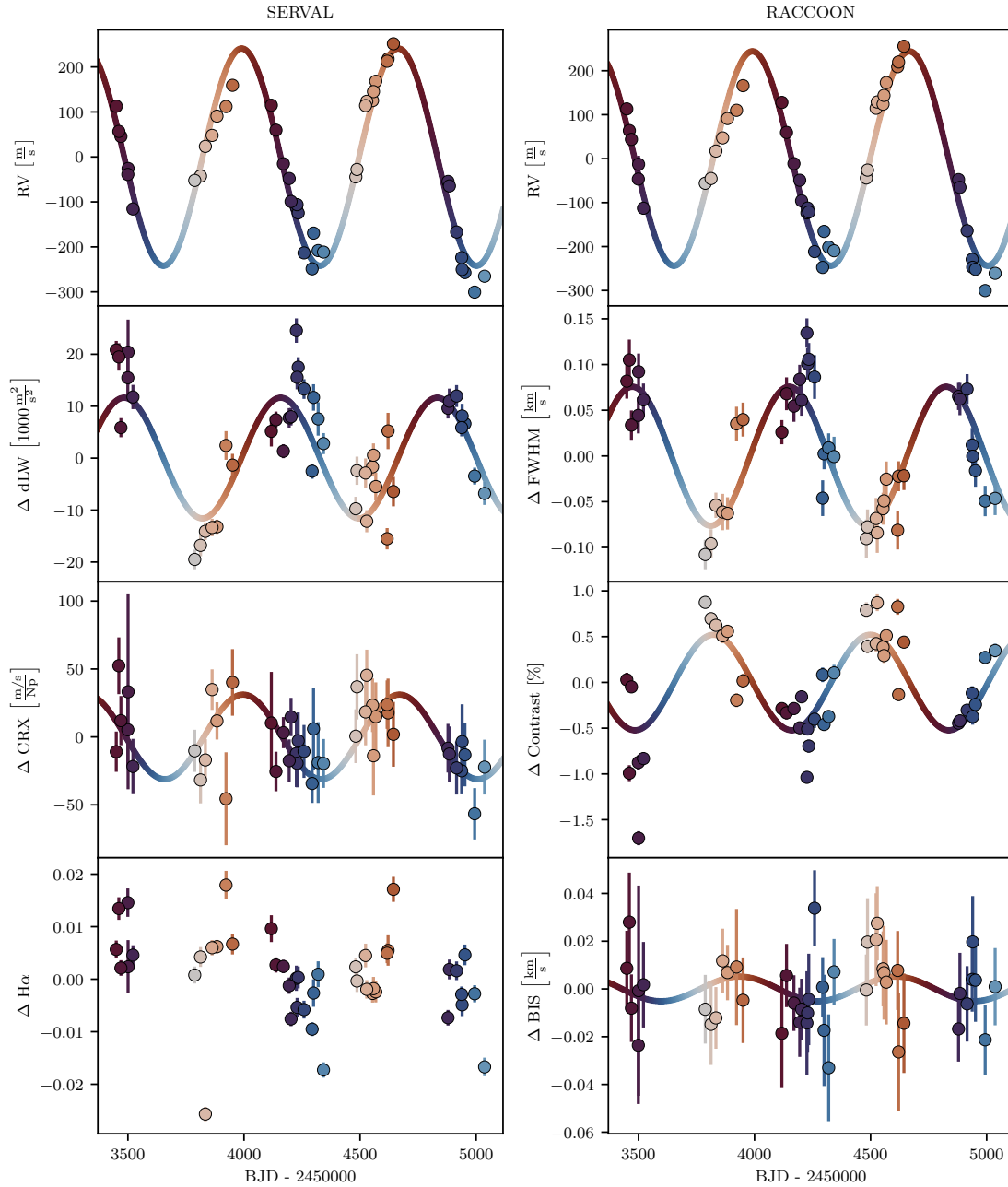


Fig. 4.5.: Observed (data points) and simulated (lines) RVs and activity indicators of the 44 HARPS spectra acquired prior to 2015 plotted against time. The same color-coding as in Fig. 4.4 was applied. The mean RV was subtracted from both the SERVAL and RACCOON RV time series, as well as the mean of each indicator time series. The color-coded solid lines are sinusoidal fits to the simulated spectra computed for the best $l = 1, m = 1$ mode. The simulation is able to reproduce the amplitudes and phases of all indicators, although some (real) indicators suffer from large scatter. As the simulations focus solely on the stellar photosphere, no meaningful variation of the $H\alpha$ indicator can be simulated.

4.4.3 Simulation of a dipole, retrograde ($l = 1, m = 1$) oscillation mode

In order to explain these peculiar correlations, we simulated a set of models using the `pyoscillot` simulation suite detailed in Sect. 4.3. Motivated by oscillatory convective modes as published by Saio et al. (2015), we tested different configurations for dipole ($l = 1$) modes using the stellar parameters ($T_{\text{eff}} = 4500$ K, $\log g = 2.0$, $[\text{Fe}/\text{H}] = 0.0$, $\zeta = 4822$ m s⁻¹) for the base spectrum as discussed in Sect. 4.2.

We include the chromatic effect of limb darkening and the effect of convective blueshift. For the latter, we calculated the CCF bisectors for all measured bisectors of giant stars from Gray (2005) and compared them to the observed CCF bisectors for NGC 4349 No. 127. The best match was found for the bright giant star β Boo. We note, however, that the inclusion of the convective blueshift plays a minor role in modeling the relative variations of the activity indicators and mostly provides an offset for the absolute value of the BIS.

Using the RV period and the stellar properties, the ratio between the horizontal and radial oscillation components can be estimated as $K = 1856 \pm 404$. Therefore, the oscillation is dominated by the horizontal components, such that the product $K \cdot v_{\text{osc}}$ is the decisive input parameter and should be interpreted in conjunction (since changes in v_{osc} can be balanced out by changing K). This behavior was confirmed through test simulations. K was fixed to $K = 1856$ when searching for the best fitting parameters.

Initial tests at different inclination angles revealed that retrograde ($m = 1$) modes are the only dipole modes capable of reproducing the observed correlations for NGC 4349 No. 127, as the other allowed modes would either lead to much smaller amplitudes in the indicators ($m = 0$) or to inverse phase relations ($m = -1$). We examine this behavior more closely in Sect. 4.5.1 and focus on $l = 1, m = 1$ modes for the current discussion. We examine the amplitudes for inclination $i = 90^\circ$ (equator-on), which maximizes the amplitude for the $|m| = 1$ modes. We also restrict the models to only include one isolated oscillation mode.

We further find that the scale of the temperature variations δT_{eff} directly influences the amplitudes of all activity indicators and the RV. Nevertheless, as the CRX captures the wavelength dependence of the RV, it is the most sensitive indicator to the δT_{eff} parameter. At the same time, the variations of the CRX are strongly influenced by the chromatic limb-darkening law. At maximum RV, the visible and projected θ and ϕ components of the $l = 1, m = 1$ oscillation are entirely positive. As the RVs are dominated by the horizontal components, the strongest contribution stems from the cells at the limb of the star due to the projection onto the line of sight. The limb darkening suppresses their contribution, such that the overall RV is reduced compared to a model without limb-darkening correction. However, as the limb-darkening law is chromatic, this reduction is stronger at shorter

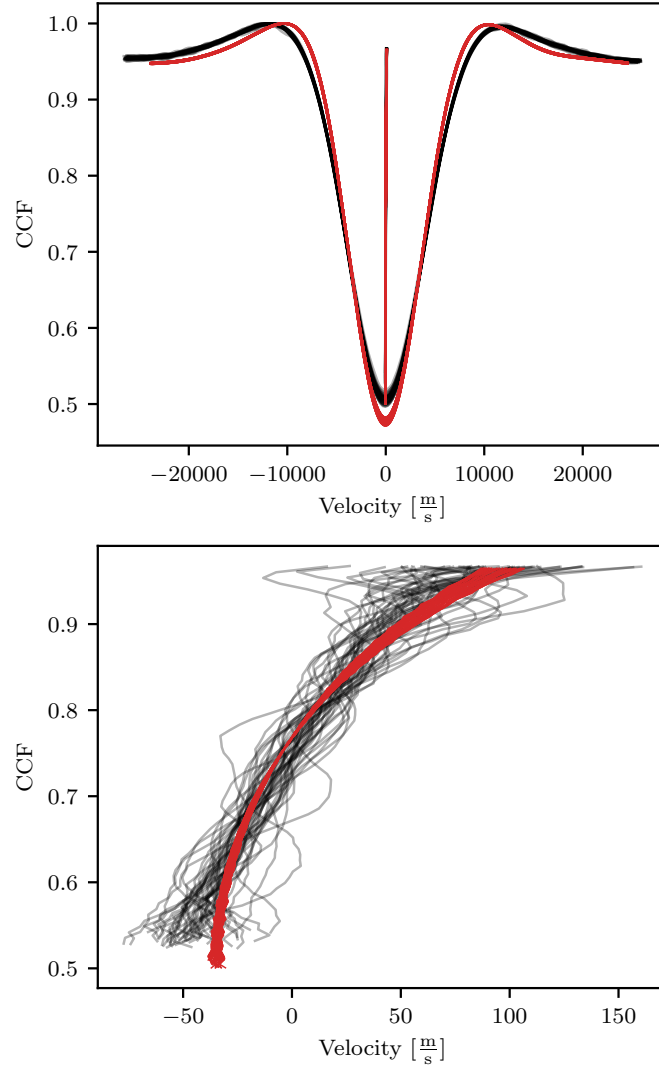


Fig. 4.6.: CCFs and bisector profiles for the observed spectra (black) and the simulated spectra (red). Top: CCFs plotted against the velocity shift for the observed and simulated spectra. The CCFs were shifted with the RV to lie on top of each other. The measured bisector for each line is overplotted. Bottom: Zoomed-in image of the measured bisectors. The simulated bisectors (red) show much less scatter than the observed ones, but generally follow the same rightward trend.

wavelengths, leading to a larger RV at longer wavelength and hence a positive CRX at positive RV. This accounts for the majority of the positive CRX-RV correlation.

Only small temperature variations are therefore consistent with the data, as an increase in δT_{eff} at phase shift $\psi_T = 0$ increases the CRX-RV slope. However, at such small scales the scatter within the data complicates an exact determination. We therefore estimated a value $\delta T_{\text{eff}} = 2.5$ K predicted for an oscillatory convective mode as presented in Fig. 6 of Saio et al. (2015). We determined this value based on the luminosity of the star and

Tab. 4.2.: Parameters used for the retrograde dipole oscillation model.

Parameter	Value
T_{eff}	4500 K
$\log g[\text{cm s}^{-2}]$	2.0
$[\text{Fe}/\text{H}]$	0.0
l	1
m	1
P	674.0 d
v_{osc}	0.30 m s^{-1}
K	1856
v_{rot}	1700 m s^{-1}
ζ	4822 m s^{-1}
δT_{eff}	2.5 K
ψ_T	0°
i	90°
N_{grid}	150×150

the radial amplitude that minimized the residuals between the simulations and the real data for the other observables. We note that the models presented by Saio et al. (2015) at the luminosity of NGC 4349 No. 127 are only available for lower stellar masses. A higher temperature variation is therefore possible.

For small temperature variations, the simulations become rather insensitive to small deviations of the phase shift between the temperature variation and the radial displacement, given the scatter in the real data. This phase shift is predicted to be small, $\psi_T \lesssim 0.1 \cdot \pi$ (Saio et al., 2015). We therefore fixed this value to $\psi_T = 0$, such that the temperature is largest when the radial displacement is at its maximum.

With these initial considerations, we ran a large number of models varying v_{rot} and v_{osc} , finally selecting the model (by eye) that minimizes the residuals between the simulations and the real data for all observables. We simulated 40 synthetic spectra spread over the time span of the real observations (prior to the fiber change) and reduced these using SERVAL and RACCOON. We find that the amplitudes of the activity indicators and the RVs and their phase relations are reproduced using $v_{\text{rot}} = 1700 \text{ m s}^{-1}$ and $v_{\text{osc}} = 0.30 \text{ m s}^{-1}$. We summarize the best values for all simulation parameters in Table 4.2.

4.4.4 Comparison between the data and the oscillation model

Equipped with the non-radial oscillation model, we compare the observed correlations with the simulated ones in Fig. 4.4. The aim is to test whether such an oscillation is able to explain the observed behavior.

The oscillation model predicts a positive correlation between CRX and RV (top left panel). We fitted the correlation with a linear relation and determined the slope $m_{\text{sim}} = 0.129 \pm 0.001 \text{ Np}^{-1}$ (black line). The overplotted, colored lines encode the phase information on the linear relation. The simulated data points deviate only marginally from the linear relation and were left out for visual clarity. The slope is consistent with the actual slope measured for the real data $m_{\text{real}} = 0.101 \pm 0.021 \text{ Np}^{-1}$ with a deviation of 1.3σ .

For the dLW, contrast, and FWHM, closed-loop correlations very similar to the observed correlations are predicted. We plot fitted ellipses to the simulated indicator-RV correlations that closely follow the synthetic data points (which were therefore left out for visual clarity) in Fig. 4.4, applying the same color-coding. An offset for the RV zero points was fitted and removed between the real and synthetic data sets. We stress again that we show the absolute deviation from the respective mean of each time series. The absolute values between the FWHM and contrast of the CCF of the real and synthetic observations are slightly offset as not all influences can be modeled adequately.

We also had to downscale the simulated dLW variations by a multiplicative factor of 0.098 to match the real dLW variations. As the dLW is a differential quantity sensitive to the second derivative of the SERVAL templates, which are separate for the real and simulated data sets, such a multiplicative factor is expected when comparing separate dLW time series (Zechmeister et al., 2018). We find that the scaling factor is on the order of unity when using the same template for both reductions, which however reduces the precision of individual RV and indicator determinations. The multiplicative factor is presumably caused by the (slightly) different widths of the real and simulated spectral lines (see also Sect. 4.4.5). It is furthermore linked to deviations from the assumption of Gaussian spectral lines due to the oscillation, which are fundamental to the definition of the dLW (Zechmeister et al., 2018). We note that, due to this scaling factor, the amplitude of the dLW holds little quantitative information. The phase relation with the RV, however, holds valuable information to validate the simulations.

It can be seen from Fig. 4.4 that all variations of the activity indicators, the relative phases, and the directions of correlations are well reproduced. We tested whether radial, p-mode (solar-like) oscillations can explain the residual scatter present in the activity indicators. From the residual scatter in the RVs, we calculated associated temperature variations of $\delta T_{\text{eff}} \sim 0.9 \text{ K}$ using the scaling relations by Kjeldsen & Bedding (1995). Fine-tuning v_{osc} to reproduce the residual scatter in the RVs, we find that the activity indicators are in principle sensitive to the p-mode oscillations, but the amplitudes are too small to explain the observed residuals. We assume that instrumental effects and other intrinsic, stellar noise sources, such as granulation, dominate the residual scatter.

The CRX is sensitive to the wavelength dependence of the RVs and thus to temperature variations on the stellar surface, as well as the limb-darkening coefficients. We find the interplay of limb darkening and the oscillations to be the dominating influence. As

the limb-darkening contrast decreases toward redder wavelength and the resulting RV is dominated by the horizontal components at the limb of the star, the resulting RV amplitude is larger in the redder part of the spectrum and hence the CRX is positively correlated with the RV. Its slope is commonly referred to as chromaticity (Zechmeister et al., 2018).

In comparison, the temperature variations have only minor influence on the observed CRX-RV slope. If we simulate an (unphysical) oscillation model setting $\delta T_{\text{eff}} = 0$ K, the resulting slope of the CRX-RV correlation is reduced slightly to $m_{\delta T=0K} = 0.1213 \pm 0.0003 \text{ Np}^{-1}$, even closer to the real correlation. A limb-darkening model adapted to the stellar parameters of NGC 4349 No. 127 could therefore be beneficial, but is beyond the scope of this work.

The variations of the line shape indicators (dLW, FWHM, contrast) are mainly influenced by the interplay between the oscillation at the edge of the stellar disk (for which the dominating horizontal components are most directly oriented along the line of sight) and the rotational broadening. This can be easily understood as the oscillation velocities at the limb directly affect the flanks of the broadened spectral lines, thus introducing variations of the line width and depth, or introducing asymmetries.

Figure 4.5 shows the RV and indicator time series data acquired pre 2015. We fitted sinusoids to the simulated time series and color-code these in the same way as the real data. The simulations are able to reproduce the amplitudes and phases of the RVs and all activity indicators, although large scatter is present in some of the real indicators. We note that the simulations also predict small variations of the BIS at the same period as the RVs that are consistent with the observed data, thus adding another argument in favor of the oscillation model. Large errors and high scatter in the real data likely obscure these variations, so that they are not detected in the GLS periodogram search in Fig. 4.3.

No meaningful $H\alpha$ variations can be predicted by the models since the simulations focus solely on the stellar photosphere, while the $H\alpha$ variations are mostly caused by chromospheric processes (Kürster et al., 2003). Whether such chromospheric (and likely magnetic) processes could be linked to the oscillations is unknown. We note that similar connections between stellar oscillations and magnetic fields have been proposed (see, e.g., Lèbre et al. 2014; Georgiev et al. 2023; Konstantinova-Antova et al. 2024).

4.4.5 Cross-correlation profiles

In Fig. 4.6 (top), we plot the real, observed CCF profiles from the RACCOON reduction for NGC 4349 No. 127 (black) as well as the modeled profiles (red). While the CCF shapes are reasonably well reproduced, slight differences in the absolute values of the CCF width (FWHM) and its contrast remain. We therefore plot the differences from the respective means in Fig. 4.4 and Fig. 4.5.

Offsets between the simulated and the real CCF profiles are to be expected as not all influences can be modeled accurately. These include the real instrumental profile of the HARPS spectrograph, which we model as a Gaussian, and the intrinsic line shapes inherent to the PHOENIX models. These are given with fixed microturbulent broadening values for each model. For the base PHOENIX model employed in the simulation, microturbulence $\xi = 1.49 \text{ km s}^{-1}$ was used, somewhat lower than expected for our star (see Table 4.1). Due to these inherent differences, the line shapes cannot be reproduced accurately.

We also find that the rotational velocity v_{rot} plays an important role in reproducing the amplitudes of the line shape indicators (dLW, FWHM, contrast), with higher rotation velocities generally producing larger variations. At the same time, v_{rot} influences the absolute width of the CCF profile. We find a smaller rotation velocity ($v_{\text{rot}} = 1.7 \text{ km s}^{-1}$) to be generally in good agreement with the observed variations for NGC 4349 No. 127. We note that more recent determinations of the star's rotation velocity are larger (see Table 4.1), but find good agreement with the rotation velocity determined by Carlberg et al. (2016). However, due to the inherent differences of the PHOENIX spectra to the real spectrum of the star, we caution against using this value as a determination of the rotation velocity of NGC 4349 No. 127.

The bottom panel of Fig. 4.6 portrays a zoomed-in image of the calculated bisector profiles. We observe that the general bisector shape is well reproduced by the convective blueshift model based on β Boo (Gray, 2005). However, we find the bisector shape to have negligible effect on the observables presented in Fig. 4.4 and Fig. 4.5, apart from providing an offset for the absolute value of the BIS.

4.4.6 Photometric variations

For many types of intrinsic variations manifested in RV data, such as stellar spots or radial oscillations, photometric variability is expected and can provide independent constraints on their properties (see, e.g., Hojjatpanah et al. 2020). One V-band photometric data set, already discussed by Delgado Mena et al. (2018), is available for the star from the All Sky Automated Survey (ASAS) at Las Campanas Observatory (Chile) (Pojmanski & Maciejewski, 2004). We use only grade A and B results as suggested by Delgado Mena et al. (2023).

In Fig. B.2 (top), we plot the ASAS-3 data (dots) against time. We overplot binned data points (black rectangles) with bin size 67.4 d (10% of the RV period) to add some visual clarity. There is significant scatter at the ~ 0.1 mag level, albeit without obvious periodicity. We overplot the predicted V-band variations from the simulated dipole oscillation caused by the temperature fluctuations. These were derived by integrating the product

of the simulated spectra and the Bessel V-band filter curve¹¹ and rescaling to the median magnitude present in the ASAS-3 data set. The simulations predict a sinusoidal variation at the RV period with an amplitude of 0.003 mag. This lies well below the average ASAS-3 error for NGC 4349 No. 127 of 0.051 mag and below the scatter present in the ASAS-3 data set. It would therefore be plausible that the photometric variation stemming from the oscillation would not be detected by the ASAS-3 photometry. We thus conclude that the available photometry does not argue against the oscillation hypothesis. We discuss the available photometry in more detail and comment on the findings by [Delgado Mena et al. \(2018\)](#) in Sect. B.2.

ASAS-3 is reported to achieve a differential accuracy of 0.01 mag for ideal, bright targets ([Pojmanski & Maciejewski, 2004](#)), which is still larger by a factor of 3 than the photometric amplitude predicted by the simulation. The star was further observed in the TESS full-frame images in sectors 11, 37, 38, 64, and 65. However, the short duration of each individual sector, the long gaps between the available sectors, and instrumental offsets between them prevent us from analyzing the TESS photometry on timescales similar to the RV period. Future *Gaia* data releases might provide the necessary photometric precision and timescales to detect such variability.¹² However, as the star is relatively bright, systematic effects might hinder this analysis.

The calculation of the photometric variability is based solely on the temperature variations on the stellar surface, neglecting surface-area and surface-normal variations. The latter are small at the velocity amplitudes considered but would violate the assumption of spherical symmetry of the star, complicating the calculation of the velocity fields. Given the small amplitudes, we find this simplification justified.

We note, however, that [Townsend \(1997\)](#) argues to include surface-area and surface-normal variations when predicting photometric variations of non-radial oscillations. However, the oscillation amplitudes considered are much larger than in the case of NGC 4349 No. 127 and their K values range between 0 and 1. The differences between simulations considering these geometrical surface variations and those that do not (see their Fig. 6) seem to become less pronounced toward larger K (as in our case). The surface-normal variations mainly act to avoid an unphysical photometric minimum at $K \sim 0.85$ with the differences being on the order of a factor 2 to 3 otherwise. It can therefore be assumed that the overall photometric variability would not be affected enough to be easily detectable by the ASAS-3 photometry.

With the presented results, we show that a retrograde, dipole ($l = 1, m = 1$) oscillation mode is fully consistent with the radial velocity variations and the variations of all studied activity indicators, including the amplitudes and phase relations, as well as the available

¹¹<http://spiff.rit.edu/classes/phys440/lectures/filters/bess-v.pass>

¹²<https://www.cosmos.esa.int/web/gaia/science-performance>

photometry. We therefore conclude that non-radial oscillations are indeed present in the star and cause the observed periodic patterns.

4.5 Other oscillation modes

Having established that a retrograde $l = 1$ mode is able to reproduce the observables, we further aim to qualitatively address the question whether, alternatively, other oscillation modes are also capable to reproduce the same behavior.

4.5.1 $l=1$ modes

Motivated by the models for dipole oscillatory convective modes presented by [Saio et al. \(2015\)](#), we first study the characteristics of $l = 1$ modes, for which the azimuthal orders $m = (-1, 0, 1)$ are possible. We chose the same parameters as presented above, aiming to understand the qualitative differences for the different modes. We simulated the different oscillation modes at 20 epochs each.

We first note that different modes have different inclination angles at which the RV amplitudes are maximized or minimized. In case of the $l = 1$ modes, the RV amplitudes are maximized when viewed equator-on ($i = 90^\circ$) for $|m| = 1$, while the $m = 0$ mode has maximum RV amplitude when viewed pole-on ($i = 0^\circ$) ([Chadid et al., 2001](#); [De Ridder et al., 2002](#)). We therefore ran the simulations at different inclination angles and present the intermediate inclination angle $i = 45^\circ$, for which the amplitudes for the $|m| = 1$ and $m = 0$ modes are comparable.

Figure 4.7 shows the results for radial velocity (top left) and the spectral diagnostics for the $l = 1, m = -1$ mode (red), $l = 1, m = 0$ mode (black), and $l = 1, m = 1$ mode (blue) plotted against time. We fitted sinusoids to the variations (except for FWHM, dLW, and contrast in the case of $m = 0$) to highlight the phase relations. The differences between the exact simulated data points and the sinusoids are negligible.

We first note that all three modes are capable of producing RV variations with similar amplitudes and would thus, in principle, be able to explain the RV variations for NGC 4349 No. 127. While the $|m| = 1$ modes are in phase, the $m = 0$ mode is phase-shifted. However, we note that an artificial phase shift can be added (and was used to match the retrograde mode with the real observations) to match the $m = 0$ mode to the real RVs.

What cannot be altered, though, are the phase relations between the RV and the spectral diagnostics. First, we observe that for the line shape diagnostics (FWHM, dLW, contrast) the $m = 1$ and $m = -1$ modes are roughly in antiphase with each other. The $m = 0$

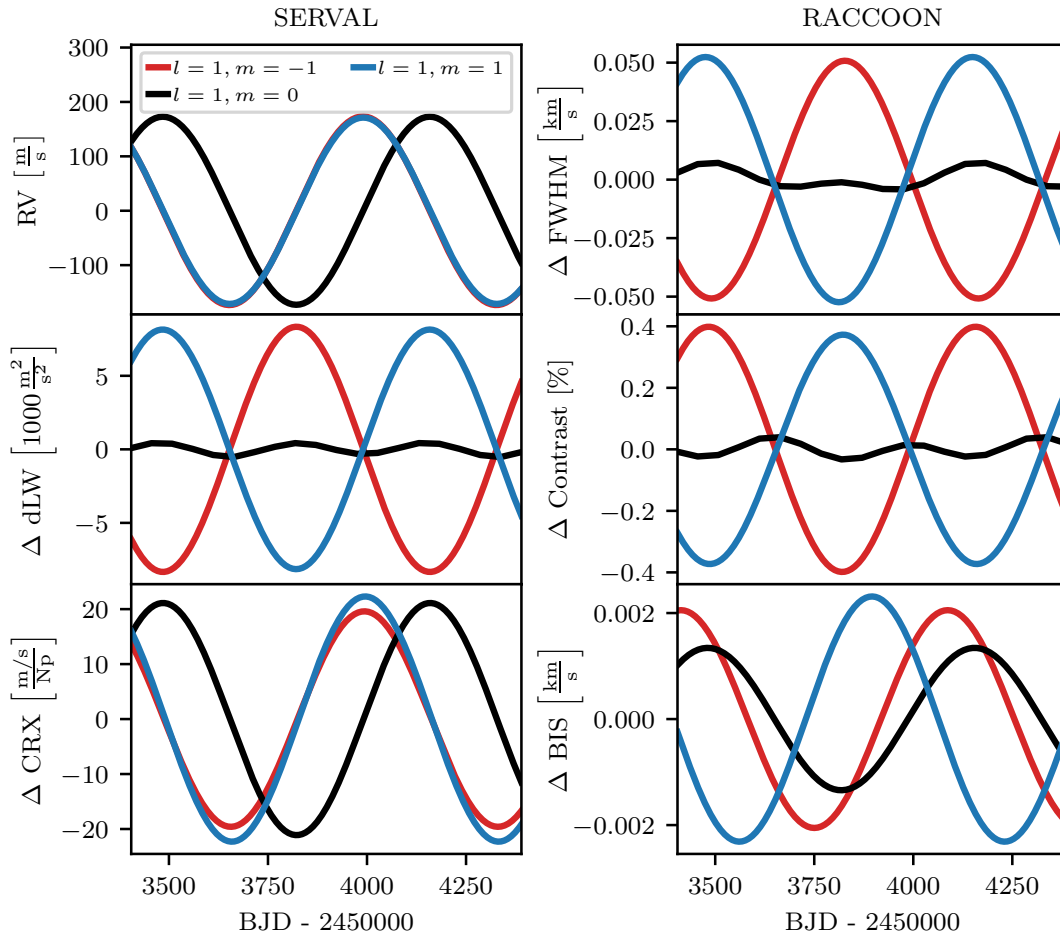


Fig. 4.7.: RVs and activity indicators of dipole oscillation modes plotted against time at inclination angle $i = 45^\circ$. Sinusoids were fitted to all time series except for the FWHM, dLW, and contrast in case of $m = 0$, for which the simulated points were interconnected. While all three modes cause similar RV variations (top left panel), the phase relations between the RVs and the line shape indicators, as well as their amplitudes, are notably different. The CRX (bottom left) shows a similar behavior for all three modes. The dLW variations were rescaled with a common factor of 0.1.

mode shows much smaller line shape variations that are not perfectly sinusoidal (and therefore presented here by connecting the simulated data points) and, most notably, vary at roughly half the RV period. The behavior can be explained as the azimuthal (ϕ) component of the axisymmetric $m = 0$ mode is in all cases 0. Thus, the interplay between the ϕ oscillation component and the rotation vector, which causes the majority of the line shape variations as it influences the flanks of the rotationally broadened line profiles, is not present in the $m = 0$ mode. The now solely dominating θ component of the $m = 0$ oscillation is symmetric with respect to the rotation axis and thus leads to much smaller line shape variations.

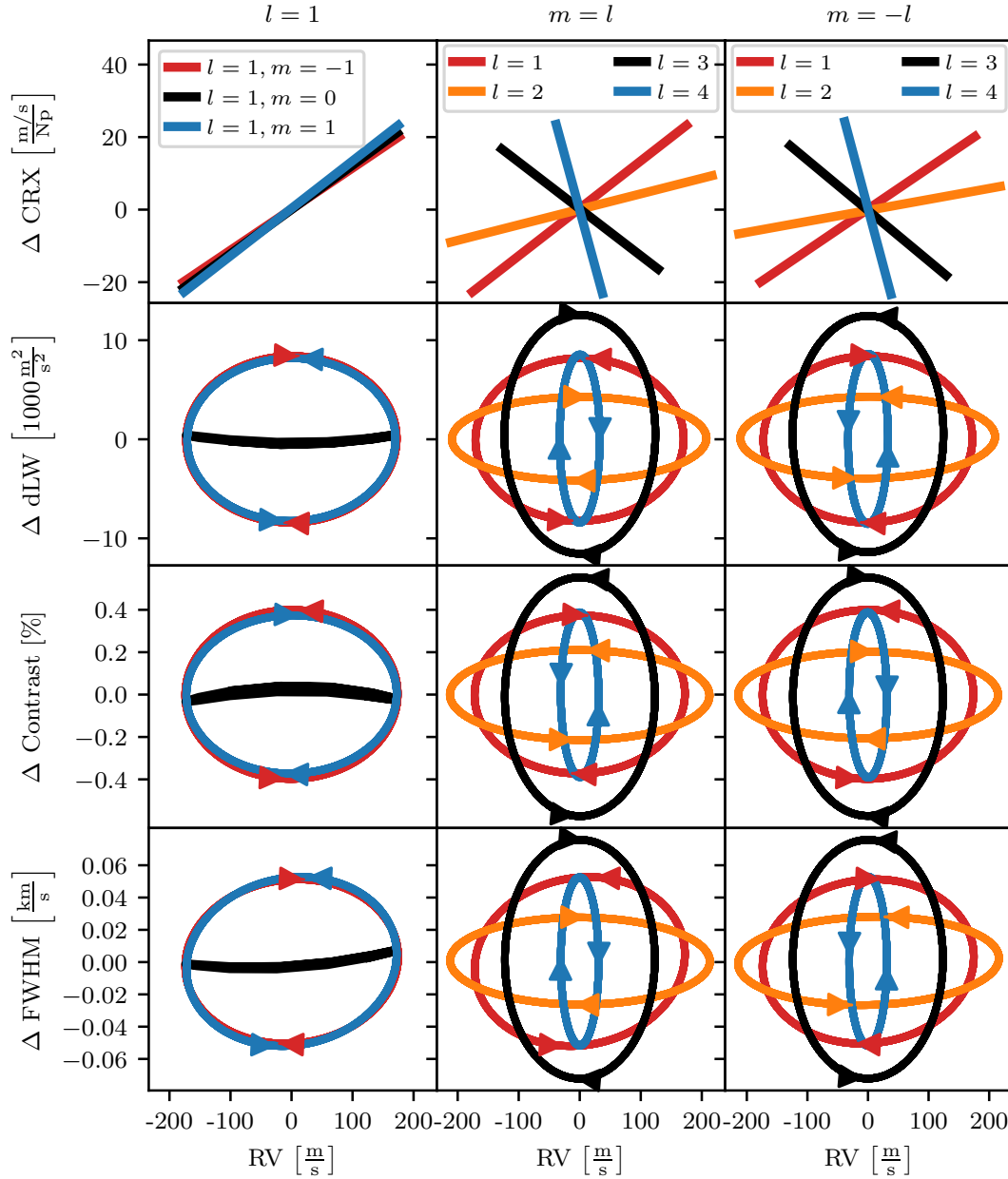


Fig. 4.8.: Correlation plots between the activity indicators and the RVs for modes with $l = 1$ (left column), $m = l$ (center column), and $m = -l$ (right column). Linear correlations were fitted for the correlation between CRX and RV. For the line shape diagnostics, ellipses were fitted when appropriate. Arrows indicate the temporal dependence of the ellipses. The individual modes are specified in the legend at the top of each column. The simulated dLW variations were rescaled with a common factor of 0.1.

We also show the phase relations and their directions of correlations in Fig. 4.8 (left column). The dLW, contrast, and FWHM are plotted in the bottom three panels, respectively. We fitted ellipses to the correlations and present the direction of correlation when

appropriate. Figure 4.8 reveals that both $|m| = 1$ modes create closed-loop correlations, while the $m = 0$ mode leads to an “arc-like” correlation, clearly not consistent with the real data for NGC 4349 No. 127.

For the two $|m| = 1$ modes, we note that the time dependence of the correlation is reversed (indicated by the arrows), a consequence of the phase shifts of the line shape indicators in Fig. 4.7. While the retrograde $m = 1$ mode shows an anti-clockwise correlation for the dLW and FWHM (and therefore clockwise for the contrast, as for NGC 4349 No. 127), the prograde $m = -1$ mode correlates with a reversed time dependence and thus cannot explain the real variations.

It is furthermore evident from Fig. 4.7 (bottom left panel), that the CRX is in all cases roughly in phase with the RV with only slightly different amplitudes. These lead to similar positive correlations between CRX and RV in Fig. 4.8 (top left panel). The similarity of the CRX variations stems from the fact that the wavelength-dependent limb darkening in interplay with the horizontal components at the limb of the star is dominating the CRX amplitude. The CRX variation is therefore, for all $l = 1$ modes considered, in phase with the RV variation. This relation holds true as long as the temperature variation δT_{eff} is small. The CRX-RV correlation thus seems to be a sensitive indicator for the l -mode.

The slight differences in the CRX amplitudes (and therefore the slopes of the correlation) stem from the interplay between the small temperature variation $\delta T_{\text{eff}} = 2.5 \text{ K}$ and the rotational broadening of the spectral lines. That is, the temperature variation by itself has a small effect on the RVs and the CRX, as it slightly increases or decreases the flux from either side of the rotationally broadened line profile, introducing line asymmetries that are measured as RV shifts. As the contrast (flux ratio) between the slightly hotter and cooler halves of the star is less pronounced at longer wavelengths, this effect is wavelength dependent and thus captured by the CRX. For the $m = -1$ and $m = 1$ modes, for instance, the temperature variation is phase-shifted by 180° . Thus, the effect of temperature alone enhances the RV and CRX amplitudes in the $m = 1$ case, while it decreases both amplitudes in the $m = -1$ case. The CRX-RV correlation for the $m = 0$ mode coincides with the effect given by the limb darkening alone.

Figure 4.7 finally presents the BIS variations (bottom right panel). Sinusoidal variations at the period of the RV are predicted for all three m -modes, albeit with different amplitudes and phase relations. However, as the variations for NGC 4349 No. 127 cannot be detected given the noise of the data, no strong conclusion can be drawn from the BIS indicator in this case. All of the above findings are valid at all inclination angles that produce non-zero RV variations for the individual modes.

The fact that $m = 0$ modes lead only to small line shape variations is somewhat discouraging when considering the possibility of applying the same analysis to other evolved stars, suggested to be false positive planet hosts. If an $m = 0$ mode is equally likely, and

considering the typical scatter in the real time series of activity indicators, it seems very challenging to detect the line shape variations predicted for this mode. Only the CRX (and BIS) variation and its correlation with the RV are predicted to be similar as for NGC 4349 No. 127 and could provide the most direct hint for non-radial oscillations in the case of an $m = 0$ mode. However, if stemming from non-radial oscillations, the amplitude of the CRX variations also depend directly on the amplitude of the oscillation velocity v_{osc} . Therefore, identifying oscillations based on the CRX at much smaller RV amplitudes could be challenging with the typical data sets.

In principle, all m -modes can be expected to be excited, albeit possibly at different amplitudes and periods in the presence of rotation. For NGC 4349 No. 127, considering only dipole ($l = 1$) modes, it seems most straight-forward to explain the data with a single $l = 1, m = 1$ mode. In reality though, a combination of all three m -modes could be the most plausible scenario. Such a combination, however, could also be difficult to detect.

If all three m -modes are excited to the same amplitude, and neglecting at first the change in oscillation periods due to rotation, cancellation effects between the $m = 1$ and $m = -1$ modes remove the largest part of the variations present in FWHM, contrast, and dLW (as these are in antiphase for the $m = 1$ and $m = -1$ modes), while resulting in a large RV variation. Only the variations in CRX would likely remain above a detectable threshold, a behavior that we confirmed with test simulations. The resulting RV curves of a combination of all m -modes can be well approximated as the simple sum of the individual RV curves for each mode shown in Fig. 4.7. Therefore, a combination of all three modes at equal and constant amplitudes leads to a phase shift of the RV curve.

In the presence of rotation, the frequencies $\nu_{l,m}$ for different azimuthal quantum numbers m are split (see, e.g., Aerts 2021). This frequency split can be approximated as

$$\nu_{l,m} - \nu_{l,0} = \frac{m}{P_{\text{rot}}} \left(1 - \frac{1}{l(l+1)} \right) \quad (4.10)$$

(Chen & Li, 2017; Brickhill, 1975). For oscillation periods comparable to the rotation period, this can lead to large period changes.

A superposition of sinusoidal signals at different periods and amplitudes can lead to RV curves potentially resembling multi-planetary signals. Moreover, if such signals are insufficiently sampled in context of exoplanet surveys and interpreted as single-planet signals, a change in period, amplitude, or phase of the RV curve might be deduced. This could potentially offer an explanation for the amplitude changes and phase shifts detected in the cases of γ Dra (Hatzes et al., 2018) and Aldebaran (Reichert et al., 2019), although more thorough modeling would be necessary. We also note that a period modulation has recently been reported for some long-period variables showing long secondary periods

(Takayama, 2023). Of course, in the context of oscillations, it is also plausible to assume that the oscillation periods themselves are not constant.

4.5.2 Higher-order l -modes

While Saio et al. (2015) discuss that dipole oscillatory convective modes have properties that resemble the period-luminosity relations of sequence D variable giant stars, higher-order l -modes could also cause false positive planet detections. To understand qualitatively how different quantum numbers l affect the simulation results, we simulated (with the same settings) all possible modes up to $l = 4$.

Motivated by the finding that the $l = 1, m = 1$ is the only dipole mode consistent with the data for NGC 4349 No. 127, we plot the correlations between the indicators and the RV for the $m = l$ modes in the central column of Fig. 4.8. We also show the variations plotted against time in Fig. B.4. As in the previous section, we present the results at the inclination angle $i = 45^\circ$, but note that the results are qualitatively consistent across all inclination angles that produce significant amplitudes in the RVs. We fitted linear correlations for the CRX plotted against RV (top) and elliptical relations for the line shape indicators. All relations follow the simulated data points closely, such that the latter were omitted. Only slight deviations from the linear CRX correlations are present. However, as these are much smaller than the scatter in the real data, we still approximated these with linear relations for visual clarity.

We first note that different RV amplitudes are predicted. While naively one would expect the RV amplitude to decrease for higher-order l -modes due to increasing cancellation effects, the behavior is not as straight-forward for non-radial oscillations dominated by the horizontal components. This behavior can be understood as the partial derivatives in Eq. 4.2 and Eq. 4.3 introduce a factor m that increases the respective amplitudes as well as (slightly) different normalization factors that were introduced in Eq. 4.1. The physical horizontal velocity components therefore differ for different modes with the same input velocity v_{osc} . As v_{osc} is a-priori not well constrained, differences in the RV amplitudes can be overcome when attempting to match a mode to the real data.

Furthermore, sinusoidal variations at the period of the RV are predicted for all indicators. The phase differences between the indicators and the RVs again provide insights to identify the modes. For the line shape indicators FWHM and dLW, the phase shift is positive for the $l = 1, m = 1$ mode, while it is negative for the higher-degree $m = l$ modes. The behavior of the contrast is reversed. This leads to an inversion of the temporal direction of the elliptical correlations in Fig. 4.8. This already disqualifies the higher-degree $m = l$ modes from being consistent with NGC 4349 No. 127.

However, we find the opposite behavior for the $m = -l$ modes, plotted in the right column of Fig. 4.8 and Fig. B.5. For $l \geq 2$, modes with $m = -l$ produce sinusoidal variations with an anti-clockwise correlation for dLW and FWHM with the RV. The amplitudes of these line shape variations generally depend on the oscillation amplitude v_{osc} and the rotation velocity v_{rot} and could therefore (to some extent) be adapted in an attempt to match NGC 4349 No. 127. From this finding alone, these higher-order modes would therefore be able to explain the observables for NGC 4349 No. 127.

Again, we find the CRX to be the most decisive indicator to identify the mode. As presented in the top panels of Fig. 4.8, the CRX correlates linearly with the RV for all modes. However, the slope of the correlation depends critically on the mode. While the dipole $l = 1$ (red) mode has a positive slope very similar to the real data, the $l = 2$ (orange) mode has a decreased but still positive slope. Increasing the quantum number l decreases the slope further, making it progressively negative for $l = 3$ (black) and $l = 4$ (blue). This behavior is nearly identical for both $m = l$ and $m = -l$ modes, and is roughly consistent for all m -modes for the same order l . The same effect is also evident in the phase shifts between the different CRX time series and the RVs in Fig. B.4.

The behavior can be understood due to the geometry of the projected and combined oscillation velocities in interplay with the wavelength-dependent limb darkening. The modes are in all cases dominated by the horizontal components (due to the high K factor). For the low-order $m = l = 1$ mode, maximum RV was reached when the projected ϕ component of the oscillation was fully positive. The wavelength-dependent limb darkening then decreases the overall maximum RV to a larger extent in the blue vs. the red part of the spectrum. This leads to a chromatic RV, captured by a maximum positive CRX at time of maximum positive RV, and therefore the observed positive chromaticity.

For modes with $l = |m| = 3$ and $l = |m| = 4$ the dominating ϕ component facing the observer is never fully positive. Maximum RV is then reached when the central part of the disk is receding from the observer, while at the same time thin strips at the limb of the star have negative RV values. As these thin strips of cells are most affected by the limb darkening, its wavelength-dependent reduction of RV now has the inverse effect. That is, it diminishes the negative parts and thus increases the overall RV. As this effect is more prominent in the blue vs the red, the phase of maximum CRX is now phase-shifted by half a period with respect to the phase of maximum RV. As a consequence, a negative CRX-RV correlation is observed.

The $l = |m| = 2$ mode is intermediate. While the ϕ component can still entirely be positive, the θ component already presents a similar effect as detailed for the $l > 2$ modes. As the θ component is generally smaller in summed projected velocities, this acts only to decrease the CRX-RV slope. Of course, the exact CRX-RV slopes depend on the choice of limb-darkening parameters, but the overall trend can be expected to be insensitive to the exact set of parameters.

To further study this behavior, we simulated even higher l -modes, observing that the slopes start to alternate between uneven (positive slope) and even (negative slope) l -modes, as can be expected from geometrical considerations. However, due to the ever increasing cancellation effects, simulated RV and indicator amplitudes quickly drop and would thus require much larger values of v_{osc} to be detectable.

Finally, we note that these considerations are only valid for small temperature variations (here $\delta T_{\text{eff}} = 2.5 \text{ K}$), for which the limb darkening dominates the chromatic behavior. Increased temperature variations change the CRX-RV slope and thus make mode identification based on CRX measurements ambiguous.

As the overall behavior of the $l = 2, m = -2$ mode resembles the retrograde, dipole mode discussed in Sect. 4.4, we tested whether we could reproduce the data for NGC 4349 No. 127 with this mode. While the CRX-RV correlation can be reproduced with a slightly increased temperature variation $\delta T_{\text{eff}} \sim 4 \text{ K}$, the amplitudes of the line shape indicators, especially the FWHM and contrast of the CCF, were somewhat smaller than presented for the $l = 1, m = 1$ simulation for all sets of parameters considered. However, given the scatter of the real data, they provide a fit nearly as good as presented in Sect. 4.4. Due to the increased rotation velocity ($v_{\text{rot}} = 4.5 \frac{\text{km}}{\text{s}}$), necessary to increase the amplitude of the FWHM variations, and the altered oscillation geometry, the amplitude of the BIS variation is increased by a factor ~ 9.6 compared to Fig. 4.5, yielding a sinusoidal variation slightly larger but still comparable to the scatter in the BIS data. It is unclear whether this signal would have been picked up in the HARPS data set. We therefore cannot exclude the possibility of an $l = 2, m = -2$ mode as the cause of the variations.

In general, we find that most modes with $m \neq 0$ for $l \leq 4$, produce similar sinusoidal variations of the RVs and indicators which lead to elliptical correlation plots with reversed directions for the two opposite m -modes. One exception are $|m| = 1$ for $l \geq 3$ at specific inclination angles that resemble the arc-like correlations for $m = 0$. However, examining this behavior more closely is beyond the scope of this work. The CRX-RV slopes are always very similar for all m -modes for one quantum number l . The $m = 0$ modes always show a similar behavior to the $l = 1, m = 0$ mode presented in the previous section and can thus always be refuted for NGC 4349 No. 127.

4.6 Discussion

The aim of this study was to test whether non-radial oscillations are capable of explaining the variations of the RVs and the activity indicators of the cluster giant NGC 4349 No. 127. With the data and model presented in Sect. 4.4, we can confirm that the variations of the

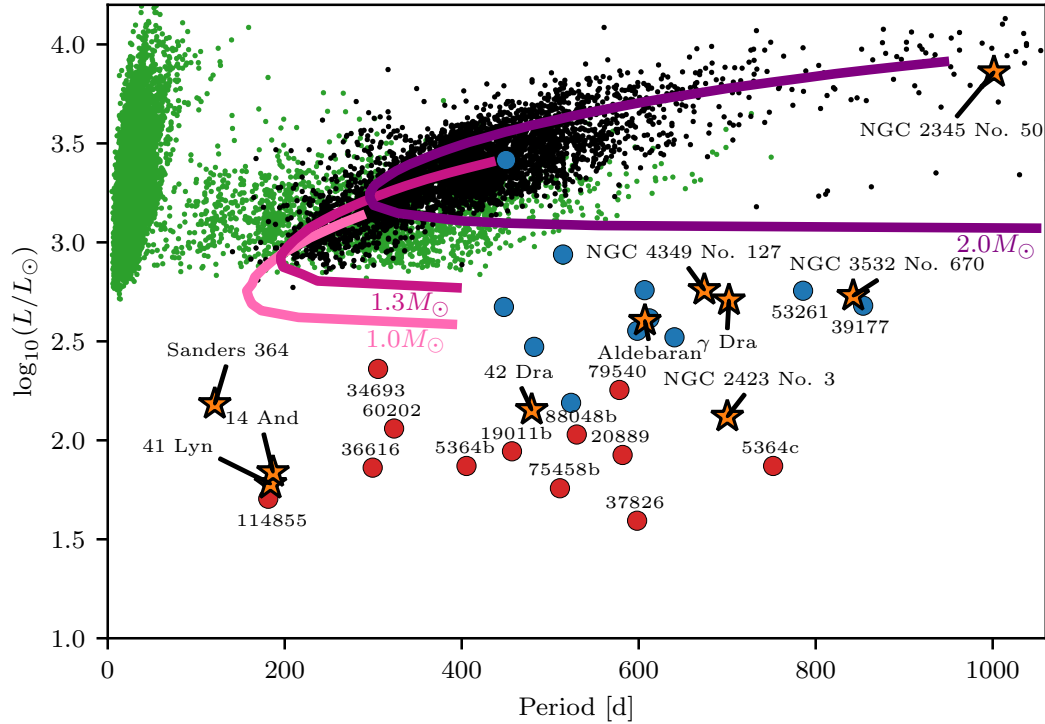


Fig. 4.9.: Period-luminosity plot adapted from Reichert et al. (2019) showing the location of giant stars with RV variations of unknown intrinsic origins (orange star markers). The green dots are photometrically variable giant stars identified by the OGLE survey, while the black dots are the subset of these showing long secondary periods. Overplotted in shades of purple are models of oscillatory convective modes (mixing length parameter of 1.2), as presented by Saio et al. (2015). We also overplot confirmed planets orbiting giant stars from the Lick RV survey (see, e.g., Wolthoff et al. 2022) with their respective HIPPARCOS identifiers in red and (mostly unpublished) planet candidates from the same RV survey in blue. NGC 4349 No. 127 lies in close vicinity to some stars with established intrinsic RV variations, suggesting a common origin for the phenomenon. This impression is further enhanced by the clear separation of the regions in which the confirmed planets and planet candidates fall.

RVs and indicators are indeed of intrinsic origin and are consistent with a model of a retrograde, dipole oscillation mode. Here, we put these findings into the context of previously reported false positive exoplanets and discuss whether the non-radial oscillations could be oscillatory convective modes. We further discuss that magnetic activity, as suggested by Delgado Mena et al. (2018), is incompatible with the observations.

4.6.1 Oscillatory convective modes

In Fig. 4.9, we adapt Fig. 8 of Reichert et al. (2019), showing the location of NGC 4349 No. 127 along with the locations of other giant stars (orange star markers) with established

intrinsic RV variations (some of which were formerly thought to host planets or brown dwarfs) in a period-luminosity plot. We do not include ϵ Cyg, as the RV variations of the star are likely caused by the heartbeat phenomenon (Heeren et al., 2021). Luminosities and periods were taken from the respective publications that refute the planets. For Sanders 364, the luminosity was taken from the *Gaia* DR3 determination of astrophysical parameters (Creevey et al., 2023). We note that Zhou et al. (2023) find RV periodicity at several periods (224 d, 281 d, 333 d, 530 d, 777 d) longer than the published planet period at 121 d by Brucalassi et al. (2014, 2017), such that the position of the star could move significantly parallel to the x-axis of Fig. 4.9.

It is evident that NGC 4349 No. 127 lies in close vicinity to the refuted planet hosts γ Dra (Hatzes et al., 2018) and Aldebaran (Reichert et al., 2019). We also show the locations of variable giant stars in the Large Magellanic Cloud from the OGLE survey (Soszyński et al., 2009) in green and stars which show long secondary periods in black (see Reichert et al. 2019 for details). We further plot the models taken from Saio et al. (2015) for a mixing length parameter of $\alpha = 1.2$.

Overplotted in red are known planets from the Lick survey (see a recent overview in Wolthoff et al. 2022), along with their HIPPARCOS identifiers, and planet candidates identified in the same survey in blue. The latter group has (semi-)periodic RV signatures, but either high RV jitter or otherwise complicated RV curves, which are challenging to model with Keplerian orbits. The two systems HIP 53261 and HIP 39117 were classified as planet candidates by Tala Pinto et al. (2020) and are also listed with their HIPPARCOS identifiers.

There appears to be a perceptible distinction between the groups of confirmed planets on the one hand and planet candidates and false positives on the other. The latter mostly accumulate close to the region with periods between 500 d and 1000 d and luminosities $2.3 \lesssim \log_{10}(L/L_{\odot}) \lesssim 3.2$. We find two refuted planetary systems, 42 Dra and NGC 2423 No. 3, to be quite close to established planet hosts. We also find a group of three false positive planet hosts (Sanders 364, 41 Lyn, 14 And) to be located at much lower luminosities and much shorter periods. As Reichert et al. (2019), we note that increased luminosity is also linked to increased levels of RV jitter, which makes the confirmation of exoplanets more challenging.

However, increased RV jitter alone cannot explain the individual cases of most refuted planet systems, which show large-amplitude RV variations, such as the star discussed in this work. As Hatzes et al. (2018) and Reichert et al. (2019) argue, if one were to extend the low-mass models of oscillatory convective modes toward longer periods, they would presumably cross the region covered by Aldebaran, NGC 4349 No. 127, γ Dra, and NGC 3532 No. 670. Another cluster giant, NGC 2345 No. 50, appears to be close to the high-luminosity end of the Saio models. 42 Dra, NGC 2423 No. 3, Sanders 364, 41 Lyn, and 14 And seem to have luminosities that are too low to be in good agreement with the

Saio models. As the last three also exhibit shorter periods, one can suspect that another mechanism could be present in these stars, such as the rotational modulation of stellar spots as suggested by [Teng et al. \(2023b\)](#).

We also note that many of the stars with longer-period RV variations, including NGC 4349 No. 127 ($M = 3.01 \pm 0.24 M_{\odot}$), are significantly more massive than predicted by the Saio models. These include γ Dra ($M = 2.14 \pm 0.16 M_{\odot}$; [Hatzes et al. 2018](#)), NGC 3532 No. 670 ($M = 3.05 \pm 0.23 M_{\odot}$), NGC 2423 No. 3 ($M = 2.03 \pm 0.14 M_{\odot}$), and NGC 2345 No. 50 ($M = 5.84 \pm 0.61 M_{\odot}$) ([Tsantaki et al., 2023](#)). All of these would need to have higher luminosities to be consistent with the Saio models. Only Aldebaran ($M = 0.91^{+0.04}_{-0.02} M_{\odot}$; [Stock et al. 2018](#)) and 42 Dra ($M = 0.98 \pm 0.05 M_{\odot}$; [Döllinger et al. 2009](#)) have lower masses. Therefore, only Aldebaran is in good agreement with the low-mass models of [Saio et al. \(2015\)](#).

For NGC 4349 No. 127, as detailed in [Sect. 4.2](#), a lower mass $M = 2.20^{+0.38}_{-0.20} M_{\odot}$ is also possible, which is however also linked to a lower luminosity $\log_{10}(L/L_{\odot}) \sim 2.3$. We also note that the models could be altered significantly by a more sophisticated treatment of convection ([Saio et al., 2015](#)).

Overall, we find that the properties (mode, amplitude of temperature variation) of the presented oscillation model seem to be consistent with the predictions for oscillatory convective modes. We nevertheless are cautious to conclude that the Saio models provide a good match given the stellar properties and period of the variation. More detailed modeling of their properties would be very valuable.

As discussed by several authors (e.g., [Reichert et al. 2019](#); [Döllinger & Hartmann 2021](#); [Delgado Mena et al. 2023](#)), a suspicious accumulation of false positive planet detections in the vicinity of NGC 4349 No. 127 is evident. As the non-radial oscillation model convincingly explains the variations of the star, a generalization to other stars with similar parameters seems plausible.

On the other hand, an alternative explanation for the long secondary periods of stars on sequence D is binarity. In this scenario, a brown dwarf or low-mass stellar companion enveloped by a comet-like dust cloud causes the photometric variations by obscuring the stellar disk ([Soszyński, 2007](#); [Soszyński & Udalski, 2014](#)), a proposal supported by the detection of secondary eclipses in mid-infrared photometry for a subsample of variable stars showing long secondary periods ([Soszyński et al., 2021](#)).

While a brown dwarf is indeed consistent with the RVs, this scenario nevertheless seems implausible for NGC 4349 No. 127, as it would not be clear how the line shape and CRX variations could be explained. If we, for the sake of the argument, assume that the brown dwarf exists, is engulfed in a dusty cloud, and is transiting the star, then transit durations are on the order of $T_{\text{transit}} \sim 22$ d, even if one were to assume a radius of $10 R_{\odot}$ for the dust cloud. In principle, the Rossiter-McLaughlin effect can explain the line shape

variations during the transit itself. But since we observe a near sinusoidal variation, for instance, for the FWHM, the variations out of transit would remain unaccounted for. It would be even more problematic in the cases of Aldebaran or γ Dra, which show RV amplitude changes or phase shifts that are hard to explain with an orbital companion. This scenario can thus not explain the observables.

It is, of course, possible that the variability on sequence D, mostly detected via photometry, is simply not related to the intrinsic RV variations of the discussed giants. Moreover, it is possible that even within the small group of these false positive planet hosts, different intrinsic mechanisms are at work. For NGC 4349 No. 127, non-radial oscillations provide the most convincing explanation for all observables to date. Whether these are linked to oscillatory convective modes or not remains uncertain.

4.6.2 Magnetic activity

Delgado Mena et al. (2018) propose the rotational modulation of magnetic spots as the origin of the RV variations. However, the available photometry and the newly presented activity indicators lead us to refute the spot hypothesis.

If magnetic surface spots cause the RV periodicity, significant photometric variations are to be expected. Following Hatzes (2002), we can roughly estimate the required spot filling factor to produce RV variations with amplitude $A_{RV} = 235.6 \frac{\text{m}}{\text{s}}$ (see Fig. 4.2) as $f = 7.3\%$, using $v \sin i = 4.81 \frac{\text{km}}{\text{s}}$ (Tsantaki et al., 2023). Hatzes (2002) used $T_{\text{eff}} = 5800 \text{ K}$ and $T_{\text{spot}} = 4600 \text{ K}$ for the effective temperatures of the stellar photosphere and the star spot, respectively. Downscaling the spot temperature to yield the same flux ratio as considered by Hatzes (2002), but at effective temperature $T_{\text{eff}} = 4417 \text{ K}$ (Tsantaki et al., 2023), yields a temperature difference $\Delta T_{\text{spot}} = 914 \text{ K}$ between photosphere and spot. Assuming black body radiation, we calculate the flux in a Bessel V-band filter for a photosphere with a star spot of filling factor f to be reduced by 5.7% compared to the flux of a photosphere with no spot present. This corresponds to a magnitude difference of $\Delta V \sim 0.06 \text{ mag}$.

We searched for the largest amplitude consistent with the ASAS-3 V-band photometry by fitting sinusoids with fixed periods in a box of size 100 d around the best RV period $P = 674.0 \text{ d}$. The largest amplitude present in the data is $A_V = 0.006 \pm 0.003 \text{ mag}$, an order of magnitude lower than predicted by our rough estimate. We further show in Sect. B.2 that the apparent periodicity at roughly half the RV period is caused by the window function of the ASAS-3 observations. We therefore conclude that there are no photometric variations at periods related to the RV period in the ASAS-3 data set that are consistent with the prediction.

Another strong argument against the RV variations being caused by star spots is the positive correlation between GRX and RV in Fig. 4.4 (top left panel). If spots were to cause

the RV variation, one would expect the CRX to be anticorrelated with the RV (negative chromaticity), as the contrast (flux ratio) between the cool spot and the stellar photosphere decreases toward longer wavelengths (Reiners et al., 2010; Barnes et al., 2011; Tal-Or et al., 2018; Baroch et al., 2020; Lafarga et al., 2021). The same relation holds for hot active regions (Reiners et al., 2013). Thus, the positive chromaticity observed for NGC 4349 No. 127 is challenging to explain with a spot model, while it is a natural consequence of the limb darkening in case of dipole non-radial oscillations.

We note that Delgado Mena et al. (2023) recently discussed other magnetic structures that locally reduce convection and lead to RV variations without photometric variations. However, it is not clear if such structures could explain any of the correlations present for NGC 4349 No. 127. We therefore find the oscillation hypothesis more convincing.

4.7 Summary

We presented a reanalysis of archival HARPS spectra of the cluster giant NGC 4349 No. 127, which was originally thought to host a brown dwarf orbital companion (Lovis & Mayor, 2007). Delgado Mena et al. (2018, 2023), however, refute the brown dwarf's existence based on variations of the FWHM of the CCF and the $H\alpha$ index. This makes NGC 4349 No. 127 another example of a group of giant stars with RV periodicities that mimic orbital companions, but are of unknown intrinsic origin.

We first presented additional activity indicators available through the use of the SERVAl and RACCOON reduction pipelines, revealing that, along with the FWHM, the contrast of the CCF, the dLW, and the CRX also have significant periodicity at the proposed orbital period. We therefore affirm the findings of Delgado Mena et al. (2018, 2023) and unequivocally refute the orbital companion. Furthermore, we find a significant, positive correlation between the CRX and the RVs, as well as closed-loop correlations between the RVs and dLW, FWHM, and contrast, respectively, a result of sinusoidal variations with phase shifts close to $\pi/2$.

We presented the simulation software `pyoscillot`, capable of simulating synthetic HARPS spectra, along with their respective RVs and activity indicators, based on a model of non-radial oscillations in the photosphere of a star. Such non-radial oscillations were previously proposed to cause the intrinsic RV variations that mimic orbital companions.

We showed that an isolated, low-amplitude, retrograde, dipole ($l = 1, m = 1$) oscillation reproduces the periodicities and amplitudes of the RVs and all activity indicators, along with their respective phase relations and thus the Lissajous figures of their correlations. The oscillation model also predicts low-amplitude photometric variations at the orbital

period, which are well below the detection threshold of the available ASAS-3 data, and thus cannot be ruled out.

We also showed that other dipole ($l = 1$) modes, while producing similar RV variations, are inconsistent with the activity indicators measured for NGC 4349 No. 127 and present the expected variations for all modes. We showed that the CRX is the only indicator yielding variations for all azimuthal orders m allowed for dipole ($l = 1$) modes, while the line shape diagnostics are mostly inconspicuous for the $l = 1, m = 0$ mode. In the presence of scatter in the CRX data, such modes and combinations of different $l = 1$ modes could therefore be difficult to detect.

Moreover, we explored higher-order modes, showing that modes with $m = l$ and $m = -l$ show similar behavior to the $l = 1, m = 1$ mode. The $l = 2, m = -2$ mode cannot entirely be ruled out as the cause of the observed variations. In general, the CRX provides the most direct approach to differentiate between modes, but it is also affected by the scale of the temperature variations employed, and thus cannot be used to rule out modes unambiguously.

We finally showed that the stellar parameters of NGC 4349 No. 127 are broadly consistent with the models of oscillatory convective modes (Saio et al., 2015) put forth to cause non-radial oscillations of bright giant stars. We showed that reliable planet detections, on the one hand, and more uncertain planet systems and false positives, on the other, are separated in a period-luminosity plot. This suggests that the same intrinsic phenomenon might be present in the latter group. We note, however, that the masses of most giant stars with intrinsic RV signatures are higher than predicted by the models of Saio et al. (2015). We further give arguments that the correlations observed for NGC 4349 No. 127 cannot be explained by magnetic spots.

We conclude that the RV variations of NGC 4349 No. 127 are likely caused by a retrograde, dipole ($l = 1, m = 1$) non-radial oscillation. We also provide, for the first time, a testable model capable of explaining the intrinsic RV variations discussed in the literature.

The case of NGC 4349 No. 127 shows the importance of acquiring a set of reliable and precise activity indicators targeting the shape of spectral lines and the wavelength dependence of the RV. However, as $m = 0$ modes do not show large variations of the shape of spectral lines, and would only be detected by the CRX, which often suffers from significant scatter, long-term RV monitoring remains crucial in order to detect any changes in the amplitude, period, or phase of the RV variation.

Applying the same analysis to other evolved stars with similar luminosities and RV periods could offer valuable insights to constrain their (potential) intrinsic nature. This analysis may thus contribute to verifying the reliability of the planet population orbiting evolved stars.

Distinguishing planets from intrinsically induced radial velocity signals in evolved stars

Details of authorship: The contents of this chapter have been accepted for publication as a journal article in *Astronomy & Astrophysics* (Spaeth et al., 2025).¹ The plots, analysis, and main body of text was contributed by me. Valuable support with the design and implementation of the analysis, along with suggestions for the presentation of the results, has been contributed by my co-authors, Sabine Reffert, Trifon Trifonov, Adrian Kaminski, Simon Albrecht, Frank Grundahl, Mads Fredslund Andersen, Andreas Quirrenbach, and Pere L. Pallé, as well as the anonymous referee. The presentation is almost identical to the revised version submitted in the language editing stage. Figures 5.6, 5.7, and 5.8 have been moved from the appendix to the main text. The figures and tables have been rescaled for better visibility. The appendix of the article was moved to Appendix C.

5.1 Introduction

The majority of the over 5750 exoplanets confirmed to date have been detected via the transit technique ($\sim 75\%$) and the radial velocity (RV) method ($\sim 19\%$).² Each of the exoplanet detection methods, however, has intrinsic biases that leave a large part of the exoplanet parameter space still to be explored.

For instance, main-sequence stars more massive than about $1.5 M_{\odot}$ are challenging to target in both transit (due to the larger radii) and RV surveys. For the latter, the achievable RV precision is limited due to high surface temperatures resulting in a small number of absorption lines, which are significantly broadened by high rotation rates (Sato et al., 2003; Galland et al., 2005; Johnson et al., 2007; Lagrange et al., 2009; Assef et al., 2009). An alternative to studying the population of planets around these stars is to target their evolved counterparts, which have significantly cooled down and slowed their rotation velocities, resulting in numerous narrow absorption lines that contain valuable Doppler

¹Licensed under CC BY 4.0 (<https://creativecommons.org/licenses/by/4.0/>).

²<https://exoplanetarchive.ipac.caltech.edu/>

information. So far, around 150 planets orbiting giant stars have been detected,³ the vast majority of which were found using the RV method.

A recent study by [Wolthoff et al. \(2022\)](#) summarizes the planet occurrence rate around giant stars through a combined analysis of three large RV surveys. They show a positive planet-metallicity correlation, as previously found also for main-sequence stars ([Fischer & Valenti, 2005](#); [Udry & Santos, 2007](#)) and for giants ([Reffert et al., 2015](#)). Furthermore, [Wolthoff et al. \(2022\)](#) report a peak in the planet-occurrence rate at host masses $M = 1.68 \pm 0.59 M_{\odot}$ and at orbital periods of around 2 yr.

However, the RV method applied to giant stars faces two important challenges. On the one hand, short-term p-mode (solar-like) oscillations lead to intrinsic RV jitter with amplitudes around 10 to 20 m s^{-1} , even for relatively stable giant stars ([Hekker et al., 2006](#)). The amplitude of these p-mode oscillations increases as the stars become more evolved and luminous ([Hekker et al., 2008](#)), and thus the oscillations present more of a challenge for such giants. However, as the periods of these oscillations are typically on scales of hours to days, they can be dealt with as a white noise component in the context of exoplanet surveys targeting companions with orbital periods of several hundred days. Nevertheless, while this short-term RV jitter complicates the detection of low-mass ($M \lesssim 1 M_{\text{Jup}}$) planetary companions, the detection of planets of higher masses is not impacted.

On the other hand, what is more problematic is the suspicion that the RV signals of some of the most luminous evolved planet hosts are in fact caused by poorly understood intrinsic stellar processes instead of planetary companions. The first identified case was γ Dra ([Hatzes et al., 2018](#)), which showed stable large-amplitude RV variations with a period of $P \sim 700$ d during nearly eight years of RV monitoring before amplitude changes and phase shifts became apparent. Other stars with RV signals with similar periods have been found in subsequent studies and include Aldebaran ([Reichert et al., 2019](#)), ϵ Cyg ([Heeren et al., 2021](#)), 42 Dra ([Döllinger & Hartmann, 2021](#)), Sanders 364 ([Zhou et al., 2023](#)), HD 135438 ([Lee et al., 2023](#)), and four evolved stars in open clusters: NGC 2423 No. 3, NGC 2345 No. 50, NGC 3532 No. 670, and NGC 4349 No. 127 ([Delgado Mena et al., 2018, 2023](#)). For several of the stars, the RV variations had previously been attributed to planetary companions. We stress that all of these stars are very luminous ($L > 100 L_{\odot}$) and that false-positive detections seem to occur frequently only for stars with radii $R \gtrsim 21 R_{\odot}$ and RV periods between 300 d and 800 d ([Döllinger & Hartmann, 2021](#)). Planets around less luminous giants are generally not contested.

The arguments to refute orbital companions as the origin of the RV signals of these luminous giants are quite varied. The orbital companions for γ Dra, Aldebaran, ϵ Cyg, and 42 Dra have been ruled out based on arguments of the coherence and stability of the RV signal, which are only possible after extensive, long-term RV monitoring. The planet

³<https://www.lsw.uni-heidelberg.de/users/sreffert/giantplanets/giantplanets.php>

around Sanders 364 was ruled out, as periodicity at multiple periods was detected (Zhou et al., 2023). On the other hand, for the cluster giants presented by Delgado Mena et al. (2018, 2023), orbital companions have been ruled out based on variations of the activity indicators identified with the High Accuracy Radial Velocity Planet Searcher (HARPS; Mayor et al. 2003). Unfortunately, such additional spectral diagnostics are mostly only available from pressure and temperature stabilized spectrographs with stable instrumental profiles. Furthermore, since not all published planets have been monitored on sufficiently long timescales or have a large set of reliable activity indicators available, there could, in principle, be more as yet unidentified false-positive planets around the most luminous giants, especially around those that have been announced on the basis of sparse RV sampling.

Furthermore, the origin of these intrinsic RV variations is still uncertain. The long RV periods typically rule out radial pulsations (Hatzes & Cochran, 1993; Cox et al., 1972; Hatzes et al., 2018; Reichert et al., 2019). The modulation of magnetic surface spots is one possibility, but it would in most cases lead to a larger photometric variability than detected (Reffert et al., 2015). More exotic magnetic processes, potentially linked to convection, that could lead to RV variations without associated photometric variations have been suggested (Delgado Mena et al., 2023; Rolo et al., 2024), but they remain poorly studied. For the binary star ϵ Cyg, the heartbeat phenomenon was put forth (Heeren et al., 2021), but it cannot explain the variations for single stars. Finally, non-radial oscillations have been discussed for a long time as being a potential source of intrinsic RV variations (Hatzes & Cochran, 1994; Hatzes, 1996; Hatzes & Cochran, 1998b).

Oscillatory convective modes have been proposed as the origin of non-radial oscillations in very luminous photometrically variable giant stars (Saio et al., 2015), although it is unclear whether these would be applicable for the less luminous giants within the group of false positives. In a recent study, we have shown that simulations of an $l = 1, m = 1$ non-radial oscillation can reproduce the variations of the RVs and the activity indicators of NGC 4349 No. 127 (Spaeth et al., 2024), an evolved cluster giant reported to host a brown-dwarf companion (Lovis & Mayor, 2007) but the finding has since been refuted by Delgado Mena et al. (2018, 2023). However, it remains to be seen if other stars can be shown to have similar signatures.

The goal of this study is three-fold. (i) Our initial motivation was to investigate whether a number of so-far unpublished planet candidates identified in the Lick RV survey of giant stars are exoplanets or false-positives by intrinsic variations. These candidates were followed up using spectrographs from the Stellar Observations Network Group (SONG) and the Calar Alto high-Resolution search for M dwarfs with Exoearths with Near-infrared and optical Echelle Spectrographs (CARMENES). (ii) With nearly 25 years of RV data and a set of activity indicators commonly used to target planets orbiting main-sequence stars, we further aimed to test which metrics that determine the difference between planets and

Tab. 5.1.: Stellar parameters derived by Stock et al. (2018).

HIP	HD	Id.	Evol. state	$P(\text{state})$	M (M_{\odot})	R (R_{\odot})	L (L_{\odot})	T_{eff} (K)	[Fe/H] (dex)	$\log g$ (cm s^{-1})	$B - V$ (mag)	Hpscat (mag)
7607	9927	ν Per	HB	0.70	$1.54^{+0.25}_{-0.16}$	$21.6^{+0.3}_{-0.5}$	$154.6^{+2.3}_{-3.4}$	4385^{+16}_{-17}	0.07 ± 0.10	$1.96^{+0.07}_{-0.08}$	1.28	0.004
7884	10380	ν Psc	RGB	0.56	$1.40^{+0.18}_{-0.17}$	$34.5^{+1.7}_{-1.6}$	$331.4^{+18.7}_{-16.7}$	4197^{+52}_{-53}	-0.27 ± 0.10	$1.51^{+0.08}_{-0.09}$	1.35	0.005
16335	21552	σ Per	RGB	0.54	$1.53^{+0.18}_{-0.12}$	$35.9^{+0.8}_{-0.7}$	$357.6^{+13.5}_{-15.2}$	4184^{+9}_{-9}	-0.20 ± 0.10	$1.51^{+0.04}_{-0.05}$	1.37	0.006
38253	63752		HB	0.88	$2.43^{+0.21}_{-0.63}$	$71.7^{+10.8}_{-10.2}$	$1374.9^{+889.6}_{-776.4}$	4058^{+7}_{-7}	-0.35 ± 0.10	$1.06^{+0.06}_{-0.05}$	1.45	0.006
46390	81797	α Hya	HB	1.00	$2.40^{+0.23}_{-0.11}$	$58.8^{+0.4}_{-0.5}$	$868.0^{+7.4}_{-17.9}$	4086^{+8}_{-3}	-0.05 ± 0.10	$1.29^{+0.06}_{-0.02}$	1.44	0.007
47959	84561	18 Leo	RGB	0.98	$0.93^{+0.05}_{-0.03}$	$36.3^{+1.6}_{-1.9}$	$296.5^{+24.7}_{-29.5}$	3981^{+2}_{-2}	-0.32 ± 0.10	$1.27^{+0.11}_{-0.01}$	1.49	0.008
64823	115478		RGB	0.90	$1.42^{+0.16}_{-0.13}$	$18.6^{+0.4}_{-0.6}$	$109.0^{+4.6}_{-6.4}$	4335^{+14}_{-14}	0.10 ± 0.10	$2.09^{+0.03}_{-0.08}$	1.30	0.005
73620	133165	110 Vir	HB	0.69	$1.13^{+0.34}_{-0.12}$	$12.1^{+0.4}_{-0.6}$	$70.3^{+2.2}_{-2.3}$	4800^{+79}_{-40}	-0.30 ± 0.10	$2.43^{+0.05}_{-0.16}$	1.03	0.005
75458	137759	ι Dra	HB	0.88	$1.29^{+0.17}_{-0.16}$	$11.9^{+0.1}_{-0.2}$	$57.2^{+0.8}_{-0.5}$	4622^{+15}_{-24}	0.11 ± 0.10	$2.40^{+0.07}_{-0.06}$	1.17	0.005
84671	156681	66 Her	RGB	0.68	$1.00^{+0.11}_{-0.09}$	$47.8^{+1.8}_{-1.7}$	$471.8^{+36.5}_{-31.9}$	3899^{+8}_{-9}	-0.21 ± 0.10	$1.09^{+0.05}_{-0.04}$	1.54	0.009
88048	163917	ν Oph	HB	1.00	$2.74^{+0.12}_{-0.09}$	$14.1^{+0.3}_{-0.3}$	$107.0^{+2.2}_{-2.3}$	4943^{+32}_{-29}	0.06 ± 0.10	$2.59^{+0.02}_{-0.03}$	0.99	0.004
89826	168775	κ Lyr	HB	0.91	$2.25^{+0.46}_{-0.20}$	$18.6^{+0.3}_{-0.4}$	$138.2^{+2.6}_{-3.2}$	4595^{+21}_{-20}	0.15 ± 0.10	$2.24^{+0.04}_{-0.03}$	1.16	0.005

Notes. Presented are the stellar parameters for the most likely evolutionary state (Evol. state) with its probability $P(\text{state})$. Metallicities were adopted from Hekker & Meléndez (2007). We also list $B - V$ colors and the photometric scatter present in the HIPPARCOS data (ESA, 1997).

intrinsic variations are sensitive to intrinsic phenomena in evolved stars. (iii) Last, we aim to present further intrinsically RV-variable stars as well as their observational fingerprints, hoping to contribute toward a better physical understanding of the intrinsic mechanism present in giant stars that can mimic planetary companions quite convincingly in RV data. For this purpose, we present ten such planet candidates along with two secure exoplanet systems. For simplicity, we include all orbital companions of substellar minimum mass within the term “planet” unless stated otherwise.

The paper is structured as follows. In Sect. 5.2, we give an overview of the sample and the stellar parameters followed by a summary of the observations in Sect. 5.3. In Sect. 5.4, we discuss the RV time series data along with several metrics aimed at differentiating between planets and intrinsic processes causing the (semi-)periodic RV variations. These metrics are discussed star-by-star in Sect. 5.5. In Sect. 5.6, we explore the most promising planet candidate, HIP 64823, remaining after the activity analysis. Finally, we discuss potential astrophysical origins of the intrinsic variations in Sect. 5.7 and summarize our findings in Sect. 5.8.

5.2 Sample and stellar parameters

The giant stars considered in this work were originally part of the Lick RV survey, which started in 1999 and targeted 373 bright ($V \leq 6$) G and K giants. The Lick sample initially comprised 86 K giants, selected to be photometrically stable and not part of multiple systems from the HIPPARCOS catalog (Frink et al., 2001; ESA, 1997). The stellar sample was extended in 2000 and 2004, relaxing the constraints on photometric stability and adding stars with higher masses and bluer colors. However, the actual level of photometric variability remained below 0.01 mag for most stars (Reffert et al., 2015).

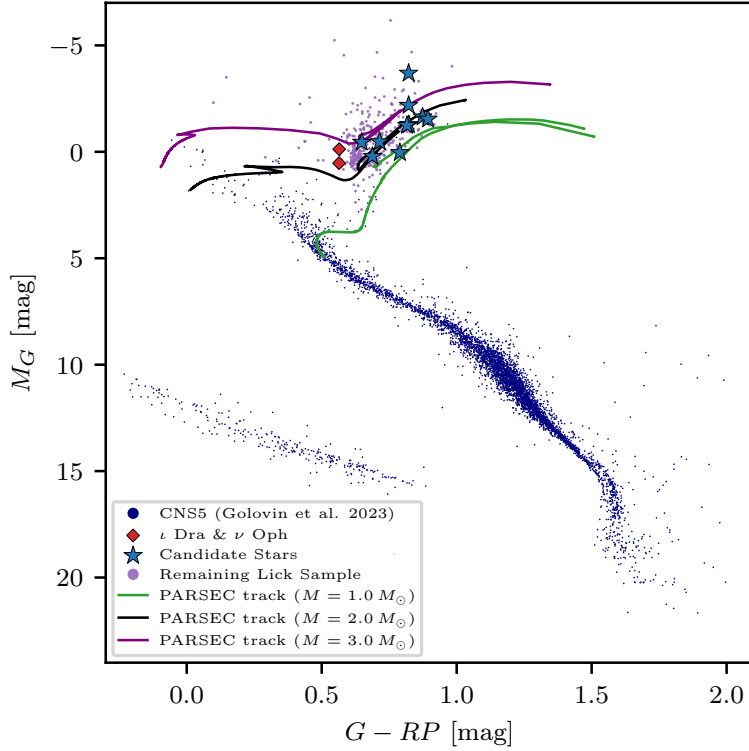


Fig. 5.1.: Color-magnitude diagram based on *Gaia* DR3 photometry showing the location of the sample stars using blue star markers as well as red diamonds for the two published planet hosting giants ι Dra and ν Oph. We also plot the location of the remaining 361 giant stars within the Lick sample in purple. For comparison, we overplot the fifth catalog of nearby stars (CNS5) (Golovin et al., 2023) in dark blue and three adjacent evolutionary tracks for $1M_{\odot}$ (green), $2M_{\odot}$ (black), and $3M_{\odot}$ (purple) taken from PARSEC (Bressan et al., 2012).

Overall, 18 planets in 15 stellar systems present in the Lick sample of giant stars have been confirmed either by our own or other groups (Frink et al., 2002; Hatzes et al., 2006; Reffert et al., 2006; Sato et al., 2007; Liu et al., 2008; Schwab, 2010; Wittenmyer et al., 2011; Mitchell et al., 2013; Trifonov et al., 2014; Lee et al., 2014; Ortiz et al., 2016; Takarada et al., 2018; Quirrenbach et al., 2019; Luque et al., 2019; Tala Pinto et al., 2020; Hill et al., 2021; Teng et al., 2023a). A recent overview is also presented by Wolthoff et al. (2022). Furthermore, a number of stars were identified as periodic RV-variable stars, making them planet-host candidates. 20 stars of the latter group, along with three confirmed planet hosts were monitored using CARMENES starting in 2017 (see Sect. 5.3). Notably, the 20 planet candidates also include HIP 16335, for which a planetary companion was published by Lee et al. (2014), but that we classified as a candidate. In this work, we exclude stars with long-period (much longer than the combined Lick-CARMENES baseline) stellar companions as the uncertainty of the outer companions' orbits significantly hinders the analysis. We further exclude two stars that will be the focus of future dedicated

publications. The remaining sample of 12 stars thus comprises ten giants that were considered to be candidates to host planets with periods between one and eight years after the Lick survey concluded as well as two published planet hosts, namely ι Dra (HIP 75458) (Frink et al., 2002; Hill et al., 2021) and ν Oph (HIP 88048) (Quirrenbach et al., 2011, 2019), which were added to the CARMENES observations for comparison.

The stellar parameters for the Lick giant star sample have been derived by Stock et al. (2018) using Bayesian inference on a grid of stellar evolutionary models, implemented in the fitting tool *SPOG+*.⁴ The stellar parameters in the most likely evolutionary state, either on the red giant branch (RGB) or horizontal branch (HB), are presented in Table 5.1. Many of the stars are relatively luminous. The stars are roughly evenly distributed between the RGB and HB (five vs seven). The solar-like oscillations of HIP 75458 and HIP 89826 have been analyzed as part of asteroseismic studies (Zechmeister et al., 2008; Hill et al., 2021; Campante et al., 2023; Malla et al., 2024). The derived asteroseismic parameters are consistent with those in Table 5.1.

Figure 5.1 shows the loci of the 12 stars, as well as the remaining 361 giants comprising the Lick sample, within a *Gaia* DR3 (Gaia Collaboration et al., 2016, 2023) color-magnitude diagram. For the stars not present in the *Gaia* catalog due to their brightness (including HIP 46390), we converted the HIPPARCOS photometric measurements (ESA, 1997) into the *Gaia* passbands.⁵ To provide a visual reference, we overplot the fifth catalog of nearby stars (CNS5; Golovin et al. 2023) and three PARSEC evolutionary tracks (Bressan et al., 2012) for different stellar masses at solar metallicity.

5.3 Observations

5.3.1 Lick observations

The observations at UCO/Lick Observatory started in 1999 using the 0.6 m Coudé Auxiliary Telescope (CAT) and the Hamilton Echelle Spectrometer (Vogt, 1987) with a measured resolving power $R \sim 50\,000$ at 6000 \AA (Reffert et al., 2015). The survey used the iodine technique described by Butler et al. (1996) and aimed for an RV precision of 5 to 8 m s^{-1} (Reffert et al., 2015). The Hamilton spectrograph covers a wavelength range of approximately $3400\text{--}9000\text{ \AA}$ (Fischer et al., 2013). However, the RV determination is limited to the regime spanning roughly $5000\text{--}5800\text{ \AA}$, due to the use of the iodine cell. The observations ended in 2011 when the iodine cell at Lick was damaged (Fischer et al., 2013). A continuation of the survey using the 72 cm Waltz Telescope located at Landessternwarte

⁴<https://github.com/StephanStock/SPOG>

⁵https://gea.esac.esa.int/archive/documentation/GDR2/Data_processing/chap_cu5pho/sec_cu5pho_calibr/ssec_cu5pho_PhotTransf.html

Heidelberg (Tala et al., 2016) is expected to start in 2025. Overall, 1127 Lick spectra are available for the 12 stars with a time baseline of approximately 12 years. We use the standard Lick RV reduction.

5.3.2 Lick H α index

Since the line spread function of the Lick spectra is comparably unstable (Tala Pinto et al., 2020), and due to the inclusion of the iodine cell, activity indicators targeting the shape of the stellar spectral lines only yield low precision (see, for instance, Reffert et al. 2006). No such indicators are therefore used in this work.

An individual spectral line that is present in the Lick wavelength range, lies outside the iodine regime, and is known to be sensitive to chromospheric activity (Kürster et al., 2003), is the H α line (6562.8 Å). To quantify the variability of its core, we improved upon the work by Staudt (2020), who calculates H α indices for the Lick spectra based on the definition by Boisse et al. (2009). Since the standard wavelength regions used by Staudt (2020) and Boisse et al. (2009) were strongly affected by telluric lines, we searched for relatively unaffected regions within the spectral order containing the H α line and slightly redefine the H α index as

$$H\alpha = \frac{F_{H\alpha}}{\sum_{i=1}^5 F_i}, \quad (5.1)$$

with $F_{H\alpha}$ being the flux in a 0.4 Å region centered on the core of the H α line and F_{1-5} being the fluxes in five smaller comparison regions in the continuum. These are defined as [6538.5 Å, 6540.5 Å], [6565.0 Å, 6567.0 Å], [6576.0 Å, 6578.0 Å], [6582.5 Å, 6584.5 Å], and [6595.0 Å, 6597.0 Å]. The uncertainties were calculated by quadratically adding the contributions of the estimated intensity error using the $\beta\sigma$ procedure (Stoehr et al., 2008; Czesla et al., 2018) and the influence of an imperfect wavelength shift by performing a Monte Carlo simulation (Staudt, 2020). The H α time series is treated as two separate data sets due to small offsets caused by a CCD camera exchange in April 2004 (some spectra testing the new CCD have already been acquired in 2002/2003).

5.3.3 SONG observations

After the Lick observations concluded, select giants from the Lick survey were monitored using the 1 m robotic SONG telescope located on Tenerife, Spain (Andersen et al., 2014; Fredslund Andersen et al., 2019). The SONG spectrograph is a high-resolution ($R \sim 90\,000$), cross-dispersed échelle spectrograph. Similar to the Lick survey, SONG employs the iodine cell technique to derive precise RVs (Grundahl et al., 2017). The SONG

spectrograph covers the wavelength range 4400–6900 Å (Grundahl et al., 2017), with RVs derived from the regime 5000 Å to 6300 Å (Heeren et al., 2023).

Of the 12 stars in the sample, four (HIP 38253, HIP 46390, HIP 47959, and HIP 75458) were included in the SONG observations. Overall 1030 spectra with sufficient S/N are available from SONG between March 2015 and December 2023. We obtained the RVs using the pyodine reduction software (Heeren et al., 2023). No standard activity indicators are available from the SONG observations. We note that some spectra, especially for HIP 75458, were taken as part of other observing campaigns aiming to study short-term variations. In these cases, several (typically less than five, in two nights more than ten) spectra were taken in the same night. Nevertheless, we refrain from binning the spectra, as retaining the full time resolution of the measurements can help to constrain the short-term jitter during the RV modeling.

5.3.4 CARMENES observations

First CARMENES observations for the ten planet candidates were taken between 2017 and 2018 (with a single additional spectrum from 2016). These include archival spectra from other observation programs. The CARMENES observations were continued, after an unfortunate gap, from 2021 to 2023 for the full sample, including the confirmed planet hosts.

The CARMENES spectrograph (Quirrenbach et al., 2014), installed at the 3.5 m telescope at Calar Alto, Spain, offers two independent channels acquiring spectra in different wavelength regimes simultaneously. The visual (VIS) channel covers the regime 5200 Å to 9600 Å, with a resolving power $R \sim 94\,600$. The near-infrared (NIR) channel continues the coverage at longer wavelengths from 9600 Å to 17 100 Å with a resolving power $R \sim 80\,400$.⁶

We reduced the CARMENES data using two reduction pipelines. The standard SERVAL reduction pipeline (Zechmeister et al., 2018) uses a coadded stellar template to derive the RVs using least squares minimization. The pipeline furthermore yields several activity indicators, namely the chromatic index (CRX), differential linewidth (dLW) (see Zechmeister et al. 2018 for their definitions), and several line indicators: H α (6562.8 Å), Na I D1 (5895.9 Å), Na I D2 (5889.9 Å), and the Ca II infrared triplet (IRT) lines at 8498.0 Å, 8542.1 Å, and 8662.1 Å. For brevity, we refer to the line indicators as NaD $_i$ and CaIRT $_i$, respectively. These indicators have been shown to be sensitive to chromospheric activity (see, for instance, Kürster et al. 2003; Díaz et al. 2007; Martínez-Arnáiz et al. 2011; Martin et al. 2017; Schöfer et al. 2019; Huang et al. 2024; Gehan et al. 2024).

⁶<https://carmenes.caha.es/ext/instrument/index.html>

Due to the brightness of the stars ($V \leq 6$ mag), they are excellent filler targets and have been observed in variable, sometimes even quite bad, observing conditions. As a consequence, the S/N of the individual observations varies, although it is generally high. Additionally, in some good nights exposure times were increased in an attempt to reach sufficient S/N in the simultaneous Fabry-Pérot exposures to measure the instrumental drift over the course of the night (Schäfer et al., 2018). As a consequence, a few observations have S/N exceeding the standard SERVAL limits of 500 and 400 for the visual and near-infrared channels, respectively. To avoid any non-linear effects due to a saturation of the CCD affecting all observations, we first created a SERVAL template using only spectra below the standard SERVAL S/N limits, which we then used to derive the RVs and activity indicators for all spectra. Other than that, we use the standard settings of the SERVAL pipeline for the two respective CARMENES channels. We note that this includes the selection of only a subset of the NIR spectral orders, as many orders suffer from severe telluric contamination (Reiners et al., 2018; Nagel et al., 2023).

We furthermore derived the RVs and activity indicators by calculating the cross-correlation function (CCF) with a weighted binary mask by using the RACCOON reduction software (Lafarga et al., 2020). The RACCOON pipeline yields spectral diagnostics such as the full width at half maximum (FWHM) and contrast of the CCF, as well as the bisector inverse slope (BIS). By default, masks are only provided for M dwarfs targeted in the CARMENES GTO sample (Reiners et al., 2018; Ribas et al., 2023). We therefore calculated new masks for each star using the functionality provided by RACCOON and the SERVAL templates detailed above. The RACCOON RVs are generally in good agreement with the SERVAL results. The deviation of the RV results between the SERVAL and RACCOON results have a standard deviation $\sigma = 3.3 \text{ m s}^{-1}$ and $\sigma = 11.6 \text{ m s}^{-1}$ for VIS and NIR, respectively. The larger deviations in the near infrared are expected due to a lower number of usable lines as reported by Lafarga et al. (2020). For the analysis presented in Sect. 5.4, we always use the RVs as derived by SERVAL, and complement these with the FWHM, contrast, and BIS measurements derived by RACCOON.

Although it was attempted to obtain instrumental drift measurements for the spectra simultaneously, exposure times were often too short to ensure sufficient Fabry-Pérot exposures in the second fiber of the CARMENES spectrograph. For these spectra, the instrumental drift was modeled over the night with a third-order polynomial using the drift measurements from the sky calibration frames and all stellar spectra (including other programs). The quality of the fits was ensured by eye. The fits were generally found to sufficiently describe the nightly variation of the instrumental drift. From these fits, the drifts for the individual spectra were interpolated. The uncertainties of the drift measurements were derived by quadratically adding the uncertainty of the polynomial fit at the observing time of the spectrum, derived via a Monte Carlo simulation, and the weighted standard deviation of the residuals of the drift measurements (after subtracting the third order polynomial) over the course of the night. The drifts are typically smaller

than the stellar jitter of the evolved stars. Nevertheless, there are several nights that show strong instrumental drifts or offsets that lead to large outliers in the RVs if not corrected properly. We further correct the spectra for nightly zero-points measured from CARMENES RV standard stars and provided through the CARMENES consortium. These are typically found to be small.

We carefully cross-checked the spectra with any reported issues in the CARMENES observing logs and the routine analysis carried out by the CARMENES consortium to ensure the data quality. Twelve spectra with reported issues were removed from the analysis. We further removed four spectra for which the peak S/N per pixel is below 30 as well as five overexposed spectra in VIS and NIR each. Finally, we removed two spectra that were taken at very high airmass ~ 2.9 in the transition between nautical and civil twilight in eastern observing direction. These showed strong outliers in the activity indicators. Finally, we remain with 337 spectra from the CARMENES VIS and NIR channels each for all 12 stars. We note that not all 337 spectra are pairs of contemporary VIS and NIR observations since readout issues in one detector still allow the use of the other channel. As for the SONG data, we refrain from binning any data points, even though in the earlier CARMENES observation campaigns multiple spectra were taken in the same nights for some stars.

Overall, we are left with 1127 Lick spectra, 1030 SONG spectra, and 337 spectra from each of the CARMENES channels, totaling 2831 spectra for all 12 stars. Combined, these cover the time frame from 1999 to 2023, albeit with a large gap between 2011 and 2017 for many of the stars. An overview of the number of spectra per instrument, as well as the observational baseline is given in [Table 5.2](#). Although the number of CARMENES observations for most stars is significantly smaller than that from Lick and SONG, we consider the observational baseline sufficient to reliably detect the large-amplitude RV variations. However, for certain stars, such as HIP 46390, HIP 73620, or HIP 89826, the CARMENES sampling was suboptimal. This could result in smaller-amplitude variations, such as those potentially present in the CARMENES activity indicators, not being reliably detected. We also note that the two secure planets hosts were only added to the CARMENES sample in 2021. However, both were relatively densely sampled, allowing for periodicity close to the main RV period ($P \sim 500$ d) to be identified with confidence.

5.4 Results

5.4.1 Radial velocity time series and Keplerian fits

The ten evolved RV-variable stars to be examined in this work were found to be planet candidates after the conclusion of the Lick RV survey in 2011. Each of the stars has larger variations in the RVs than expected from the p-mode oscillations even for these relatively

Tab. 5.2.: Number of spectra collected per instrument along with the observational time baselines (years in parentheses).

HIP	Lick	SONG	CARM-VIS	CARM-NIR
7607	82 (2000–2011)		39 (2017–2023)	39 (2017–2023)
7884	92 (2000–2011)		29 (2017–2023)	28 (2017–2023)
16335	71 (2000–2011)		47 (2017–2023)	47 (2017–2023)
38253	74 (1999–2011)	102 (2015–2022)	23 (2017–2023)	24 (2017–2023)
46390	79 (2000–2011)	289 (2015–2022)	18 (2016–2023)	19 (2016–2023)
47959	70 (2000–2011)	114 (2015–2022)	17 (2017–2023)	18 (2017–2023)
64823	42 (2000–2011)		25 (2017–2023)	26 (2017–2023)
73620	98 (2000–2011)		22 (2017–2022)	22 (2017–2022)
75458	193 (2000–2011)	525 (2015–2023)	27 (2021–2023)	26 (2021–2023)
84671	123 (1999–2011)		34 (2017–2023)	34 (2017–2023)
88048	150 (2000–2011)		17 (2021–2023)	16 (2021–2023)
89826	53 (2000–2011)		39 (2017–2023)	38 (2017–2023)
TOTAL	1127	1030	337	337

luminous stars. These variations have further been found to be periodic with (mostly) a single dominating peak in a periodogram of the Lick RVs (see, for instance, the Lick panels in Figs. 5.6 and 5.7). However, the RVs of each of the systems are challenging to model with orbital companions due to remaining systematics in the RVs; therefore, we refrained from publishing these as planet detections. Thus, a strong selection bias toward (semi-)periodic, but challenging RV variability is inherent to the star sample. On the other hand, with the addition of the more recent SONG and CARMENES data, this makes the stars ideal for studying differences between real planets and intrinsic processes in giant stars.

For many of the stars, the SONG and CARMENES RVs, which span a much more recent time window than the Lick observations, show periodicity at different periods than present in the Lick RVs. This leads to complex and often multi-periodic combined RV periodograms. We examine this behavior more closely in Sect. 5.4.4 and note that this finding already challenges the existence of most of the potential planets. Nevertheless, in order to provide baseline models to test and treat all stars homogeneously, we performed simple one-planet Keplerian fits to the RV data, motivated by the mono-periodicity present in the Lick RVs and attempting to model the most dominant periodicity.

We performed a dynamic nested sampling (Skilling, 2004, 2006; Higson et al., 2019) of the parameter posterior distributions as provided by the DYNesty (Speagle, 2020; Kozlov et al., 2024; Feroz et al., 2009) implementation in the Exo-Striker RV fitting tool (Trifonov, 2019).⁷ We used broad uniform priors, specified in Table C.1, and adopted the mode of the posterior distributions for the further analysis. As the RV jitter is typically much larger than the instrumental scatter, we adopted a single RV jitter term σ_{jitter} for all

⁷<https://github.com/3fon3fonov/exostriker>

instruments. For the two secure planet systems, HIP 75458 and HIP 88048, we used a double-Keplerian model motivated by the detection of a second long-period brown-dwarf companion in the former system (Hill et al., 2021), and the multi-planetary system comprised of two brown dwarfs for the latter (Quirrenbach et al., 2011, 2019). We stress that the final Keplerian models presented for the ten RV-variable stars merely serve to describe the most dominating RV variability in the data, and should not be interpreted as planet detections. These models are tested in the following sections.

The best model inferred from the nested sampling is portrayed in Fig. 5.2 and given in Table 5.3. We also give estimates of the expected p-mode jitter following the scaling relations of Kjeldsen & Bedding (1995) and Kjeldsen & Bedding (2011). The main difference between the two scaling relations is that the latter, apart from the luminosity L and mass M of the star, additionally depends on the effective temperature T_{eff} and the mode lifetime τ_{osc} (Kjeldsen & Bedding, 2011). This is based on the assumption that the power in the velocity fluctuations due to acoustic oscillations behaves similarly to the fluctuations due to granulation. Müller (2019) investigates the applicability of both scaling relations to the Lick sample and finds considerable mismatches especially for cooler stars. Within this study, the modeled jitter for most stars tends to be more consistent with the generally lower estimates by Kjeldsen & Bedding (1995), see Table 5.3, than the updated scaling relations by Kjeldsen & Bedding (2011), despite the mentioned shortcomings of the applicability to giant stars of the former.

Several of the stars show varying periodicity in the different data sets. Many of these show multi-modality in the parameter posterior distributions that lead to difficulties in determining the best fit parameters. The most severe of these cases is HIP 46390, for which the default wide prior often picks up a long-period variability at $P \sim 1200$ d, which is however only present in the SONG data set and coincides with a peak in the SONG window function as can be seen in Fig. 5.6. We thus constrained the period prior to $\mathcal{U}(100 \text{ d}, 1000 \text{ d})$ for this star.

For the two published planet systems, HIP 75458 and HIP 88048, the derived orbital parameters are consistent with the more detailed models by Hill et al. (2021) and Quirrenbach et al. (2019), respectively. Revising the orbital parameters is beyond the scope of this publication.

5.4.2 Radial velocity residual analysis

Having modeled the RV variations of the 12 stars using Keplerians, our goal is to examine several standard tools used to confirm the presence of planets in contrast to an intrinsic origin of these RV variations. In this section, we first describe each metric for the whole sample before discussing the results star-by-star in Sect. 5.5.

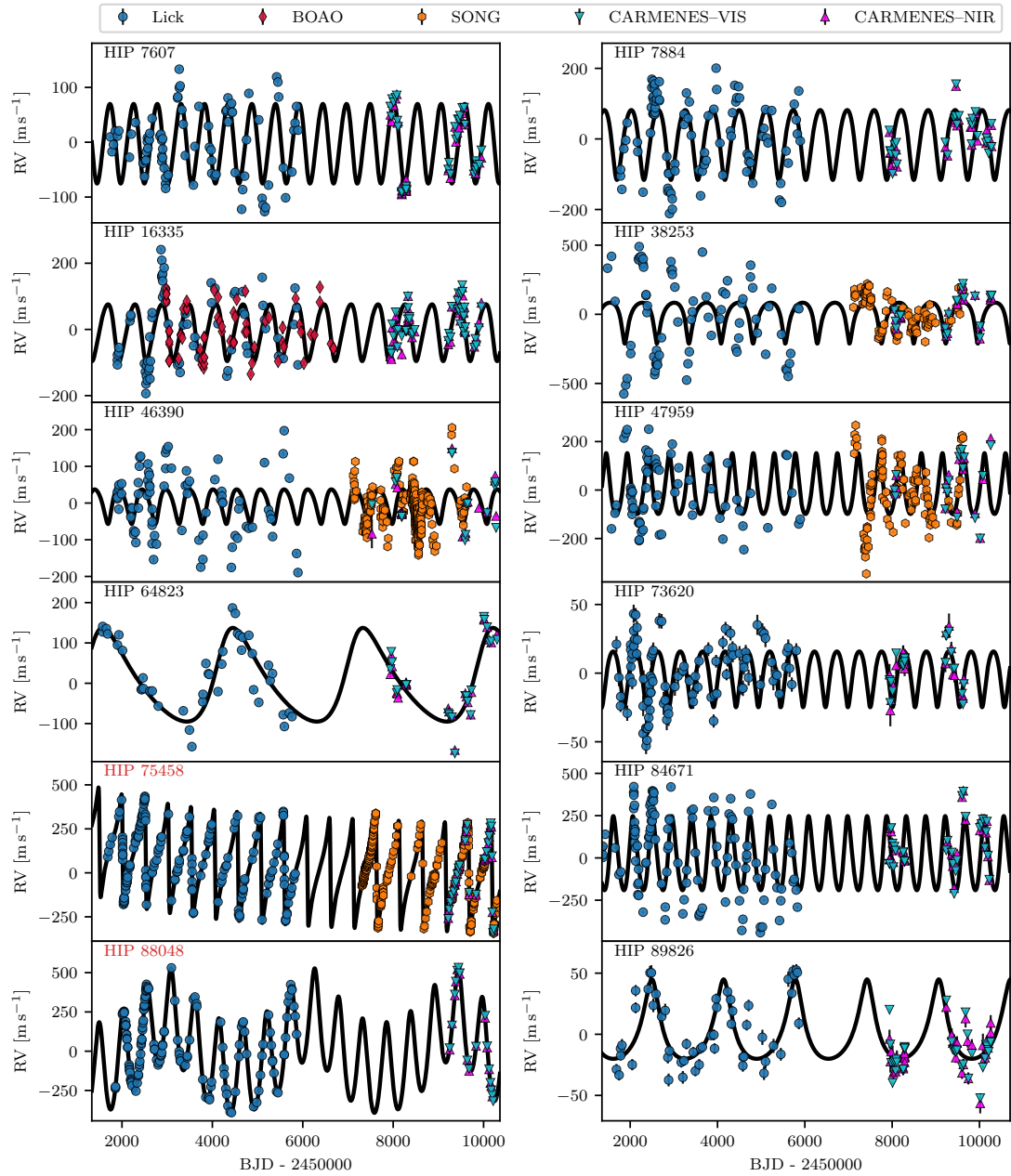


Fig. 5.2.: Best Keplerian models for the 12 stars in the sample. The error bars of the RVs, representing the formal uncertainties of the measurements, are typically smaller than the markers. The identifiers of the two planet hosts, HIP 75458 and HIP 88048, are marked in red. Significant intrinsic RV jitter is present for most of the stars.

Tab. 5.3.: Keplerian parameters obtained through nested sampling.

HIP	P (d)	K (m s ⁻¹)	σ_{jit} (m s ⁻¹)	$\sigma_{\text{jit}}(\text{K\&B95})$ (m s ⁻¹)	$\sigma_{\text{jit}}(\text{K\&B11})$ (m s ⁻¹)
7607	523.3	72.7	33.0	23.5 ± 3.5	61 ± 13
7884	618.0	99.1	62.9	55.4 ± 8.2	181 ± 38
16335	597.3	85.8	51.9	54.7 ± 6.7	173 ± 28
38253	735.3	148.1	164.6	132 ± 84	380 ± 250
46390	523.8	47.3	55.2	84.6 ± 7.9	237 ± 29
47959	481.3	125.7	97.2	74.6 ± 8.8	375 ± 48
64823	2878.1	116.3	36.7	18.0 ± 2.3	50.8 ± 8.8
73620	512.5	20.3	13.3	14.5 ± 3.1	29.9 ± 9.5
75458 b	510.9	310.0	11.7	10.4 ± 1.5	23.5 ± 4.7
75458 c	28193.7	153.3			
84671	447.2	219.6	135.0	110 ± 15	580 ± 100
88048 b	529.9	289.1	7.5	9.1 ± 0.7	10.7 ± 1.0
88048 c	3173.4	175.0			
89826	1642.6	32.5	12.8	14.4 ± 2.3	25.2 ± 5.8

Notes. For HIP 75458 and HIP 88048, we present the period P and semi-amplitude K for both orbital companions labeled as “b” and “c”, respectively. $\sigma_{\text{jit}}(\text{K\&B95})$ and $\sigma_{\text{jit}}(\text{K\&B11})$ denote the respective p-mode jitter estimates based on [Kjeldsen & Bedding \(1995\)](#) and [Kjeldsen & Bedding \(2011\)](#).

For some false-positive planet detections around giant stars, such as γ Dra ([Hatzes et al., 2018](#)), Aldebaran ([Reichert et al., 2019](#)), or ϵ Cyg ([Heeren et al., 2021](#)), the existence of the proposed planets have been ruled out as changes of the amplitudes, phases, or periods of the RV variability have been detected on long timescales. Similar suspicions arise when attempting to model many of the stars in this sample using Keplerians.

One straightforward way to illustrate such problematic cases is to assess the residual variability in the data through a periodogram search. Figure 5.3 portrays the maximum likelihood periodograms (MLPs) ([Zechmeister et al., 2019](#)) of the RVs in the left column, as well as the MLPs of the residuals in the right. We mark the RV period of the best Keplerian model as the red vertical lines. It is known that SONG RVs can suffer from spurious yearly or half-yearly periodicity ([Heeren et al., 2023](#)). Therefore, we plot the MLPs of the residuals excluding the SONG data in blue, while we plot the data set including the SONG data in orange.

The main advantage of the MLP, in contrast to the more established generalized Lomb-Scargle (GLS) periodogram ([Zechmeister & Kürster, 2009](#)), is that an independent noise term is fitted for each period probed in the periodogram analysis, which is important for the luminous giant stars in our sample (see Table 5.3). We computed the MLPs with an oversampling factor of 50 and derived the false alarm probabilities (FAP) following the independent frequency method summarized by [VanderPlas \(2018\)](#)

$$\text{FAP} = 1 - (1 - \exp(-\Delta \ln \mathcal{L}))^{N_{\text{eff}}}, \quad (5.2)$$

with $\Delta \ln \mathcal{L}$ being the log-likelihood difference to a constant model and $N_{\text{eff}} = \Delta f \Delta T$ estimating an effective number of independent frequencies. Here, Δf is the range of the probed frequencies, while ΔT is the range of the time interval covered by the data set. In Fig. 5.3, we overplot the FAPs of 5% (dashed), 1% (dash-dotted), and 0.1% (dotted) as gray horizontal lines.

As long as the star-planet interactions due to tidal forces are small, which is generally to be expected for the relatively long-period variations considered in this work, the RV variations caused by a single planet should occur at a stable, largely unchanging period. For a well-behaved planetary system, one can therefore expect that no periodicity remains in the RV data in the adjacent period region after removing the best Keplerian model.

It can be seen from Fig. 5.3 that several of the stars (for instance HIP 7607, HIP 7884, HIP 16335, HIP 38253, HIP 46390, HIP 47959, HIP 73620, and HIP 84671) have significant residual power very close to the best period of the fit, indicating that the RVs are not mono-periodic. Due to the proximity of the residual periods, and given the masses needed to explain the dominant RV variations with planetary companions, which are all Jovian or higher, strong stability constraints rule out additional companions at these periods. From this relatively simple test alone, we can therefore conclude that planetary companions are unlikely explanations in these cases.

In comparison, for the two published planet systems, HIP 75458 and HIP 88048, the best fits remove the power close to the RV periods almost completely. We note that for HIP 75458 some significant peaks (after removing the SONG data) are left in the proximity of the Kepler period of ι Dra b. Several of these peaks are close to alias periods between the Keplerian period and peaks in the combined window function. These peaks are likely a consequence of the large eccentricity of the orbit of ι Dra b. All residual peaks for ι Dra have much lower $\Delta \ln \mathcal{L}$ than the original peak corresponding to the planet period. This is in contrast to the aforementioned challenging cases.

Two planet candidates, HIP 64823 and HIP 89826, stand out as there is no residual power close to the RV period. Both also show the longest periodicity (see Table 5.3) among the planet candidates. We conclude that testing the residual RVs for significant periodicity can be a simple check for a multi-periodic (and thus likely intrinsic) behavior of the RV variations.

5.4.3 Infrared test

Another approach that mostly emerged in the context of RV variability caused by star spots, is to test whether the RV signal is consistent at optical and infrared wavelengths. For star spots, as the contrast ratio between a cool spot and the stellar surface is much smaller in the infrared than in the optical, the RV variation introduced by a spot is generally expected

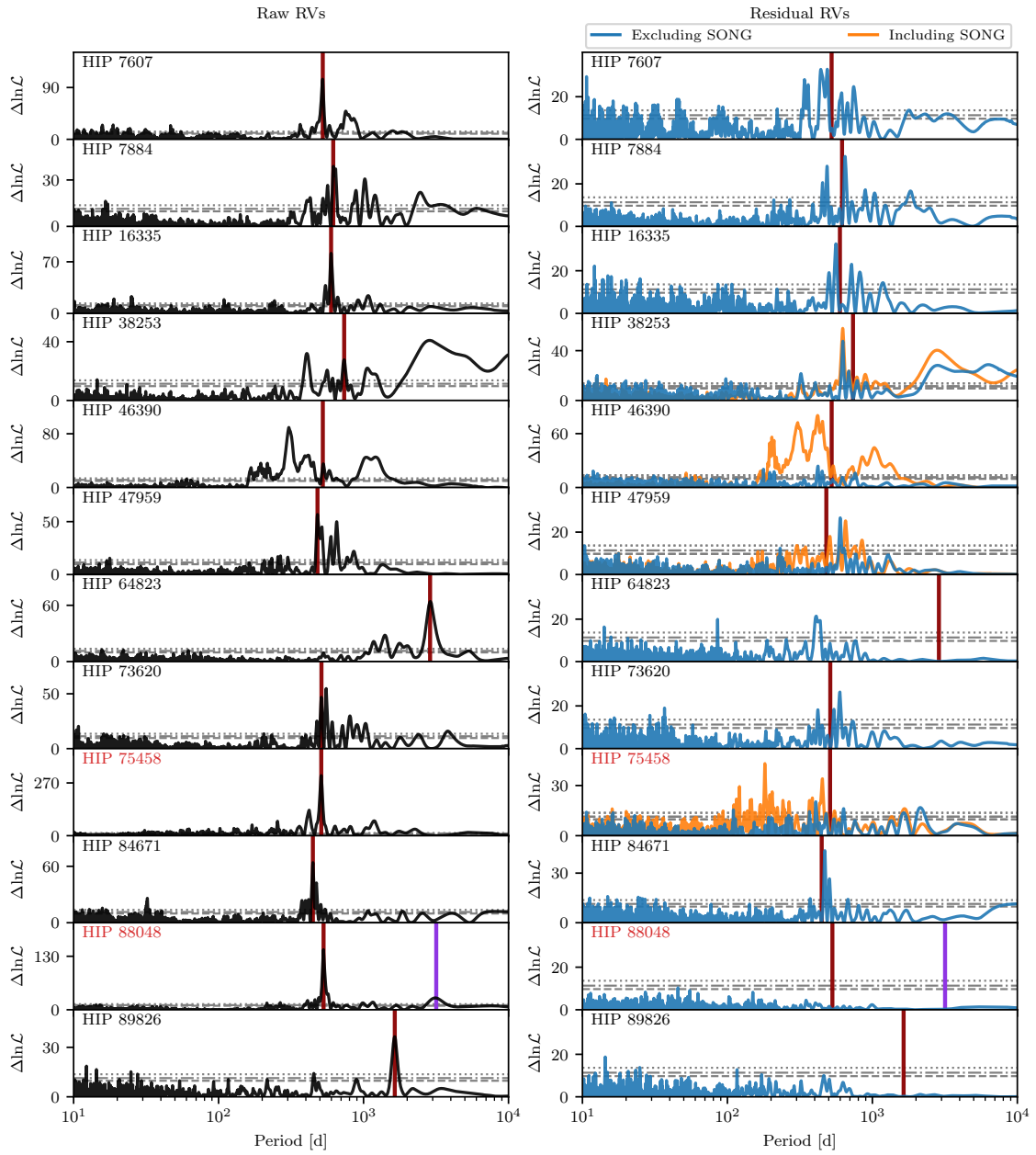


Fig. 5.3.: Maximum likelihood periodograms of the RVs (left) and the residuals (right) after subtracting the best Keplerian model. As the SONG RVs are known to show spurious RV periodicity at a one-year period (Heeren et al., 2023), we plot the MLPs of the residual RVs excluding the SONG data in blue, while the periodograms including the SONG data are shown in orange. The FAPs of 5% (dashed), 1% (dash-dotted), and 0.1% (dotted) are plotted as gray horizontal lines. The identifiers of the two planet hosts, HIP 75458 and HIP 88048, are marked in red. Significant periodicity remains close to the strongest RV period after removing the best fit for many of the stars.

to be smaller in the infrared compared to the optical (Desort et al., 2007; Huélamo et al., 2008; Reiners et al., 2010). As the photometric amplitudes of pulsating stars are known to be different in optical and infrared passbands as well (Percy et al., 2001), one can also expect the infrared test to be applicable in the context of suspected non-radial oscillations in RV data (Mitchell et al., 2013; Trifonov et al., 2014, 2015; Ortiz et al., 2016). In contrast, a planetary companion should induce a consistent RV signal in all wavelength regimes.

To first order, one can expect that the semi-amplitude K is the only changing parameter when fitting contemporary RVs taken in the VIS and NIR channels of CARMENES. We thus kept all parameters but K fixed from the previous modeling detailed in Sect. 5.4.1 and performed another dynamic nested sampling of the posterior distribution of K using only the CARMENES–VIS and CARMENES–NIR data, respectively. We adopted the mode of the distributions and derived the uncertainties by identifying the interval around the mode that encompasses 68% of the posterior samples, corresponding to a 1σ credibility interval. We ensured the unimodality of each distribution by eye. We stress that we only compare the semi-amplitudes between the two CARMENES channels. These can, in some cases, be inconsistent with the determined semi-amplitudes using the whole data set, indicating that the RV signals are not stable over long time frames but can also be a consequence of sparse sampling.

We plot the results of the infrared test in Fig. 5.4. We find no significant differences between the amplitudes of the variations derived from the CARMENES–VIS and CARMENES–NIR data. For several of the very luminous stars, large error bars due to the large RV jitter and relatively few data points, sampling only two to three phases of the RV variations, reduce the informative value of the infrared test.

In Spaeth et al. (2024), we present a simulation of an $l = 1, m = 1$ non-radial oscillation that can reproduce the variations of the RVs and the activity indicators for the false-positive brown-dwarf host NGC 4349 No. 127 (Delgado Mena et al., 2018, 2023). Using the same simulation settings as in Spaeth et al. (2024) to derive hypothetical RVs in the CARMENES–VIS and CARMENES–NIR channels leads to semi-amplitudes $K_{\text{VIS}} = 249.6 \text{ m s}^{-1}$ and $K_{\text{NIR}} = 257.6 \text{ m s}^{-1}$, respectively, a relative difference of about 3%. This would, for most of the stars, be insignificant given the derived uncertainties in the presence of large stellar jitter. Thus, we conclude that the absence of significant differences between semi-amplitudes derived in the optical and the infrared cannot rule out a non-radial oscillation model.

We note that these findings are only valid for relatively small temperature variations employed in the simulations (here $\delta T_{\text{eff}} = 2.5 \text{ K}$), for which the chromatic limb-darkening correction dominates the chromatic behavior of the RVs. For larger temperature variations and other oscillation modes, the relative amplitude difference between infrared and visual RVs can change slightly compared to the presented case. However, our test simulations,

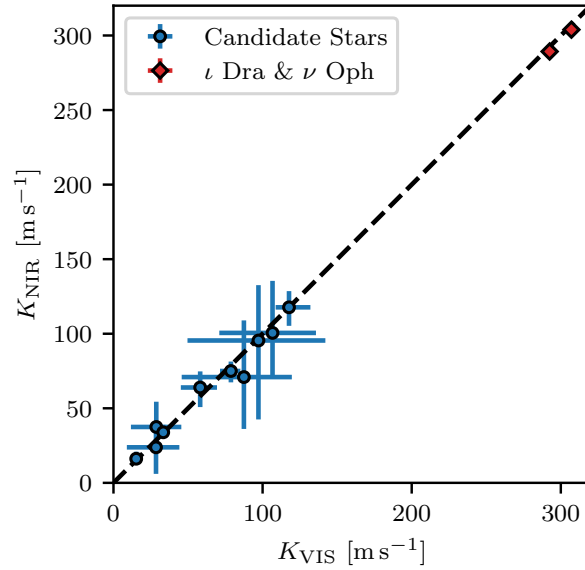


Fig. 5.4.: Semi-amplitudes K from the CARMENES–NIR channel plotted against the semi-amplitudes in the VIS channel. We highlight the two secure planet hosts, ι Dra and ν Oph as red diamonds, while we show the planet candidates in blue. For ι Dra and ν Oph, only the inner orbital components are examined due to the short baseline of the CARMENES observations.

including more extreme values and different oscillation modes, did not reveal any significant increase in the relative RV difference between the VIS and NIR channels, while maintaining photometric variations comparable to those of the stable stars in this sample. The infrared test is thus not sensitive enough to validate or disprove potential planets orbiting evolved stars.

5.4.4 Analysis of the activity indicator time series

State-of-the-art, stabilized spectrographs, such as CARMENES, acquire a set of activity indicators simultaneous to the RVs. These activity indicators have proven to be very useful in the study of magnetic activity, as manifested in star spots or plages, in RV surveys that target main-sequence or low-mass stars. [Delgado Mena et al. \(2018, 2023\)](#) have used activity indicators measured by HARPS successfully to rule out a number of exoplanets around cluster giants, showing that these indicators are also applicable to giant stars, for which magnetic activity is not necessarily the major concern.

Correlation analysis

In [Spaeth et al. \(2024\)](#), we show that the HARPS activity indicators for NGC 4349 No. 127, a known false-positive host ([Delgado Mena et al., 2018, 2023](#)), show peculiar correlations with the RVs. The CRX and the RVs are slightly positively correlated, while the dLW, FWHM, and contrast of the CCF have “closed-loop”, Lissajous-like correlations with the RVs. We further show that these are the correlations expected from an $l = 1, m = 1$ non-radial oscillation mode.

Motivated by these findings, we scanned the Lick $H\alpha$ measurements and the CARMENES activity indicators for similar correlations with the RVs. By eye, we did not find any reliable closed-loop correlations in the sample. These could potentially be obscured by variations due to short-term p-mode oscillations, or the superposition of different modes ([Spaeth et al., 2024](#)). We further note that the RV amplitudes of the planet candidates in this sample are typically smaller than those of NGC 4349 No. 127, which makes the identification of such correlations more challenging.

Lacking indications for more complex correlations, we systematically tested the activity indicators and RVs for linear correlations. For each of the activity indicators and corresponding RV time series, we fitted for a linear relation. We assessed the significance of the resulting slope by performing a permutation test. That is, we uniquely permuted the pairs of variables $N = 10\,000$ times and counted the number of simulated slopes m with $|m| \geq |m_{\text{real}}|$. The two-tailed p -value of the significance of the measured slope is then defined, following [Ernst \(2004\)](#) and [Phipson & Smyth \(2010\)](#), as

$$p = \frac{N_{|m| \geq |m_{\text{real}}|} + 1}{N + 1}. \quad (5.3)$$

We define correlations with $0.1\% \leq p < 5\%$ as tentative correlations, while we regard $p < 0.1\%$ as significant. We computed p -values for all correlations without applying any threshold to the slope beforehand. The combined results of the linear correlation analysis can be seen in [Fig. 5.5](#). We observe that only three of the stars, HIP 7607, HIP 84671, and HIP 89826 show any significant correlations. Only the former two show correlations in more than one indicator. That is surprising since we can find strong arguments against planets as the cause of the RV variations for a majority of the stars based on other metrics. In contrast to the case of NGC 4349 No. 127, we also do not find correlations between the CRX and the RVs in the CARMENES VIS channel for any of the stars.

On the other hand, we observe that all stars show at least one tentative correlation between the indicators and the RVs, even the two secure systems HIP 75458 and HIP 88048. Of course, these two systems could in principle also be contested, but given the extremely well-behaved RV variations of both systems with a large eccentricity in case of HIP 75458 and well-studied dynamical constraints for HIP 88048 ([Quirrenbach et al., 2019](#)), there

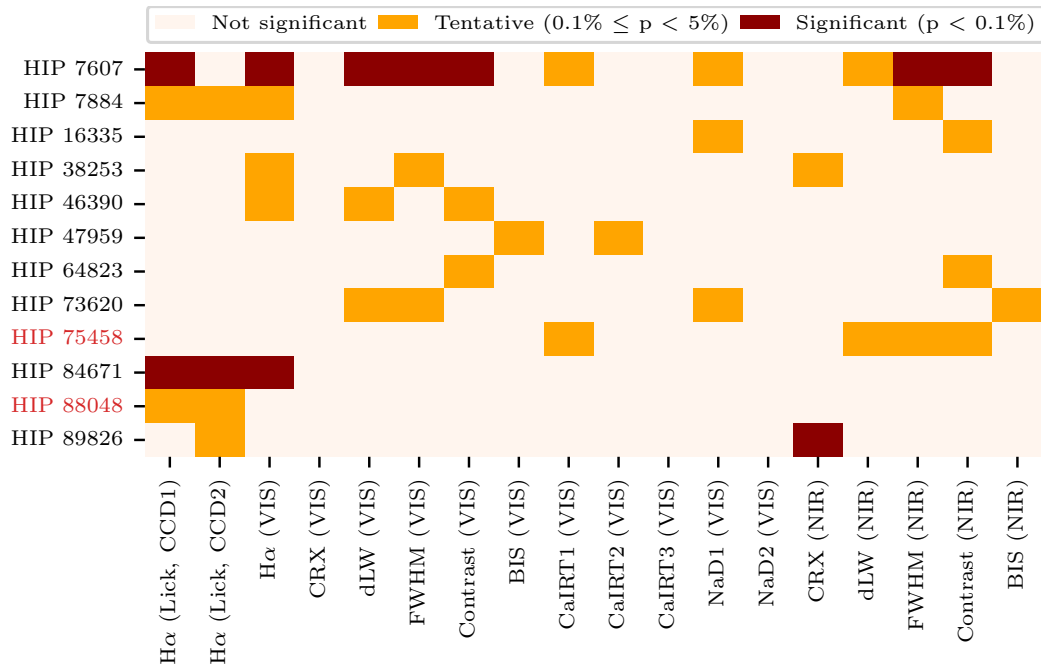


Fig. 5.5.: Results of the linear correlation analysis. For each star we show the significance of the linear correlation between the activity indicator labeled on the x-axis and the respective RV data set. Red colors indicate significant ($p < 0.1\%$) linear correlations, while orange colors represent tentative ($0.1\% \leq p < 5\%$) correlations. The identifiers of the two planet hosts, HIP 75458 and HIP 88048, are marked in red.

are good reasons to assume that the planetary systems around these stars are real. In fact, it rather reflects the relatively poor performance of the simple linear correlation analysis.

This can be understood since searching for linear correlations in this way is sensitive to different kinds of variations of the activity indicators. These could, for instance, be linked to the known short-term p-mode pulsations or the stellar rotation and might be completely unrelated to any RV periodicity introduced by a planet. Such short-term variations in the activity indicators, combined with long-period RV variations of a different origin, can lead to spurious correlations. We thus conclude that a simple linear correlation analysis is not apt to differentiate between planets and intrinsic variations for the majority of the stars and argue in favor of more sophisticated metrics such as the periodogram analysis discussed in the following. We note that a combination of a well-behaved linear correlation with a finding of clear periodicity at the RV period could be helpful to remove the contribution of the intrinsic signal from the RVs (see, for instance, [Robertson et al. 2014](#)).

Activity periodogram analysis

To assess whether the activity indicators vary at periods linked to the established RV periodicity, we employ a periodogram search using MLPs. We present the results for all stars in Figs. 5.6 and 5.7. These show the combined MLPs for all time series (RVs and activity indicators) of all instruments available for each star. Again, we overplot as gray horizontal lines the FAPs of 5% (dashed), 1% (dash-dotted), and 0.1% (dotted). We generally refer to peaks with $0.1\% \leq \text{FAP} < 5\%$ to be tentatively significant, while we consider peaks with $\text{FAP} < 0.1\%$ to be significant. We further overplot the period for each Keplerian model (see Table 5.3) as thick, vertical, dark red lines and label their respective periods at the top of each panel. We also show the aliases of the RV period, computed with the strongest peak in each respective window periodogram, as thinner red lines, while we portray three harmonics and sub-harmonics of the RV period with lower opacity. The periodograms of the window functions were computed as discrete Fourier transforms and are plotted in the bottom panel. The strongest window peak for each instrument was detected in the range between 300 d and the baseline of the respective time series and is marked as the colored arrows on the x -axis of the panel. Following VanderPlas (2018), periodicity at the alias frequencies or the harmonics of the RV period should be regarded with caution. We note that many of the window functions show multiple peaks. However, we refrain from computing and plotting the aliases for each peak to avoid a cluttering of the plot. The results of the activity periodogram analysis are discussed on a star-by-star basis in Sect. 5.5.

DBSCAN cluster analysis

A useful way to summarize and detect associated periodicity in multiple CARMENES activity indicators is presented by Kemmer et al. (2024). Following this approach, we first detected all peaks by their FAPs and periods in the MLPs of all CARMENES activity indicators (both channels). We note that the process allows for multiple peaks of the same indicator time series to be detected. Next, we employed the DBSCAN (Ester et al., 1996) clustering algorithm available through `scikit-learn` (Pedregosa et al., 2011) on all identified peaks with $\text{FAP} < 50\%$. We tested different settings for the DBSCAN parameter ϵ , which defines the maximum distance between two peaks to be considered neighbors, setting it to one-third of the width of the peaks in the periodogram as estimated by $\delta f = (t_{\max} - t_{\min})^{-1}$. We found this value to provide good results at the long periods of interest in this work. We limited the identified clusters to have at least three peaks, with at least one of the peaks having tentative ($\text{FAP} < 5\%$) significance. We further limited the cluster search to periods longer than 100 d, to only target periodicity close to the dominating, long-period variations of the RVs.

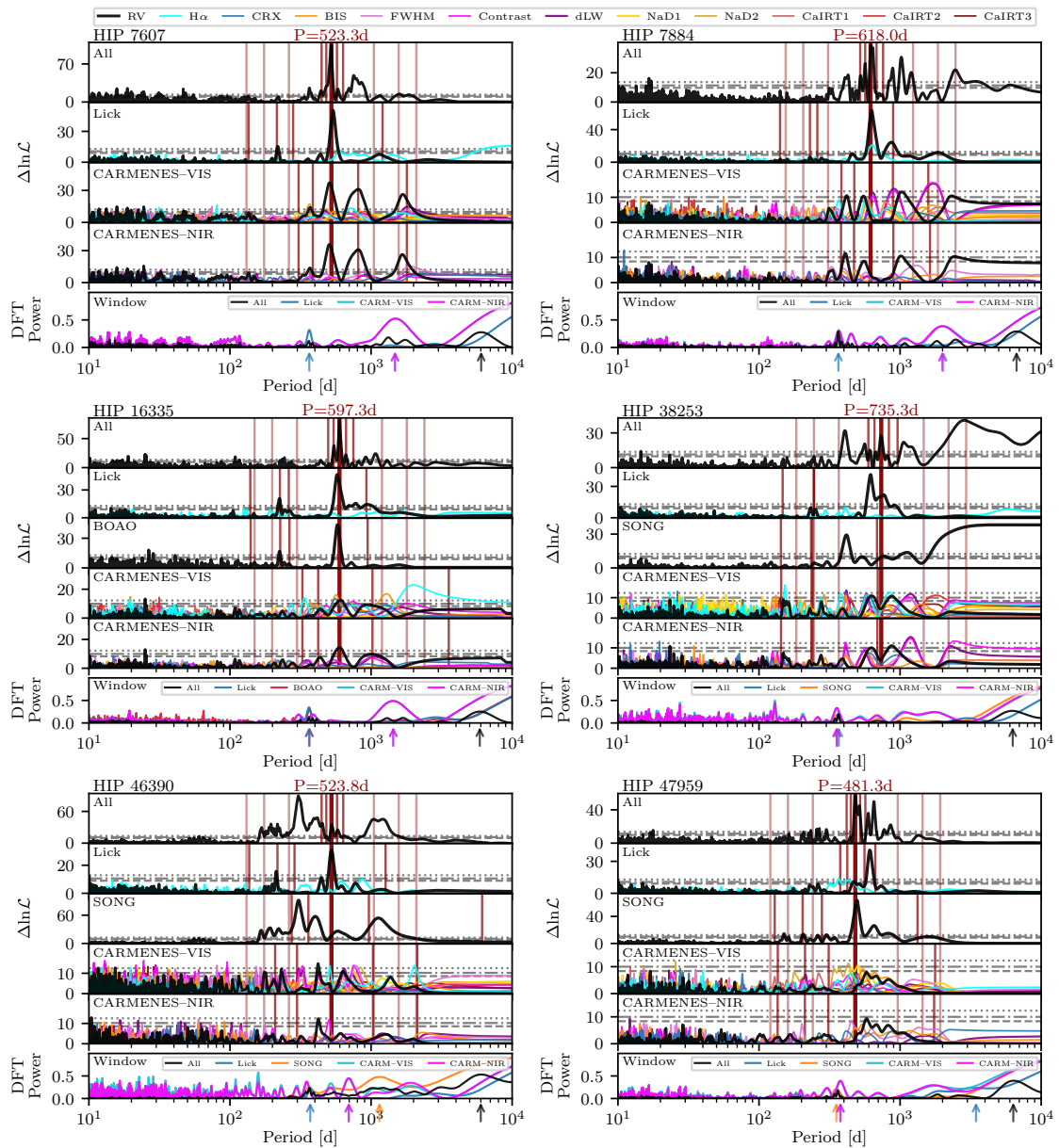


Fig. 5.6.: Maximum likelihood periodograms for six sample stars. The top panel for each star portrays the combined RV MLP. In the remaining panels, we show the MLPs of the RVs (black) and activity indicators (see legend) for each instrument. The FAPs of 5% (dashed), 1% (dash-dotted), and 0.1% (dotted) are plotted as gray horizontal lines. The bottom panel shows the instruments' window functions derived as discrete Fourier transforms (DFTs). The thick, red, vertical line indicates the period of the Keplerian fit (see Table 5.3). The alias periods, corresponding to the most significant peak in the respective window function, are shown as thinner lines. The positions of these window peaks are marked with colored arrows in the bottom panels. Notably, the CARMENES VIS and NIR window functions largely overlap. Additionally, we display the harmonics and sub-harmonics of the period of the Keplerian fit as red lines with lower opacity.

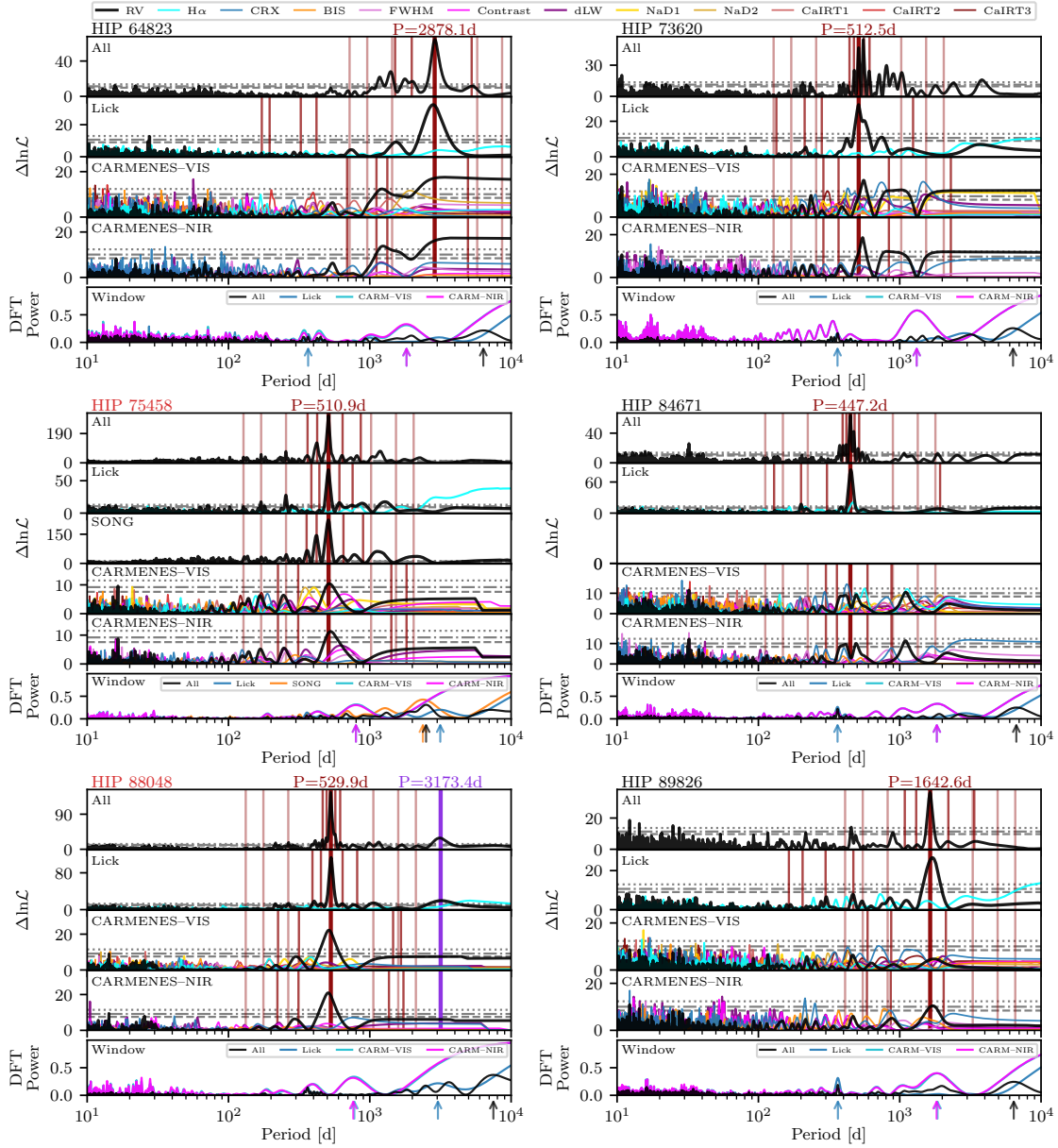


Fig. 5.7.: Maximum likelihood periodograms for the remaining six stars. The same description as in Fig. 5.6 applies. The FAPs of 5% (dashed), 1% (dash-dotted), and 0.1% (dotted) are plotted as gray horizontal lines. The identifiers of the two planet hosts, HIP 75458 and HIP 88048, are marked in red. For HIP 80488, we mark the second significant periodicity, corresponding to the outer brown-dwarf companion, as the violet, vertical line. We omit plotting its aliases and harmonics for visual clarity.

The results of the cluster analysis are plotted in Fig. 5.8. These are discussed in detail on a star-by-star basis in the following. In general, we find that a majority of the stars whose RV variations are likely intrinsically induced show clustered activity periodicity close to the main RV period. These findings are mostly contributed by the VIS channel, which, however, also has several additional line indicators in contrast to the NIR. Somewhat unsurprisingly, we often find that the line shape indicators (dLW, BIS, contrast and FWHM of the CCF) vary at similar periods and thus form activity clusters. However, we often also find contributions to the same clusters from other indicators, including the CRX and the chromospheric indicators targeting the H α and NaD lines.

5.5 Combined results for individual stars

In this section, we discuss the results star-by-star, aiming to determine whether planets or intrinsic variations are causing the observed RV variations.

5.5.1 HIP 7607

The horizontal branch giant HIP 7607 (*v* Per) shows strong and clearly significant RV periodicity close to the fitted period of $P = 523.3$ d in the Lick and both of the CARMENES data sets in Fig. 5.6 (top left). For both instruments, periodicity can also be found at the respective alias periods (thinner, red lines). We note that the peaks in the Lick RV MLP ($P = 538$ d, see also Hekker et al. 2008) and the CARMENES RV MLPs (both $P = 508$ d) are slightly offset. However, given the relatively short baseline of the CARMENES observation and the width of the peaks, this difference cannot be regarded as significant.

Examining the activity indicators in Fig. 5.6, we find a number of peaks with tentative significance in the vicinity of the RV period in the CARMENES VIS channel. The most significant peak (FAP $\sim 0.1\%$) is contributed by the NaD2 line at $P = 491$ d, slightly offset from the RV period. Further tentative peaks close-by can be found by the dLW, contrast, and BIS indicators. Further periodicity in the activity indicators is also present close to the alias period of the fitted RV period. The DBSCAN cluster analysis in Fig. 5.8 (top left) reveals two clusters of activity variability centered at $P = 478$ d (cyan) and $P = 572$ d (orange). Together, the activity indicators clearly cast doubts on the planetary nature of the RV signal.

The doubts are further strengthened by several significant correlations present between the activity indicators and the RVs, as evident from Fig. 5.5. However, as discussed in Sect. 5.4.4, the overall mixed results of the correlation analysis reduce the informative value of such correlations. The final and strong argument against the planetary nature

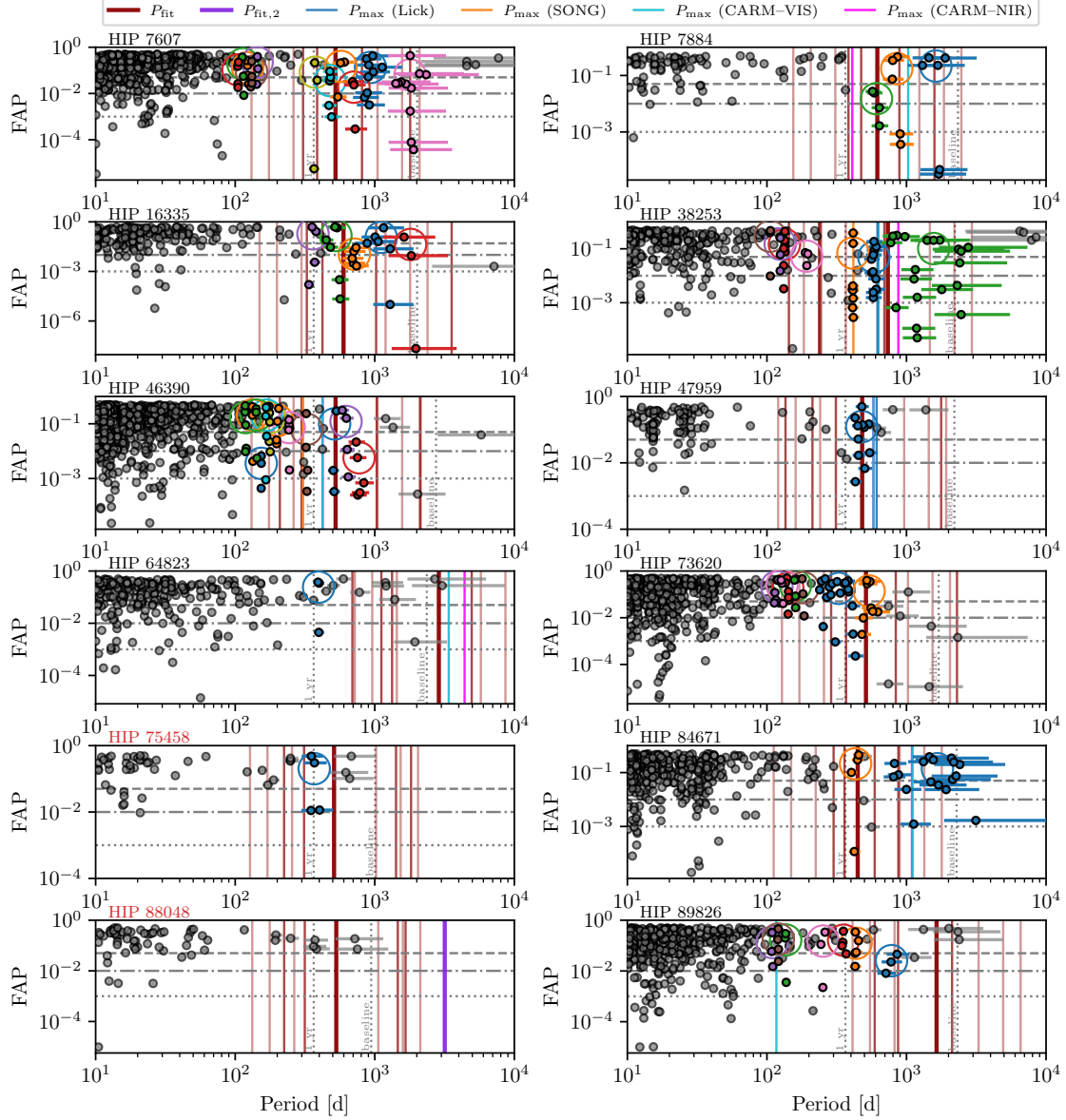


Fig. 5.8.: Results of the DBSCAN clustering algorithm. In each panel, all identified peaks in the MLPs of the CARMENES activity indicators are shown as filled circles. Arbitrarily colored circles represent activity peaks assigned to clusters by DBSCAN, while gray circles indicate peaks that are not part of any cluster. The larger, empty circles indicate the center periods and FAPs of the clusters. We further overplot the FAP levels of 5% (dashed), 1% (dash-dotted), and 0.1% (dotted) as horizontal gray lines, and the fitted RV period (thick), its aliases (thin, based on the VIS window function), and harmonics (lower opacity) as vertical red lines. Furthermore, for stars where individual instruments exhibit a strongest period that deviates from the fitted period by at least 10% (restricted to $100 \text{ d} < P_{\text{max}} < 5000 \text{ d}$), we overplot the strongest RV period detected in the MLP of the respective instrument using vertical, colored lines specified in the figure legend. The identifiers of the two planet hosts, HIP 75458 and HIP 88048, are marked in red. For the latter, we also mark the periodicity of the outer orbital companion in violet.

of the RV signal comes from analyzing the residual RVs. As can be seen in Fig. 5.3, there is significant periodicity left at $P = 441$ d, $P = 489$ d, $P = 614$ d, and other more distant periods. Similar systematics in the residuals of the Lick data of HIP 7607 have been noted by Quirrenbach et al. (2011). Trying to explain this additional periodicity with another orbital companion requires a minimum mass exceeding $1 M_{\text{Jup}}$, which would make the proposed system unstable. It is thus much more likely to be a manifestation of a multi-periodic incoherent type of RV variation that is linked to intrinsic processes.

5.5.2 HIP 7884

One star that highlights the usefulness of the periodogram analysis of activity indicators is HIP 7884 (ν Psc), a bright ($V = 4.4$ mag) K3 giant star likely located on the RGB (see Table 5.1). Focusing first on the Lick RV MLP in Fig. 5.6 (top right), one can clearly see the dominant and highly significant peak in the RV periodogram at $P = 628$ d. However, in the CARMENES RVs (third and fourth panels) no significant periodicity can be found at that period, revealing peaks at $P = 418$ d, $P = 549$ d, and $P = 1028$ d in the VIS instead, with peaks in the NIR at similar periods. As a consequence, the MLP of the combined RVs (top panel) reveals a complex structure, reducing the significance of the most prominent peak compared to the Lick data set alone, and introducing further peaks close-by. These findings likely indicate that the periodic variation present in the Lick data set, is not present in the CARMENES RVs, which cover a more recent time baseline. Analyzing the residual periodogram in Fig. 5.3, one can see this behavior manifested as a second peak, a mere 30 d distant in period space.

Examining the available activity data in Fig. 5.6, one can find a significant peak of the Lick $H\alpha$ measurements at the period of the Lick data, as well as peaks of the dLW and the contrast of the CCF of the CARMENES VIS channel, which are both evident at the RV period and at its alias frequencies (thinner, red lines). Thus, a planetary origin of the RV periodicity can be excluded. The activity peaks in the CARMENES data appear to belong to a cluster (including tentative peaks from the CARMENES $H\alpha$ indicator and the BIS) centered very close to the fitted period (Fig. 5.8). One further observes two clusters centered at the two long-period aliases of the RV period. Despite these significant detections of activity variations at the RV period, there are only tentative correlations present in Fig. 5.5. These include the two time series of Lick $H\alpha$ measurements, as well as the $H\alpha$ indicator derived from the visual CARMENES channel. Each of the $H\alpha$ time series shows a tentative positive correlation with the RVs. The FWHM of the CCF of the NIR channel is also tentatively positively correlated with the RVs.

Combining all the above findings, these observations make HIP 7884 another example of a giant star whose measured RVs, when viewed in isolation, seemed to be consistent with an orbital companion for over 12 years. However, by using a much longer RV baseline

and acquiring reliable activity indicators, its cause can decisively be concluded to be of intrinsic origin.

5.5.3 HIP 16335

One of the most interesting stars within the sample is HIP 16335 (σ Per), which was published to host a planetary companion with minimum mass $m_p \sin(i) = 6.5 \pm 1.0 M_{\text{Jup}}$ in a $P = 579.8 \pm 2.4$ d orbit by Lee et al. (2014). The authors used RV data from the Bohyunsan Observatory Echelle Spectrograph (BOES) at the Bohyunsan Optical Astronomy Observatory (BOAO) in Korea, along with activity indicators derived from the Ca II H line, and studied the bisector variations of the Ni I 6643.6 Å line. They find no periodicity or correlations with the RVs. We include the BOAO data set as published by Lee et al. (2014) in this analysis.

While the peaks in the BOAO and Lick RV MLPs (Fig. 5.6), which are roughly contemporary, are clearly apparent and strongly significant, the RVs in the CARMENES visual channel show a much less significant peak, which is further slightly offset to $P = 609$ d. The infrared RVs of CARMENES show a strong peak at $P = 599$ d. However, two strong peaks close to the originally published planet period emerge in the CARMENES–VIS activity indicator MLPs: Both the CRX and the BIS of the visual channel have significant peaks at $P = 559$ d and $P = 565$ d, respectively, close to the originally published planet period $P = 579.8 \pm 2.4$ d (Lee et al., 2014). We further note additional peaks of the VIS H α indicator, the CCF contrast, and the BIS in the vicinity of the alias and harmonic periods of the RVs.

The DBSCAN clustering algorithm presented in Fig. 5.8 shows two adjacent clusters neighboring the RV period, which shows that there is further, tentative periodicity of activity indicators close-by. We note that the two significant peaks in the CRX and BIS are attributed to the cluster centered at $P = 527$ d (green).

The strong evidence against the planetary companion is further enhanced when looking at the residuals of the RV fit in Fig. 5.3. After subtracting the best planet fit, significant variability with a period $P = 561$ d remains, a mere 37 d offset from the fitted period. This additional variability can hardly be explained by a second orbital companion fulfilling stability constraints. Instead, we interpret it to be a sign of a non-constant periodicity or amplitude of the RV signal. Altogether, these findings strongly argue against the planetary nature of the RV signal of HIP 16335 and thus contradict the findings by Lee et al. (2014).

5.5.4 HIP 38253

HIP 38253 (HD 63752) is the most luminous star in the sample and shows relatively large-amplitude RV variations with $K \sim 148.1 \text{ m s}^{-1}$. First hints of an intrinsic origin have already been found by [Hekker et al. \(2005\)](#). Examining the MLPs in [Fig. 5.6](#) confirms these findings.

The Lick RVs show a dominant peak at $P = 619 \text{ d}$, with a small side-lobe and secondary peak at $P = 766 \text{ d}$. In contrast, the SONG data set, bridging between the Lick RVs and the most recent CARMENES observations, does not show the same periodicity but instead a most dominant peak at $P = 416 \text{ d}$, and further power at longer periods. This shorter-period peak is, however, no longer present in the CARMENES data set, which rather shows two less significant peaks at $P = 631 \text{ d}$ and $P = 874 \text{ d}$. It is thus apparent that RV variations at inconsistent periods are present in data sets spanning different time windows. This is also evident from the complex structure of the combined MLP in the top panel. The nested sampling algorithm reveals $P_{\text{fit}} = 735.3 \text{ d}$ to be the modal value of the period posterior distribution, which shows a slight bimodal structure. It is clear that this RV variation is not stable and cannot be caused by a planetary companion, which would be expected to be consistently present in all data sets. This is also evident from the rather unsatisfying mono-periodic fit to the RV data in [Fig. 5.2](#).

Due to this multi-periodicity in the RV data, the activity time series is more challenging to interpret. Taking a look at the clustering results in [Fig. 5.8](#), it is evident that a strong cluster of significant activity indicator periodicity is present very close to the RV period present in the SONG data set (marked as the orange line). The most dominant peaks stem from the line shape indicators (dLW, FWHM and contrast of the CCF, BIS) in the VIS, but also partially in the NIR. There are further tentative peaks by the $H\alpha$ and CaIRT2 lines in the vicinity, as apparent from [Fig. 5.6](#).

Close to the strongest period in the Lick RVs ($P = 619 \text{ d}$, blue line) is another, less significant, cluster of activity variations, apparent both in the line shape indicators in VIS and NIR, as well as the $H\alpha$ line, and the CRX in the VIS. Finally, there appears to be another cluster of activity variations present at somewhat longer periods. While there is no significant peak exactly at the fitted RV period, it appears that each tentative peak of the CARMENES RVs is accompanied by at least tentative variability in the activity indicators.

As noted for the whole sample, the correlation analysis reveals only tentative correlations between the activity indicators and the RVs. This result is surprising given the strong support for an intrinsic origin of the RV variations. It strengthens our conclusion that a simple linear correlation analysis cannot properly capture the complexities of the relations between activity indicators and RVs for giant stars. It can likely be understood as a consequence of the multi-periodic nature of the variations in both the RVs and the

indicators. Looking at the residual RVs in Fig. 5.3, it is clear that significant residual periodogram power is present in the vicinity of the fitted RV period, confirming this multi-periodicity. We conclude that the RV variations of HIP 38253 are of intrinsic origin.

5.5.5 HIP 46390

Somewhat similar to HIP 38253 is the behavior of the very bright ($V = 1.97$ mag) giant HIP 46390 (Alphard, α Hya, HD 81797), although the amplitude of the variations is much smaller ($K \sim 47.3 \text{ m s}^{-1}$). Again, the strongest peak in the Lick data set (2000–2011) at $P = 524$ d is not dominant in the later SONG observations (2015–2022), which have the strongest periodogram peak at $P = 306$ d (see Fig. 5.6). The most recent CARMENES observations (2016–2023) show their most significant periodicity at $P = 422$ d. As for HIP 38253, this also rules out the presence of a stable planetary system for HIP 46390, which coincidentally is the second most luminous star in the sample. As mentioned in Sect. 5.4.1, the nested sampling algorithm shows multimodal posterior distributions with different periodicities being picked up in different runs of the algorithm. The final model used in this work is mostly dominated by the Lick RVs, with the SONG RVs showing a clear phase shift in a phase-folded RV plot.

Subtracting the best Keplerian model from the RVs and examining the residual periodogram in Fig. 5.3, we find that there remain several significant peaks when including the SONG data (orange). Removing the SONG data set from the analysis, we find that there is residual periodicity with significant peaks at $P = 422$ d and $P = 451$ d (blue periodogram). Thus, the best model cannot remove all variability close to its modeled period.

Examining the activity indicator periodograms in Fig. 5.6 and their clustering in Fig. 5.8, we find a significant peak by the CARMENES–VIS $H\alpha$ indicator (FAP = 0.03%) close to the Lick period. This activity peak is attributed to a small cluster, jointly with a tentative peak by the contrast of the CCF in the NIR channel, centered at $P = 515$ d. Close to the SONG RV period ($P = 306$ d, orange line in Fig. 5.8) that dominates the combined RV periodogram, we find a close cluster at $P = 325$ d of significant and tentative peaks mostly contributed by the dLW and contrast of the CCF in the VIS, as well as the NaD2. Thus, the dominant RV periodicity in the SONG RVs also seems to be present in the variations of the spectral lines as measured by CARMENES. Finally, we observe a tentative peak by the dLW close to the most prominent RV peak in the CARMENES data set. As with many other stars, we find only tentative correlations between the $H\alpha$ indicator, dLW, and CCF contrast on the one hand, and the RVs on the other. Taken together, there is overwhelming evidence that the RV variations observed for HIP 46390 are of intrinsic origin, with changing periodicity on timescales of a quarter of a century.

5.5.6 HIP 47959

HIP 47959 (18 Leo, HD 84561) is another relatively luminous star within our sample. Examining Fig. 5.6 (bottom right panel), the RV variations can again be shown to have varying periodicity in different time windows. While the Lick RVs show dominant periodicity at $P = 611$ d, the SONG data taken at later epochs have a shifted peak at $P = 495$ d, with a secondary peak at $P = 654$ d, close to the Lick RVs. The former periodicity dominates the RV period determined through the nested sampling ($P = 481.3$ d). The CARMENES data do not yet show a significant peak but have their strongest periodicities at $P = 580$ d in both channels. The combination of all available RV data then leads to a relatively complex periodogram apparent in the top panel. Following from this multi-periodic behavior, one can find a number of significant peaks close to the removed period in the residuals (Fig. 5.3).

Adding to these strong arguments against a planetary nature of the RV variations, we can find a number of tentative peaks in the activity indicators of the CARMENES channels (mainly the VIS), with some periodicity (both significant and tentative) present in the Lick $H\alpha$ indicator at somewhat shorter periods. Analyzing these using the DBSCAN clustering algorithm in Fig. 5.8, we find a strong cluster at $P = 478$ d, coinciding closely with the fitted RV periodicity that was mainly dominated by the SONG RVs. It is thus evident that the RV variations are again of intrinsic origin. Despite these indications of intrinsic RV variations, only two tentative correlations are found between the activity indicators and the RVs, namely, for BIS and CaIRT2. This illustrates again the shortcomings of the correlation analysis.

5.5.7 HIP 64823

HIP 64823 (HD 115478) stands out within the sample as the candidate star with the longest-period RV variation, with a period of $P = 2878.1$ d. It is likely ($P = 90\%$) located on the RGB (Stock et al., 2018). HIP 64823, unfortunately, was not part of the SONG observations, such that only Lick and CARMENES data are available. The baseline of the latter is furthermore a little shorter than one whole period of the RV variations such that an exact determination of the RV periodicity in the CARMENES data is not yet possible. Nevertheless, an increase of the likelihood at the period of the Lick RVs can be seen in Fig. 5.7.

Analyzing the activity indicators both in Figs. 5.7 and 5.8 suffers from the same limitation. We do find a tentative peak of the NaD2 line at $P = 1940$ d, which, however, closely coincides with a peak in the window function of the CARMENES observations (bottom panel). Apart from that, there is (so far) no indication of any significant periodicity

at periods similar to the RV period in either plot. While we cannot rule out a long-period activity variation with certainty, we conclude that the NaD2 variation is likely a consequence of the sampling of the observations.

The linear correlation analysis reveals two tentative correlations between the RVs and the contrast of the CCF in both the VIS and NIR channels. The p -values of the correlations are 3.3%, and 3.2% in the VIS and the NIR, respectively. However, we note that the correlation between the contrast of the CCF and the RVs is of opposite sign in both channels. That is, it is anti-correlated in the VIS, while it is positively correlated in the NIR. Combined with our general finding that the correlation analysis seems to be relatively ineffective for the giant stars in this work, we find it likely that these correlations are mostly a consequence of large uncertainties in the determination of the CCF parameters coupled with a relatively small number of measurements, as well as short-term jitter or the potential presence of intrinsic variations at shorter periods (see Sect. 5.6).

Analyzing the residuals in Fig. 5.3, we find the closest significant periodicity at $P = 410$ d, with a slight secondary peak at $P = 436$ d. In contrast to the previous stars, this additional periodicity does not seem to be a sign of a changing periodicity of the dominating period. Overall, we conclude that the CARMENES data available so far do not argue against the planetary nature of the RV periodicity. However, due to the insufficient baseline of the CARMENES observations, we cannot conclusively exclude any connection to intrinsic processes. We thus conclude that HIP 64823 remains a good planet candidate and examine the Keplerian model in more detail in Sect. 5.6.

5.5.8 HIP 73620

The second least luminous star in the sample, HIP 73620 (110 Vir, HD 133165), has the smallest RV variations of the sample with semi-amplitude $K \sim 20.3 \text{ m s}^{-1}$, only marginally larger than the estimated and expected jitter $\sigma_{\text{jit}} \sim 13.3 \text{ m s}^{-1}$. The star is located in the red clump (Alves, 2000; Laney et al., 2012). Examining Fig. 5.7, one can observe a rather complex combined periodogram structure with the period $P = 512.5$ d being picked up by our nested sampling approach. This period coincides with the dominant periodicity in the Lick data set. The CARMENES RVs show a slightly offset peak at $P = 554$ d in the VIS channel, and at $P = 547$ d in the NIR. In the vicinity, we further observe several peaks present in the CRX and dLW of the VIS channel with varying levels of FAPs.

When analyzed using the DBSCAN algorithm in Fig. 5.8, we find a cluster of peaks centered at $P = 539$ d, very close to the RV period. We note, however, that two of the peaks each stem from the CRX and dLW indicators. We further observe four tentative correlations for dLW, FWHM, and NaD1 in the VIS, as well as between the BIS and the RVs in the NIR. Using the period information from the RV residuals in Fig. 5.3, we find that subtracting

the best fit reveals periodicity close-by at $P = 597$ d, $P = 544$ d, and $P = 421$ d, with the central period closely coinciding with the CARMENES periodicity. The latter finding indicates that the shift of the periodicity in the CARMENES RVs is likely real and not a consequence of insufficient sampling of the phase curve. Overall, we conclude that the relatively small RV variations (within the context of this sample) of HIP 73620 are most likely caused by intrinsic variations instead of a planetary companion. Nevertheless, the star would benefit from continued observations to increase the temporal baseline and acquire additional measurements of activity indicators before a firm conclusion can be drawn.

5.5.9 HIP 75458

Next, we examine HIP 75458 (ι Dra, HD 137759), one of two published planet systems hosting a super-Jovian exoplanet in a 511 d, very eccentric orbit (Frink et al., 2002). The RVs further show a long-period trend (Zechmeister et al., 2008; Kane et al., 2010) attributed to a further-out brown-dwarf companion (Hill et al., 2021). The star was observed using SONG and added to the CARMENES sample in 2021.

Examining the periodograms in Fig. 5.7, one can observe that the strong RV periodicity at $P = 510.9$ d is consistently present in all data sets. Due to the very eccentric orbit of ι Dra b (named Hypatia by the IAU) and the sinusoidal nature of the periodogram analysis, one can identify clear and significant periodicity also at the harmonics and aliases of the RV period. Examining the activity indicators, there is no strong peak at the planet period. We observe tentative periodicity of the NaD1 and NaD2 lines at $P = 402$ d and $P = 349$ d, respectively. However, we note that these periods are also in proximity to one year, which suggests a connection to variable observing conditions or telluric contamination. This suspicion is reinforced by the DBSCAN clustering algorithm (Fig. 5.8), which detects a cluster of peaks (two of which are insignificant) centered at $P = 368$ d. We thus find no evidence against the planetary hypothesis from the activity time series analysis.

As mentioned in Sect. 5.4.4, we find tentative correlations (see Fig. 5.5) between the RVs and the CaIRT1 line in the VIS, as well as the dLW, FWHM, and contrast of the CCF in the NIR, with the latter having a p -value $p = 0.3\%$ close to the significance threshold. It is noteworthy that all three indicators that show these tentative correlations in the NIR are based on similar variations of the spectral line shape (see, for instance, Zechmeister et al. 2018), and are thus not entirely independent. As discussed in Sect. 5.4.2, we find two significant peaks in the residual periodogram, excluding the SONG RVs, at $P = 407$ d and $P = 634$ d. Both are much less significant than the initial peak caused by the orbital companion and lie in proximity to alias periods of the Keplerian period and the structured, combined window function. We thus suspect that these are a consequence of the large

eccentricity of the orbit of ι Dra b, which might be imperfectly constrained by the orbital fit.

Overall, we observe some noteworthy features in the activity indicator and residual analysis of ι Dra. However, individually we regard none of these as strong arguments against a planetary nature of the RV signal. Moreover, the Keplerian orbit has a very high eccentricity ($e \sim 0.71$), which can hardly be mimicked by, for instance, non-radial oscillations. It is further extremely well determined and fulfills all stability constraints (Hill et al., 2021). The star is furthermore the least luminous star in the sample ($L \sim 57 L_{\odot}$) with radius $R \sim 12 R_{\odot}$, placing it relatively far away from the region of suspicious planet detections identified by Reichert et al. (2019) and Döllinger & Hartmann (2021). We therefore have no reason to question the existence of ι Dra b. The results in this section rather emphasize that none of the metrics, particularly the correlation analysis, provide definitive conclusions regarding the existence of a planet responsible for the RV signal.

5.5.10 HIP 84671

HIP 84671 (66 Her, HD 156681) belongs to the most luminous stars in the sample with $L \sim 472 L_{\odot}$. It shows similar behavior to the two even more luminous sample stars, HIP 38253 and HIP 46390. While the RV periodicity at $P = 447.2$ d is strongly present in the Lick data set (see Fig. 5.7), it is not properly picked up in the CARMENES RV MLPs (black lines). The strongest peak in the vicinity of the fitted period is instead caused by the CRX in the VIS at $P = 423$ d, with further tentative peaks close to the alias periods from the CRX and the $H\alpha$ line. We further find a long-period signal at $P = 1105$ d in the VIS (and $P = 1094$ d in the NIR) to be the most significant peaks in the CARMENES RVs. This peak is accompanied, however, by an even more significant peak in the $H\alpha$ indicator. These are not present in the longer Lick time series. Finally, we find a significant peak in the Lick $H\alpha$ time series, within the peak width of the peak in the Lick RV MLP. Combining the peak information into the cluster analysis in Fig. 5.8, one can observe a cluster centered at 432 d (very close to the fitted period), with another longer-period cluster potentially linked to the long-period RV variation present in the CARMENES data.

The $H\alpha$ variations in both Lick and CARMENES are also significantly correlated with the RVs, albeit likely linked to different periodicity in the different instruments. These correlations are all with a positive sign, strengthening the significance of the finding. HIP 84671 thus appears as one of the few stars for which the correlation analysis can provide useful additional information. Subtracting the Keplerian model leads to residuals with additional significant periodicity at $P = 470$ d and $P = 506$ d. Thus, we conclude that the RV variations with a large semi-amplitude $K \sim 220 \text{ m s}^{-1}$ are of intrinsic origin.

5.5.11 HIP 88048

The other published planetary system in our sample orbits HIP 88048 (ν Oph, HD 163917) and consists of two brown-dwarf companions identified by [Quirrenbach et al. \(2011, 2019\)](#). The MLP analysis in [Fig. 5.7](#) reveals no tentative or significant peaks in the vicinity of the RV period of ν Oph b ($P = 529.9$ d), and likewise, no significant clusters are detected in [Fig. 5.8](#). We do observe a number of insignificant peaks by the Lick $H\alpha$, and CARMENES $H\alpha$, NaD1, and CaIRT2 indicators close to the one-year period.

The period of the outer brown-dwarf companion at $P = 3173.4$ d is much longer than the baseline of the CARMENES observations. Therefore, no reliable conclusions can be drawn from the CARMENES activity indicators for that period. We do find, however, a rise of the likelihood for the Lick $H\alpha$ indicator at even longer periods, which does not seem to be directly connected to the RV period of ν Oph c. This long period is at the limit of the baseline of the Lick observations (4009 d) and could also be linked to aging effects of the Lick CCDs. This trend of the $H\alpha$ indicator is likely also causing the two tentative correlations between the Lick $H\alpha$ indicators and the RVs (see [Fig. 5.5](#)), with p -values of $p = 1.8\%$ and $p = 2.7\%$ for the first and second Lick CCD, respectively. No correlations are detected between the CARMENES activity indicators and the RVs.

After removing the two-planet model from the RVs, we do not find any significant power close to the orbital periods in [Fig. 5.3](#). Overall, we thus conclude that there are no indications in the CARMENES data that argue against the real nature of the inner brown-dwarf companion, while the outer is still outside the baseline of the CARMENES observations.

5.5.12 HIP 89826

HIP 89826 (κ Lyr, HD 168775) is the second star among the planet candidates that stands out due to the relatively long-period nature of the RV variations which have a fitted period of $P = 1642.6$ d. Looking at [Fig. 5.7](#), these are clearly apparent in the Lick data set, while they are (still) insignificant in the CARMENES–VIS RVs and only tentatively present in CARMENES–NIR. However, the baseline of the CARMENES RVs is only a few hundred days longer than the fitted period, which is a potential reason for the lack of significance in the CARMENES measurements. The semi-amplitude of the RVs, $K \sim 32.5$ m s⁻¹, is relatively small compared to the average of the sample and compared to the jitter $\sigma_{\text{jit}} = 12.8$ m s⁻¹ likely caused by short-term pulsations and expected for this star. This can provide an additional explanation for the lack of periodicity in the VIS data set. Finally, the measurements (see [Fig. 5.2](#)) do not ideally sample the phase curve of the proposed planet due to a gap in the CARMENES data in 2019 and 2020.

Analyzing the activity indicators in Fig. 5.7, we find no significant periodicity at the Keplerian period. We find two tentative peaks by the CARMENES–NIR CRX and BIS close to the second harmonic of the RVs, which also form a small cluster with another tentative peak of the CARMENES–VIS CRX indicator centered at $P = 781$ d (see Fig. 5.8). Another tentative cluster of peaks can be found close to the fourth harmonic of the Keplerian period.

We further find a significant correlation between the RVs and the CRX in the NIR channel (see Fig. 5.5), likely linked to the tentative periodicity of the CRX at the second harmonic of the RV period. We also find a tentative correlation (with p -value close to being significant) between $H\alpha$ and the RVs using the second Lick CCD. Removing the Keplerian fit from the RVs and analyzing the residual MLP in Fig. 5.3 does not reveal any residuals peaks in the vicinity.

Altogether, we conclude that the CARMENES activity indicators so far do not decisively rule out a planet causing the RV variations. Nevertheless, since the long-period signal of the RV variations is not yet properly picked up by the CARMENES data given the sizable stellar jitter, we conclude that continued observations would be necessary to reveal its origin.

5.5.13 Summary of the results

Overall, we can find strong reasons to suspect that the RV variations of seven out of the ten planet candidates are caused by intrinsic processes. These are the stars HIP 7607, HIP 7884, HIP 38253, HIP 46390, HIP 47959, HIP 84671, and, notably, the published planet host HIP 16335 (Lee et al., 2014). We further lean toward an intrinsic origin of the RV variations of HIP 73620. The CARMENES activity indicators so far do not rule out a planetary origin of the long-period RV variations of HIP 89826, but continued monitoring is necessary to draw firm conclusions. For HIP 64823, we favor the planet hypothesis, which is examined in more detail in Sect. 5.6.

For the two comparison stars, HIP 75458 and HIP 88048, we find some tentative correlations between activity indicators and the RVs, which likely highlights the limitations of this analysis. We do not find any significant periodic signals in the activity indicators which would argue against the existence of the orbital companions. For HIP 75458, we note some residual periodicity, which is likely due to the large eccentricity of the orbit.

We generally conclude that testing for linear correlations does not provide strong and reliable insights for distinguishing between planets and intrinsic processes. We further find that the infrared test is not sensitive enough in the presence of large RV jitter and relatively little data. Overall, we find that a very long baseline of RV measurements is necessary to detect the subtle differences between the intrinsically induced variations

and real planets. A detection of different periods in different time windows, as well as an analysis of the residual RVs can provide the strongest clues toward the origin of the RVs. We note that the most luminous stars in the sample (HIP 38253, HIP 46390, and HIP 84671) seem to show the strongest signs of changing periodicities in data sets taken at different epochs and with different instruments. A complementary periodogram analysis of activity indicators can often confirm these signals to be of intrinsic origin. We cannot identify any indicator that would consistently be more sensitive than the others in our analysis.

5.6 The long-period planet candidate HIP 64823

5.6.1 Radial velocity modeling

In Sect. 5.5, we find that the long-period planet candidate HIP 64823 stands out from the rest of the sample as there are currently no indications from the activity analysis or the RV residuals that argue against a planet causing the RV periodicity. Furthermore, the RV variation with a period $P = 2878$ d is, by far, the longest among the planet candidates, and far outside the typical range of periods detected to be false positives, which is several hundred days.

The best one-planet model presented in Fig. 5.2 has stellar jitter $\sigma_{\text{jit}} = 36.7 \text{ m s}^{-1}$, which lies between the jitter estimates $\sigma_{\text{jit}} = 18.0 \pm 2.3 \text{ m s}^{-1}$ (Kjeldsen & Bedding, 1995) and $\sigma_{\text{jit}} = 50.8 \pm 8.8 \text{ m s}^{-1}$ (Kjeldsen & Bedding, 2011). Thus, we tested whether some residual periodic signal was absorbed into the jitter estimate in the one-planet model.

Examining the RV residuals in Fig. 5.3, we find significant periodicity at several periods, with the most prominent peaks consisting of two blended peaks with maxima at $P = 410$ d and $P = 436$ d, as well as other peaks at $P = 85.6$ d and $P = 15.7$ d. We tested a 2-planet model (2P) with a uniform period prior $\mathcal{U}(300 \text{ d}, 500 \text{ d})$ for the inner planet, trying to capture the most significant periodicity. We give the full set of priors in Table C.2. The resulting model attributes a period $P = 438$ d to the inner companion. We compare the Bayesian evidence resulting from the nested sampling run and find a moderate improvement of $\Delta\mathcal{Z} = 3.41$ ($\Delta\text{BIC} = -2.8$; Trotta, 2008) compared to the one-planet model. We further find that the estimated RV jitter is only reduced to $\sigma_{\text{jit}} = 31.5 \pm 3.6 \text{ m s}^{-1}$, still exceeding the lower estimate by Kjeldsen & Bedding (1995).

Examining the activity MLPs in Fig. 5.7, however, we find several peaks of the activity indicators in the period region between 100 d and 500 d, with a tentative peak of the CaIRT2 line at $P = 397$ d, not far off the residual period of the RVs or the period of the inner planet in the two-planet model. We thus suspect that the periodicity at shorter

periods might be linked to stellar activity or another form of intrinsic variability and attempt to model it using a Gaussian process (GP) regression model as implemented via the `celerite` (Foreman-Mackey et al., 2017) package included in the Exo-Striker. While cool spots such as those commonly found for low-mass dwarfs are practically ruled out by the low level of photometric variability ($H_{\text{p}}\text{scat} \sim 0.005$ mag), other sources of intrinsic variations, such as variable levels of convection or long-period stellar oscillations, are not well understood for giant stars. We thus attempted to model these variations with a commonly used but flexible rotational kernel defined by Foreman-Mackey et al. (2017). The kernel is characterized by the amplitude of the covariance B , the kernel period P , the coherence timescale L representing the decay of correlations over time, and a dimensionless factor C that adjusts the relative contributions of the periodic and constant terms.

In initial tests, using a joint model combining the contributions of the outer planetary candidate and the GP (1P+GP) and broad priors, we found that the GP mostly preferred a kernel period $P \sim 460$ d but with small coherence timescales, which tended to overfit the short-term noise inherent to the RVs of the giant due to p-mode pulsations. Similar to Stock et al. (2023, their Fig. 2), we observed a triangular shape in the L - P plane of the posterior samples. That is, we detected many samples having small L but spanning a large range of periods P , as well as a distinct branch of solutions close to $P \sim 460$ d extending to larger values of L . We thus restricted the lower limit of the prior on L to 450 d and clipped this plateau.

We selected a rather constrained prior on the factor C ($U(0, 1)$), expecting the oscillating component to have a significant contribution. The final 1P+GP model is presented in Fig. 5.9 (top left), decomposing the contributions of the planet (top right), and the contribution of the GP (bottom left). We find that the Bayesian evidence $\Delta\mathcal{Z} = 33.3$ and $\Delta\text{BIC} = -72.7$ of the 1P+GP model are strongly favored compared to the one-planet model, as well as the two-planet model. We tested that the period prior has an insignificant effect on the Bayesian evidence computed for model comparison with the two-planet model. The residual RV scatter modeled as jitter results in $\sigma_{\text{jit}} = 13.7_{-4.8}^{+4.7} \text{ m s}^{-1}$, which is consistent with the jitter estimate by Kjeldsen & Bedding (1995). The determined kernel period is $P_{\text{GP}} = 459_{-38}^{+72}$ d. Given the strongly favored 1P+GP model compared to the two-planet model, we find the suspicion justified that the variability at $P \sim 400$ d is caused by intrinsic variations rather than another planetary candidate. We give the mode of the posterior distributions in Table 5.4 and provide the corner plot of the posterior samples in Fig. C.1. The GP parameters are not very well constrained. We specifically find a broad distribution for the hyperparameter C_{GP} . We stress that we regard HIP 64823 as a planet host candidate due to the insufficient time baseline of the CARMENES observations that cannot entirely rule out that the long-period variations could be caused by intrinsic processes.

Tab. 5.4.: Results of the 1P+GP nested sampling modeling.

Parameter	Unit	Value
K	(m s ⁻¹)	125 ⁺¹⁶ ₋₁₇
P	(d)	2827 ⁺⁶¹ ₋₄₈
e		0.33 ^{+0.12} _{-0.11}
ω	(deg)	315 ⁺²⁰ ₋₂₁
M_0	(deg)	8 ⁺²⁷ ₋₁₀
σ_{jit}	(m s ⁻¹)	13.7 ^{+4.7} _{-4.8}
$\text{RV}_{\text{off,Lick}}$	(m s ⁻¹)	-49 ⁺²⁶ ₋₂₇
$\text{RV}_{\text{off,NIR}}$	(m s ⁻¹)	133 ⁺³² ₋₃₂
$\text{RV}_{\text{off,VIS}}$	(m s ⁻¹)	-124 ⁺³² ₋₃₂
B_{GP}	((m s ⁻¹) ²)	2902 ⁺¹⁸⁷¹ ₋₁₀₁₅
P_{GP}	(d)	459 ⁺⁷² ₋₃₈
L_{GP}	(d)	484 ⁺⁴³³ ₋₃₄
C_{GP}		0.04 ^{+0.74} _{-0.04}
a_{p}	(au)	4.40 ^{+0.19} _{-0.13}
$m_{\text{p}} \sin(i)$	(M_{Jup})	10.4 ^{+1.4} _{-1.9}
T_0	(BJD)	2451510 ⁺⁹² ₋₂₀₂

Notes. M_0 represents the mean anomaly at the epoch of the first data point (BJD = 2451572.029297). T_0 denotes the time of periastron passage and was derived from the best fit parameters. For each parameter, we give the mode of the posterior distribution. As uncertainties, we adopt the interval around the mode that encompasses 68% of the posterior samples. For the GP timescale L_{GP} , due to the large plateau of low timescale solutions, the mode of the very asymmetric posterior is close to the prior boundary at 450 d. The GP hyperparameter C_{GP} is poorly constrained. The full posteriors can be seen in Fig. C.1. a_{p} and $m_{\text{p}} \sin i$ were derived from the best parameters above. The uncertainties include the uncertainties of the stellar mass. If excluded, the uncertainties reduce to $a_{\text{p}} = 4.40^{+0.07}_{-0.04}$ au and $m_{\text{p}} \sin(i) = 10.4^{+1.3}_{-1.7} M_{\text{Jup}}$.

5.6.2 Stacked Bayesian GLS analysis

Another test to distinguish RV periodicity caused by planets from those caused by intrinsic processes is proposed by [Mortier & Collier Cameron \(2017\)](#). The idea is to test whether the periodogram power of an RV signal increases by adding new data points as expected from a long-lived, coherent periodic signal. [Mortier & Collier Cameron \(2017\)](#) use stacked Bayesian GLS (S-BGLS) periodograms based on the formalism by [Mortier et al. \(2015\)](#). The S-BGLS periodograms have been used successfully to distinguish stellar activity from planets around main-sequence dwarfs or T Tauri stars (see, for instance, [Zaire et al. 2024](#); [Von Stauffenberg et al. 2024](#); [Burt et al. 2024](#); [Dalal et al. 2024](#); [Dreizler et al. 2024](#)). The S-BGLS and similar tests have also been successfully applied to rule out the orbital companions around the giant stars Aldebaran ([Reichert et al., 2019](#)) and Sanders 364 ([Zhou et al., 2023](#)).

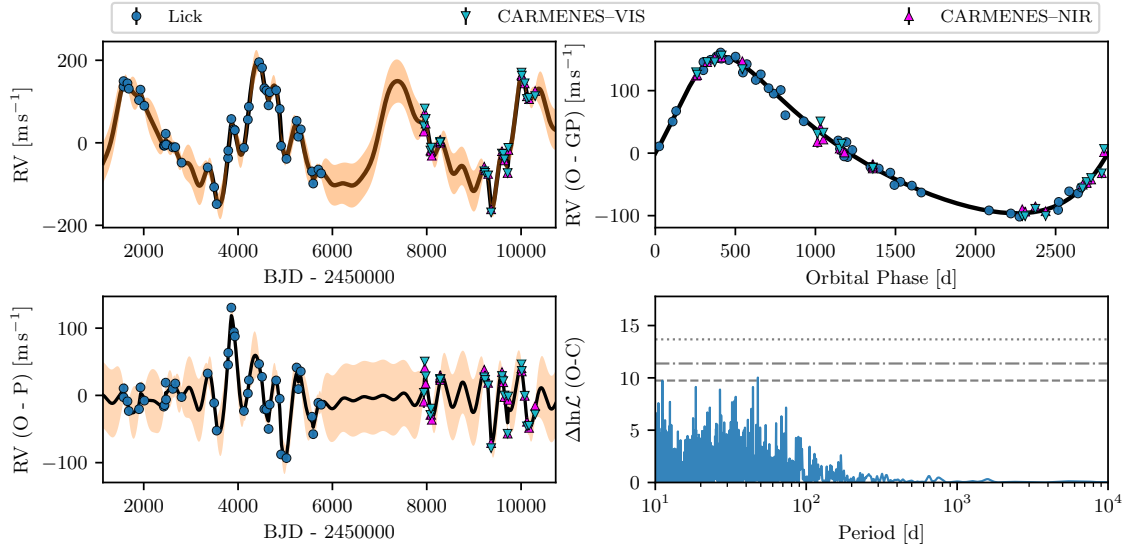


Fig. 5.9.: Model combining a long-period planet with a GP model at shorter periods for HIP 64823. Top left: The combined 1P+GP model fitted to the data. Top right: RV residuals after subtracting the GP model, phase-folded to highlight the contribution of the planet. Bottom left: RV residuals after removing the contribution of the planet to highlight the GP model. Bottom right: Residual RV periodogram showing only tentative periodicity at shorter periods. The FAPs of 5% (dashed), 1% (dash-dotted), and 0.1% (dotted) are plotted as gray horizontal lines.

However, similar to Zhou et al. (2023), we find the color map representation of the S-BGLS (see Fig. 1 in Mortier & Collier Cameron 2017) somewhat subjective to interpret. Instead, we opt for an approach similar to that by Hatzes (2013), Reichert et al. (2019), and Zhou et al. (2023), as also proposed by Mortier & Collier Cameron (2017). That is, we plot the growth of the significance of the periodic signal, as expressed by the ratio between the amplitude of the sinusoidal A , derived by the circular S-BGLS periodogram, and its uncertainty σ_A , as a function of the number of data points N that have been added in in sequence. The S-BGLS power was evaluated at the period of the best Keplerian model. These are portrayed in Fig. 5.10, as the blue lines. Due to the presence of secure long-period orbital companions in the HIP 75458 and HIP 88048 systems, we prewhitened the data sets for these stars by subtracting the contributions of the respective other orbital companions in the analysis. For HIP 88048, we also plot the growth of the signal of HIP 88048 c in orange. For HIP 75458, we omit plotting the change of the significance of the outer long-period companion, as its phase curve is only fractionally sampled.

As can be seen for both published planet hosts, HIP 75458 and HIP 88048, the significance of A can drop significantly in parts of the data set. However, these can be the results of an inadequate sampling of the RV phase curve in the presence of stellar jitter. For HIP 75458, for instance, the SONG spectrograph took numerous spectra in subsequent nights. Coupled with the eccentric orbit of HIP 75458 b and the sizable stellar jitter, these

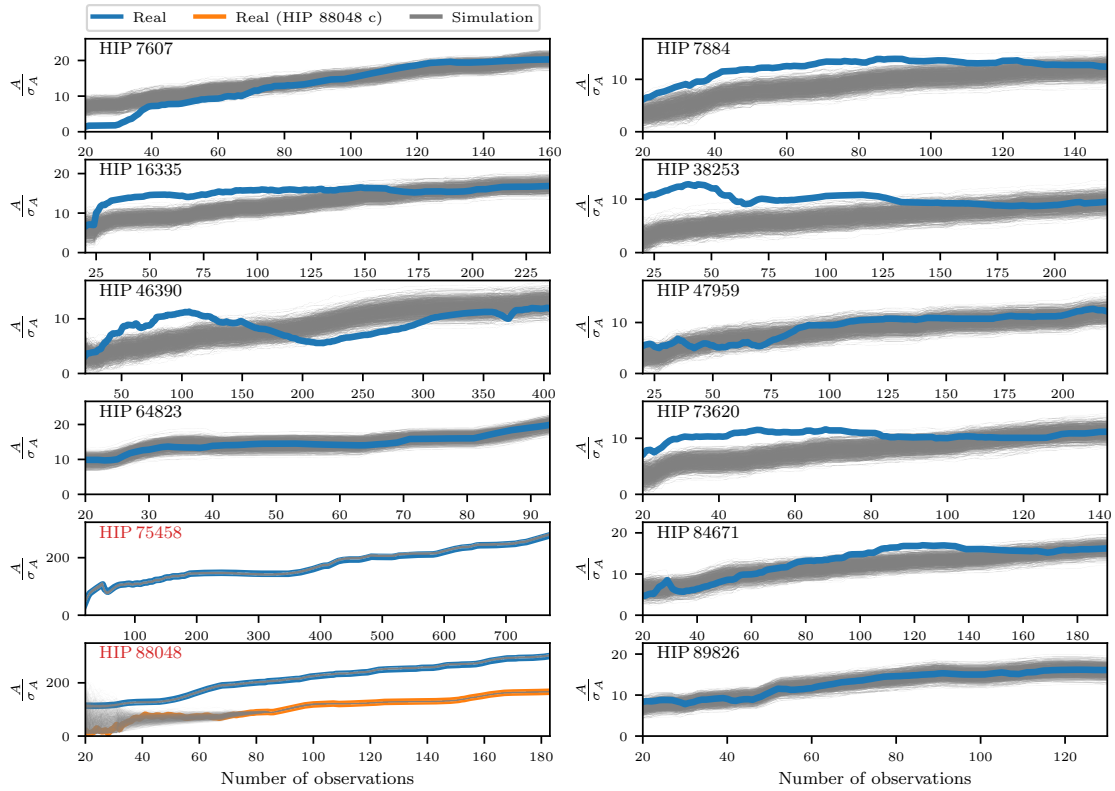


Fig. 5.10.: Significance of the amplitude A as a function of the number of observations. The real data are portrayed in blue, while the 1000 realizations of the simulated data are portrayed as gray lines. We evaluated the S-BGLS at the period of the best Keplerian models summarized in Table 5.3. For the two secure planet hosts, HIP 75458 and HIP 88048 (identifiers marked in red), the simulated relations are plotted on top of the real ones for increased visibility. For HIP 88048, we further plot the significance of the long-period signal in orange. The contributions of the respective other companions were subtracted for the two secure systems.

spectra in practice mostly contribute stellar “noise” and reduce the significance of the determined RV signal. This also helps one understand why the color maps of the S-BGLS analysis can sometimes be misleading for giant stars.

To study how the significance of A would evolve if the Keplerian model can adequately describe the data, we simulated 1000 realizations of the Keplerian model evaluated at the epochs of the real spectra and adding a Gaussian noise component with the standard deviation set to the RV jitter of the star. The latter was also used as a white noise component for the weights to compute the S-BGLS (see Mortier & Collier Cameron 2017). These simulations are plotted as the gray lines. As one can see for both HIP 75458 and HIP 88048, the simulated significances follow the real data very closely, including the drop of the significance in certain parts of the relation. We note the change of the significance of A for HIP 88048 c (orange) is initially very noisy and behaves slightly differently than the simulated relations. However, this can easily be explained by the long-period nature

of the orbit, which has the longest period among all systems apart from HIP 75458 c, as well as the relative dense sampling of the early Lick observations (see Fig. 5.2) compared to other long-period planet candidates such as HIP 64823.

To allow for a fair comparison of the model of HIP 64823 against the other planet candidates, we used the one-planet model with its respective jitter as given in Table 5.3. As can be seen from Fig. 5.10, HIP 64823, along with HIP 89826, are the only planet candidates for which there are no striking differences between the real data and the simulated relations. For all other stars, there are parts of the relation in which the real data behave differently than the model. The relation for HIP 47959 does not deviate as strongly from the simulations as for most other planet candidates. Nevertheless, especially in the early part of the relation, the significance of the real data increases less quickly than the simulations predict. We note that, by definition, the simulated and real significances converge at large N , as the Keplerian models were derived using the complete data sets.

It has to be noted that the test, in essence, can only examine whether a specific Keplerian model including its RV jitter is consistent with the whole data set. Thus, altering the Keplerian models, for instance by including additional orbital components, which are however challenged based on dynamical assumptions, could alter the interpretation of this specific S-BGLS test. Nevertheless, having tested different models for the planet candidates we could not find any differences in the interpretation. We thus conclude that HIP 64823 and HIP 89826 are the only planet candidates that can be consistently described by the Keplerian models. For the latter, the CARMENES data are not yet sufficient to draw reliable conclusions. For HIP 64823, we conclude that the exoplanet of minimum mass $m_p \sin(i) = 10.4_{-1.9}^{+1.4} M_{\text{Jup}}$ with orbital period $P = 2827_{-48}^{+61} \text{ d} \sim 7.75 \text{ yr}$ is likely real. Nevertheless, as the baseline of the CARMENES observations is still too short to properly test the activity indicators and given the general poor understanding of the physical nature of long-period intrinsic variations of giant stars, we regard HIP 64823 b as a planet candidate until confirmed by further RV monitoring.

5.7 Discussion

In recent years, a number of intrinsically variable giant stars, some of which had previously been reported to host planets using RV data, have been identified (Hatzes et al., 2018; Delgado Mena et al., 2018, 2023; Reichert et al., 2019; Heeren et al., 2021; Döllinger & Hartmann, 2021; Teng et al., 2023b; Zhou et al., 2023; Lee et al., 2023). Given the varying temporal baselines of RV data sets and availability of activity indicators, there could be more false positives among luminous evolved planet hosts. These could have an impact on occurrence rate studies if not treated carefully. Wolthoff et al. (2022), for instance, perform several “homogenizing cuts” to their underlying sample to remove very

luminous ($\log_{10}(L/L_{\odot}) > 3$) giants, as well as stars with complex RV signatures. Thus, they reduce the impact false-positive planet detections could have on their conclusions. Despite this careful treatment, the published “planet host” HIP 16335 (Lee et al., 2014) is included as such in their analysis, although we now conclude that its variations are intrinsic.

Within the literature, there is no consensus which process causes these false-positive detections. One candidate could be the rotational modulation of stellar surface features such as hot plages or cool spots. Unfortunately, for most of the stars there are no reliable estimates of the rotation periods due to a lack of photometric variations (see also Table 5.1). This lack of variations, however, also generally argues against large stellar spots (Reffert et al., 2015; Reichert et al., 2019).

On the other hand, the variations of surface features linked to magnetic activity are yet largely unexplored. As suggested by Delgado Mena et al. (2023, and references therein), magnetic structures on giant stars could locally suppress convection, potentially leading to RV variations without associated photometric variations. This idea seems plausible, given the detection of a weak magnetic surface field of Pollux (Aurière et al., 2009, 2013, 2021), which varies on similar timescales as the RVs. These RV variations have been attributed to an exoplanet companion (Hatzes et al., 2006; Reffert et al., 2006). Recent simulations show that this magnetic field could be dynamo-driven and that the strength of the magnetic field is coupled to the scale of convection cells (Amard et al., 2024). Rolo et al. (2024) discuss a connection between the amplitudes of the activity indicator variations and the Li abundance of the stars. Their work includes the intrinsically variable giants discussed in Delgado Mena et al. (2023), for several of which the $H\alpha$ index is shown to be periodic close to the RV period. All of these stars are Li-rich, potentially providing another link toward magnetic activity, as high Li abundance is associated with enhanced chromospheric activity (Snedden et al., 2022). Interestingly, strong magnetic fields have also been detected in the cores of some giant stars using *Kepler* data (Li et al., 2022; Deheuvels et al., 2023; Li et al., 2023). Of the 12 stars in this sample, literature Li abundance measurements are available for eleven. None of them were found to be Li-rich. (Brown et al., 1989; Lèbre et al., 2006; Liu et al., 2014; Charbonnel et al., 2020).

In this context, we find it noteworthy that the chromospheric activity indicators, namely those targeting the $H\alpha$, NaD, and CaIRT lines, which are sensitive to magnetic activity (Sarkis et al., 2018), show at least tentative periodic variations at periods similar to the RVs for several of the stars examined in this work. Thus, a connection between magnetic activity and RV variations resembling planets seems plausible. However, further modeling of the RV curves remains challenging lacking a better physical understanding of the magnetic surface fields and convection patterns of giants. It also remains uncertain whether such variations in the chromospheric indicators might also be attributed to other intrinsic mechanisms.

Another promising alternative, long-period non-radial oscillations, was already discussed for giant stars by [Hatzes & Cochran \(1993\)](#). More recently, [Hatzes et al. \(2018\)](#) propose that the RV variations of the luminous giant γ Dra show a beating of different periods that seem to be most elegantly explained by non-radial oscillations. [Hatzes et al. \(2018\)](#) also propose that this new type of variability might be linked to oscillatory convective modes which have been developed by [Saio et al. \(2015\)](#) to explain the so-called sequence D in the period-luminosity plot of bright, variable giants showing long-secondary periods (LSPs) ([Wood et al., 1999](#)). Although contested in the literature as the origin of these LSPs (see, for instance, [Soszyński & Udalski 2014](#); [Soszyński et al. 2021](#); [Goldberg et al. 2024](#)), [Hatzes et al. \(2018\)](#) and [Reichert et al. \(2019\)](#) argue that γ Dra and Aldebaran occupy a region in a period–luminosity plot that could be crossed by an extrapolation of the models by [Saio et al. \(2015\)](#). This could make oscillatory convective modes a plausible explanation for the RV variations. In [Spaeth et al. \(2024\)](#), we use this idea to show that a simple model of an $l = 1, m = 1$ non-radial oscillation could explain the RV variations, as well as the correlations with the available activity indicator, for the known false-positive evolved planet host NGC 4349 No. 127 ([Delgado Mena et al., 2018, 2023](#)). Although more massive, NGC 4349 No. 127 has a similar luminosity to that of γ Dra and Aldebaran, and shows RV variations of similar period.

Having identified seven additional giant stars with RV variations that resemble planets (at least during part of their temporal baseline) that we regard to be securely of intrinsic origin, we can update Fig. 8 of [Reichert et al. \(2019\)](#) (and Fig. 9 in [Spaeth et al. 2024](#)). In [Fig. 5.11](#), we show luminous and variable giant stars identified in the OGLE-III survey ([Soszyński et al., 2009](#)) as small green dots, with the subset of those showing LSPs on sequence D in black. We further plot models of oscillatory convective modes for different stellar masses taken from [Saio et al. \(2015\)](#) in different shades of pink. On top, we present published planet hosts from the Lick survey as red circles, stars that show RV curves resembling planets but have been shown to be of intrinsic origin as blue star markers, and remaining planet candidates, or stars for which we regard the analysis to not yet provide clear conclusions, as cyan hexagons. We highlight the stars examined within this work, marking these with their HIPPARCOS identifiers, while we show the literature stars with somewhat reduced sizes and lighter shades. We exclude the lower-luminosity false-positive hosts 41 Lyn and 14 And ([Teng et al., 2023b](#)) from this analysis. The RV periodicity of both stars closely aligns with a half-yearly cycle, accompanied by a strong yearly signal in the window function. These characteristics suggest that the observed periodicities are more likely related to the observational sampling than to a physical process.

As can be seen, the clear distinction between the secure planet hosts and the false-positive detections highlighted by [Reichert et al. \(2019\)](#) becomes somewhat less striking as more stars are included. While we can still observe a clear trend that the false-positive detections mostly occur for larger luminosities, we can see several such false positives also in the transition region, among these HIP 7607. We note that one of the supposedly confirmed

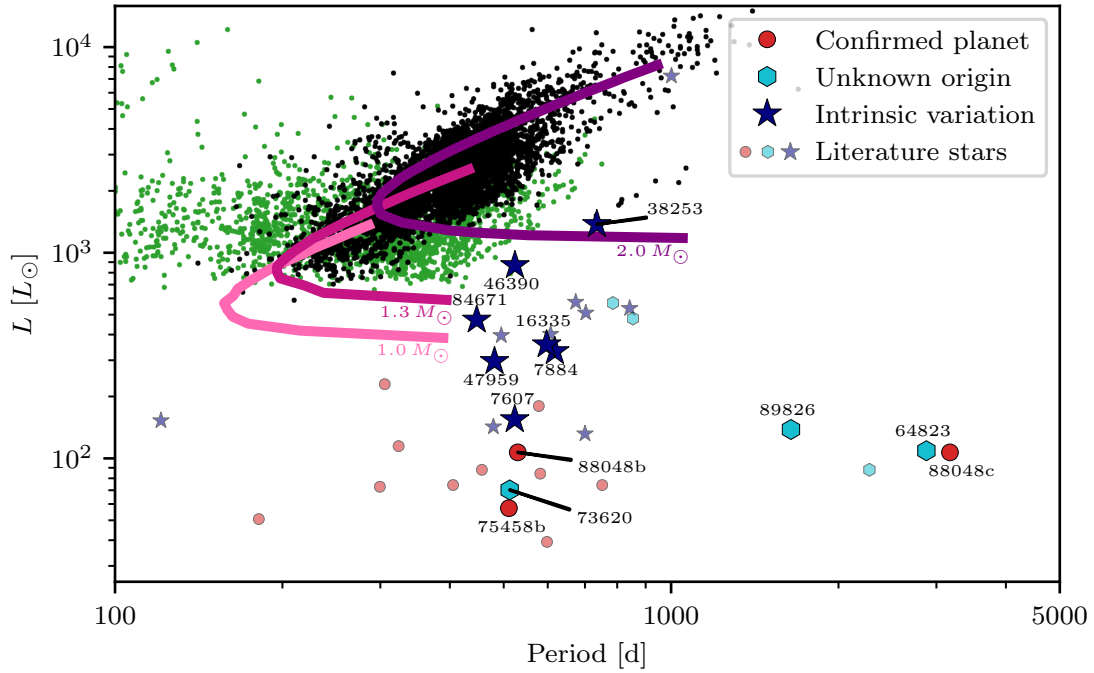


Fig. 5.11.: Luminosity of the stars plotted against the RV period. Variable stars from the OGLE survey are plotted in green, with the subset of those showing LSPs on sequence D plotted in black. Overplotted in pink are models from the expected relations of oscillatory convective modes (Saio et al., 2015) for different stellar masses. We plot confirmed planets within the Lick sample as red circles, and confirmed intrinsically RV-variable stars that mimic planets as blue star markers. Stars with as yet undecided origins of their RV variations are shown as cyan hexagons. Stars taken from the literature are shown with reduced marker sizes and lighter shades. We mark the HIPPARCOS identifiers of the stars discussed in this work. We omit plotting the short-period planet hosts HIP 89587 (Teng et al., 2023a) and HIP 70791 (Takarada et al., 2018) for visual clarity. The plot is adapted from Fig. 8 of Reichert et al. (2019) and Fig. 9 of Spaeth et al. (2024).

planet hosts in the transition region, HIP 60202 (Liu et al., 2008), was recently challenged by Teng et al. (2023b) due to additional periodicity in the residuals RVs that would be challenging to attribute to an additional companion due to dynamical constraints, akin to the results of the residual analysis in Sect. 5.4.2 in this work. We also find HIP 16335, whose published planet is likely a misidentified intrinsic signal according to our analysis, to be in close vicinity to other intrinsically variable giants, including γ Dra. The two stars with RV variations of unknown origin at high luminosities, 3 Cnc and 44 UMa (Tala Pinto et al., 2020), have convincing Keplerian models but lack a set of reliable activity indicators other than Lick H α measurements, which were inconspicuous for these stars. Noteworthy is also the location of HIP 73620, whose RV variations fall within the region occupied by stars who are considered to be secure planet hosts. Although we favor an intrinsic origin of the RV variations, we cannot rule out a planetary companion with certainty. However,

assuming our assessment of an intrinsic origin to be correct, this would certainly make the distinction between the groups of the secure hosts and the intrinsically RV-variable stars less clear. However, we also note that HIP 73620 shows the smallest amplitude among the stars in this study.

Finally, we note the locations of HIP 64823 and HIP 89826, which fall far outside the period regime in which the other false positives have been found. In terms of their luminosity they fall into the transition region between the secure planets and the RV-variable stars. At least for HIP 64823, this further supports our interpretation that the RV variations are best explained by a planetary companion. HIP 89826 remains uncertain.

In Fig. 5.12, we select all stars that are intrinsically RV variable and those of so-far unknown origin from Fig. 5.11, and plot their semi-amplitude K against their luminosity. We observe that the majority of the stars follows a roughly linear trend with increased K for higher luminosities. We note two strong outliers at high luminosities, which are HIP 46390 and HIP 38253. Especially for the latter, the amplitude in the Lick RVs alone would be somewhat larger than the amplitude derived combining the Lick data with the SONG and CARMENES measurements (see Fig. 5.2), such that it might also lie at higher K depending on the part of the RV curve that was observed. We emphasize that we also include more likely planet candidates, such as HIP 64823, among the stars of unknown origin.

We further mark the estimated p-mode jitter derived using the scaling relations by Kjeldsen & Bedding (1995) for three different stellar masses in shades of red. These give a rough lower limit of semi-amplitude K that could have been detected. That is, it is possible that the linear trend is merely a consequence of selection effects due to the higher short-term jitter that would likely prevent the detection of longer-period RV variability for more luminous stars. Nevertheless, we find the observed trend noteworthy as it might contribute toward a physical interpretation. A similar trend (expressed in terms of $\log g$, which, however, correlates with L and that can also be observed for our stars) has already been discussed by Hatzes & Cochran (1998b).

Overall, we have to conclude that the full picture remains elusive. We can certainly strengthen the finding that planet detections around giant stars with luminosities $L \gtrsim 125 L_{\odot}$ should be regarded with caution. We, however, also note the suspicion that HIP 73620, which has much lower luminosity, has intrinsically induced RV variations. While we can somewhat strengthen the suggestions by Hatzes et al. (2018) and Reichert et al. (2019), that an extrapolation of the models of oscillatory convective modes could explain the majority of the false-positive sample, we also find hints of variations in the chromospheric activity indicators for several of the stars, which might suggest a link toward magnetic activity of, perhaps, rather exotic nature. Unlike the case of NGC 4349 No. 127 (Delgado Mena et al., 2018, 2023; Spaeth et al., 2024), we do not find distinctive correlations between the activity indicators and the RVs for any of our stars, which could

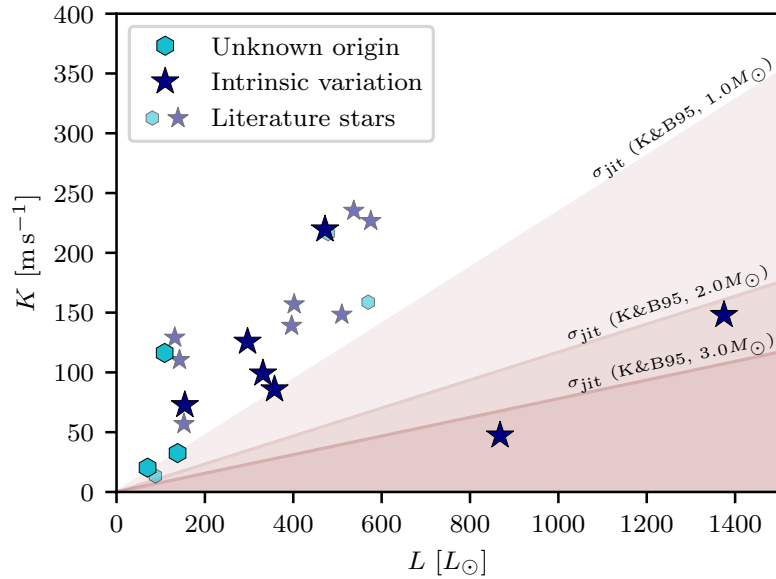


Fig. 5.12.: Semi-amplitude K of the intrinsically RV-variable stars (blue star markers) and the stars with as yet unknown origin of their RV variations (cyan hexagons) plotted against the luminosity. The literature stars are plotted with reduced sizes. We further plot the estimated p-mode jitter following the scaling relations by [Kjeldsen & Bedding \(1995\)](#), labeled K&B95, for three different stellar masses. We observe that many of the stars follow a roughly linear relation between the amplitude of their RV variation and the luminosity. Two outliers at large L but small K are noted. These are HIP 46390 and HIP 38253. We exclude the very luminous star NGC 2345 No. 50 from the plot for visual clarity.

be easily interpreted as the fingerprints of a single dominating oscillation mode. However, we discuss in [Spaeth et al. \(2024\)](#) that a superposition of different modes along with sizable stellar jitter can hide such correlations. We also note that NGC 4349 No. 127 was also shown to have periodic variations in the $H\alpha$ indicator ([Delgado Mena et al., 2018, 2023](#)), which might suggest that such chromospheric activity could also be linked to oscillations. More detailed investigations, both from the observational and the theoretical sides, are certainly necessary to resolve the mysterious RV variations of luminous evolved stars.

5.8 Summary

The goal of this study was to test ten bright evolved stars identified as planet candidates after the conclusion of the 12-year Lick RV survey for the presence of planets using the SONG and CARMENES spectrographs. We further aimed to assess the effectiveness of different standard metrics used in the literature to differentiate between planets and intrinsic variations when applied to giant stars. Finally, we were motivated to also

highlight the false-positive detections in order to provide new evidence of the observational fingerprints of the mysterious RV variations of luminous giant stars.

We find that seven out of the ten former planet candidate stars have an intrinsic origin of their RV variations. These are HIP 7607, HIP 7884, HIP 38253, HIP 46390, HIP 47959, HIP 84671, and (most notably) HIP 16335. Significantly, HIP 16335 was previously reported by Lee et al. (2014) to host a $6.5 M_{\text{Jup}}$ minimum mass giant exoplanet in a 579.8 d orbit, which we reveal to be a misidentified intrinsic RV signal. Furthermore, we lean toward an intrinsic origin for the (comparably) low-amplitude RV variations of HIP 73620, whereas we cannot draw reliable conclusions for HIP 89826. Finally, we find that HIP 64823 remains a promising candidate to host a long-period planet ($P \sim 2827_{-48}^{+61}$ d), and we showed that a GP model can be used to explain residual variability at shorter periodicity. However, as the baseline of the CARMENES observations is not yet long enough, we cannot confirm the presence of the exoplanet candidate with minimum mass $m_p \sin(i) = 10.4_{-1.9}^{+1.4} M_{\text{Jup}}$ with certainty.

Although the RV variations of most of the intrinsically variable giants are convincingly not caused by exoplanet companions, we find that testing the consistency of the RV amplitude between the optical and the infrared is not effective enough to rule out the possibility that the giants are being orbited by planets given the large stellar jitter. We further find that testing for linear correlations between the activity indicators and the RVs does not detect the majority of the false-positive planet hosts and thus caution relying solely on such metrics. We instead find that for the most luminous stars, clear changes of the dominating periodicity on timescales of tens of years can be observed. A similar effect is also apparent from analyzing the residual RVs, which often show significant remaining periodicity close to the proposed orbital period, which we interpret as the consequences of changing periods or amplitudes. We also observed that testing the consistency of the best Keplerian model with the real data, based on the significance of the amplitude derived from stacked Bayesian GLS periodograms, reliably picks out the false-positive hosts. For such tests, long-term RV monitoring is critical.

Generally, we find that analyzing the CARMENES activity indicators using maximum likelihood periodograms as well as a DBSCAN cluster analysis can, in most cases, detect the intrinsic variability. However, a detailed analysis combining the findings from different indicators is necessary to rule out planetary companions with certainty, as the signals in the activity indicators are typically not very strong, meaning that they can be easily missed. We also observed that even for the well-studied exoplanet host HIP 75458, there are hints in the activity indicators and RV residuals that suggest the current metrics may not be entirely robust at differentiating between planetary and stellar activity signals.

Finally, we discuss the additional detection of intrinsically RV-variable giant stars mimicking exoplanets in the context of other false-positive evolved planet hosts. We find that the general trend that most false positives have high luminosities holds up, but we also found

one suspicious case at lower luminosity. We observed a slight trend of increasing RV amplitudes with increasing luminosity. Given the high luminosities of the majority of the stars, a connection to oscillatory convective modes (Saio et al., 2015) seems plausible. However, we do not find any clear correlations between the activity indicators and the RVs in this sample, which would allow for a more detailed assessment of potential oscillation modes (Spaeth et al., 2024). We also note that for several of the stars in the sample and in the literature, chromospheric activity indicators contribute to refuting the planetary companions. These might suggest a connection to magnetic or convective processes in these giants. The phenomenon as a whole remains poorly understood.

With this work, we hope to contribute to a better physical understanding of RV variations of luminous giant stars, which convincingly mimic exoplanet companions. Future research both from the observational and theoretical side are certainly necessary to ultimately resolve the mystery.

The Waltz radial velocity survey: Steps toward routine observations

This chapter gives an overview of the status of the Waltz project, summarizes my contributions to enable routine scientific observations, and presents first on-sky tests.

The success of the Waltz project was enabled by a collaborative effort with valuable contributions by numerous staff members of the LSW workshop, former and current staff members of the LSW scientific personnel, as well as interns, bachelor's, master's, and PhD students. I will highlight their contributions throughout the main text. My contributions were to improve and maintain the control software, conduct the first scientific observations, perform a first analysis of the CTI effect noticed for the Waltz CCD, streamline the data reduction process, and resolve most issues, whether minor or major, that emerge in the process of establishing routine observations. My contributions to the Waltz infrastructure are summarized in [Sect. 6.3](#). The analysis of the CTI effect and the first scientific results from the Waltz project are presented in [Sects. 6.4](#) and [6.5](#), respectively.

6.1 Motivation and survey goals

The main motivation of this thesis was to improve our understanding of the planet population orbiting giant stars, which are an ideal laboratory to study the effect of stellar evolution on planetary systems and to search for planets orbiting intermediate-mass stars. In the introduction ([Sect. 1.2](#)), I discuss that the long-period regime among these planets, while likely present when looking at our own solar system, is still relatively unexplored. I have further studied the origin of the mysterious RV variations measured for very luminous giants, some of which might host planets, while others might rather be intrinsically variable. In one case ([Chapt. 4, Spaeth et al. 2024](#)), using HARPS activity indicators, a non-radial oscillation could be identified as the most promising alternative. However, studying a larger sample of luminous giants in [Chapt. 5 \(Spaeth et al., 2025\)](#) leads to the conclusion that long-term RV monitoring is the most critical information to rule out or confirm planets. Finally, a sizable fraction of giants hosting planet candidates are additionally orbited by stellar companions, which provides the opportunity to study planet formation scenarios in binary systems. These longer-period signals, however, also

complicate the confirmation of the planets. Consequently, long-term RV monitoring is essential when trying to grasp the full picture of the planet population around giants.

Due to practical considerations, such long-term monitoring is challenging to obtain using external observational facilities, especially when offsets between instruments should be avoided. Consequently, smaller telescopes committed to specific science cases can fill an important gap. One such survey, within the context of which this PhD thesis is situated, was the Lick RV survey of giant stars (see [Sect. 1.5](#)). Unfortunately, after twelve years of operations, the survey had to be stopped as the iodine cell was damaged ([Fischer et al., 2013](#)). For continued monitoring, it was decided to build a new échelle spectrograph to be mounted at LSW's Waltz telescope aiming for an RV precision of $\sigma_{RV} \lesssim 5 \text{ m s}^{-1}$.

6.2 Instrument overview

This section aims to provide a brief overview of the setup of the Waltz telescope and spectrograph. The instrument and specific subsystems have been described in much more detail by [Tala et al. \(2016\)](#), [Tala Pinto \(2019\)](#), and [Heeren \(2021\)](#), on which the following is largely based. The instrument control software, the control hardware setup, and interconnections between the components are described in [Spaeth \(2019\)](#).

6.2.1 The Waltz telescope and dome

The Waltz telescope, depicted in [Fig. 6.1](#), is operated in Nasmyth focus with a 72 cm primary mirror. It saw first light in 1906 and, at the time, was one of the largest telescopes in the world. Throughout its history it was mainly operated to conduct spectroscopic research (see, e.g., [Gaida & Rosa 1980](#)). It was measured by [Tala Pinto \(2019\)](#) to have a focal ratio $F/20.4$, leading to a focal length $f_T = 14.7 \text{ m}$ and a plate scale of 14.04 as mm^{-1} . After a mirror recoating in early 2024, the primary and secondary mirror are coated using an enhanced Aluminum coating, while the tertiary mirror is currently still operated with the previous, regular Aluminum coating. The secondary mirror can be moved along the optical axis for focusing ([Ruh, 2019](#)). The telescope is equatorially mounted and controlled via a DELTACODE mount control system ([Schneider, 2013](#)). It is equipped with encoders on both rotation axes. The telescope, as well as all other components, can be controlled from the Waltz main computer ([Spaeth, 2019](#); [Ruh, 2019](#); [Tala Pinto, 2019](#); [Kuhlbrodt, 2019](#); [Roth, 2020](#); [Wicker, 2020](#); [Heeren, 2021](#); [Wolfgramm, 2021](#); [Götz, 2022](#); [Stork, 2024](#)). An additional Starlight Xpress Lodestar X2 CCD Camera ([Starlight Xpress, 2014](#)) is mounted at the telescope tube to aid with telescope pointing.



Fig. 6.1.: The Waltz telescope peering into the evening sky.
Credit: Moritz Kirschner (mail@moritzkirschner.com)

The telescope is situated inside a landmarked, wooden dome, remotely controlled using a ScopeDome USB Card (ScopeDome, 2016; Roth, 2020; Jacobi, 2024b). The dome slit is currently opened and closed manually, but is planned to be mechanized (Frey, 2020).

6.2.2 Frontend

The frontend mounted on the telescope tube is depicted in Fig. 6.2 and was designed, updated, and described by Tala et al. (2016), Tala Pinto (2019), and Heeren (2021). The light from the telescope first hits the elliptical pickup mirror, which is angled by 45° and reflects the light into the direction of the science fiber. The pickup mirror can be moved out of the telescope beam using a software-controlled stepper motor to allow calibration light, injected via an optical fiber, to pass through to the science fiber. The pickup mirror is equipped with tip/tilt actuators (Newport, 2018) for accurate guiding (Götz, 2022).

The light reflected from the pickup mirror next passes through a glass cell filled with iodine gas, heated to 55°C (Kuhlbrodt, 2019). The iodine gas imprints numerous, fine absorption lines onto the stellar spectrum which, following the approach by Butler et al. (1996), are used to derive precise RVs (see Sect. 1.6.2). Similar to the pickup mirror, the iodine cell can be moved out of the telescope beam to, for instance, allow template observations.

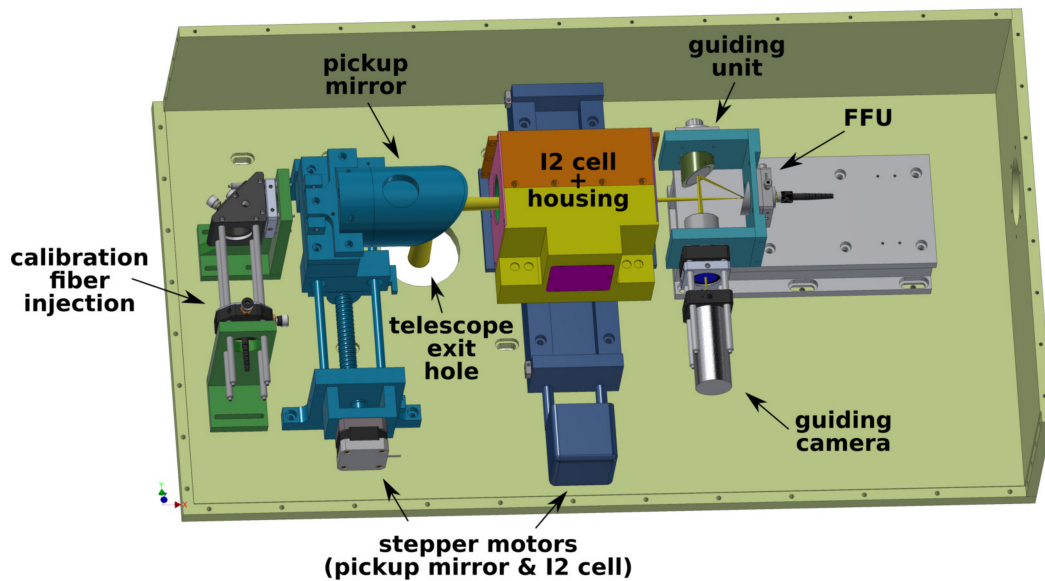


Fig. 6.2.: Model of the frontend. The incoming light is reflected from the pickup mirror and passes through the iodine cell into the pinhole and the fiber-feeding unit (FFU). The reflected light from the pinhole mirror is used for guiding. The pickup mirror and iodine cell can be moved in and out of the telescope beam. The pickup mirror was equipped with tip/tilt actuators for stable guiding (not depicted). Calibration light can be fed into the frontend via the fiber mount at the left. Credit: Heeren (2021) and Marcelo Tala Pinto

After the iodine cell, in the telescope’s focal plane, sits the pinhole mirror. This mirror is angled by 15° to reflect the majority of the telescope’s 3.2×2.4 arcmin field of view (Götz, 2022) into the Starlight Xpress Lodestar X2 CCD Camera, used for guiding. In the center of the mirror lies the pinhole, with a diameter of $265 \mu\text{m}$ – equivalent to 3.7 as on-sky (Tala et al., 2016; Tala Pinto, 2019; Heeren, 2021) – through which light enters the fiber-feeding unit, as designed by Heeren (2021). The rectangular fiber with a cross-section of $33 \times 132 \mu\text{m}$ then leads the light into the spectrograph situated on the ground floor. Yet missing is the image-slicer that will be 3D-printed onto the science fiber to convert the telescope’s circular PSF into a slit shape before coupling into the fiber. This is estimated to increase the coupling efficiency to about $\sim 80\%$ (Heeren, 2021).

6.2.3 Spectrograph

The Waltz spectrograph is based on initial designs and tests by Gutcke (2011) and Grill (2015), supervised and supported by Dr. Christian Schwab and Dr. Julian Stürmer. The final assembly of an updated design was completed and described by Heeren (2016) and Tala et al. (2016), with further updates described in Tala Pinto (2019) and Heeren (2021). The following aims to briefly summarize these sources.

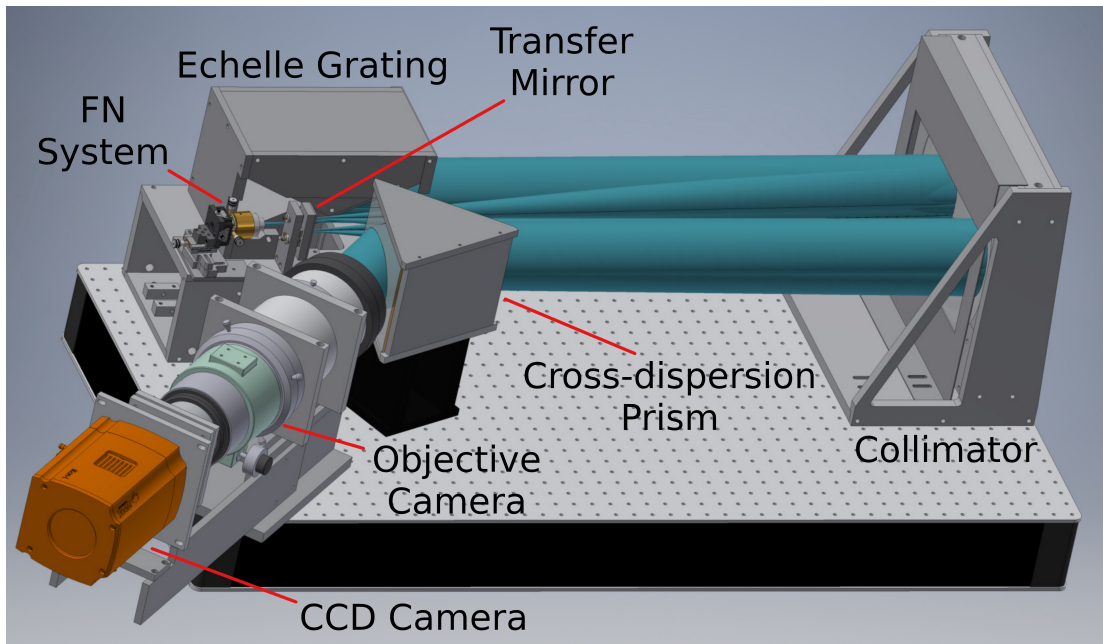


Fig. 6.3.: Model of the spectrograph. The light (turquoise) enters through the FN System, is collimated by the collimator mirror and dispersed by the échelle grating. It undergoes three additional reflections from the collimator and transfer mirrors before being cross-dispersed by a prism and imaged onto the CCD camera. Credit: [Heeren \(2021\)](#)

The spectrograph, depicted in [Fig. 6.3](#), is a cross-dispersed échelle spectrograph in white pupil configuration. The focal number (FN) System, through which the light enters into the spectrograph, transforms the F/5.5 fiber output to the working F/10 focal ratio of the spectrograph and focuses the beam onto the collimator mirror with a focal length $f_{\text{coll}} = 900$ mm. The collimated beam is reflected onto the échelle grating with 31.6 lines/mm and a blaze angle of 63.9° ([Heeren, 2016](#)). Following the white-pupil design, the diffracted beam is reflected back onto the collimator. The second reflection from the collimator mirror is slightly offset from the FN System and focused onto a flat transfer mirror, due to a small rotation of the échelle grating by 0.5° with respect to instrument's main optical axis. After another reflection from the collimator mirror, the diffraction orders are cross-dispersed by a prism. Finally, the beam is focused by a Takahashi quadruplet achromat camera onto the Andor iKon-L 936 back-illuminated CCD detector.

The CCD detector is powered by an uninterruptible power supply (UPS) and permanently air-cooled to a working temperature of $T_{\text{CCD}} = -70^\circ\text{C}$ (see [Sect. 6.3.1](#)). The Takahashi camera has recently been equipped with a ZWO Electronic Automatic Focuser by bachelor student Julius Hohmann. The spectrograph has a theoretical resolving power $R \sim 60\,700$ ([Tala Pinto, 2019](#)) and covers the wavelength range from 450 nm to 750 nm. However, the RV determination is limited to the iodine regime between 500 nm and 620 nm.

In the initial design, a Hamamatsu H9319-11 photomultiplier tube (PMT) was located beneath the échelle grating, measuring time-resolved variations in the photon flux in the 0th diffraction order to compute photon-weighted midpoints and aid in the selection of the exposure time. However, light levels have consistently been measured to be insufficient to accomplish either task for fainter stars. The PMT was thus moved to a new location beneath the transfer mirror (see Sect. 6.3.3).

For educational purposes, the spectrograph's encasing was built with a plexiglass top panel. A removable cover made of KAPA Fix polyurethane foam plates was added.

6.2.4 Additional components and infrastructure

The calibration unit is equipped with an LED lamp, as well as a quartz-tungsten halogen lamp for order tracing. Although intended to be combined with a beam splitter (Tala Pinto, 2019; Kuhlbrodt, 2019), they are currently still used independently. For initial wavelength calibration, the calibration unit further incorporates a Thorium-Argon (ThAr) hollow cathode lamp. The latter was recently replaced (January 2025) by a new lamp using Thorium-oxide instead of Thorium, produced by Green Scientific. Each of the lamps is fiber-fed into a software-controlled fiber switcher (Wicker, 2020), whose output is fed into the frontend as depicted in Fig. 6.2.

Further hardware components that complete the Waltz setup for efficient observations are detailed in Spaeth (2019). These include a Cloud Sensor II weather station, as well as an OMEA 3M Mono Camera from Alcor-Systems, used as an all-sky camera to monitor the observing conditions (Häffner, 2020; Wicker, 2020). Recent additions also include temperature and humidity sensors that monitor the conditions in the spectrograph room and in the dome. I further incorporated measurements from the external weather station located on the LSW and operated by the City of Heidelberg into the observation infrastructure. The whole Waltz infrastructure can be controlled via the main Waltz PC using the `waltzcontrol` software (Spaeth, 2019).

The scientific data obtained with the Waltz are automatically backed up to a dedicated data reduction computer and to the Waltz database¹, thanks to the efforts by master student Vivek Reddy Pininti. The extraction of the raw spectra is based on the CERES code (Brahm et al., 2017), the reduction of the RVs is performed by the `pyodine` software (Heeren, 2021; Heeren et al., 2023). The infrastructure was set up by Dr. Paul Heeren and bachelor student Paul Steimle. I streamlined the data reduction process for future operations and smooth integration with the Waltz database.

¹Accessible from within the LSW network via <http://1x53:3002>

6.3 Improvements to the Waltz infrastructure

To enable routine science observations, some hardware and software issues had yet to be resolved. In this section, I give an overview of the scientifically relevant improvements.

6.3.1 Miscellaneous improvements

- The two StarlightXpress CCD cameras, used for telescope pointing and guiding, frequently experienced connection problems, especially under high USB loads. The problem was identified to be caused by the `indi`² software architecture employed in the initial `waltzcontrol` implementation (Spaeth, 2019). To solve the issue, I implemented the USB protocol of the Lodestar X2 CCD camera directly.³ I further decoupled the camera communication module from the main `waltzcontrol` software into a dedicated process utilizing the Linux `systemd` service manager.⁴ The communication between the camera module and the main software is now loosely coupled using an in-memory instance of a `redis` database.⁵

Apart from fixing the connection problems, this also led to an improvement of the image readout speed. Using `indi`, the image latency due to readout and data transfer was measured to be of the order of ~ 350 ms, increasing up to ~ 700 ms, if both cameras were read out simultaneously. With the improved implementation, the image latency decreased consistently to ~ 290 ms, independent of whether the camera readouts coincide. This new approach further allows for the readout of only a subset of the whole image area, which is sufficient for guiding. This allows the latency to decrease to ~ 133 ms which, vice versa, increases the maximum guiding frequency possible. It further enables future tests for improved guiding parameters and, in principle, allows for an efficient stacking of images for bright stars for which long exposures, which average over seeing variations, saturate the image.

- For increased thermal stability and to avoid condensation on the Andor iKon-L 936 CCD camera, it was decided to cool the camera continuously to $T_{\text{CCD}} = -70^\circ\text{C}$. However, as stressed in the CCD's software development kit (SDK, Andor Technology 2016), uncontrolled heat ups from temperatures below $T_{\text{CCD}} = -20^\circ\text{C}$ must be avoided, as thermal stresses could damage the CCD chip. The camera was thus connected to an APC Smart-SRT3000RMXLI uninterruptible power supply (UPS) (APC by Schneider Electric, 2015) with enough battery capacity to power the CCD camera as well as the main Waltz PC for several minutes during power outages

²Instrument Neutral Distributed Interface: <https://indilib.org/>

³Based on the software: <https://jocular.readthedocs.io/en/latest/>

⁴<https://systemd.io/>

⁵<https://redis.io/>

(which have occurred in the past). Initial tests of the UPS were performed by Polat (2023), with the final hardware and software setup completed by me.

In order to safely operate the CCD camera continuously, I decoupled the CCD camera communication module from the main `waltzcontrol` software into its dedicated `systemd` service, implementing the communication between the GUI and the service via `redis`. The `apcupsd`⁶ service, which handles events recognized by the UPS, such as power outages, was set up to issue a regular shutdown of the main PC. In Linux, a shutdown event triggers a `SIGTERM` signal to all running `systemd` processes. Utilizing this native behavior, I configured the CCD service such that it gracefully heats up the CCD upon receiving a `SIGTERM` signal, before terminating the service. The system further sends a notification to the research group’s `pumble` channel. The timeout for the `SIGTERM` to be completed was set to 30 min. The regular shutdown of the system was configured to require root privileges.

- The implementation of the “stop and read” functionality for the Andor iKon-L 936 CCD camera was developed by Wolfgramm (2021) and Heeren et al. (2021). It uses an external trigger provided by a Transistor Transistor Logic (TTL) signal sent by an Arduino Uno connected to a Raspberry Pi.⁷ This implementation was debugged, reworked, and integrated into the updated camera communication architecture.

I further improved the timing of the exposures via two timestamps measured on the Raspberry Pi: one before sending the command to the Arduino to set the TTL signal and one after receiving its response. The time difference between the two timestamps is about $\delta t \sim 1$ s. It was determined, by ear, that the camera exposure occurs $t \sim 200$ ms prior to receiving the response from the Arduino, with the remaining 800 ms corresponding to the communication time and internal time of the CCD to process the trigger signal. This 200 ms offset is currently used to determine the exact exposure start. The timestamps are relayed to the main software via `redis`.

This measurement, naturally, is quite imprecise. It is thus relevant to estimate its effect on the barycentric velocity correction (BVC). Assuming a pessimistic $\sigma_t = 1$ s uncertainty on the start and stop of the exposure, the uncertainty of the geometric midpoint is $\sigma_{t,\text{mid}} = 0.71$ s. Following Tronsgaard et al. (2019), the change of the BVC on short timescales is dominated by Earth’s rotation and thus a difference in the BVC can be estimated following their Eq. 8. At the geographical latitude of the Waltz telescope, the maximum rate of change of the BVC is $-1.3 \text{ m s}^{-1} \text{ min}^{-1}$ for a star with declination $\delta = 0^\circ$ at the horizon. Thus, the uncertainty of the midpoint corresponds to a BVC shift of the order $\delta(\text{BVC}) \sim 1.5 \text{ cm s}^{-1}$ in the most extreme case. This is about two orders of magnitude smaller than the targeted RV precision

⁶<https://wiki.debian.org/apcupsd>

⁷pi@calibration.site

of the Waltz project and can thus be regarded as sufficiently precise. I note that during normal operations, the BVC is based on the PMT measurements (Sect. 6.3.3).

6.3.2 Realignment of the telescope and spectrograph

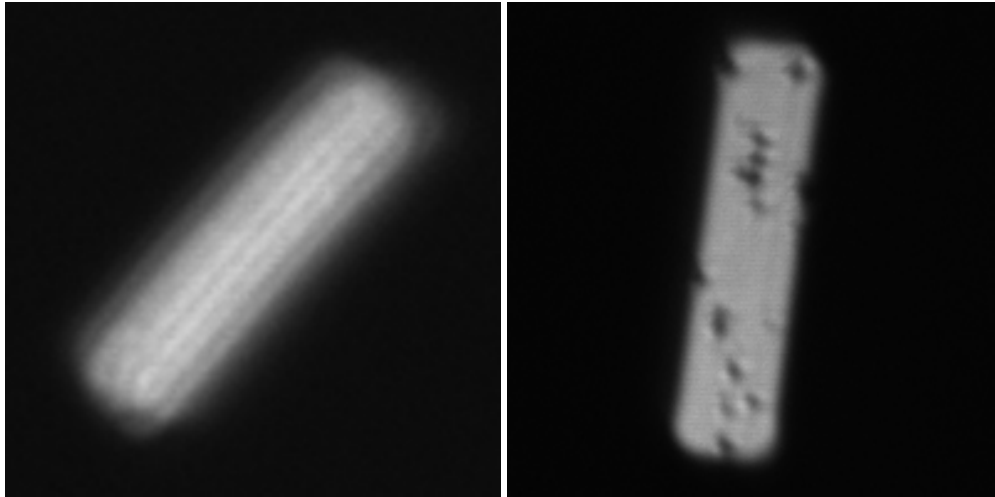
During initial on-sky tests between the end of 2022 and 2023, it was noticed that the light levels measured in the spectra were considerably smaller than expected. Among other factors, this was attributed to contamination on several reflective surfaces. As a consequence, the telescope's primary and secondary mirrors, as well as the spectrograph's collimator and transfer mirrors, were recoated by the company Tafelmaier using enhanced Aluminum, advertised to reach a reflectivity of roughly 96.5% at 520 nm. I note that the old tertiary mirror is still in use, as a new mount is required to install the recoated mirror.

The recoated mirrors were reinstalled, and the telescope was aligned jointly with the LSW workshop and Dr. Julian Stürmer. We also realigned the Waltz spectrograph, jointly with Dr. Stanimir Letchev. During the alignment, it was noticed that the spot of a single mode fiber illuminated by a Helium-Neon laser was deformed after being transmitted through the FN system, which was consequently removed and tested in the lab.

The FN system, as designed by Tala Pinto (2019), consists of two achromat lenses fixed into a brass tube that sits on a translation stage for alignment with respect to the spectrograph. However, as can be seen in Fig. 6.4a, the image of the spare Waltz science fiber is not properly focused when using the fixed FN system. Removing the two lenses from the FN System and aligning these separately, produces a much sharper image as shown in Fig. 6.4b. This indicates that the two lenses, when integrated into the FN System, are misaligned. Unfortunately, this misalignment cannot be amended with the current design. It was decided to use the current FN System aiming for an updated design in the future.

The FN System was reintegrated into the spectrograph and the latter was realigned. The median resolving power over the whole detector ranges between $R \sim 57\,250 - 59\,000$, with peak resolving powers close to and above the theoretical resolving power $R \sim 60\,700$ (Tala Pinto, 2019) mostly on the left end of the detector. The resolving power was measured on ThAr lines following Heeren (2021). We measured the throughput of the spectrograph to be roughly 38% using a Helium-Neon laser and a single-mode fiber.

The science fiber was furthermore realigned with the pinhole mirror within the fiber-feeding unit in the frontend (see Fig. 6.2) using an additional CCD camera equipped with a microscope objective. Back-illuminating the science fiber using a torchlight in the spectrograph room enabled to visualize the fiber as can be seen in Fig. 6.5.



(a) Image of the spare Waltz science fiber through the fixed FN system. Image was taken in the lab. (b) Image of the fiber after aligning the two lenses separately. Image was taken in the lab.

Fig. 6.4.: The spare Waltz science fiber imaged by the FN system. Images are not to scale.

An exact comparison of the signal levels before and after the mirror recoating and science fiber alignment is challenging due to variable weather conditions and airmass. For the two stars, for which the most comprehensive data sets are available, σ Dra and ι Dra, signal levels per time interval have increased by a factor of 1.75 and 2.53, respectively. These were calculated as the ratio between the mean $\frac{(S/N)^2}{t_{\text{exp}}}$ prior to and after the changes. The S/N throughout the text is computed at the peak of the blaze function in the diffraction order which lies just above 5500 \AA , in the center of the iodine region. It is measured per pixel and

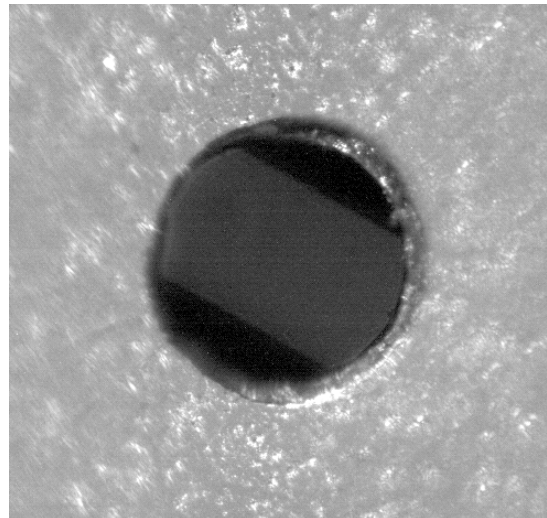


Fig. 6.5.: The fiber aligned behind the pinhole.

evaluated close to $\lambda = 5528 \text{ \AA}$ but can shift slightly. With these increased light levels, it is now possible to achieve $S/N > 100$ for stars of 6th magnitude within 30 minutes of exposure. On the night of February 1, 2025, for instance, $S/N = 137.0$ was achieved for the $V = 6.00$ mag star HIP 22220, and $S/N = 150.7$ for HIP 27280 ($V = 5.77$ mag). On a particularly good night, even $S/N = 156.2$ was reached for HIP 22220. Thus, the faintest stars within the Lick sample are now accessible to the Waltz.

In Fig. 6.6, I plot the average S/N measured for each star per square root of the exposure time expressed in minutes against the V band magnitudes as listed on SIMBAD. The data points can be fitted with an exponential relation following $S/N = 335.8 \cdot \exp(-0.431 \cdot V)$.

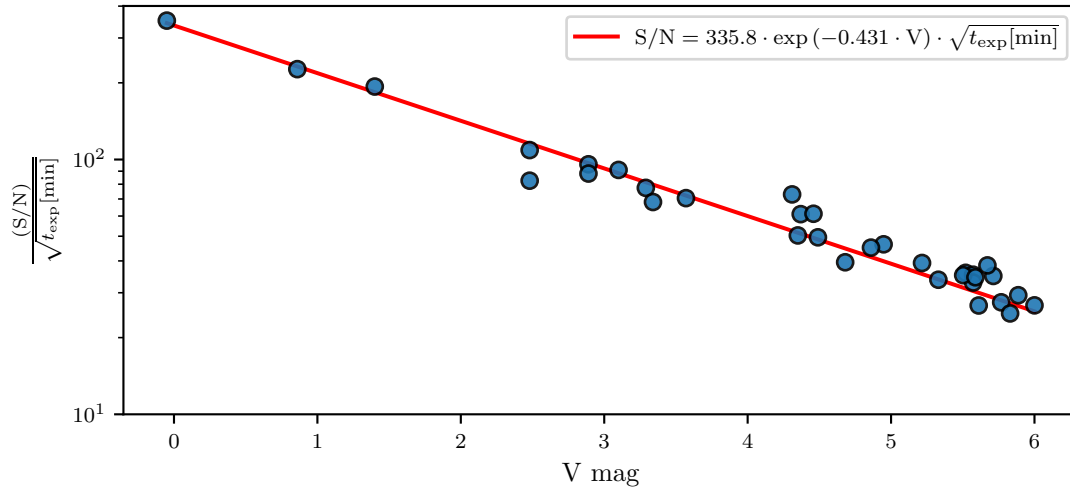


Fig. 6.6.: S/N per $\sqrt{t_{\text{exp}} [\text{min}]}$ as a function of V magnitude. Measurements for individual stars are shown in blue. An exponential relation was fitted to the data (red line).

$\sqrt{t_{\text{exp}} [\text{min}]}$ to predict the S/N for any star after a given exposure time. For a star of magnitude 6, one can thus expect $S/N \approx 139$ after 30 minutes of exposure. Naturally, the exact signal levels depend on airmass and observing conditions.

6.3.3 Relocation of the PMT

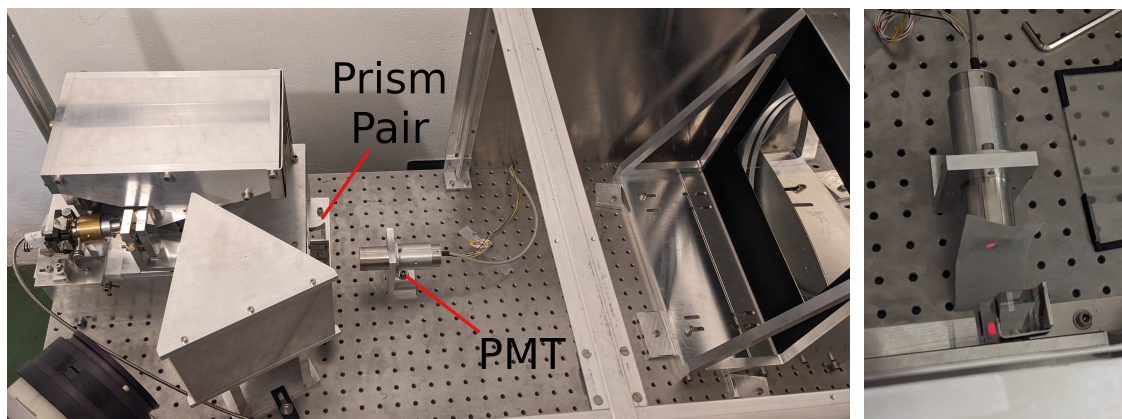
After the on-sky commissioning of the PMT (October 2022) at its initial location beneath the échelle grating, targeting the photon flux of the zeroth order, it was noticed that light levels were too low to reliably estimate any flux variations for stars fainter than $V = 4$ mag. At first, it was attempted to decrease the dark level of the PMT measurements, by improving the light tightness of the spectrograph room and by building a spectrograph encasing made out of KAPA Fix polyurethane foam plates, contributed by the LSW workshop. Although the dark level decreased drastically, light levels for faint stars remained too low.

During the realignment of the spectrograph (see Sect. 6.3.2), it was attempted to improve the alignment of the PMT. However, even using a bright Helium-Neon laser, no major increase in the light levels could be achieved. The most likely explanation is that the mounting of the échelle grating blocks the majority of the light in the zeroth diffraction order. I thus proposed to move the PMT to a new location.

The choice of the Waltz CCD and the transfer mirror was motivated such that the free spectral range (FSR) of diffraction orders 79 to 129 are covered completely on the chip (Heeren, 2016). In consequence, parts of the spectrum outside the FSR of each order are

cut off by the transfer mirror, which has a reflective surface of height 50 mm. This light can be used to measure time-resolved flux variations without loss of light on the CCD.

Due to spatial constraints, a pair of prisms (effectively used akin to a periscope) is used to redirect the part of the beam, which would not hit the transfer mirror, backward and to a lower height on the optical bench. The new location of the PMT, as well as the prism pair, can be seen in Fig. 6.7a. A Helium-Neon laser was used for alignment (see Fig. 6.7b).



(a) The new location of the PMT and the prism pair, directing parts of the spectrum that are cut off by the transfer mirror into the photometer. (b) Alignment using a Helium-Neon laser.

Fig. 6.7.: Setup of the new PMT location.

This new approach captures wavelength regimes beyond the CCD's imaging area across different spectral orders. As a result, the light detected by the PMT can be roughly considered white. The Hamamatsu H9319-11 PMT is sensitive in the regime $\lambda \sim 300 \text{ nm} - 650 \text{ nm}$, with its most sensitive range being $\lambda \sim 320 \text{ nm} - 500 \text{ nm}$.

In Fig. 6.8 (top), I plot the PMT counts acquired over one hour without exposing it to any light source. The dark level is found to be of the order of 12.2 counts per 100 ms interval of the PMT. I note that at this low level, the granularity of the PMT measurements starts to become a concern. That is, the PMT transmits its measurements only in steps of four counts. The dark level remained unaffected when lights were switched on in adjacent rooms, confirming the spectrograph's light-tightness.

In comparison, in the bottom panel, I plot a 30 min measurement of the $V = 6.00 \text{ mag}$ G giant HIP 22220 measured at airmass 1.05 on a typical observation night (February 1, 2025) in Heidelberg. In context of the Waltz RV survey, this corresponds roughly to the faint limit of the giant sample. As can be seen, the mean level of the PMT time series is 165.8 counts per 100 ms interval. Considering the dark level of the PMT and the shot noise, this corresponds to $S/N = 12.4$ per PMT interval, sufficient for calculating photon-weighted midpoints. The PMT measurements were included into the Waltz data reduction software (`waltzdrs`) by Bachelor student Silas Janke to compute a photon weighted barycentric correction following Tronsgaard et al. (2019).

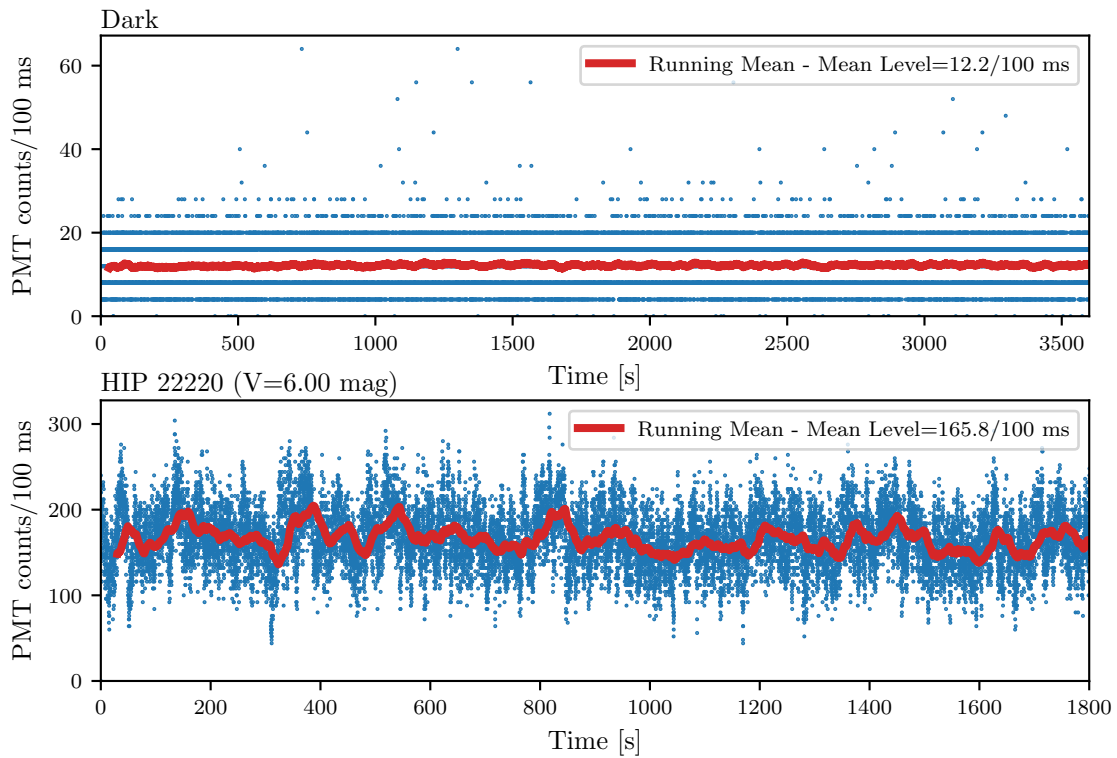


Fig. 6.8: PMT measurements of the dark level and of a faint star. Top: One hour of PMT measurements without light exposure. Bottom: 30 minutes of PMT measurements for the faint star HIP 22220 measured on February 1, 2025.

Relationship between S/N and PMT counts

The second important goal of the PMT measurements is to utilize the “stop and read” functionality of the CCD and estimate the current S/N according to the accumulated PMT counts during an exposure. This is especially important in variable observing conditions.

To estimate the relationship, I plot in Fig. 6.9 the S/N per pixel at $\lambda \sim 5528 \text{ \AA}$ against the accumulated PMT counts. I only include stars measured after the replacement of the telescope mirrors and realignment of the spectrograph, up until and including February 17, 2025. I restrict the analysis to measurements taken in the new, horizontal orientation of the CCD (see Sect. 6.4.3) and exclude measurements for which parts of the detector were overexposed. Finally, I subtract the contribution of the dark level of the PMT as determined above. I note that I plot the accumulated PMT counts divided by a factor 100, which was chosen to yield more convenient numbers within the `waltzcontrol` GUI.

In the photon noise limit, one can expect $S/N \propto \sqrt{S}$. I thus fit a square root relation to the data, which is shown as the black, dashed line. The proportionality factor was determined to be $A = 0.910 \pm 0.003$. As can be seen, the individual relations slightly deviate for different stars. This can be easily explained as a consequence of observing stars

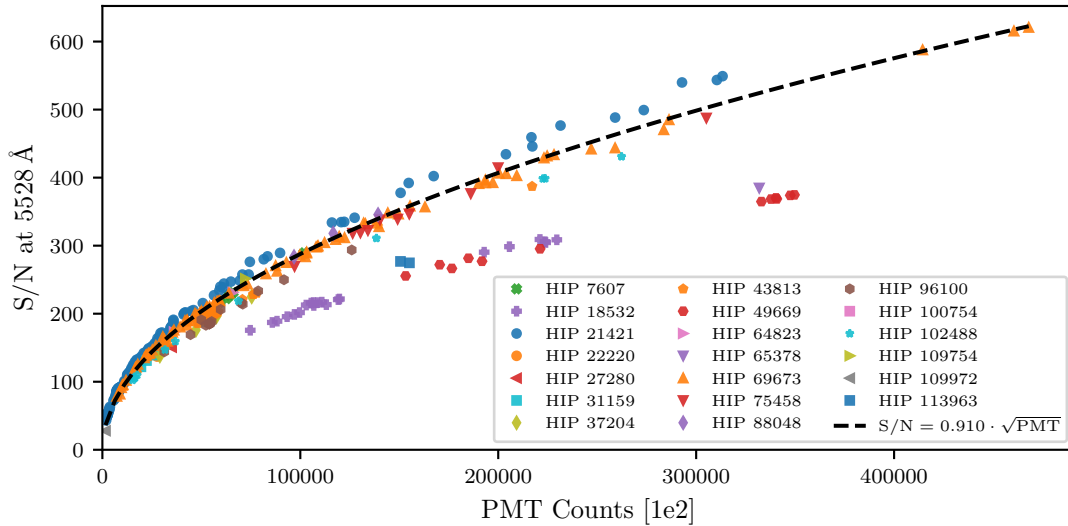


Fig. 6.9.: S/N at 5528 Å plotted against the accumulated PMT counts. A square root relation following $S/N = 0.910 \cdot \sqrt{PMT}$ was fitted to the data. The hot main-sequence stars HIP 18532, HIP 49669, HIP 65378, and HIP 113963 were excluded from the fit.

with different spectral types, for which the integrated light measured by the PMT and the S/N measured at a specific wavelength have different ratios. As the relationship is most important for the stars within the G and K giant sample, I excluded the A- and B-type stars HIP 18532 (purple crosses), HIP 49669 (red hexagons), HIP 65378 (purple triangle), and HIP 113963 (blue squares) from the fit. While, one can also see considerable scatter within the giant star sample, the relation is sufficiently constrained to allow a rough estimate of the expected S/N. The relation was implemented into the `waltzcontrol` GUI.

6.4 The CTI effect

6.4.1 Characterization

Following first on-sky tests on the RV standard star σ Dra in late 2022, an anticorrelation between the RVs and the S/N was noticed. Based on suggestions by Dr. Mathias Zechmeister and Dr. Adrian Kaminski, the Charge Transfer Inefficiency (CTI) of the CCD camera was suspected to influence the RVs. The CTI quantifies the percentage of charges accumulated within a pixel that is not shifted to the adjacent pixel during readout. The residual charges are left in the trailing pixels along the clocking path (Zhao et al., 2021).

Figure 6.10 (top left) presents a zoom-in into a dark frame acquired with the Waltz CCD deliberately cooled to only $T_{CCD} = -30^\circ\text{C}$. Several warm pixels can be observed, which

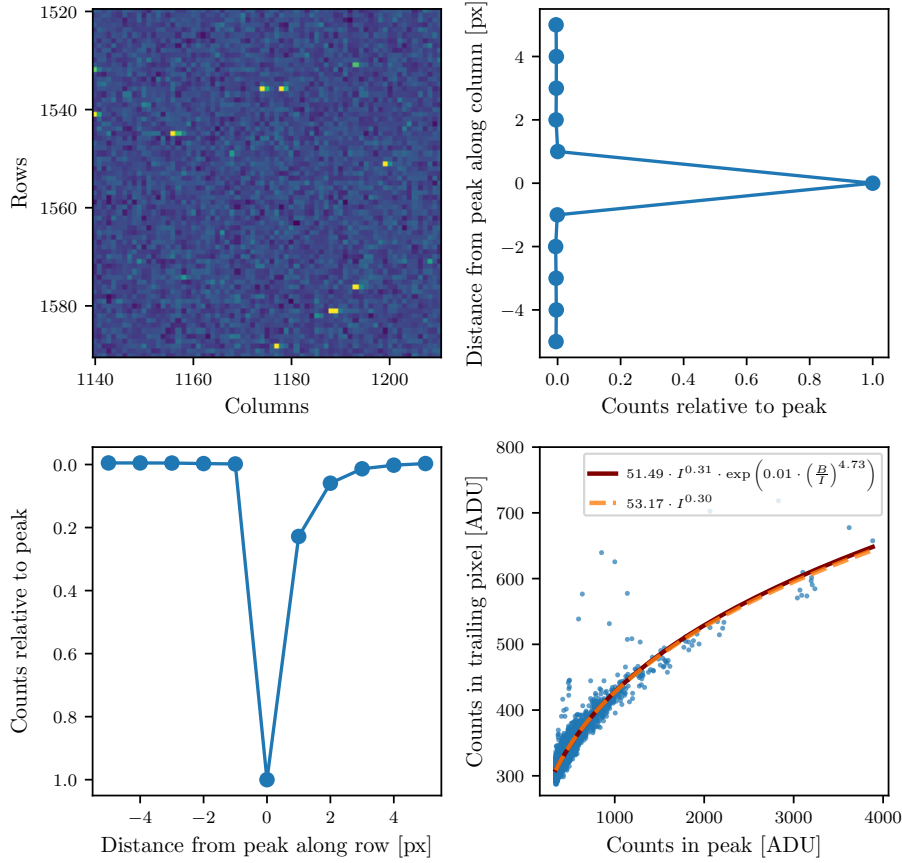


Fig. 6.10.: The CTI effect visualized using warm pixels in a dark frame. Top left: A zoom-in into a dark frame. Top right: Average CCD counts relative to the warm pixel along columns. Bottom left: Relative counts in neighboring pixels along rows. I note the inverted y-axis. Bottom right: Counts in the first adjacent pixel on the right side of a warm pixel plotted against the counts in the warm pixel. Eq. 6.1 (red, solid line) and a simplified power law (orange, dashed line) were fitted.

appear to have a tail of increased pixel counts along the CCD rows toward the right. In the top right and bottom left panels, I combine the information of 9928 warm pixels measured in five subsequent dark frames to assess the average shape of rows and columns containing warm pixels. For each of the dark frames, I remove the median of the CCD counts to estimate the bias and dark current background, although the latter is negligible for the $t_{\text{exp}} = 20$ s exposures. I detect warm pixels as those with count values exceeding 5σ . For each of these, I store the five adjacent pixels in both directions along the CCD columns and rows. These are averaged for the columns in the top right panel, and for the rows in the bottom left. While there is no increase of the pixel counts along the columns, a clear increase of the counts toward the right can be seen along the rows. The y-axis was inverted for the latter. We assume that this effect is caused by the CTI of the CCD.

In the initial configuration, the direction along the CCD rows, i.e., the direction along the serial register, coincided with the direction of dispersion. Thus, it is reasonable to assume that spectral lines might be distorted due to this readout effect. [Bouchy et al. \(2009\)](#) found a similar correlation between the RVs and the S/N with the SOPHIE spectrograph. They showed that the correlation can be corrected iteratively and that the CTI effect for each pixel x can be described using the empirical relation developed by [Goudfrooij et al. \(2006\)](#)

$$CTI(x) = \alpha \cdot I(x)^{-\beta} \cdot \exp\left(-\gamma \cdot \left(\frac{B(x)}{I(x)}\right)^\delta\right), \quad (6.1)$$

in which B quantifies the background level. I plot in the bottom right panel of [Fig. 6.10](#), the CCD counts measured in the first adjacent pixel on the right of each warm pixel against the counts measured in the warm pixel. I fit for the relation given by [Eq. 6.1](#) (red, solid line), which convincingly describes the data. I note that I did not remove the background level from the CCD counts, using it as the background level B instead. This results in a more convincing fit. That is surprising, since the background is predominantly dominated by the bias, as the dark level of the CCD is very small. The bias, however, is not actually present in the form of a charge within the pixel potential wells, but is instead only an offset voltage applied to the readout node. Opposite to what is observed, one would thus actually not expect the bias level to be relevant for the CTI effect.

Nevertheless, there clearly is a form of CTI effect present in the Andor CCD, noticeable only along the rows, with a clear signal dependence. Thus, on a stellar spectrum, the effect would result in a signal dependent distortion of spectral lines, which could be measured as spurious RV shifts. As the tail extends to the right, corresponding to increasing wavelengths, a stronger distortion would lead to a positive RV shift. As the relative shift decreases with increasing signal intensity, an anticorrelation between the RVs and the S/N is expected.

As the resulting fit has only a weak dependence on the exponential term in [Eq. 6.1](#), I also fit for a simplified power law relation (orange, dashed line), which, given the available data, yields an equally convincing fit. The fact that either relation fits the data suggests a relatively constant effect along the CCD rows. If the effect were strongly dependent on the position within the row, one would expect the relation to be strongly smeared out, as the counts in the adjacent pixel would be iteratively accumulated during each shift.

Also surprising is that the CTI effect is only visible along the rows, which correspond to the direction of the serial register, as was confirmed with the CCD's manufacturer, with the trails pointing away from the amplifier. Usually, the CTI effect is much stronger along the CCD columns ([Goudfrooij et al., 2006](#); [Bouchy et al., 2009](#); [Zhao et al., 2021](#)). In our case, however, the CTI effect seems to appear in the serial register. Combining these findings, one can argue that the Andor CCD chip presents a fundamentally different effect than described by [Goudfrooij et al. \(2006\)](#) or [Bouchy et al. \(2009\)](#). The CTI effect gets slightly stronger using lower horizontal shift rates (default for the Waltz is the second

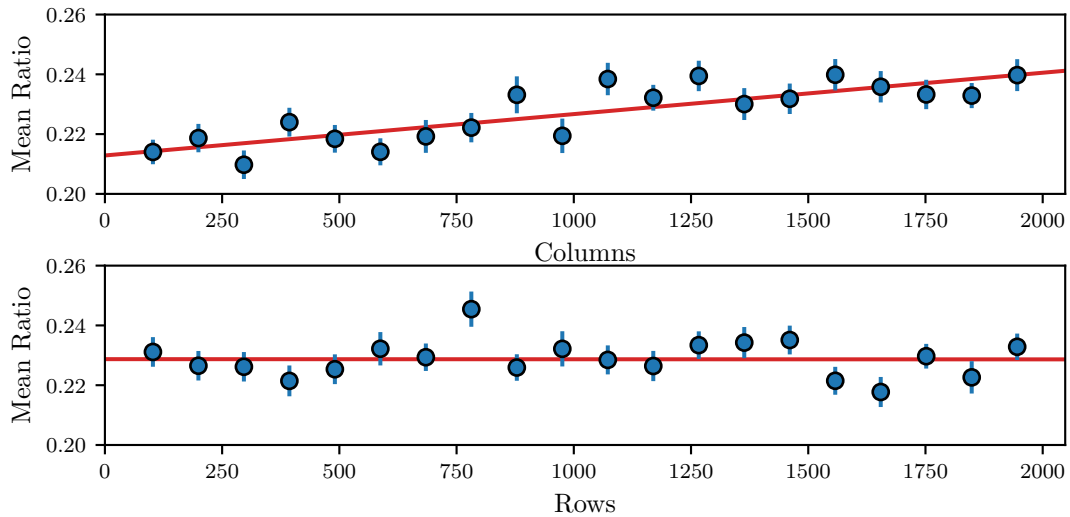


Fig. 6.11.: Binned count ratios between the first adjacent pixel to the right and the warm pixels as a function of the CCD columns (top) and rows (bottom). Top: The mean ratio calculated in 20 bins over the detector as a function of the CCD columns. A linear relation with slope $m = (1.38 \pm 0.19) \cdot 10^{-5} \text{px}^{-1}$ was fitted to the data. Bottom: The mean ratio calculated in 20 bins over the detector as a function of the CCD rows. The linear fit with slope $m = (0.004 \pm 0.19) \cdot 10^{-5} \text{px}^{-1}$ is consistent with a constant.

slowest at 1.0 MHz) and slightly increases using higher pre-amplifier gains. However, it is consistently present and thus cannot be prevented using different settings. There are furthermore indications of it being dependent on the CCD temperature.

In Fig. 6.11, I plot the CCD count ratio between the first adjacent pixel and the warm pixel as a function of the CCD columns (top) and rows (bottom). I bin the 9928 warm pixels of the five dark frames into 20 bins and fit for linear relations. I stress that the ratio is again calculated having removed the background. The mean ratio across the whole chip is 0.228. I fit linear models and find a significant slope of $m = (1.38 \pm 0.19) \cdot 10^{-5} \text{px}^{-1}$ as a function of the CCD columns (i.e., along the CCD rows). In the perpendicular direction, a linear fit is consistent with a constant model ($m = (0.004 \pm 0.19) \cdot 10^{-5} \text{px}^{-1}$). From the top panel, one can again see that the effect cannot solely be the consequence of an iterative charge transfer deficiency per pixel, as one otherwise would suspect the relation to start near zero in columns close to the amplifier.

It can be concluded that the strength of the CTI effect is independent of the vertical distance from the readout register, while it is slightly dependent on the horizontal distance from the amplifier. This is consistent with the findings by Janke (2023) using ThAr spectra, and shows that the effect is originating from within the readout register or is caused by the amplifier. One can also see that the effect is mostly constant over the chip with only a weak distance-dependent component. One cannot observe any jumps in its strength, which indicates that it is not caused by “traps” in specific pixels (e.g., Crowley et al. 2016).

6.4.2 Correcting the CTI effect

Iterative CTI correction

Two approaches were considered to mitigate the influence of the CTI effect on the RVs. The first is to calibrate the CTI effect and implement a software correction on the raw CCD images. As an alternative, as the effect seems to only be present along the CCD rows, I proposed to rotate the Andor CCD.

Bachelor student Jonas Reichert and [Stange \(2023\)](#) developed first attempts to correct the effect iteratively. Built on these initial tests, [Jacobi \(2024a\)](#) and [Vakhidov \(2024\)](#) calibrated the parameters using “CTI sequences” measured for bright stars on-sky, that is, RVs for a single star measured sequentially at a range of different S/N. Their approach is fundamentally based on the iterative correction following [Bouchy et al. \(2009\)](#), however, using a simplified power law relation $CTI(x) = \alpha \cdot I(x)^{-\beta}$, as the background in the CCD images is relatively small. With this iterative correction, [Vakhidov \(2024\)](#) is able to correct the correlation between the RVs and the S/N (see Fig. 6.2 in [Vakhidov 2024](#)).

Using the determined parameters, I can test the CTI correction on the sequence of dark frames. In [Fig. 6.12](#), I plot the pixel count ratios along the CCD rows containing warm pixels. I show the original, uncorrected shapes as blue circles, while I show the correction based on [Vakhidov \(2024\)](#) as red squares. The same 9928 warm pixels as above were used. The background was subtracted prior to calculating the ratios. For the CTI-corrected version, I use a median filter to remove a background trend of 500 counts across the CCD rows. I further plot a suggested, improved relation in orange, which is discussed below. As can be seen, the CTI correction by [Vakhidov \(2024\)](#), while performing well on the RVs, cannot entirely suppress the CTI effect on the warm pixels.

Further insight is also given by observing the corrected pixel count ratios over the CCD chip as shown in [Fig. 6.13](#). The middle panel shows the 9928 warm pixels across the CCD chip, color-coding their individual count ratios (first adjacent pixel along the row divided by the warm pixel). One can see that the CTI correction undercorrects the CTI effect at the left and right edges of the CCD, while it overcorrects in the center. On average, the CTI effect is reduced to a mean ratio of 0.104. The trend over the chip can also be seen in the binned averages as a function of the CCD columns (top). As a function of the CCD rows (right), the dependence remains consistent with a constant.

Several factors might explain why the CTI correction by [Vakhidov \(2024\)](#) performs well on the RVs but poses challenges when applied to the warm pixels. Firstly, the stellar spectra used by [Vakhidov \(2024\)](#) have typically much higher counts per pixel. Thus, it is possible that the fitted relation by [Vakhidov \(2024\)](#) performs better at higher signal levels not probed here. Also, to obtain a usable number of warm pixels, the CCD was

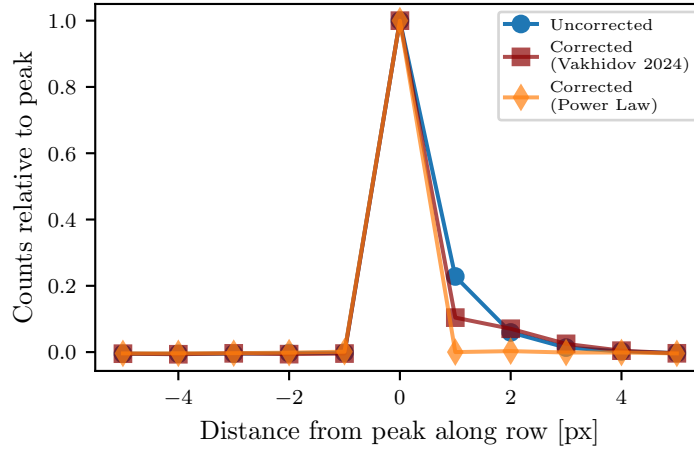


Fig. 6.12.: Mean shape of 9928 rows containing warm pixels. I plot the average count ratios between pixels adjacent to a warm pixel and the counts in the warm pixel along the CCD rows. The uncorrected pixels are shown as blue circles. The CTI corrected pixels following Vakhidov (2024) are shown as red squares. A proposed, improved CTI correction based on a constant correction using a power law relation is shown as orange diamonds. The same warm pixels are used to compare the shapes.

deliberately cooled to only $T_{\text{CCD}} = -30^\circ\text{C}$, while the RVs were typically measured using $T_{\text{CCD}} = -50^\circ\text{C}$ or $T_{\text{CCD}} = -70^\circ\text{C}$. Nevertheless, based on the general findings above, it seems reasonable to question the assumption that the CTI effect is iterative and present in each pixel, as described in Eq. 6.1.

Suggestion of an improved correction

Combining the above results, I can propose a first attempt at an improved relation. I assume that the CTI correction should not be performed iteratively but rather as a single correction for each pixel, consisting of a dominant constant term and an additional adjustment based on the distance from the amplifier along the row. For simplicity, I assume that a power law relation sufficiently describes the functional dependence. Calibrating the relation (by eye) results in a quantification of the CTI effect as:

$$CTI(x + 1) = \alpha \cdot (1 + \epsilon \cdot x) \cdot I(x)^{-\beta}. \quad (6.2)$$

The parameters are $\alpha = 53.171$, $\beta = -0.309$, and $\epsilon = 7.691 \cdot 10^{-5} \text{ px}^{-1}$. The latter encodes the slight increase of the CTI effect dependent on the pixel position x along the CCD rows. Eq. 6.2 yields the expected counts due to the CTI effect in pixel $x + 1$, calculated from the counts measured in pixel x . It is computed once for the entire frame, subtracted from the frame shifted by one pixel, and then added back to the unshifted frame to maintain a constant total count. I stress that, counterintuitively, the relation is best fitted when

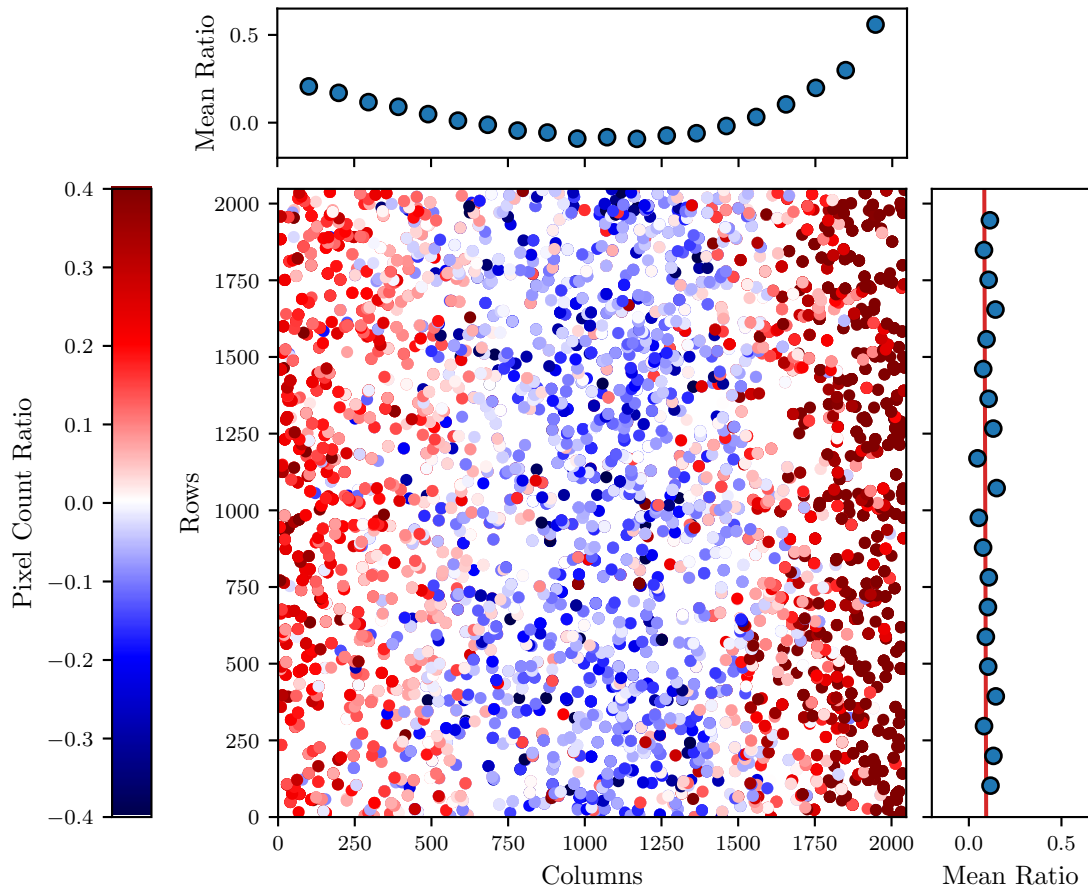


Fig. 6.13.: Pixel count ratios after applying the CTI correction by Vakhidov (2024) over the CCD chip. Middle: The 9928 warm pixels color-coded by the corresponding count ratio plotted over the chip. Top: The count ratios as a function of the CCD columns averaged in 20 bins. Right: The count ratios as a function of the CCD rows averaged in 20 bins. A linear relation, consistent with a constant, was fitted to the data.

not removing the bias level. This might suggest that the effect occurs in the readout electronics rather than in the sensitive area of the chip or in the readout register. The suggested correction can be seen as orange diamonds in Fig. 6.12. It successfully corrects the majority of the CTI effect. The mean ratio after the CTI correction is $-1.02 \cdot 10^{-6}$, and the slopes both along the rows and columns are consistent with zero (not plotted).

Figure 6.14 presents a preliminary test to correct a single CTI sequence of Aldebaran acquired on February 7, 2023. The change of the RVs (arbitrary zero point) is plotted against $(S/N)^2$, as a proxy for the signal level. The uncorrected RVs (blue) have a slope of $m = -32.8 \pm 5.9 \frac{\text{m s}^{-1}}{(S/N)^2}$. This slope is reduced to $m = -11.8 \pm 5.5 \frac{\text{m s}^{-1}}{(S/N)^2}$ (red), which is consistent with a constant model within 3σ . I note that a reduction of the slope was observed also for other CTI sequences, however, some sequences were not as strongly reduced. Thus, the updated CTI correction seems to have the potential to correct the RVs but requires further calibration. It would be important to perform the analysis at the same

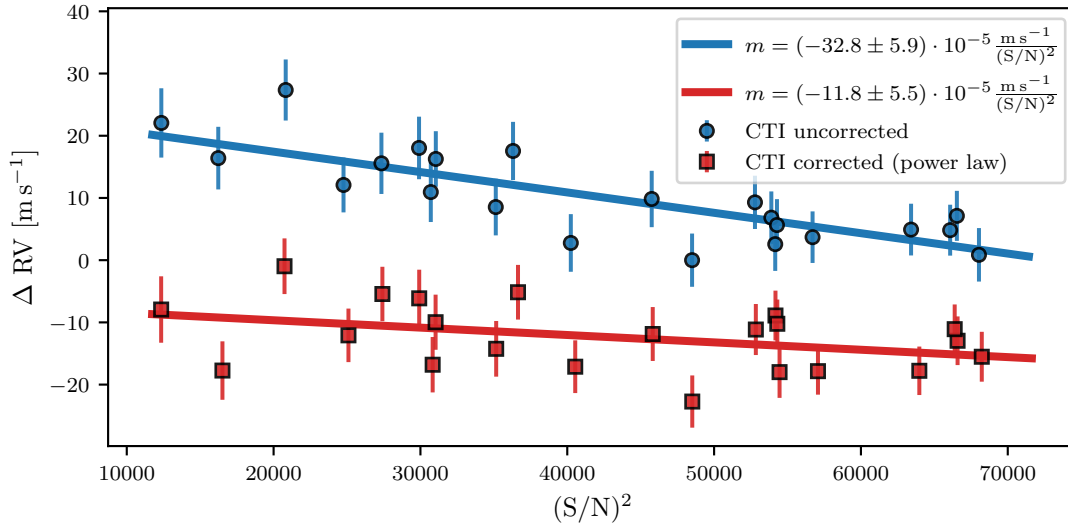


Fig. 6.14.: Preliminary CTI correction test for Aldebaran. The change of the RVs is plotted against $(S/N)^2$, as a proxy for the signal level on the CCD. Linear relations were fitted to both the uncorrected (blue), and corrected (red) CTI sequences (see legend).

CCD temperature (typically $T_{\text{CCD}} = -50^\circ\text{C}$), as used during the observations, and using a much larger number of dark frames, ideally extending to higher counts.

6.4.3 Rotation of the CCD

The alternative is to rotate the CCD, as, luckily, the CTI effect seems to be only present along the rows. After a rotation, the CTI effect would thus be directed along the cross-dispersion direction, which would much less, if at all, influence the spectral line shapes. The rotation of the CCD was enabled by the LSW workshop, and on-sky tests comparing CTI sequences for the same star in different CCD orientations were conducted in July 2024. Figure 6.15 presents three CTI sequences for the very bright star Arcturus. Plotted in blue is a sequence recorded on July 30, 2024, in the original CCD orientation (which internally is referred to as the vertical CCD orientation, as the cables of the CCD stick out on the left side when viewed from behind). On the x-axis, I plot $(S/N)^2$ (measured at $\lambda = 5528 \text{ \AA}$) as a proxy for the signal level. For each sequence, I subtract the RV minimum and plot only measurements with $S/N < 650$. Higher signal levels start to saturate the chip. A power-law, motivated by the simplified CTI correction based on Eq. 6.1 was fitted to the data. A significant exponent $b = 0.538 \pm 0.050$ is found for the old configuration.

In contrast, I plot two CTI sequences in red which were taken on July 29th and July 30th in the horizontal CCD orientation (cables of the CCD sticking out at the bottom). The minimum RV is subtracted from both nights before combining the sequences. As can be

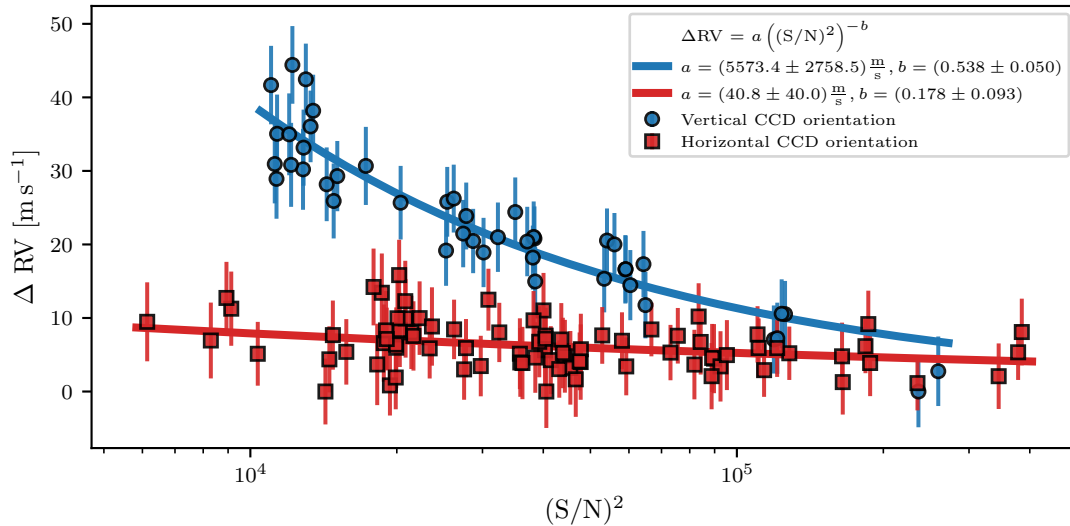


Fig. 6.15.: RV vs. $(S/N)^2$ for the vertical (blue) and horizontal (red) CCD orientations for Arcturus. Power-law relations were fitted to both CTI sequences (see legend).

seen, the trend is strongly reduced. The exponent of the power law $b = 0.178 \pm 0.093$ is consistent with zero within 2σ . For a fair comparison, the same template spectrum (taken in the updated CCD orientation) was used when reducing both data sets. Additional CTI sequences taken for other stars, revealed consistent results. However, it was found that the effect can persist when using a template taken in the old configuration, as can be expected since the CTI effect would affect both template and regular science observations.

Whether the effect is entirely vanished is challenging to establish, as the bright giants used for these sequences show short-term RV variations on much larger scales. It would thus be advisable to monitor future RVs for any suspicious correlations. In the presented case, the remaining RV difference between a spectrum acquired with $S/N = 50$ and $S/N = 650$ (the rough saturation limit) would be of the order of 6 m s^{-1} . Such an effect could still be explained, by a smaller CTI effect along the CCD columns, or could be caused by the curvature of spectral orders across the chip. In typical observations, however, it is common to aim for a particular S/N level (e.g., Zhao et al. 2021), which would further reduce the impact. If a correction can be calibrated with confidence, as currently planned using data from the SONG spectrograph, which used the same CCD detector, it might still be worth to consider correcting the raw CCD data, even in the horizontal orientation.

Overall, it can be concluded that the CTI effect does not substantially influence the RVs in the horizontal CCD orientation. Since August 2024, the serial register is thus oriented perpendicular to the spectral orders. Two drawbacks come with this new orientation. The first is that damaged CCD columns could affect the full range of spectral orders. Luckily, no such defects are present on the Waltz CCD. The second drawback affects the ThAr spectra,

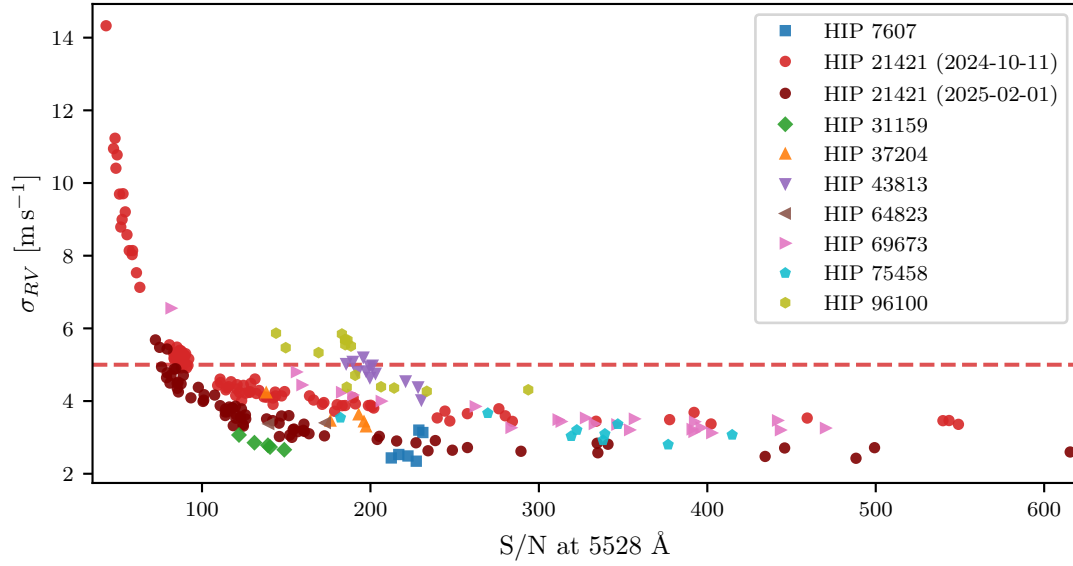


Fig. 6.16.: RV uncertainties σ_{RV} as a function of the S/N of the spectra for different stars. The horizontal, dashed line indicates an RV precision of 5 m s^{-1} .

which are used for an initial wavelength solution. In the red part of the spectrum, several bright lines saturate the CCD exposures. In the horizontal orientation, the saturation trails now run parallel to the spectral orders, which naturally deteriorates the wavelength solution in these orders. Luckily, as the RV determination is restricted to the iodine regime ($\lambda \sim 5000 \text{ \AA} - 6200 \text{ \AA}$ is now in use), these spectral orders do not affect the reduced RVs.

6.5 First on-sky tests of the Waltz RV survey

6.5.1 Formal RV uncertainties

I plot in Fig. 6.16 the formal RV uncertainties σ_{RV} derived by the pyodine pipeline (Heeren et al., 2023) of all spectra acquired in the horizontal CCD orientation (since August 2024). I only include stars for which updated template measurements are available. As expected, the uncertainties, to first order, are inversely proportional to the S/N. At high S/N, the uncertainties are as low as $\sigma_{RV} = 2.3 \text{ m s}^{-1}$. The targeted RV precision of 5 m s^{-1} is drawn as the horizontal, dashed line. Most stars have better precision for $(S/N) \gtrsim 150$.

When analyzing the relation in more detail, one observes that the RV uncertainties depend on the star. For instance, HIP 96100 and HIP 43813 have slightly higher uncertainties. This could be a consequence of the quality of the template or the weighting algorithm of pyodine. The latter is based on the scatter in the RVs of the individual chunks, as

wells the scatter between different chunks (Heeren et al., 2023), such that the individual observations also influence each other’s uncertainties. Thus, when only few are available, observations at low S/N can influence the uncertainties of the entire time series. This scatter might, however, also be related to the exact spectral characteristics of the star, such as the number, depth, and width of spectral lines, as well as their variations. It can also be influenced by the exact position of the chunks within the spectrum. In any case, it would be advisable to study the influence of the stellar template and the chunking algorithm on the RV determination to ensure a sufficient quality.

The RVs of Aldebaran (HIP 21421) are of special interest. I color-code two times series taken on 2024-10-11 (light red) and 2025-02-01 (dark red). These seem to form distinctive branches in the high S/N regime, with somewhat lower uncertainties observed on 2025-02-01. On the same night, I acquired the stellar template, which could explain the lower uncertainties. This could be caused by a similar LSF between the science spectra and the template. Vice versa, one can suspect that the LSF fitted on the night 2024-10-11 negatively influences the RV precision. This could argue for the necessity of an improved LSF model or better starting parameters to be employed in the `pyodine` pipeline. One approach to use Hermite polynomials instead of a MultiGaussian LSF model was presented by Jessen (2022). It is, furthermore, currently investigated whether template spectra could be extracted from a combination of all regular science observations. On the other hand, it is also plausible that the smaller required barycentric shift between the template and the iodine spectra could play a role. Such effects can certainly be studied in more detail given more data. In any case, it can be concluded that the formal RV uncertainties satisfy the goal of achieving RV precision better than 5 m s^{-1} .

6.5.2 Short-term RV stability

To study the instrument’s short-term stability, I acquired several time series spanning from 30 min to 2.5 h for a number of stars, which are shown in Fig. 6.17. These include measurements for the bright stars Aldebaran (HIP 21421) and Arcturus (HIP 69673), as well as fainter stars such as HIP 31159 ($V = 5.8 \text{ mag}$) and HIP 37204 ($V = 5.6 \text{ mag}$). The mean formal uncertainties, as well as the RMS of the RVs are indicated in the legends. For none of the time series, the RMS of the RVs exceeds 8 m s^{-1} . The largest RMS are observed for the two faint stars (apart from the top left panel, see below) which, however also have the longest window durations of 2.5 h, timescales on which the p-mode pulsations become relevant. Using simple scaling relations (e.g., Coelho et al. 2015), one can estimate the periods of maximum power of the p-mode oscillations as $P_{\text{max}} \sim 7.7 \text{ h}$ and $P_{\text{max}} \sim 4.6 \text{ h}$ for HIP 31159 and HIP 37204, respectively, not that far off the 2.5 hours sampled in the observations. The rough amplitudes can be estimated following Kjeldsen & Bedding (1995) and are $A \sim 11.25 \text{ m s}^{-1}$ and $A \sim 7.7 \text{ m s}^{-1}$, respectively. Especially, for HIP 31559,

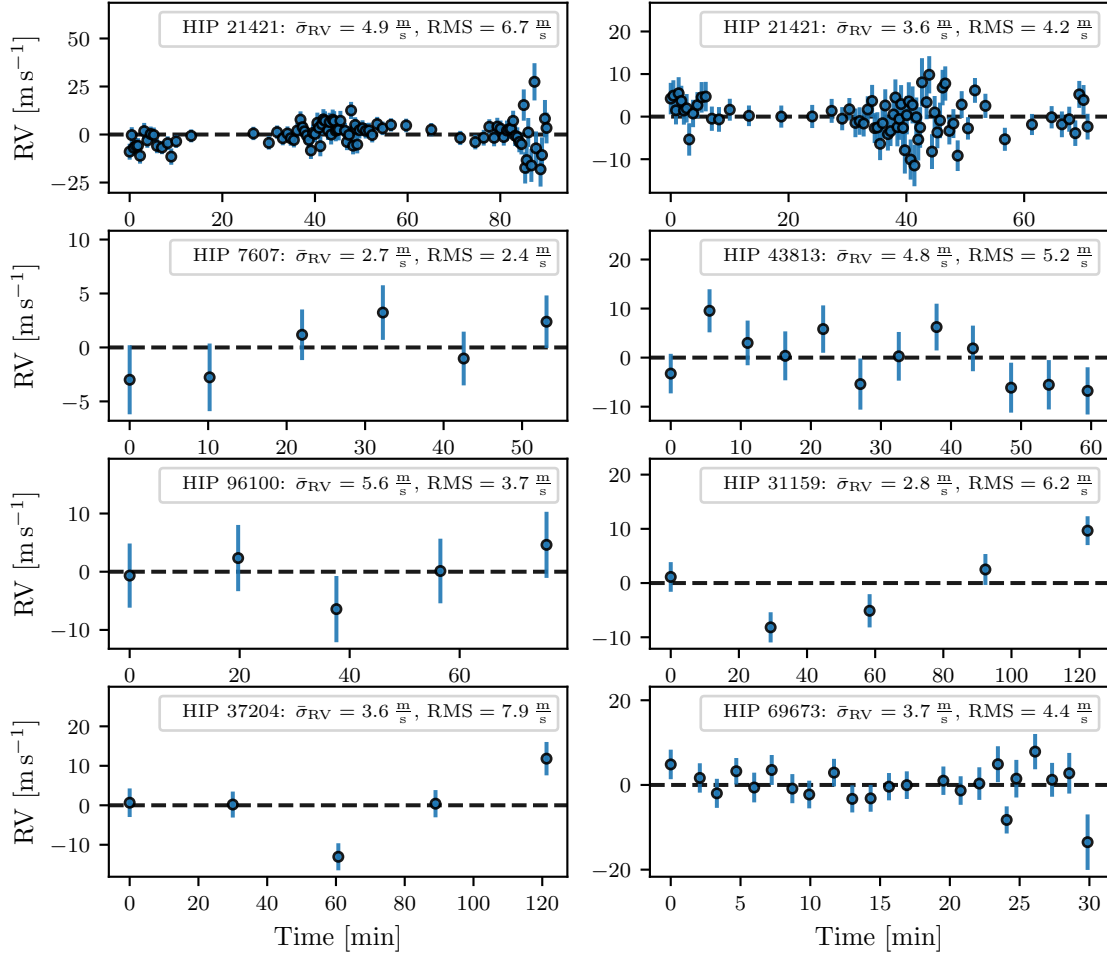


Fig. 6.17.: RV time series for different stars taken in short sequence. The mean formal error $\bar{\sigma}_{\text{RV}}$, as well as the RMS of the RVs are indicated in the legends.

one might indeed suspect that the variation resembles a periodic variation. Thus, it seems reasonable to assume that the increased scatter might be due to the p-mode oscillations. I note that for Aldebaran, since the time series were part of “CTI sequences”, deliberately extending to very low S/N, the scatter and mean formal errors are somewhat inflated.

If the uncertainties are reliably estimated, one can expect the RMS of the measurements to be consistent with $\text{RMS} = \sqrt{\bar{\sigma}_{\text{RV}}^2 + \sigma_{\text{jit}}^2}$, with σ_{jit} encapsulating both the (unknown) stellar RV jitter, and any scatter caused by the instrument. σ_{jit} is of the order of 2.5 m s^{-1} for most time series. For the first time series of HIP 21421 (including the low S/N spectra), the jitter is $\sigma_{\text{jit}} = 4.6 \text{ m s}^{-1}$, while it is $\sigma_{\text{jit}} = 5.6 \text{ m s}^{-1}$ and $\sigma_{\text{jit}} = 7.0 \text{ m s}^{-1}$ for HIP 31159 and HIP 37204, respectively. The latter are consistent with the p-mode jitter. For HIP 7607 and HIP 96100, the formal errors exceed the RMS of the measurements. One can thus conclude that no large RV drifts can be measured on short timescales and any instrumental

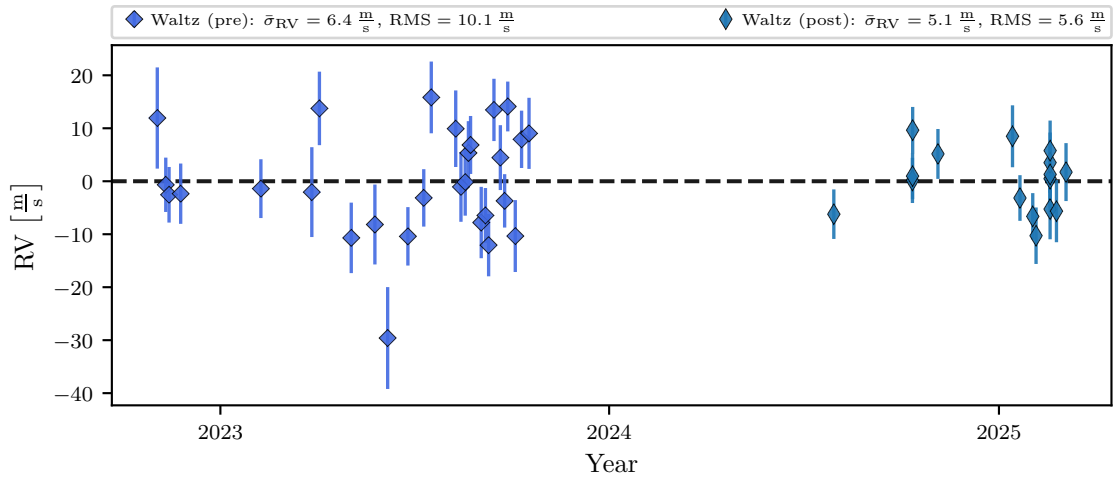


Fig. 6.18.: Long-term Waltz RV time series for σ Dra. The old spectrograph configuration (pre) is portrayed as wider diamonds, while the updated configuration (post) is shown as narrow diamonds.

scatter, not accounted for in the formal uncertainties, is likely of the order 2.5 m s^{-1} or below, neglecting the inflated jitter for the CTI sequence of HIP 21421.

6.5.3 Long-term RV stability

To test the long-term RV stability, we continuously observed the main-sequence star σ Dra (HD 185144, HIP 96100), commonly used as an RV standard (Vogt et al., 2014). Fig. 6.18 shows the Waltz RV measurements. The data prior to the spectrograph realignment (pre) are shown as wider diamonds, while the data taken in the updated configuration (post) are shown as narrow diamonds. Both data sets were reduced separately but using a template taken in the new configuration. The mean of each data set was subtracted. I did not apply a CTI correction to the data taken in the old configuration, due to the problems discussed in Sect. 6.4.2. Instead, I removed all spectra with $S/N < 100$ to reduce its impact. Nevertheless, these data are less reliable and show considerably higher scatter than the RVs measured in the updated configuration. It, however, also has to be noted that the observation process and the spectrograph underwent regular updates prior to the realignment and thus other effects might play a role. 28 spectra are included which were taken in the old configuration, while 16 spectra are available in the updated state.

The updated configuration yields mean RV uncertainties $\bar{\sigma}_{RV} = 5.1 \text{ m s}^{-1}$, with $\text{RMS} = 5.6 \text{ m s}^{-1}$, resulting in an unaccounted jitter component of $\sigma_{\text{jit}} = 2.4 \text{ m s}^{-1}$. The star is also used as a standard star for the Hertzprung SONG spectrograph located on Tenerife, Spain (Grundahl et al., 2007; Andersen et al., 2014; Grundahl et al., 2017; Fredslund Andersen et al., 2019), which utilizes a similar spectrograph design and, originally, used the same

CCD camera. Their RV measurements resulted in a curious RV periodicity close to one year with an amplitude up to 20 m s^{-1} (Heeren et al., 2023). The CTI effect is now suspected to play a role in this likely spurious RV variation. Using a different CCD camera for roughly one year to date, the updated SONG data has significantly smaller scatter and does not show the same periodicity (F. Grundahl, priv. comm.). The mean error of the recent SONG data is $\bar{\sigma}_{\text{RV,SONG}} = 2.0 \text{ m s}^{-1}$, with $\text{RMS}_{\text{SONG}} = 3.1 \text{ m s}^{-1}$, resulting in $\sigma_{\text{jit,SONG}} = 2.4 \text{ m s}^{-1}$, exactly matching the jitter unaccounted for in the Waltz RV measurements. Using data from HIRES and the Lick Observatory Automated Planet Finder, Vogt et al. (2014) discuss the possibility of a periodic RV variation with an amplitude of the order $K \sim 1.35 \text{ m s}^{-1}$ with a roughly 300 d period, which could be caused by a planet or by intrinsic variations. Their best model results in an additional stellar jitter $\sigma_{\text{jit}} = 0.6 \text{ m s}^{-1}$ such that σ Dra can only be regarded as an RV standard star on the 1 m s^{-1} level, somewhat lower than, but still similar to, the findings by SONG and Waltz. Butler et al. (2017) attributes a periodic RV variation of similar amplitude to a much longer period $P = (2644 \pm 197) \text{ d}$.

While the older data is less reliable, one can still deduce that there are no strong trends observable on timescales of about one year. As expected, the mean error $\bar{\sigma}_{\text{RV}} = 6.4 \text{ m s}^{-1}$ and $\text{RMS} = 10.1 \text{ m s}^{-1}$ are larger than in the updated configuration. Overall, one can conclude that in the updated configuration, the residual jitter, which is not accounted for in the formal uncertainties, does not exceed that of other instruments, such as SONG.

6.5.4 Testing the RVs on an established planet host

Finally, I can test the performance of the Waltz spectrograph on the K giant ι Dra (HIP 75458), which was part of the Lick sample and the first giant shown to host an exoplanet (Frink et al., 2002). The RVs were later observed to follow a long-term trend (Zechmeister et al., 2008; Kane et al., 2010), attributed to a further-out companion with mass likely in the brown-dwarf regime (Hill et al., 2021). In Fig. 6.19, I plot the Waltz RVs (blue diamonds) jointly with the RVs from the Lick, SONG, and CARMENES spectrographs (see legend) on top of the two-body Keplerian model presented in Chapt. 5 (Spaeth et al., 2025). To test for consistency of the Waltz data with the model, I merely fitted for an offset between the model and the RVs using the Exo-Striker (Trifonov, 2019).

I reduced the data taken before and after the spectrograph realignment and CCD rotation separately, but used the same template acquired in the updated configuration. For the old configuration, I removed data with $S/N < 100$ to lower the impact of the CTI effect. As two dedicated CTI sequences were part of the observations in the old configuration, I removed all but the spectrum with the highest S/N for each respective night. These spectra would otherwise be most strongly affected by the CTI effect and also dominate the RV offset. The Waltz RVs can be observed to follow the Keplerian model convincingly.

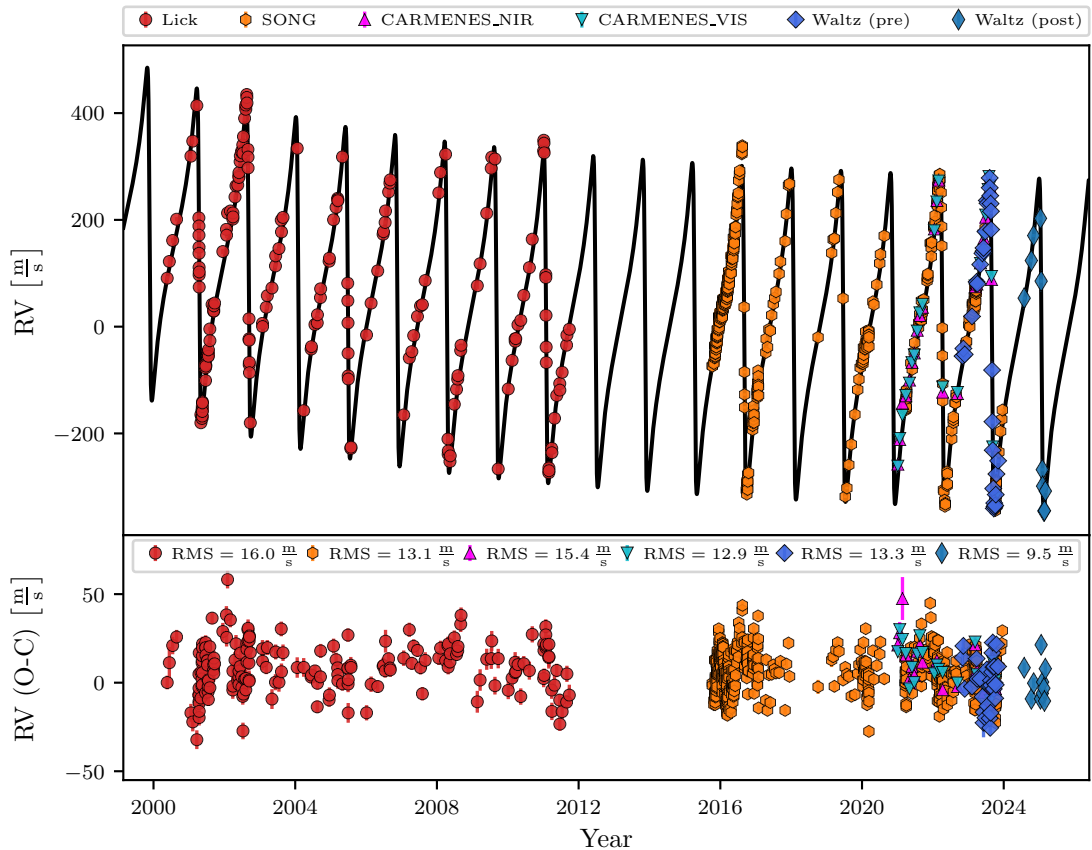


Fig. 6.19.: Waltz RVs for ι Dra, plotted jointly with RVs from Lick, SONG, and CARMENES, on top of the two-body Keplerian model. Residuals are plotted in the bottom panel.

The 30 data points available in the old configuration show a somewhat larger residual scatter (see bottom panel and legend) than the updated configuration. The ten data points in the updated configuration have $\text{RMS} = 9.5 \text{ m s}^{-1}$, which is the smallest scatter among all instruments. This is certainly due to the small number of data points available. I note that the intrinsic RV jitter component fitted for this specific model, $\sigma_{\text{jit}} = 13.5 \text{ m s}^{-1}$, is somewhat larger than the modal jitter reported in [Chapt. 5](#). This is due to the fact that the modal values of the individual parameters' posterior distributions were adopted, such that the resulting model can have larger residual scatter than given by the mode of the posterior distribution of the RV jitter. Although only a few observations are yet available, the initial results indicate high precision and accuracy in the RV measurements.

6.6 Outlook and future plans

Combining the above findings, the Waltz spectrograph is shown to be ready for routine science observations. The early results indicate that the Waltz RV survey achieves its

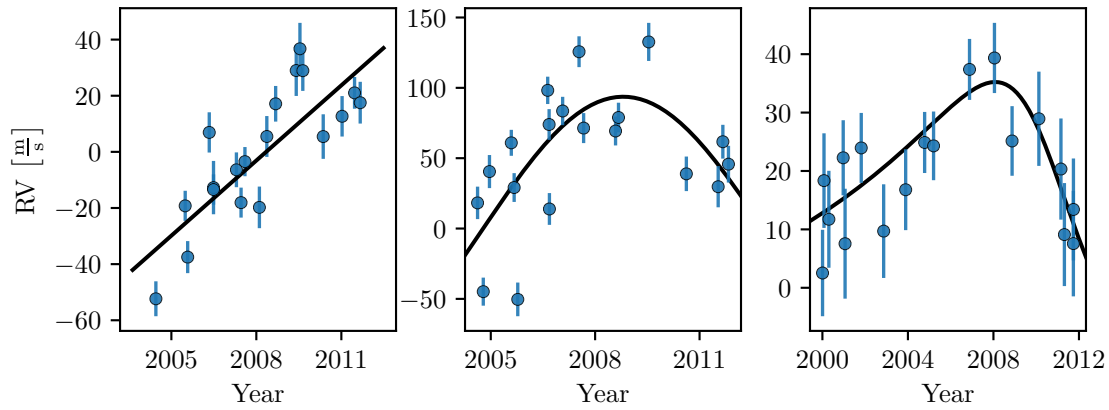


Fig. 6.20.: Lick RVs for three example stars showing long-term trends (left) or signs of long-term periodicity which could be consistent with orbital companions of planetary or brown-dwarf masses (middle, right). One RV outlier was clipped from the right panel.

targeted precision of about 5 m s^{-1} (Tala et al., 2016) for all stars within the Lick sample. Light levels are still expected to increase by the inclusion of an image slicer on the science fiber, and by replacing the telescope’s tertiary mirror. The largest increase, however, is expected from an improved guiding algorithm as discussed by Kuhn (2025). Nevertheless, even with the current setup we achieve formal RV uncertainties $\sigma_{\text{RV}} < 5 \text{ m s}^{-1}$ for stars of 6th magnitude within 30 minutes of exposure. Finally, the CTI effect does not seem to influence the RVs in the updated configuration.

The greatest advantage of the Waltz telescope is its continuous availability to the LSW exoplanet group, as well as its long-term prospects. Combined with the Lick data, this enables a search for the far-out companions orbiting the brightest giants in the night sky. Examples of Lick candidates showing long-term trends (left) or signs of long-period periodicity, which could be consistent with planetary or brown-dwarf companions (middle and right), are shown in Fig. 6.20. Much can also be learned from the continued monitoring of the stars presented in Chapt. 5 (Spaeth et al., 2025), as well as from planet candidates in binary systems. Naturally, such surveys require a large commitment to conduct observations. It is thus necessary to reduce the required effort as much as possible by enabling remote observations or even automating the telescope entirely.

The main concern for remote observations is the safety of the telescope, which could be damaged by collisions with the floor or other objects, could be exposed to rain or high humidity, or could rotate too far and damage cables. Next to numerous software safety checks (Spaeth, 2019), we thus installed additional hardware limit switches on the telescope axes (tilt limit switch is still missing), and installed additional sensors measuring the environmental conditions. Furthermore, I installed a Raspberry Pi night vision camera with a wide field of view equipped with an additional infrared light board, chosen specifically to have peak intensity at $\lambda \sim 940 \text{ nm}$, dropping to near zero close to $\lambda \sim 850 \text{ nm}$. It is thus outside the spectrograph’s wavelength regime (limited at



Fig. 6.21.: The Waltz telescope monitored in infrared light during the night of October 11, 2024.

$\lambda \sim 760 \text{ nm}$). No indication of any contamination from the infrared lights could be found in the spectra, the PMT counts, or on the guide camera. First successful remote observations from the office were conducted in October 2024 (see Fig. 6.21).

To enable remote observations from home, the dome slit needs to be automated, which is currently under development. The absolutely critical safety concerns are that the dome can be reliably closed in case of rain or high humidity, and that the telescope can be monitored and switched off if in danger. I note that during normal operations, the `waltzcontrol` software should avoid any dangerous situations for the telescope. It would further be necessary to develop solutions in case of network problems or power outages. To account for the former, one could implement an automatic shutdown (closing the dome, switching off the telescope) if the Waltz PC is offline for an extended period of time. For power outages, it would be advisable to investigate whether the already installed UPS could be extended to also power the telescope until safely parked, or at least switched off in a controlled fashion (to avoid it tracking again immediately when power is restored). With respect to the dome, the currently planned solution involves the use of a battery such that closing the dome would be possible even in the event of a power outage. Nevertheless, triggering to close the dome if a power outage is noticed would be advisable. With such precautions and careful tests, remote observations are expected to be possible soon.

The step toward automated observations naturally requires even more careful planning, as well as the development of emergency procedures, such as an alerting system. First tests are currently under consideration to streamline and automate the target selection process, pointing, and guiding. Future progress will reveal the necessary steps and precautions to enable full automation. In any case, the Waltz is poised to become one of only a handful of telescopes in Germany roaming our night sky in search for planets.

Conclusions

In the introduction (Sect. 1.11), I formulated three goals of this thesis. These were to (I) increase the number of planets orbiting giants with short orbital periods, (II) enhance our understanding of the planet controversy at intermediate periods, and (III) enable future studies to search for long-period planets. In this final chapter, I summarize the results of this thesis and give an outlook on future developments.

7.1 Summary of the results

In Chapt. 2, I discussed the RV non-detection of the main-sequence astrometric binary candidate HD 113283. I showed that the spurious detection was likely caused by *Gaia*'s scanning law. The false positive was later independently identified by ESA's *Gaia* team, along with three further cases, and attributed to a software bug.¹ Independent of our findings, this triggered an internal investigation into the *Gaia* astrometric orbit solutions, to rule out further false positives. This underscores the importance of such non-detections to improve the processing of future *Gaia* data sets, especially given the expected increase of discoveries of lower-mass companions.

I further presented in Chapt. 2, the RV follow-up using FIES of two evolved TESS transiting candidates, TOI 1489 and TOI 1684. In both cases, the RVs ruled out planets. For TOI 1489, more recent TESS sectors showed that the transit signal was not consistently present, suggesting its origin to be intrinsic to the star. For TOI 1684, combining the FIES RVs with the findings by J. Zhang (priv. comm, 2025), revealed the giant star to be situated in a triple star system, with a low-mass dwarf star eclipsing the secondary K dwarf companion at the candidate period.

To study a potential origin of the planet controversy surrounding luminous giants (see Sect. 1.9), I introduced the simulation code `pyoscillot` in Chapt. 3. The code allows for the study of the observational effects of non-radial oscillations on spectroscopic data. I explained its fundamentals and examined how the oscillation parameters and stellar settings impact the observables. I showed that for oscillation modes with small temperature variations, the amplitude difference between optical and infrared wavelengths is small. Furthermore, I discussed that, aside from the stellar rotation velocity, the oscillation's

¹<https://www.cosmos.esa.int/web/gaia/dr3-known-issues>

velocity amplitude has the strongest influence on the amplitudes of activity indicators. This suggests that intrinsically RV-variable giants with large RV amplitudes are more easily detected in the activity indicators compared to stars with smaller RV amplitudes.

I applied these general findings to the false-positive planet host NGC 4349 No. 127 (Lovis & Mayor, 2007; Delgado Mena et al., 2018, 2023), showing in Chapt. 4 (Spaeth et al., 2024) that a model of an $l = 1, m = 1$ non-radial oscillation can reproduce the observed correlations between the activity indicators and the RVs. The oscillation model also predicts amplitudes consistent with the observations, including those of the BIS and the photometry, which were both found to be non-variable at the RV period. Thus, the `pyoscillot` simulations of non-radial oscillations provide the first model with directly testable predictions to explain the planet controversy. It remains to be seen whether other stars show similar signatures.

In light of this finding, in Chapt. 5 (Spaeth et al., 2025), I analyzed ten planet candidates identified in the Lick survey (see Sect. 1.5), combining RV data from Lick, SONG, and CARMENES. For these planet candidates, the CARMENES activity indicators did not show any clear correlations with the RVs, as observed for NGC 4349 No. 127. This can be explained by the typically smaller RV amplitudes. While periodicity in the indicators can contribute to ruling out the planetary candidates, the most significant conclusions can be drawn from a very long RV baseline, which allows for the detection of changes of the amplitudes or periodicities, or of adjacent periodicity in the RV residuals.

Comparing the amplitudes between the optical and near-infrared channels revealed no significant differences, consistent with a non-radial oscillation model. Interestingly, we detected significant periodicity in several of the chromospheric activity indicators, suggesting a potential link to convective or magnetic processes as proposed by Delgado Mena et al. (2023) (see also Sect. 1.10.2). Overall, seven out of the ten stars were shown to be intrinsically RV-variable, while two stars remained inconclusive. The RGB star HIP 64823 was found to host a promising planet candidate with period $P = 2827_{-48}^{+61}$ d and minimum mass $m_p \sin(i) = 10.4_{-1.9}^{+1.4} M_{\text{Jup}}$. In general, we conclude that a long RV time series, spanning 25 years or longer, is crucial to confirm or rule out planets with periods of several hundred days orbiting luminous giants.

Obtaining such long RV baselines is difficult using external observational facilities. Thus, I presented in Chapt. 6 the status and the first on-sky tests of the Waltz RV project at Landessternwarte, Heidelberg, aiming to continue the Lick RV survey. I discussed improvements to the hardware and software, showing that light levels have been improved sufficiently to allow observations of the faintest stars within the sample ($V = 6$ mag). I analyzed the implications of the CTI effect present on the Waltz CCD, whose impact has largely been mitigated by a rotation of the CCD. Furthermore, I tested the on-sky performance of the spectrograph. Formal RV uncertainties as low as $\sigma_{\text{RV}} = 2.3 \text{ m s}^{-1}$ could be achieved. The instrument was further estimated to be stable over short timescales at

levels below 2.5 m s^{-1} , while the longer-term stability on timescales of several months was shown to be consistent with the SONG spectrograph. It can be concluded that the Waltz telescope is ready for science observations and capable of achieving the intended RV precision $\sigma_{\text{RV}} \lesssim 5 \text{ m s}^{-1}$ for the entire Lick sample. This opens the possibility for further monitoring of the intrinsically RV-variable stars and the planet candidate HIP 64823 identified in [Chapt. 5](#), as well for targeting long-period planets.

7.2 Future of planet detections orbiting giants

7.2.1 Short-period planets

The main challenge I faced, when attempting to follow-up transiting candidates orbiting giants, was the small number of targets bright enough to be observed within reasonable time constraints using two- to three-meter-class telescopes, for which public observing time is most readily available. Indeed, vetting the public TOIs left only a handful of suitable candidates. One reason for this low number of candidates, was the reliance on published TOIs, which are based on the standard SPOC ([Jenkins et al., 2016](#)) and QLP ([Huang et al., 2020](#)) pipelines. These, however, are optimized for transit detections around main-sequence stars. For instance, they apply detrending algorithms to remove low-frequency instrumental systematics and, in the case of the QLP pipeline, longer-period stellar variability ([Huang et al., 2020](#)). Thus, the inherently longer transiting signals around more evolved stars pose a challenge to these pipelines.

For this reason, [Saunders et al. \(2022\)](#) presents the dedicated `giants` pipeline, optimized for detecting transiting signals on giants in TESS full-frame images.² Using this pipeline, their program “Giants Transiting Giants” has achieved a number of detections around subgiants and mildly evolved giants ([Saunders et al., 2022, 2024, 2025](#); [Grunblatt et al., 2022, 2023, 2024](#); [Pereira et al., 2023](#)). However, even in this dedicated pipeline a Gaussian smoothing filter is used to remove trends on timescales longer than 2 d ([Saunders et al., 2022](#); [Grunblatt et al., 2023, 2024](#)). These timescales are, however, similar to the transit durations when targeting more evolved giants (following, e.g., [Winn 2010](#)), which presents a further challenge apart from the reduced transit depths. The observation strategy of TESS, covering the majority of the sky for only 27 days at a time, further disfavors planet detections around more evolved giants, as their planets are necessarily at somewhat longer periods, thus limiting the number of transits per sector.

The upcoming PLATO mission ([Rauer et al., 2024](#)) would, in principle, have a better suited observing strategy to detect transiting planets orbiting giants. While the underlying

²<https://github.com/nksaunders/giants>

fundamental limits, i.e., the shallow transit depths and the increased intrinsic noise, are still a limiting factor, PLATO will cover two large pre-selected regions of the sky for (likely) two years each (Nascimbeni et al., 2022, 2025; Rauer et al., 2024) and achieve lower instrumental noise levels (Matuszewski et al., 2023). An increased number of transits and a lower noise level would increase the S/N and thus the detection probability (Matuszewski et al., 2023). Unfortunately, the main science goal of PLATO is to detect Earth-like planets orbiting main-sequence dwarfs (Rauer et al., 2024). Due to constraints on data downlink, light curves will only be available for pre-selected stars, which excludes giants (Nascimbeni et al., 2025). Detecting transiting planets orbiting more evolved giants will likely remain challenging for the foreseeable future.

In recent years, a number of short-period ($P \lesssim 100$ d) planets have been found orbiting giants in RV surveys. These include, for instance, TYC 3667-1280-1 b ($P \sim 26$ d, Niedzielski et al. 2016), 24 Boo b ($P \sim 30$ d, Takarada et al. 2018), and HIP 89587 b ($P \sim 21$ d, Teng et al. 2023a). Interestingly, the latter was part of the Lick RV survey, but the Lick data was not deemed sufficient to confirm the system. For several other stars in the Lick sample, especially ones added in 2004 (see Sect. 1.5), the number of data points is still rather small such that some short-period planets might still be hidden. With the upcoming availability of the Waltz telescope, it is possible to search for these.

7.2.2 The planet controversy around luminous giants

So far, NGC 4349 No. 127 is the only luminous giant with RV variations mimicking a brown dwarf, for which non-radial oscillations provide a convincing explanation of the observables (Chapt. 4, Spaeth et al. 2024). For the seven stars with intrinsically induced RV variations in Chapt. 5 (Spaeth et al., 2025), no clear identification of single oscillation modes was possible. One explanation, are the (mostly) smaller RV amplitudes (see Table 5.3) in the CARMENES sample compared to $K \sim 230 \text{ m s}^{-1}$ for NGC 4349 No. 127 (Delgado Mena et al., 2018). I found in Chapt. 3 that the RV amplitude of an oscillation, for a fixed rotation velocity, is directly linked to the amplitudes of the variations in the activity indicators. Different rotation velocities could also come into play but are generally difficult to measure for slowly rotating giants. A combination of different oscillation modes could also make a determination of correlations more challenging.

To assess, whether non-radial oscillations could explain other stars already found to be intrinsically RV-variable, the most direct approach would be to study the giants presented by Delgado Mena et al. (2018, 2023), most of which have relatively large RV amplitudes. In Fig. 7.1, I plot preliminary results of the correlation analysis for NGC 2423 No. 3, which was believed to host a planetary companion (Lovis & Mayor, 2007), which is, however, also likely mimicked by an intrinsic mechanism (Delgado Mena et al., 2018, 2023). Plotting the CRX and the dLW against the RVs, similar to Fig. 4.4, also shows

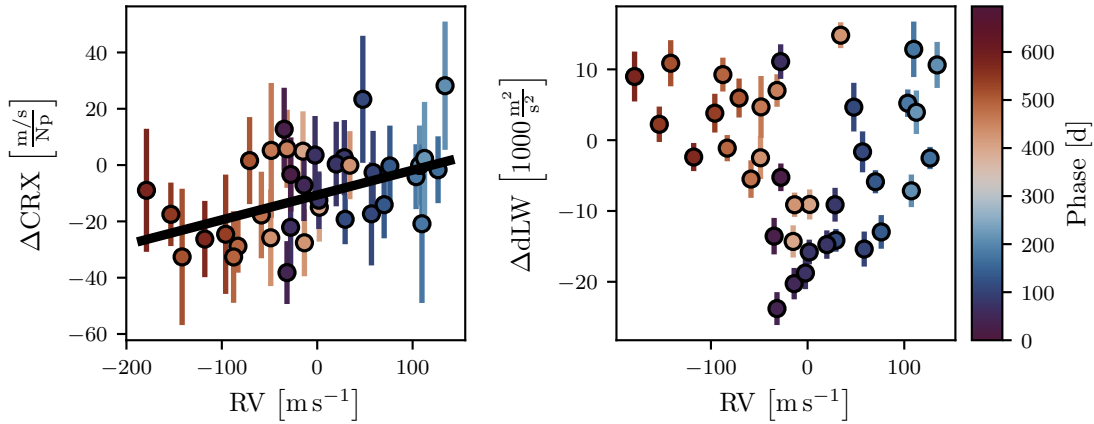


Fig. 7.1.: Preliminary correlation analysis between activity indicators and the RVs for NGC 2423 No. 3. Left: CRX plotted against the RVs. A linear relation was fitted to the data. Right: dLW plotted against the RVs. A closed-loop shape could be present.

a positive correlation between the CRX and the RVs (left). A linear fit is overlotted. The p -value of the correlation is $p = 0.3\%$ calculated via a permutation test. The dLW plotted against the RVs (right) have large scatter, but also resemble a closed-loop shape as observed for NGC 4349 No. 127. These preliminary results show that searching for similar correlations could be promising. This might especially be true for NGC 2345 No. 50 and NGC 3532 No. 670, which have even larger RV amplitudes (Delgado Mena et al., 2023).

On the other hand, the detection of variations in the chromospheric activity indicators by Delgado Mena et al. (2018, 2023), as well as for the stars in Chapt. 5, motivates to further study the possibility of convective patterns explaining the RV variations. I attempted to include the effect of surface granulation in the `pyoscillot` simulations based on models provided by H.-G. Ludwig (priv. comm.). Unfortunately, no self-consistent velocity maps were available, which could have been easily included into `pyoscillot`. In principle, however, it is possible to simulate surface phenomena such as localized velocity patterns, which could help to further understand whether such well-behaved correlations as observed for NGC 4349 No. 127 could also be caused by convective patterns. While at first glance it might seem unlikely, a further refinement of the theoretical basis is necessary before more detailed investigations are possible. In Chapt. 4, we also touch upon the possibility that the oscillations might be linked to chromospheric processes.

The main result from Chapt. 5 (Spaeth et al., 2025) was that RV baselines of 25 years or longer are most decisive to rule out or confirm the planets. In that regard, the Waltz telescope can now play a crucial role, both to confirm the findings from Chapt. 5 and to study the further behavior of the RVs. The latter might allow for more detailed modeling using, for instance, a combination of several oscillation modes potentially changing their amplitudes, phases, or periods. In light of these findings, it might also be worth to consider a detailed reanalysis of planets orbiting luminous giants published in the literature, for

instance, those with $L > 100 L_{\odot}$. If bright enough and observable from Heidelberg, one could even consider adding such systems to the Waltz target list to gain further insight into the underlying physical phenomenon.

Still, the lack of a large set of activity indicators for the Waltz spectrograph is unfortunate. [Hirschbeck \(2022\)](#) implements a measurement of the $H\alpha$ index for the Waltz based on the previous works by [Staudt \(2020\)](#). [Janke \(2024\)](#) finds the Mt. Wilson S-index targeting the Ca H and K lines to be sensitive to activity for the Lick giants. Unfortunately, the Ca lines at 3933.7 Å and 3968.5 Å fall outside the spectrograph's wavelength range (450 nm – 750 nm). Possibilities to extend the range have been discussed and could be promising. [Heeren et al. \(2023\)](#) includes a chromatic index measurement into the pyodine pipeline, which, however, suffers from the relatively short usable wavelength range due to the iodine cell. It requires further testing and calibration.

[Delgado Mena et al. \(2023\)](#) find the FWHM of the CCF to be the most sensitive photospheric activity indicator. Activity indicators targeting the spectral line shapes are not commonly acquired from iodine cell spectrographs due to the variable instrumental profiles. [Reffert et al. \(2006\)](#) discussed line bisector measurements for Pollux using a cross-correlation with a synthetic template of the Lick spectral orders outside the iodine cell regime. A similar approach may be investigated for the Waltz. It seems possible to use the simultaneous information of the spectrograph's LSF fitted for each chunk by the pyodine pipeline to mitigate the impact of the LSF variations. Studies of the latter, for instance, as a function of temperature using spectra of a Fabry-Pérot etalon, such as conducted by [Jessen \(2022\)](#), are promising for further understanding of its properties and variations. The approach could similarly enable measurements of the CCF's contrast, as well as its BIS. Of course, the lower resolving power of the Waltz compared to HARPS or CARMENES would ultimately limit the sensitivity of such metrics. Another approach that has been proposed by S. Reffert (priv. comm, 2025) could be to add a model of the variations of the stellar lines with respect to the stellar template into [Eq. 1.6](#). More detailed studies are necessary to assess the feasibility of either proposal.

Naturally, independent constraints on the existence or non-existence of planetary systems would be ideal. Estimating the minimal astrometric signatures following [Reffert & Quirrenbach \(2011\)](#) under the assumption that the signals are caused by planets, leads to signals of the order of 15 – 65 μas for the ten stars tested in [Chapt. 5](#), except HIP 64823. For *Gaia* DR5, this would correspond to $S/N < 3$, even when making the optimistic assumption that the best astrometric precision can be reached for these bright stars. In reality, the outlook is likely even less promising and it seems unlikely that *Gaia* will be able to rule out the planetary orbits and thus confirm the intrinsic origin. Long-term RV monitoring thus remains the most promising avenue.

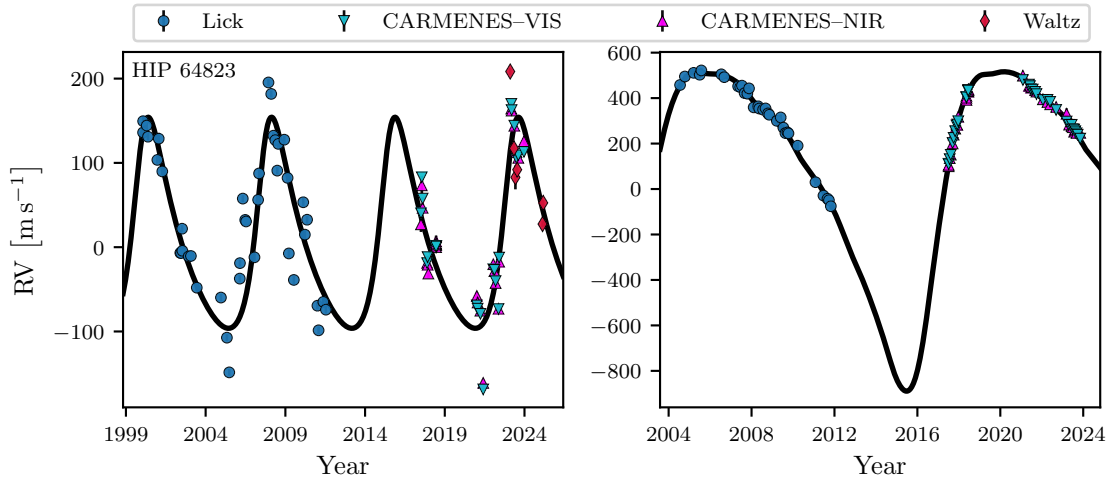


Fig. 7.2.: RV models for HIP 64823 and a planet candidate in a binary system. Left: First Waltz RVs for HIP 64823 plotted on top of the 1P+GP model from [Chapt. 5](#) (only planetary contribution). Right: Example of a planet candidate in a binary system.

7.2.3 Long-period planets and planets in binary systems

In contrast to the intrinsically variable giants, the long-period planet candidate HIP 64823 b could be a promising candidate for astrometric follow-up. Located at a distance $d \sim 99.3$ pc, the minimum astrometric signature would be $\alpha_{\min} \sim 292 \mu\text{as}$, which corresponds roughly to $S/N \sim 13$ in *Gaia* DR5 (or $S/N \sim 9$ in DR4), assuming that the best astrometric precision could be reached for the $G = 4.9$ mag ([Gaia Collaboration et al., 2023](#)) star. This would allow for an unanimous confirmation and for determining the true mass of the planet or brown dwarf. It remains to be seen whether the calibration for bright stars can be improved sufficiently to allow for the detection of this signal.

At the same time, continued RV monitoring using the Waltz telescope should be considered. First spectra of the planet candidate have already been acquired (see [Fig. 7.2](#), left). These are plotted on top of the planetary part of the 1P+GP model from [Chapt. 5](#). The oldest Waltz data points were taken at low S/N and are still affected by the CTI effect. The RVs thus merely serve to give a first impression of the trend in the Waltz data. Continued monitoring would clearly be promising, perhaps in preparation for combining the RVs with epoch astrometry from future *Gaia* data releases. If confirmed, HIP 64823 b would have the fifth longest period among planets orbiting giants.³ As discussed in [Sect. 6.6](#), there are multiple additional systems showing long-term trends, which could be indicative of planets or brown dwarfs. Monitoring of these systems could begin soon. For several of these, a combination with future *Gaia* astrometry could be investigated.

³<https://www.lsw.uni-heidelberg.de/users/sreffert/giantplanets/giantplanets.php>

Finally, there remain a number of planet candidates (or candidates for intrinsic variations) in binary systems. Several of these were observed as part of the CARMENES campaign. However, these were ultimately excluded from the study presented in [Chapt. 5](#), as the binary orbits are often not well constrained and complicate the determination of the planetary orbits. One example of a promising planet candidate is depicted in [Fig. 7.2](#) (right), which shows a large-amplitude RV variation caused by a long-period stellar companion. Upon closer examination, one can observe residual periodicity (included in the fit) at a period $P \sim 3$ yr, consistent with an $m_p \sin i \sim 1 M_{\text{Jup}}$ planet. However, as the RV curve of the binary is only partially sampled, an exact determination is challenging. Continued monitoring of such systems using the Waltz could constrain the binary orbits and thus also those of the planets. This would also enable to conduct similar studies as presented in [Chapt. 5](#), using the CARMENES data and its activity indicators much more effectively. In this particular case, the minimum RV of the binary orbit is expected to occur in mid 2029. Naturally, these binary stars are also ideal targets for combination of the RVs with astrometry from *Gaia*. Confirmation of planets in such systems can provide important inputs to planet formation theory in binary systems (e.g., [Panić et al. 2021](#)).

Of course, it is necessary to further test and improve the performance of the Waltz instrument. As discussed in [Sect. 6.6](#), a first step would be to enable remote observations to increase the use of observation time. At the same time, we still anticipate an increase of the light levels by replacing the telescope's tertiary mirror and by the inclusion of an image slicer for the science fiber. It is also required to further monitor the long-term stability of the RVs, searching for any instrumental trends that could contaminate the data. Finally, the software CTI correction for the older Waltz data should be further improved, ideally in combination with a correction for SONG, as is currently ongoing. If a software correction can be established with confidence, it might still be worth to consider correcting data taken in the rotated CCD state to remove any remaining effect.

7.3 Final remarks

With this thesis, I hope to have contributed a small step toward a better understanding of planets orbiting giants. With the Waltz telescope at hand, it is now possible to search for the so-far undiscovered long-period planet population around the brightest giants in our night sky. It might also be able to contribute toward resolving the planet controversy surrounding luminous giants, which, however, remains a fascinating problem for now. Future observational and theoretical studies will certainly be able to tackle the problem and, in the process, learn much about the physical processes in giants. There are yet many puzzles to solve and much to be learned from planets orbiting giant stars.

Personal bibliography

The following first-author publications were written during this PhD thesis and contributed to this work:

- **Spaeth, D.**, Reffert, S., Trifonov, T., Golovin, A. (2023). “Non-confirmation of the Astrometric Binary Candidate HD 113283 Using FEROS Radial Velocities”. *Research Notes of the American Astronomical Society* 7, 12, doi: <https://doi.org/10.3847/2515-5172/acb3c5>
- **Spaeth, D.**, Reffert, S., Hunt, E. L., Kaminski, A., Quirrenbach, A. (2024). “Non-radial oscillations mimicking a brown dwarf orbiting the cluster giant NGC 4349 No. 127”. *Astronomy & Astrophysics* 689, A91, doi: <https://doi.org/10.1051/0004-6361/202450163>
- **Spaeth, D.**, Reffert, S., Trifonov, T., Kaminski, A., Albrecht, S., Grundahl, F., Fredslund Andersen, M., Quirrenbach, A., Pallé P. L. (2025). “Precise radial velocities of giant stars - XVII. Distinguishing planets from intrinsically induced radial velocity signals in evolved stars”. *Astronomy & Astrophysics*, Accepted for publication (March 11, 2025) (*in press*), doi: <https://doi.org/10.1051/0004-6361/202453500>

Bibliography

- Aerts, C. 2021, *RvMP*, **93**, 015001
- Aigrain, S., Pont, F., Fressin, F., et al. 2009, *A&A*, **506**, 425–429
- Aller, A., Lillo-Box, J., Jones, D., Miranda, L. F., & Barceló Forteza, S. 2020, *A&A*, **635**, A128
- Alves, D. R. 2000, *ApJ*, **539**, 732–741
- Amard, L., Brun, A. S., & Palacios, A. 2024, *ApJ*, **974**, 311
- Anders, F., Khalatyan, A., Chiappini, C., et al. 2019, *A&A*, **628**, A94
- Anders, F., Khalatyan, A., Queiroz, A. B. A., et al. 2022, *A&A*, **658**, A91
- Andersen, M. F., Grundahl, F., Christensen-Dalsgaard, J., et al. 2014, *RMxAA Conf. Ser.*, **45**, 83
- Andor Technology. 2016, User's Guide to: SDK Software Development Kit - Software Version 2.102
- APC by Schneider Electric. 2015, Bedienungsanleitung, Smart-UPS On-Line SRT, Unterbrechungsfreie Stromversorgung
- Appourchaux, T., Antia, H. M., Ball, W., et al. 2015, *A&A*, **582**, A25
- Assef, R. J., Gaudi, B. S., & Stanek, K. Z. 2009, *ApJ*, **701**, 1616–1626
- Aurière, M., Konstantinova-Antova, R., Charbonnel, C., et al. 2015, *A&A*, **574**, A90
- Aurière, M., Konstantinova-Antova, R., Espagnet, O., et al. 2013, *Proc. IAU*, **9**, 359–362
- Aurière, M., Konstantinova-Antova, R., Petit, P., et al. 2011, *A&A*, **534**, A139
- Aurière, M., Petit, P., Mathias, P., et al. 2021, *A&A*, **646**, A130
- Aurière, M., Wade, G. A., Konstantinova-Antova, R., et al. 2009, *A&A*, **504**, 231–237
- Baliunas, S. L., Donahue, R. A., Soon, W. H., et al. 1995, *ApJ*, **438**, 269
- Baranne, A., Queloz, D., Mayor, M., et al. 1996, *A&AS*, **119**, 373–390
- Barnes, J. R., Jeffers, S. V., & Jones, H. R. A. 2011, *MNRAS*, **412**, 1599–1610
- Baroch, D., Morales, J. C., Ribas, I., et al. 2020, *A&A*, **641**, A69
- Batalha, N. M., Borucki, W. J., Koch, D. G., et al. 2010, *ApJ*, **713**, L109-L114
- Bauer, F. F., Zechmeister, M., & Reiners, A. 2015, *A&A*, **581**, A117
- Bedding, T. R. & Kjeldsen, H. 2003, *PASA*, **20**, 203–212
- Behrard, A., Dai, F., & Howard, A. W. 2022, *AJ*, **163**, 160
- Benjamin, D. J., Berger, J. O., Johannesson, M., et al. 2018, *Nat Hum Behav*, **2**, 6–10
- Berdyugina, S. V. 2008, *Proc. IAU*, **4**, 323–332
- Blackwell, D. E. & Lynas-Gray, A. E. 1994, *A&A*, **282**, 899–910
- Bochanski, J. J., Faherty, J. K., Gagné, J., et al. 2018, *AJ*, **155**, 149
- Boisse, I., Bouchy, F., Hébrard, G., et al. 2011, *A&A*, **528**, A4
- Boisse, I., Moutou, C., Vidal-Madjar, A., et al. 2009, *A&A*, **495**, 959–966
- Bonfils, X., Mayor, M., Delfosse, X., et al. 2007, *A&A*, **474**, 293
- Borucki, W. J., Koch, D., Basri, G., et al. 2010, *Sci*, **327**, 977
- Bouchy, F., Isambert, J., Lovis, C., et al. 2009, *EAS Publ. Ser.*, **37**, 247–253
- Brahm, R., Jordán, A., & Espinoza, N. 2017, *PASP*, **129**, 034002

- Bressan, A., Marigo, P., Girardi, Léo., et al. 2012, *MNRAS*, 427, 127–145
- Brickhill, A. J. 1975, *MNRAS*, 170, 405–421
- Brown, J. A., Sneden, C., Lambert, D. L., & Dutchover, Jr., E. 1989, *ApJS*, 71, 293
- Brown, T. M., Latham, D. W., Everett, M. E., & Esquerdo, G. A. 2011, *AJ*, 142, 112
- Brucalassi, A., Koppenhoefer, J., Saglia, R., et al. 2017, *A&A*, 603, A85
- Brucalassi, A., Pasquini, L., Saglia, R., et al. 2014, *A&A*, 561, L9
- Buchhave, L. A., Bakos, G. Á., Hartman, J. D., et al. 2010, *ApJ*, 720, 1118–1125
- Burkert, A. & Ida, S. 2007, *ApJ*, 660, 845–849
- Burt, J. A., Hooton, M. J., Mamajek, E. E., et al. 2024, *ApJ*, 971, L12
- Buta, R. J. & Smith, M. A. 1979, *ApJ*, 232, 213
- Butler, R. P., Marcy, G. W., Williams, E., et al. 1996, *PASP*, 108, 500
- Butler, R. P., Tinney, C. G., Marcy, G. W., et al. 2001, *ApJ*, 555, 410–417
- Butler, R. P., Vogt, S. S., Laughlin, G., et al. 2017, *AJ*, 153, 208
- Campante, T. L., Li, T., Ong, J. M. J., et al. 2023, *AJ*, 165, 214
- Campbell, B. & Walker, G. a. H. 1979, *PASP*, 91, 540
- Carlberg, J. K., Smith, V. V., Cunha, K., & Carpenter, K. G. 2016, *ApJ*, 818, 25
- Chadid, M., De Ridder, J., Aerts, C., & Mathias, P. 2001, *A&A*, 375, 113–121
- Charbonneau, D., Brown, T. M., Latham, D. W., & Mayor, M. 2000, *ApJ*, 529, L45-L48
- Charbonnel, C., Lagarde, N., Jasniewicz, G., et al. 2020, *A&A*, 633, A34
- Chen, X. & Li, Y. 2017, *ApJ*, 838, 31
- Chontos, A., Huber, D., Grunblatt, S. K., et al. 2024, [arxiv:2402.07893](https://arxiv.org/abs/2402.07893)
- Christensen-Dalsgaard, J. 2005, *Highlights Astron.*, 13, 397
- Ciceri, S., Lillo-Box, J., Southworth, J., et al. 2015, *A&A*, 573, L5
- Cochran, W. D. & Hatzes, A. P. 1990, *1318*, 148–157
- Coelho, H. R., Chaplin, W. J., Basu, S., et al. 2015, *MNRAS*, 451, 3011–3020
- Coffinet, A., Lovis, C., Dumusque, X., & Pepe, F. 2019, *A&A*, 629, A27
- Cowling, T. G. 1941, *MNRAS*, 101, 367
- Cox, J. P., King, D. S., & Stellingwerf, R. F. 1972, *ApJ*, 171, 93
- Cramer, F. 2023, *Scientific Colour Maps (8.0.1)*, [Zenodo](https://zenodo.org/record/7811111)
- Creevey, O. L., Sordo, R., Pailler, F., et al. 2023, *A&A*, 674, A26
- Cretignier, M., Francfort, J., Dumusque, X., Allart, R., & Pepe, F. 2020, *A&A*, 640, A42
- Crowley, C., Kohley, R., Hambly, N. C., et al. 2016, *A&A*, 595, A6
- Currie, T. 2009, *ApJ*, 694, L171-L176
- Czesla, S., Molle, T., & Schmitt, J. H. M. M. 2018, *A&A*, 609, A39
- Czesla, S., Schröter, S., Schneider, C. P., et al. 2019, *ASCL:1906.010*
- da Costa-Luis, C., Larroque, S. K., Altendorf, K., et al. 2021, *Tqdm: A Fast, Extensible Progress Bar for Python and CLI*, [Zenodo](https://zenodo.org/record/5311111)
- Dalal, S., Rescigno, F., Cretignier, M., et al. 2024, *MNRAS*, 531, 4464–4481
- Dall, T. H., Santos, N. C., Arentoft, T., Bedding, T. R., & Kjeldsen, H. 2006, *A&A*, 454, 341–348
- De Ridder, J., Dupret, M.-A., Neuforge, C., & Aerts, C. 2002, *A&A*, 385, 572–584
- Deeg, H. J. & Alonso, R. 2018, in *Handbook of Exoplanets*, ed. H. J. Deeg & J. A. Belmonte (Springer Cham), 117
- Deheuvels, S., Li, G., Ballot, J., & Lignières, F. 2023, *A&A*, 670, L16

- Delgado Mena, E., Gomes da Silva, J., Faria, J. P., et al. 2023, *A&A*, 679, A94
- Delgado Mena, E., Lovis, C., Santos, N. C., et al. 2018, *A&A*, 619, A2
- Delgado Mena, E., Tsantaki, M., Sousa, S. G., et al. 2016, *A&A*, 587, A66
- Delorme, J.-R., Jovanovic, N., Echeverri, D., et al. 2021, *JATIS*, 7, 035006
- Desort, M., Lagrange, A. M., Galland, F., Udry, S., & Mayor, M. 2007, *A&A*, 473, 983–993
- Díaz, R. F., Cincunegui, C., & Mauas, P. J. D. 2007, *MNRAS*, 378, 1007–1018
- Djupvik, A. A. & Andersen, J. 2010, *Highlights of Spanish Astrophysics V*, 14, 211
- Döllinger, M. P. & Hartmann, M. 2021, *ApJS*, 256, 10
- Döllinger, M. P., Hatzes, A. P., Pasquini, L., et al. 2009, *A&A*, 499, 935–942
- Dorn, R. J., Bristow, P., Smoker, J. V., et al. 2023, *A&A*, 671, A24
- Dravins, D. 1987, *A&A*, 172, 211–224
- Dreizler, S., Luque, R., Ribas, I., et al. 2024, *A&A*, 684, A117
- Dupret, M.-A., De Ridder, J., Neuforge, C., Aerts, C., & Scuflaire, R. 2002, *A&A*, 385, 563–571
- El-Badry, K., Rix, H.-W., & Heintz, T. M. 2021, *MNRAS*, 506, 2269–2295
- Eriksson, U. & Lindegren, L. 2007, *A&A*, 476, 1389–1400
- Ernst, M. D. 2004, *Stat. Sci.*, 19, 676–685
- ESA. 1997, *ESA Spec. Publ.*, 1200
- Espinoza, N., Kossakowski, D., & Brahm, R. 2019, *MNRAS*, 490, 2262–2283
- Ester, M., Kriegel, H.-P., Sander, J., & Xu, X. 1996, *Proc. 2nd Int. Conf. Knowl. Discov. Data Min.*, 226–231
- Eversberg, T. & Vollmann, K. 2015, *Spectroscopic Instrumentation: Fundamentals and Guidelines for Astronomers* (Berlin, Heidelberg: Springer)
- Feng, F. 2024, [arXiv:2403.08226](https://arxiv.org/abs/2403.08226)
- Fernandes, R. B., Mulders, G. D., Pascucci, I., Mordasini, C., & Emsenhuber, A. 2019, *ApJ*, 874, 81
- Feroz, F., Hobson, M. P., & Bridges, M. 2009, *MNRAS*, 398, 1601–1614
- Figueira, P., Santos, N. C., Pepe, F., Lovis, C., & Nardetto, N. 2013, *A&A*, 557, A93
- Fischer, D. A., Anglada-Escude, G., Arriagada, P., et al. 2016, *PASP*, 128, 066001
- Fischer, D. A., Marcy, G. W., & Spronck, J. F. P. 2013, *ApJS*, 210, 5
- Fischer, D. A. & Valenti, J. 2005, *ApJ*, 622, 1102–1117
- Fisher, R. A. 1925, *Proc. Camb. Philos. Soc.*, 22, 700
- Foreman-Mackey, D. 2016, *JOSS*, 1, 24
- Foreman-Mackey, D., Agol, E., Ambikasaran, S., & Angus, R. 2017, *AJ*, 154, 220
- Fredslund Andersen, M., Handberg, R., Weiss, E., et al. 2019, *PASP*, 131, 045003
- Frey, T. A. J. 2020, *Internship Report*, University of Heidelberg
- Frink, S., Mitchell, D. S., Quirrenbach, A., Fischer, D. A., & Marcy, G. W. 2002, *ApJ*, 576, 7
- Frink, S., Quirrenbach, A., Fischer, D., Röser, S., & Schilbach, E. 2001, *PASP*, 113, 173–187
- Gaia Collaboration, Babusiaux, C., van Leeuwen, F., et al. 2018, *A&A*, 616, A10
- Gaia Collaboration, Prusti, T., de Bruijne, J. H. J., et al. 2016, *A&A*, 595, A1
- Gaia Collaboration, Vallenari, A., Brown, A. G. A., et al. 2023, *A&A*, 674, A1
- Gaida, G. & Rosa, M. 1980, *Sterne und Weltraum*, 1/80, 9–15
- Gaidos, E., Gehrig, L., & Güdel, M. 2025, [arXiv:2502.16347](https://arxiv.org/abs/2502.16347)
- Galland, F., Lagrange, A.-M., Udry, S., et al. 2005, *A&A*, 443, 337–345
- Gandolfi, D., Parviainen, H., Deeg, H. J., et al. 2015, *A&A*, 576, A11

- Gehan, C., Godoy-Rivera, D., & Gaulme, P. 2024, *A&A*, **686**, A93
- Georgiev, S., Lèbre, A., Josselin, E., et al. 2023, *MNRAS*, **522**, 3861–3876
- Ghezzi, L., Cunha, K., Schuler, S. C., & Smith, V. V. 2010, *ApJ*, **725**, 721–733
- Ghezzi, L., Montet, B. T., & Johnson, J. A. 2018, *AJ*, **860**, 109
- Ginsburg, A., Sipócz, B. M., Brasseur, C. E., et al. 2019, *AJ*, **157**, 98
- Goldberg, J. A., Joyce, M., & Molnár, L. 2024, *ApJ*, **977**, 35
- Golovin, A., Reffert, S., Just, A., et al. 2023, *A&A*, **670**, A19
- Gomes da Silva, J., Santos, N. C., Bonfils, X., et al. 2011, *A&A*, **534**, A30
- Götz, D. A. 2022, Bachelor's thesis, University of Heidelberg
- Goudfrooij, P., Bohlin, R. C., Maíz-Apellániz, J., & Kimble, R. A. 2006, *PASP*, **118**, 1455–1473
- Gray, D. F. 1997, *Nat*, **385**, 795–796
- Gray, D. F. 2005, *PASP*, **117**, 711–720
- Gray, D. F. 2021, *The Observation and Analysis of Stellar Photospheres*, 4th edn. (Cambridge: Cambridge University Press)
- Gray, D. F. & Nagel, T. 1989, *ApJ*, **341**, 421
- Green, G. M. 2018, *JOSS*, **3**, 695
- Grill, M. 2015, Master's thesis, University of Heidelberg
- Grunblatt, S. K. 2024, [arXiv:2410.16482](https://arxiv.org/abs/2410.16482)
- Grunblatt, S. K., Huber, D., Gaidos, E., et al. 2019, *AJ*, **158**, 227
- Grunblatt, S. K., Huber, D., Gaidos, E., et al. 2017, *AJ*, **154**, 254
- Grunblatt, S. K., Huber, D., Gaidos, E. J., et al. 2016, *AJ*, **152**, 185
- Grunblatt, S. K., Saunders, N., Chontos, A., et al. 2023, *AJ*, **165**, 44
- Grunblatt, S. K., Saunders, N., Huber, D., et al. 2024, *AJ*, **168**, 1
- Grunblatt, S. K., Saunders, N., Sun, M., et al. 2022, *AJ*, **163**, 120
- Grundahl, F., Andersen, M. F., Christensen-Dalsgaard, J., et al. 2017, *ApJ*, **836**, 142
- Grundahl, F., Kjeldsen, H., Christensen-Dalsgaard, J., Arentoft, T., & Frandsen, S. 2007, *CoAst*, **150**, 300
- Gutcke, T. 2011, Bachelor's thesis, University of Heidelberg
- Häffner, L. 2020, Internship Report, University of Heidelberg
- Halbwachs, J.-L., Pourbaix, D., Arenou, F., et al. 2022, *A&A*, **674**, 14
- Hammel, B. & Sullivan-Molina, N. 2020, *Bdhammel/Least-Squares-Ellipse-Fitting: V2.0.0*, [Zenodo](https://zenodo.org/record/4411111)
- Han, I., Lee, B. C., Kim, K. M., et al. 2010, *A&A*, **509**, A24
- Harris, C. R., Millman, K. J., van der Walt, S. J., et al. 2020, *Nat*, **585**, 357–362
- Haswell, C. A. 2010, *Transiting Exoplanets* (Cambridge: Cambridge University Press)
- Hatzes, A. P. 1996, *PASP*, **108**, 839
- Hatzes, A. P. 2002, *Astron. Nachr.*, **323**, 392–394
- Hatzes, A. P. 2013, *Astron. Nachr.*, **334**, 616
- Hatzes, A. P. 2019, *The Doppler Method for the Detection of Exoplanets* (Bristol, UK: IOP Publishing)
- Hatzes, A. P. & Cochran, W. D. 1993, *ApJ*, **413**, 339
- Hatzes, A. P. & Cochran, W. D. 1994, *ApJ*, **422**, 366
- Hatzes, A. P. & Cochran, W. D. 1996, *ApJ*, **468**, 391
- Hatzes, A. P. & Cochran, W. D. 1998a, *MNRAS*, **293**, 469–478

- Hatzes, A. P. & Cochran, W. D. 1998b, in ASP Conf. Ser., Vol. 154, Cool Stars Stellar Syst. Sun, ed. R. A. Donahue & J. A. Bookbinder, 311
- Hatzes, A. P. & Cochran, W. D. 1999, *MNRAS*, 304, 109–118
- Hatzes, A. P., Cochran, W. D., Endl, M., et al. 2015, *A&A*, 580, A31
- Hatzes, A. P., Cochran, W. D., Endl, M., et al. 2006, *A&A*, 457, 335–341
- Hatzes, A. P., Endl, M., Cochran, W. D., et al. 2018, *AJ*, 155, 120
- Hatzes, A. P., Guenther, E. W., Endl, M., et al. 2005, *A&A*, 437, 743–751
- Hauschildt, P. H. & Baron, E. 1999, *J. Comput. Appl. Math.*, 109, 41–63
- Heeren, P. 2016, Master’s thesis, University of Heidelberg
- Heeren, P. 2021, PhD thesis, University of Heidelberg
- Heeren, P., Reffert, S., Trifonov, T., et al. 2021, *A&A*, 647, A160
- Heeren, P., Tronsgaard, R., Grundahl, F., et al. 2023, *A&A*, 674, A164
- Hekker, S. 2013, *Adv. Space Res.*, 52, 1581–1592
- Hekker, S. & Mazumdar, A. 2013, *Proc. IAU*, 9, 325–331
- Hekker, S. & Meléndez, J. 2007, *A&A*, 475, 1003–1009
- Hekker, S., Reffert, S., & Quirrenbach, A. 2005, [arXiv:astro-ph/0510337](https://arxiv.org/abs/astro-ph/0510337)
- Hekker, S., Reffert, S., Quirrenbach, A., et al. 2006, *A&A*, 454, 943–949
- Hekker, S., Snellen, I. A. G., Aerts, C., et al. 2008, *A&A*, 480, 215–222
- Herrero, E., Ribas, I., Jordi, C., et al. 2016, *A&A*, 586, A131
- Hestroffer, D. & Magnan, C. 1998, *A&A*, 333, 338–342
- Higson, E., Handley, W., Hobson, M., & Lasenby, A. 2019, *Stat Comput*, 29, 891–913
- Hill, M. L., Kane, S. R., Campante, T. L., et al. 2021, *AJ*, 162, 211
- Hinkle, K. H., Lebzelter, T., Joyce, R. R., & Fekel, F. C. 2002, *AJ*, 123, 1002–1012
- Hippke, M. & Heller, R. 2019, *A&A*, 623, A39
- Hirschbeck, F. M. 2022, Bachelor’s thesis, University of Heidelberg
- Hojjatpanah, S., Oshagh, M., Figueira, P., et al. 2020, *A&A*, 639, A35
- Holanda, N., Ramos, A. A., Peña Suárez, V. J., Martínez, C. F., & Pereira, C. B. 2022, *MNRAS*, 516, 4484–4496
- Holl, B., Fabricius, C., Portell, J., et al. 2022a, [arXiv:2212.11971](https://arxiv.org/abs/2212.11971)
- Holl, B., Sozzetti, A., Sahlmann, J., et al. 2022b, [arXiv:2206.05439](https://arxiv.org/abs/2206.05439)
- Holl, B., Sozzetti, A., Sahlmann, J., et al. 2023, *A&A*, 674, A10
- Howell, S. B., Sobeck, C., Haas, M., et al. 2014, *PASP*, 126, 398
- Huang, C. X., Vanderburg, A., Pál, A., et al. 2020, *RNAAS*, 4, 204
- Huang, X., He, Y., Bai, Z., et al. 2024, *ApJS*, 272, 6
- Huber, D., Carter, J. A., Barbieri, M., et al. 2013, *Sci*, 342, 331–334
- Huber, D., Chaplin, W. J., Chontos, A., et al. 2019, *AJ*, 157, 14
- Huélamo, N., Figueira, P., Bonfils, X., et al. 2008, *A&A*, 489, L9-L13
- Hunt, E. L. & Reffert, S. 2023, *A&A*, 673, A114
- Hunt, E. L. & Reffert, S. 2024, *A&A*, 686, A42
- Hunter, J. D. 2007, *Comput. Sci. Eng.*, 9, 90–95
- Husser, T.-O. 2012, 3D-Spectroscopy of Dense Stellar Populations (Göttingen: Göttingen University Press)
- Husser, T.-O., Kamann, S., Dreizler, S., et al. 2016, *A&A*, 588, A148

- Husser, T. O., Wende-von Berg, S., Dreizler, S., et al. 2013, *A&A*, 553, A6
- Jacobi, K. 2024a, Bachelor's thesis, University of Heidelberg
- Jacobi, K. 2024b, Internship Report, University of Heidelberg
- Janke, S. 2023, Internship Report, University of Heidelberg
- Janke, S. M. 2024, Bachelor's thesis, University of Heidelberg
- Jeffers, S. V., Barnes, J. R., Scheofer, P., et al. 2022, *A&A*, 663, A27
- Jenkins, J. M., Twicken, J. D., McCauliff, S., et al. 2016, in *SPIE Astronomical Telescopes + Instrumentation*, ed. G. Chiozzi & J. C. Guzman, Edinburgh, United Kingdom, 99133E
- Jenkins, J. S., Jones, H. R. A., Tuomi, M., et al. 2017, *MNRAS*, 466, 443–473
- Jeong, G., Lee, B.-C., Park, M.-G., Bang, T.-Y., & Han, I. 2022, *A&A*, 662, A12
- Jessen, A. 2022, Master's thesis, University of Heidelberg
- Johnson, J. A., Fischer, D. A., Marcy, G. W., et al. 2007, *ApJ*, 665, 785–793
- Johnson, J. L. & Li, H. 2012, *ApJ*, 751, 81
- Jones, M. I., Brahm, R., Espinoza, N., et al. 2018, *A&A*, 613, A76
- Jones, M. I., Jenkins, J. S., Brahm, R., et al. 2016, *A&A*, 590, A38
- Jones, M. I., Jenkins, J. S., Rojo, P., & Melo, C. H. F. 2011, *A&A*, 536, A71
- Kaeufl, H.-U., Ballester, P., Biereichel, P., et al. 2004, 5492, 1218–1227
- Kane, S. R., Reffert, S., Henry, G. W., et al. 2010, *ApJ*, 720, 1644–1649
- Kanodia, S. & Wright, J. 2018, *RNAAS*, 2, 4
- Kaufer, A., Stahl, O., Tubbesing, S., et al. 1999, *Msngr*, 95, 8–12
- Kemmer, J., Lafarga, M., Fuhrmeister, B., et al. 2024, *A&A* (submitted)
- Kennedy, G. M. & Kenyon, S. J. 2008, *ApJ*, 673, 502–512
- Kennedy, G. M. & Kenyon, S. J. 2009, *ApJ*, 695, 1210–1226
- Kervella, P., Arenou, F., Mignard, F., & Thévenin, F. 2019, *A&A*, 623, A72
- Kervella, P., Arenou, F., & Thévenin, F. 2022, *A&A*, 657, A7
- Kiefer, F., Hébrard, G., Lecavelier Des Etangs, A., et al. 2021, *A&A*, 645, A7
- Kjeldsen, H. & Bedding, T. R. 1995, *A&A*, 293, 87–106
- Kjeldsen, H. & Bedding, T. R. 2011, *A&A*, 529, L8
- Kochukhov, O. 2004, *A&A*, 423, 613–628
- Koleva, M. & Vazdekis, A. 2012, *A&A*, 538, A143
- Konstantinova-Antova, R., Georgiev, S., Lèbre, A., et al. 2024, *A&A*, 681, A36
- Koposov, S., Speagle, J., Barbary, K., et al. 2024, *JoshSpeagle/Dynesty: V2.1.4*, *Zenodo*
- Kovács, G., Zucker, S., & Mazeh, T. 2016, ASCL:1607.008
- Kreidberg, L. 2015, *PASP*, 127, 1161
- Kuhlbrodt, D. 2019, Bachelor's thesis, University of Heidelberg
- Kuhn, N. L. 2025, Bachelor's thesis, University of Heidelberg
- Kunitomo, M., Ikoma, M., Sato, B., Katsuta, Y., & Ida, S. 2011, *ApJ*, 737, 66
- Kürster, M., Endl, M., Rouesnel, F., et al. 2003, *A&A*, 403, 1077–1087
- Kurtz, D. 2006, *CoAst*, 147, 6–30
- Lafarga, M., Ribas, I., Lovis, C., et al. 2020, *A&A*, 636, A36
- Lafarga, M., Ribas, I., Reiners, A., et al. 2021, *A&A*, 652, A28
- Lagrange, A.-M., Desort, M., Galland, F., Udry, S., & Mayor, M. 2009, *A&A*, 495, 335
- Lamy, P., Prado, J.-Y., Floyd, O., et al. 2015, *Sol. Phys.*, 290, 2617–2648

- Laney, C. D., Joner, M. D., & Pietrzyński, G. 2012, *MNRAS*, 419, 1637–1641
- Lèbre, A., Aurière, M., Fabas, N., et al. 2014, *A&A*, 561, A85
- Lèbre, A., de Laverny, P., Do Nascimento, Jr., J. D., & de Medeiros, J. R. 2006, *A&A*, 450, 1173–1179
- Lee, B.-C., Han, I., Park, M.-G., et al. 2014, *JKAS*, 47, 69–76
- Lee, B.-C., Koo, J.-R., Jeong, G., et al. 2023, *JKAS*, 56, 35–40
- Li, G., Deheuvelds, S., Ballot, J., & Lignières, F. 2022, *Nat*, 610, 43–46
- Li, G., Deheuvelds, S., Li, T., Ballot, J., & Lignières, F. 2023, *A&A*, 680, A26
- Liebing, F., Jeffers, S. V., Reiners, A., & Zechmeister, M. 2021, *A&A*, 654, A168
- Liebing, F., Jeffers, S. V., Zechmeister, M., & Reiners, A. 2023, *A&A*, 673, A43
- Lightkurve Collaboration, Cardoso, J. V. d. M., Hedges, C., et al. 2018, ASCL:1812.013
- Lillo-Box, J., Barrado, D., Henning, Th., et al. 2014, *A&A*, 568, L1
- Lindgren, L., Klioner, S. A., Hernández, J., et al. 2021, *A&A*, 649, A2
- Liu, Y. J., Sato, B., Zhao, G., et al. 2008, *ApJ*, 672, 553–557
- Liu, Y. J., Tan, K. F., Wang, L., et al. 2014, *ApJ*, 785, 94
- Lloyd, J. P. 2011, *ApJ*, 739, L49
- Löhner-Böttcher, J., Schmidt, W., Schlichenmaier, R., Steinmetz, T., & Holzwarth, R. 2019, *A&A*, 624, A57
- Löhner-Böttcher, J., Schmidt, W., Stief, F., Steinmetz, T., & Holzwarth, R. 2018, *A&A*, 611, A4
- Lomb, N. R. 1976, *Astrophys. Space Sci.*, 39, 447–462
- Lovis, C. 2010, *Radial Velocity Techniques for Exoplanets*, ed. D. Fischer (Tucson: University of Arizona Press), 27–53
- Lovis, C. & Mayor, M. 2007, *A&A*, 472, 657–664
- Ludwig, H.-G. 2006, *A&A*, 445, 661–671
- Luque, R., Trifonov, T., Reffert, S., et al. 2019, *A&A*, 631, A136
- Luther, M. 1855, *MNRAS*, 15, 228–230
- Maldonado, J., Mirouh, G. M., Mendigutía, I., et al. 2025, *arXiv:2501.19074*
- Maldonado, J., Villaver, E., Eiroa, C., & Micela, G. 2019, *A&A*, 624, A94
- Malla, S. P., Stello, D., Montet, B. T., et al. 2024, *MNRAS*, 534, 1775–1786
- Marcy, G. W. & Butler, R. P. 1992, *PASP*, 104, 270
- Martin, J., Fuhrmeister, B., Mittag, M., et al. 2017, *A&A*, 605, A113
- Martínez-Arnáiz, R., López-Santiago, J., Crespo-Chacón, I., & Montes, D. 2011, *MNRAS*, 414, 2629–2641
- Matuszewski, F., Nettelmann, N., Cabrera, J., Börner, A., & Rauer, H. 2023, *A&A*, 677, A133
- Mayor, M., Pepe, F., Queloz, D., et al. 2003, *Msngr*, 114, 20–24
- Mayor, M. & Queloz, D. 1995, *Nat*, 378, 355–359
- McKerns, M. M., Strand, L., Sullivan, T., Fang, A., & Aivazis, M. A. G. 2012, *arXiv:1202.1056*
- McKinney, W. 2010, in *Proc. 9th Python Sci. Conf.*, ed. S. van der Walt & J. Millman, 56–61
- Mitchell, D. S., Reffert, S., Trifonov, T., Quirrenbach, A., & Fischer, D. A. 2013, *A&A*, 555, A87
- Mortier, A. & Collier Cameron, A. 2017, *A&A*, 601, A110
- Mortier, A., Faria, J. P., Correia, C. M., Santerne, A., & Santos, N. C. 2015, *A&A*, 573, A101
- Mortier, A., Santos, N. C., Sousa, S., et al. 2013a, *A&A*, 551, A112
- Mortier, A., Santos, N. C., Sousa, S. G., et al. 2013b, *A&A*, 557, A70
- Mozurkewich, D., Armstrong, J. T., Hindsley, R. B., et al. 2003, *AJ*, 126, 2502–2520

- Müller, R. G. 2019, Bachelor's thesis, University of Heidelberg
- Müller, S., Baron, J., Helled, R., Bouchy, F., & Parc, L. 2024, *A&A*, **686**, A296
- Murdin, P., ed. 2001, *Encyclopedia of Astronomy and Astrophysics* (Bristol: IOP Publishing)
- Murray, C. D. & Correia, A. C. M. 2010, in *Exoplanets*, ed. S. Seager (Tucson: University of Arizona Press), 15–23
- Mustill, A. 2024, [arXiv:2405.09399](https://arxiv.org/abs/2405.09399)
- Mustill, A. J. & Villaver, E. 2012, *ApJ*, **761**, 121
- Nagel, E., Czesla, S., Kaminski, A., et al. 2023, *A&A*, **680**, A73
- NASA. 1999, *SIM Space Interferometry Mission: Taking the Measure of the Universe*, ed. R. Danner & S. Unwin (Pasadena, NASA: JPL 400-811)
- Nascimbeni, V., Piotto, G., Börner, A., et al. 2022, *A&A*, **658**, A31
- Nascimbeni, V., Piotto, G., Cabrera, J., et al. 2025, *A&A*, **694**, A313
- Neckel, H. & Labs, D. 1994, *Sol. Phys.*, **153**, 91–114
- Newport. 2018, TRA Series - Compact Motorized Actuators
- Newville, M., Otten, R., Nelson, A., et al. 2021, Lmfit/Lmfit-Py: 1.0.3, [Zenodo](https://zenodo.org/record/5244444)
- Nicholls, C. P., Wood, P. R., Cioni, M.-R. L., & Soszynski, I. 2009, *MNRAS*, **399**, 2063–2078
- Niedzielski, A., Konacki, M., Wolszczan, A., et al. 2007, *ApJ*, **669**, 1354–1358
- Niedzielski, A., Villaver, E., Adamów, M., et al. 2021, *A&A*, **648**, A58
- Niedzielski, A., Villaver, E., Nowak, G., et al. 2016, *A&A*, **589**, L1
- Niedzielski, A., Villaver, E., Wolszczan, A., et al. 2015, *A&A*, **573**, A36
- North, T. S. H., Chaplin, W. J., Gilliland, R. L., et al. 2017, *MNRAS*, **465**, 1308–1315
- Ortiz, M., Gandolfi, D., Reffert, S., et al. 2015, *A&A*, **573**, L6
- Ortiz, M., Reffert, S., Trifonov, T., et al. 2016, *A&A*, **595**, A55
- pandas development team, T. 2024, Pandas-Dev/Pandas: Pandas, [Zenodo](https://zenodo.org/record/8111111)
- Panić, O., Haworth, T. J., Petr-Gotzens, M. G., et al. 2021, *MNRAS*, **501**, 4317–4328
- Pedregosa, F., Varoquaux, G., Gramfort, A., et al. 2011, *J. Mach. Learn. Res.*, **12**, 2825–2830
- Pepe, F., Cristiani, S., Rebolo, R., et al. 2021, *A&A*, **645**, A96
- Percy, J. R., Wilson, J. B., & Henry, G. W. 2001, *PASP*, **113**, 983–996
- Pereira, F., Grunblatt, S. K., Psaridi, A., et al. 2023, *MNRAS*, **527**, 6332–6345
- Perryman, M. 2018, *The Exoplanet Handbook*, 2nd edn. (Cambridge: Cambridge University Press)
- Perryman, M., Hartman, J., Bakos, G. Á., & Lindegren, L. 2014, *ApJ*, **797**, 14
- Petigura, E. A., Marcy, G. W., Winn, J. N., et al. 2018, *AJ*, **155**, 89
- Phipson, B. & Smyth, G. K. 2010, *Stat. Appl. Genet. Mol. Biol.*, **9**
- Pierce, A. K. & Slaughter, C. D. 1977, *Sol. Phys.*, **51**, 25–41
- Pojmanski, G. & Maciejewski, G. 2004, *Acta Astron.*, **54**, 153–179
- Polat, A. T. 2023, Internship Report, University of Heidelberg
- Press, W. H., Teukolsky, S. A., Vetterling, W. T., & Flannery, B. P. 2007, *Numerical Recipes 3rd Edition: The Art of Scientific Computing* (Cambridge: Cambridge University Press)
- Prša, A., Kochoska, A., Conroy, K. E., et al. 2022, *ApJS*, **258**, 16
- Queloz, D., Henry, G. W., Sivan, J. P., et al. 2001, *A&A*, **379**, 279–287
- Quinn, S. N., White, Timothy. R., Latham, D. W., et al. 2015, *ApJ*, **803**, 49
- Quirrenbach, A. 2010, in *Exoplanets*, ed. S. Seager (Tucson: University of Arizona Press), 157–167
- Quirrenbach, A., Amado, P. J., Caballero, J. A., et al. 2014, *SPIE Conf. Ser.*, **9147**, 91471F

- Quirrenbach, A., Reffert, S., & Bergmann, C. 2011, in *AIP Conf. Ser.*, Vol. 1331, *Planet. Syst. Main Seq.*, ed. S. Schuh, H. Drechsel, & U. Heber (AIP), 102–109
- Quirrenbach, A., Trifonov, T., Lee, M. H., & Reffert, S. 2019, *A&A*, 624, A18
- Rauer, H., Aerts, C., Cabrera, J., et al. 2024, [arXiv:2406.05447](https://arxiv.org/abs/2406.05447)
- Reffert, S., Bergmann, C., Quirrenbach, A., Trifonov, T., & Künstler, A. 2015, *A&A*, 574, A116
- Reffert, S. & Quirrenbach, A. 2006, *A&A*, 449, 699–702
- Reffert, S. & Quirrenbach, A. 2011, *A&A*, 527, A140
- Reffert, S., Quirrenbach, A., Mitchell, D. S., et al. 2006, *ApJ*, 652, 661–665
- Reichert, J., Holzwarth, R., Udem, Th., & Hänsch, T. W. 1999, *Opt. Commun.*, 172, 59–68
- Reichert, K., Reffert, S., Stock, S., Trifonov, T., & Quirrenbach, A. 2019, *A&A*, 625, A22
- Reiners, A., Bean, J. L., Huber, K. F., et al. 2010, *ApJ*, 710, 432–443
- Reiners, A., Shulyak, D., Anglada-Escudé, G., et al. 2013, *A&A*, 552, A103
- Reiners, A., Zechmeister, M., Caballero, J. A., et al. 2018, *A&A*, 612, A49
- Ribas, Á., Bouy, H., & Merín, B. 2015, *A&A*, 576, A52
- Ribas, I., Reiners, A., Zechmeister, M., et al. 2023, *A&A*, 670, A139
- Ricker, G. R., Winn, J. N., Vanderspek, R., et al. 2015, *JATIS*, 1, 014003
- Robertson, P., Mahadevan, S., Endl, M., & Roy, A. 2014, *Sci*, 345, 440–444
- Rolo, I., Delgado Mena, E., Tsantaki, M., & Gomes da Silva, J. 2024, *A&A*, 688, A68
- Roth, K. D. 2020, Master's thesis, University of Heidelberg
- Rowe, J. F., Bryson, S. T., Marcy, G. W., et al. 2014, *ApJ*, 784, 45
- Ruh, H. 2019, Internship Report, University of Heidelberg
- Ruh, H. L., Zechmeister, M., Reiners, A., et al. 2024, *A&A*, 692, A138
- Saar, S. H., Butler, R. P., & Marcy, G. W. 1998, *ApJ*, 498, L153-L157
- Saar, S. H. & Donahue, R. A. 1997, *ApJ*, 485, 319–327
- Sackmann, I. J., Boothroyd, A. I., & Kraemer, K. E. 1993, *ApJ*, 418, 457
- Saio, H., Wood, P. R., Takayama, M., & Ita, Y. 2015, *MNRAS*, 452, 3863–3868
- Santos, N. C., Udry, S., Mayor, M., et al. 2003, *A&A*, 406, 373–381
- Sarkis, P., Henning, T., Kürster, M., et al. 2018, *AJ*, 155, 257
- Sato, B., Ando, H., Kambe, E., et al. 2003, *ApJ*, 597, L157-L160
- Sato, B., Izumiura, H., Toyota, E., et al. 2008, *ASP Conf. Ser.*, 398, 4
- Sato, B., Izumiura, H., Toyota, E., et al. 2007, *ApJ*, 661, 527–531
- Saunders, N., Grunblatt, S. K., Chontos, A., et al. 2024, *AJ*, 168, 81
- Saunders, N., Grunblatt, S. K., Huber, D., et al. 2022, *AJ*, 163, 53
- Saunders, N., Grunblatt, S. K., Huber, D., et al. 2025, *AJ*, 169, 75
- Scargle, J. D. 1982, *ApJ*, 263, 835
- Schäfer, S., Guenther, E. W., Reiners, A., et al. 2018, *SPIE Conf. Ser.*, 10702, 76
- Schmidt, T. M. & Bouchy, F. 2024, *MNRAS*, 530, 1252–1273
- Schneider, K. 2013, *Deltacode - Die Ultimative Teleskopsteuerung*
- Schöfer, P., Jeffers, S. V., Reiners, A., et al. 2019, *A&A*, 623, A44
- Schrijvers, C., Telting, J. H., Aerts, C., Ruymaekers, E., & Henrichs, H. F. 1997, *A&AS*, 121, 343–368
- Schröder, C., Reiners, A., & Schmitt, J. H. M. M. 2009, *A&A*, 493, 1099–1107
- Schröder, K. P. & Smith, R. C. 2008, *MNRAS*, 386, 155–163
- Schwab, C. 2010, PhD thesis, University of Heidelberg

- ScopeDome. 2016, ScopeDome USB Card Ver. 2.1
- Setiawan, J. 2003, in *ESA SP*, Vol. 539, Earths DARWIN TPF Search Extrasolar Terr. Planets, ed. M. Fridlund, T. Henning, & H. Lacoste, 595–598
- Setiawan, J., Hatzes, A. P., von der Lühe, O., et al. 2003a, *A&A*, **398**, L19-L23
- Setiawan, J., Pasquini, L., da Silva, L., von der Lühe, O., & Hatzes, A. 2003b, *A&A*, **397**, 1151–1159
- Skilling, J. 2004, in *AIP Conf. Ser.*, Vol. 735, *AIP Conf. Proc.*, ed. R. Fischer, R. Preuss, & U. V. Toussaint (AIP), 395–405
- Skilling, J. 2006, *Bayesian Anal.*, **1**, 833–859
- Snedden, C., Afşar, M., Bozkurt, Z., et al. 2022, *ApJ*, **940**, 12
- Soszyński, I. 2007, *ApJ*, **660**, 1486–1491
- Soszyński, I., Olechowska, A., Ratajczak, M., et al. 2021, *ApJL*, **911**, L22
- Soszyński, I. & Udalski, A. 2014, *ApJ*, **788**, 13
- Soszyński, I., Udalski, A., Szymański, M. K., et al. 2009, *Acta Astron.*, **59**, 239–253
- Soto, M. G., Jenkins, J. S., & Jones, M. I. 2015, *MNRAS*, **451**, 3131–3144
- Sozzetti, A., Pinamonti, M., Damasso, M., et al. 2023, *A&A*, **677**, L15
- Spaeth, D. 2019, Master's thesis, University of Heidelberg
- Spaeth, D., Reffert, S., Hunt, E. L., Kaminski, A., & Quirrenbach, A. 2024, *A&A*, **689**, A91
- Spaeth, D., Reffert, S., Trifonov, T., & Golovin, A. 2023, *RNAAS*, **7**, 12
- Spaeth, D., Reffert, S., Trifonov, T., et al. 2025, *A&A* (in press)
- Speagle, J. S. 2020, *MNRAS*, **493**, 3132–3158
- Stange, M. 2023, Internship Report, University of Heidelberg
- Starlight Xpress. 2014, Starlight Xpress - Handbook for the SX Lodestar X2 Guide Camera
- Stassun, K. G., Oelkers, R. J., Pepper, J., et al. 2018, *AJ*, **156**, 102
- Staudt, P. 2020, Bachelor's thesis, University of Heidelberg
- Stefánsson, G., Mahadevan, S., Winn, J. N., et al. 2025, *AJ*, **169**, 107
- Steffen, J. H., Fabrycky, D. C., Agol, E., et al. 2013, *MNRAS*, **428**, 1077–1087
- Stock, S., Kemmer, J., Kossakowski, D., et al. 2023, *A&A*, **674**, A108
- Stock, S., Reffert, S., & Quirrenbach, A. 2018, *A&A*, **616**, A33
- Stoehr, F., White, R., Smith, M., et al. 2008, in *ASP Conf. Ser.*, Vol. 394, *Astron. Data Anal. Softw. Syst. XVII*, ed. R. W. Argyle, P. S. Bunclark, & J. R. Lewis, 505
- Stork, M. E. 2024, Bachelor's thesis, University of Heidelberg
- Svensson, F. & Ludwig, H. G. 2005, *A&A*, **560**, 979
- Takarada, T., Sato, B., Omiya, M., et al. 2018, *PASJ*, **70**, 59
- Takayama, M. 2023, *SAG*, **6**, 6
- Takayama, M. & Ita, Y. 2020, *MNRAS*, **492**, 1348–1362
- Tal-Or, L., Zechmeister, M., Reiners, A., et al. 2018, *A&A*, **614**, A122
- Tala, M., Heeren, P., Grill, M., et al. 2016, in *SPIE Conf. Ser.*, Vol. 9908, *Ground-Based Airborne Instrum. Astron. VI*, ed. C. J. Evans, L. Simard, & H. Takami, 99086O
- Tala Pinto, M., Reffert, S., Quirrenbach, A., et al. 2020, *A&A*, **644**, A1
- Tala Pinto, M. S. 2019, PhD thesis, University of Heidelberg
- Telting, J., Avila, G., Buchhave, L., et al. 2014, *Astron. Nachr.*, **335**, 41–45
- Temmink, M. & Snellen, I. A. G. 2023, *A&A*, **670**, A26
- Teng, H.-Y., Sato, B., Kunitomo, M., et al. 2023a, *PASJ*, **75**, 169–176

- Teng, H.-Y., Sato, B., Kuzuhara, M., et al. 2023b, *PASJ*, 75, 1030–1071
- Teng, H.-Y., Sato, B., Takarada, T., et al. 2022, *PASJ*, 74, 92–127
- Thompson, S. E., Everett, M., Mullally, F., et al. 2012, *ApJ*, 753, 86
- Thuillier, G., Claudel, J., Djafer, D., et al. 2011, *Sol. Phys.*, 268, 125–149
- Townsend, R. H. D. 1997, *MNRAS*, 284, 839–858
- Trifonov, T. 2019, ASCL:1906.004
- Trifonov, T. 2024, [arXiv:241011424T](https://arxiv.org/abs/241011424)
- Trifonov, T., Reffert, S., Tan, X., Lee, M. H., & Quirrenbach, A. 2014, *A&A*, 568, A64
- Trifonov, T., Reffert, S., Zechmeister, M., Reiners, A., & Quirrenbach, A. 2015, *A&A*, 582, A54
- Trifonov, T., Tal-Or, L., Zechmeister, M., et al. 2020, *A&A*, 636, A74
- Tronsgaard, R., Buchhave, L. A., Wright, J. T., Eastman, J. D., & Blackman, R. T. 2019, *MNRAS*, 489, 2395–2402
- Trotta, R. 2008, *Contemporary Physics*, 49, 71–104
- Tsantaki, M., Delgado-Mena, E., Bossini, D., et al. 2023, *A&A*, 674, A157
- Udem, Th., Holzwarth, R., & Hänsch, T. W. 2002, *Nat*, 416, 233–237
- Udry, S. & Santos, N. C. 2007, *ARAA*, 45, 397–439
- Vakhidov, R. 2024, Bachelor's thesis, University of Heidelberg
- Valenti, J. A., Butler, R. P., & Marcy, G. W. 1995, *PASP*, 107, 966
- Van Eylen, V., Albrecht, S., Gandolfi, D., et al. 2016, *AJ*, 152, 143
- van Leeuwen, F. 2007, *A&A*, 474, 653–664
- VanderPlas, J. T. 2018, *ApJS*, 236, 16
- Vaughan, A. H., Preston, G. W., & Wilson, O. C. 1978, *PASP*, 90, 267–274
- Veras, D. 2016, *R. Soc. Open Sci.*, 3, 150571
- Veras, D., Wyatt, M. C., Mustill, A. J., Bonsor, A., & Eldridge, J. J. 2011, *MNRAS*, 417, 2104–2123
- Villaver, E. & Livio, M. 2009, *ApJ*, 705, L81-L85
- Villaver, E., Livio, M., Mustill, A. J., & Siess, L. 2014, *ApJ*, 794, 3
- Virtanen, P., Gommers, R., Oliphant, T. E., et al. 2020, *Nat. Methods*, 17, 261–272
- Vogt, S. S. 1987, *PASP*, 99, 1214–1228
- Vogt, S. S., Allen, S. L., Bigelow, B. C., et al. 1994, in *SPIE Conf. Ser.*, Vol. 2198, *Instrum. Astron.* VIII, ed. D. L. Crawford & E. R. Craine, 362
- Vogt, S. S., Radovan, M., Kibrick, R., et al. 2014, *PASP*, 126, 359
- Von Stauffenberg, A., Trifonov, T., Quirrenbach, A., et al. 2024, *A&A*, 688, A112
- Waskom, M. L. 2021, *JOSS*, 6, 3021
- Wicker, M. M. 2020, Bachelor's thesis, University of Heidelberg
- Winn, J. N. 2010, in *Exoplanets*, ed. S. Seager (Tucson: University of Arizona Press), 55–77
- Wittenmyer, R. A., Endl, M., Wang, L., et al. 2011, *ApJ*, 743, 184
- Wolfgramm, L. J. 2021, Bachelor's thesis, University of Heidelberg
- Wolszczan, A. & Frail, D. A. 1992, *Nat*, 355, 145–147
- Wolthoff, V., Reffert, S., Quirrenbach, A., et al. 2022, *A&A*, 661, A63
- Wood, P. R. 2000, *PASA*, 17, 18–21
- Wood, P. R., Alcock, C., Allsman, R. A., et al. 1999, in *Asymptot. Giant Branch Stars*, ed. T. Le Bertre, A. Lebre, & C. Waelkens, Vol. 191, 151
- Wood, P. R. & Nicholls, C. P. 2009, *ApJ*, 707, 573–579

- Xiao, G.-Y., Teng, H.-Y., Zhou, J., et al. 2024, *AJ*, 167, 59
- Zaire, B., Donati, J. F., Alencar, S. P., et al. 2024, *MNRAS*, 533, 2893–2915
- Zechmeister, M., Dreizler, S., Ribas, I., et al. 2019, *A&A*, 627, A49
- Zechmeister, M. & Kürster, M. 2009, *A&A*, 496, 577–584
- Zechmeister, M., Reffert, S., Hatzes, A. P., Endl, M., & Quirrenbach, A. 2008, *A&A*, 491, 531–536
- Zechmeister, M., Reiners, A., Amado, P. J., et al. 2018, *A&A*, 609, A12
- Zhang, J., Huber, D., Weiss, L., & Bottom, M. 2022, in *Bull. Am. Astron. Soc.*, Vol. 54, 102.363
- Zhao, F., Lo Curto, G., Pasquini, L., et al. 2021, *A&A*, 645, A23
- Zhao, Y. & Dumusque, X. 2023, *A&A*, 671, A11
- Zhou, Q., Latham, D. W., Quinn, S. N., et al. 2023, *AJ*, 166, 160

Software acknowledgements

I acknowledge the use of the following software packages and thank the various authors for their contributions to the scientific community:

- Astropy: <http://www.astropy.org>
- astroquery: Ginsburg et al. (2019)
- batman: Kreidberg (2015)
- barycorrpy: Kanodia & Wright (2018)
- bgls: Mortier et al. (2015)
- bls: Kovács et al. (2016)
- CERES: Brahm et al. (2017)
- celerite: Foreman-Mackey et al. (2017)
- corner: Foreman-Mackey (2016)
- DYNesty: Speagle (2020); Kozlov et al. (2024); Feroz et al. (2009)
- dill: McKerns et al. (2012)
- Exo-Striker: Trifonov (2019)
- GLS: Zechmeister & Kürster (2009)
- indi: <https://indilib.org/>
- jocular: <https://jocular.readthedocs.io/en/latest/>
- juliet: Espinoza et al. (2019)
- kiwisolver: <https://kiwisolver.readthedocs.io/en/latest/>
- LaTeX-Workshop: <https://github.com/James-Yu/LaTeX-Workshop>
- lightcurve: Lightkurve Collaboration et al. (2018)
- lmfit: Newville et al. (2021)
- lsq-ellipse: Hammel & Sullivan-Molina (2020)

- Matplotlib: [Hunter \(2007\)](#)
- MLP: [Zechmeister et al. \(2019\)](#)
- nsstools: [Halbwachs et al. \(2022\)](#)
- NumPy: [Harris et al. \(2020\)](#)
- pandas: [pandas development team \(2024\)](#); [McKinney \(2010\)](#)
- pillow: <https://github.com/python-pillow/Pillow>
- pyodine: [Heeren et al. \(2023\)](#)
- PyAstronomy: [Czesla et al. \(2019\)](#); <https://github.com/sczesla/PyAstronomy>
- RACCOON: [Lafarga et al. \(2020\)](#)
- RASSINE: [Cretignier et al. \(2020\)](#)
- redis-py: <https://github.com/redis/redis-py>
- SciPy: [Virtanen et al. \(2020\)](#)
- seaborn: [Waskom \(2021\)](#)
- scanninglaw: [Green \(2018\)](#)
- scientific colour maps: [Crameri \(2023\)](#)
- scikit-learn: [Pedregosa et al. \(2011\)](#)
- TLS: [Hippke & Heller \(2019\)](#)
- SERVAL: [Zechmeister et al. \(2018\)](#)
- skyfield: <https://rhodesmill.org/skyfield/>
- SPOG+: [Stock et al. \(2018\)](#)
- tpfplotter: [Aller et al. \(2020\)](#)
- tqdm: [da Costa-Luis et al. \(2021\)](#)
- uncertainties: <https://pythonhosted.org/uncertainties/>
- vscode-ltex: <https://github.com/valentjn/vscode-ltex>

I further acknowledge the use of OpenAI's GPT-3 and GPT-4 models for assistance with language editing, grammar and spell checking, as well as coding support for Python, LaTeX, and BASH during the preparation of this work.

Data acknowledgements

I acknowledge the use of MPIA DDT at FEROS. This work is further based on ESO programs 092.A–9002(A), 095.A–9029(C), and 0109.A–9032(A) and data obtained from the ESO Science Archive Facility with DOI: <https://doi.eso.org/10.18727/archive/33>. Based on observations made with the Nordic Optical Telescope, owned in collaboration by the University of Turku and Aarhus University, and operated jointly by Aarhus University, the University of Turku and the University of Oslo, representing Denmark, Finland and Norway, the University of Iceland and Stockholm University at the Observatorio del Roque de los Muchachos, La Palma, Spain, of the Instituto de Astrofísica de Canarias. I would like to thank the staff at Lick observatory for their support and thank the CAT observers who assisted with the observations. I further used observations made with the Hertzsprung SONG telescope operated on the Spanish Observatorio del Teide on the island of Tenerife by the Aarhus and Copenhagen Universities and by the Instituto de Astrofísica de Canarias. It is further based on observations collected at the Centro Astronómico Hispano en Andalucía (CAHA) at Calar Alto, proposals F16-3.5-024, H17-3.5-014, F18-3.5-016, H18-3.5-015, 21A-3.5-051, 21B-3.5-052, 22A-3.5-051, 22B-3.5-051, 23A-3.5-051, 23B-3.5-052, operated jointly by Junta de Andalucía and Consejo Superior de Investigaciones Científicas (IAA-CSIC). Based on data from the CAHA Archive at CAB (INTA-CSIC).¹ The CAHA Archive is part of the Spanish Virtual Observatory² project funded by MCIN/AEI/10.13039/501100011033 through grant PID2020-112949GB-I00. This project has received funding from the European Union’s Horizon 2020 research and innovation programme under grant agreement No 101004719. This research has made use of the VizieR catalog access tool and the SIMBAD database, operated at CDS, Strasbourg, France. This work has made use of data from the European Space Agency (ESA) mission *Gaia* (<https://www.cosmos.esa.int/gaia>), processed by the *Gaia* Data Processing and Analysis Consortium (DPAC, <https://www.cosmos.esa.int/web/gaia/dpac/consortium>). Funding for the DPAC has been provided by national institutions, in particular the institutions participating in the *Gaia* Multilateral Agreement.

¹<http://cab.inta.es/>

²<http://svo.cab.inta-csic.es/>

Abbreviations and acronyms

Abbreviation	Meaning
ADU	Analog-to-Digital Units
ASAS	All-Sky Automated Survey
BIS	Bisector Inverse Slope
BLS	Box Least Squares
BVC	Barycentric Velocity Correction
CARMENES	Calar Alto high-Resolution search for M dwarfs with Exoearths with Near-infrared and optical Échelle Spectrographs
CARMENES-NIR	CARMENES near-infrared spectrograph arm
CARMENES-VIS	CARMENES visual spectrograph arm
Ca II IRT	Calcium II Infrared Triplet
CCD	Charge-Coupled Device
CCF	Cross-Correlation Function
CERES	Collection of Elemental Routines for Échelle Spectra
CRIRES	CRyogenic high-resolution InfraRed Echelle Spectrograph
CRX	Chromatic Index
CTI	Charge Transfer Inefficiency
dLW	Differential Linewidth
ESPRESSO	Échelle SPectrograph for Rocky Exoplanets and Stable Spectroscopic Observations
ExoFOP	Exoplanet Follow-up Observing Program
FAP	False Alarm Probability
FEROS	Fiber-fed Extended Range Optical Spectrograph
FIES	Fibre-fed Echelle Spectrograph
FFI	Full Frame Images
FFU	Fiber-Feeding Unit
FN-System	Focal Number System
FP	Fabry-Pérot
FWHM	Full Width at Half Maximum
GLS	Generalized Lomb-Scargle periodogram
HARPS	High Accuracy Radial velocity Planet Searcher
HARPSDRS	HARPS Data Reduction Software
HB	Horizontal Branch
HIRES	High Resolution Echelle Spectrometer
IP	Instrumental Profile

Continued on next page

Abbreviation	Meaning
LSF	Line Spread Function
LSP	Long Secondary Period
LSW	Landessternwarte Heidelberg
MAST	Mikulski Archive for Space Telescopes
MLP	Maximum Likelihood Periodogram
NIR	Near-infrared
OGLE	Optical Gravitational Lensing Experiment
PDCSAP	Pre-search Data Conditioning Simple Aperture Photometry
PMT	Photo-Multiplier Tube
QLP	Quick Look Pipeline
RACCOON	Radial velocities and Activity indicators from Cross-CORrelatiON with masks
RMS	Root Mean Square
RV	Radial velocity
RGB	Red Giant Branch
S/N	Signal-to-noise ratio
SAP	Simple Aperture Photometry
SERVAL	Spectrum Radial Velocity Analyser
SONG	Stellar Observations Network Group
SOPHIE	Spectrographe pour l'Observation des Phénomènes des Intérieurs stellaires et des Exoplanètes
SPOC	Science Processing Operations Center
TESS	Transiting Exoplanet Survey Satellite
TFOP	TESS Follow-up Observing Program
TFOPWG	TESS Follow-up Observing Program Working Group
ThAr	Thorium-Argon
TIC	TESS Input Catalog
TLS	Transit Least Squares
TOI	TESS Object of Interest
TTL	Transistor Transistor Logic
VIS	Visual
waltdrs	Waltz Data Reduction Software

Appendix to Chapter 2

A.1 FEROS RVs for HD 113283

Tab. A.1.: FEROS RVs for HD 113283 reduced with CERES and SERVAL.

BJD	RV[m s ⁻¹]	σ_{RV} [m s ⁻¹]	RV[m s ⁻¹]	σ_{RV} [m s ⁻¹]
	CERES	CERES	SERVAL	SERVAL
2 459 842.631 325 00	-4791.7	4.4	-3.5	3.6
2 459 845.484 986 35	-4793.8	3.2	-4.8	2.8
2 459 847.482 485 58	-4776.6	4.5	12.8	2.5
2 459 849.519 310 57	-4794.9	4.4	-2.1	4.9
2 459 851.589 461 47	-4788.7	3.8	-8.6	1.9
2 459 853.499 057 46	-4794.4	3.2	-14.5	1.8
2 459 859.489 049 39	-4799.8	3.2	-7.3	2.4
2 459 861.522 071 58	-4783.5	3.5	2.4	3.0
2 459 863.490 609 71	-4771.9	3.5	10.9	2.8
2 459 865.617 340 59	-4797.5	3.3	-13.5	3.5
2 459 868.486 953 43	-4789.3	3.0	1.9	2.5
2 459 871.492 054 02	-4790.5	3.6	-0.7	2.5
2 459 873.484 828 30	-4785.9	4.0	-0.7	3.9
2 459 877.491 159 14	-4790.2	4.8	-2.4	4.4
2 459 879.500 035 73	-4786.2	3.3	-6.8	1.6

A.2 FIES RVs for TOI 1489

Tab. A.2.: FIES RVs for TOI 1489. The RVs have been reduced by Prof. Davide Gandolfi.

BJD	RV[m s ⁻¹]	σ_{RV} [m s ⁻¹]
2 459 713.665 483 87	0.0	7.7
2 459 715.535 719 99	-22.5	6.1
2 459 717.499 669 30	-10.1	6.7
2 459 719.522 398 63	-28.6	11.8
2 459 720.628 352 79	-33.9	5.1
2 459 722.590 068 17	-19.1	6.9
2 459 724.582 205 08	-36.5	5.5
2 459 727.504 973 26	-11.3	7.3
2 459 728.594 729 23	-13.1	4.6
2 459 729.689 808 43	-18.8	7.7
2 459 732.578 820 65	-11.5	4.0
2 459 733.654 838 19	-22.1	3.1
2 459 734.604 423 24	-7.9	5.5
2 459 736.568 875 07	-22.9	8.8
2 459 737.564 883 37	-26.4	9.3
2 459 738.493 087 18	-21.0	6.3
2 459 745.611 562 33	-25.3	4.7
2 459 746.459 985 60	-21.3	8.0
2 459 747.587 159 04	-22.8	4.7
2 459 748.535 537 01	-17.1	4.5
2 459 752.622 383 40	-19.4	7.4
2 459 753.579 032 27	-18.4	7.9
2 459 754.473 511 11	-26.9	7.2
2 459 755.426 940 75	-17.1	10.2
2 459 757.597 768 01	-18.9	6.2

A.3 FIES RVs for TOI 1684

Tab. A.3.: FIES RVs for TOI 1684. The RVs have been reduced by Prof. Davide Gandolfi.

BJD	RV[m s ⁻¹]	σ_{RV} [m s ⁻¹]
2 459 541.391 064 57	0.1	5.3
2 459 541.484 919 48	-8.4	4.8
2 459 541.640 455 25	-1.3	5.5
2 459 541.738 529 13	-8.8	5.9
2 459 549.369 915 64	-5.4	4.7
2 459 549.506 339 74	-0.7	4.2
2 459 854.514 120 59	-9.7	8.3
2 459 854.615 991 93	7.7	5.9
2 459 854.737 932 90	-6.8	5.5
2 459 856.553 408 90	5.5	6.2
2 459 856.632 981 13	13.8	4.1
2 459 857.612 407 99	11.7	7.3
2 459 858.540 918 57	-6.5	6.9
2 459 858.754 884 31	12.8	4.8
2 459 859.498 779 45	12.2	6.3
2 459 859.572 738 55	10.0	5.0
2 459 859.671 556 59	10.9	3.7
2 459 859.733 284 76	16.5	5.1
2 459 860.536 368 29	-0.9	4.2
2 459 860.642 784 47	3.2	3.8
2 459 860.737 350 06	15.7	4.8
2 459 861.554 793 74	7.0	4.3
2 459 861.631 847 05	0.0	3.6
2 459 861.699 184 65	0.4	4.0
2 459 861.756 964 90	8.6	4.2
2 459 862.643 071 64	11.9	3.8
2 459 862.721 131 18	12.3	3.2
2 459 863.536 209 28	5.7	3.4
2 459 863.594 398 77	6.8	3.3
2 459 863.657 387 75	10.7	3.6
2 459 863.771 529 03	4.5	4.2
2 459 867.498 693 94	-3.4	6.3
2 459 867.602 649 40	0.8	5.1
2 459 867.666 037 05	0.9	9.0
2 459 867.736 195 48	1.0	4.0
2 459 869.497 355 79	6.1	4.9
2 459 869.602 931 96	-3.9	5.2
2 459 869.737 998 39	-7.5	4.1

Appendix to Chapter 4

B.1 Linear correlation between $H\alpha$ and RV

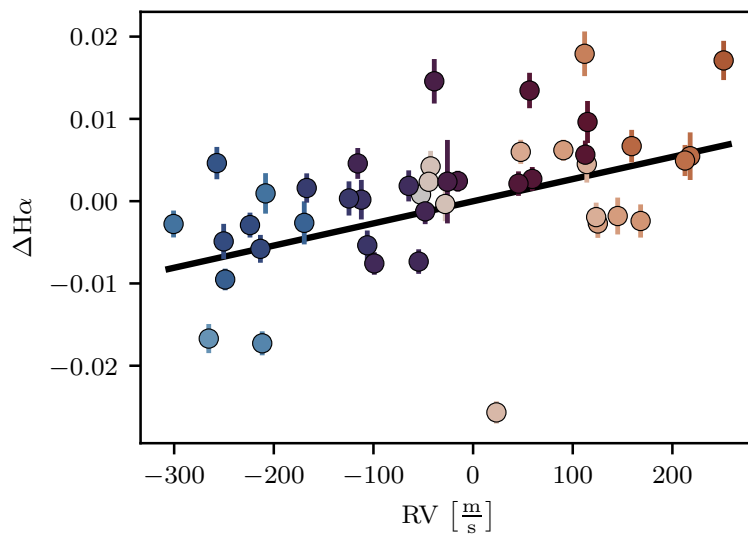


Fig. B.1.: Correlation between $H\alpha$ indicator (absolute difference from the mean) and RV for the 44 spectra acquired prior to the HARPS fiber change. The same color-coding as in Fig. 4.4 applies. A linear relation (black line) was fitted to the data. An F -test against a constant model confirms the correlation to be significant with a p -value $p(F\text{-test}) = 0.2\%$ and Pearson's r coefficient $r = 0.48$.

B.2 Discussion of the ASAS-3 photometry

In Fig. B.2 (top), we plot the available ASAS-3 data against time, color-coding the individual data points with respect to the RV period. For enhanced visibility, we further show binned data points as black rectangles. The photometric variation predicted by the $l = 1, m = 1$ oscillation model discussed in Sect. 4.4 is overplotted as the colored line and is much smaller than the scatter present in the ASAS-3 data. It is therefore reasonable to assume that the photometric variations would not have been detected in the ASAS-3 data set.

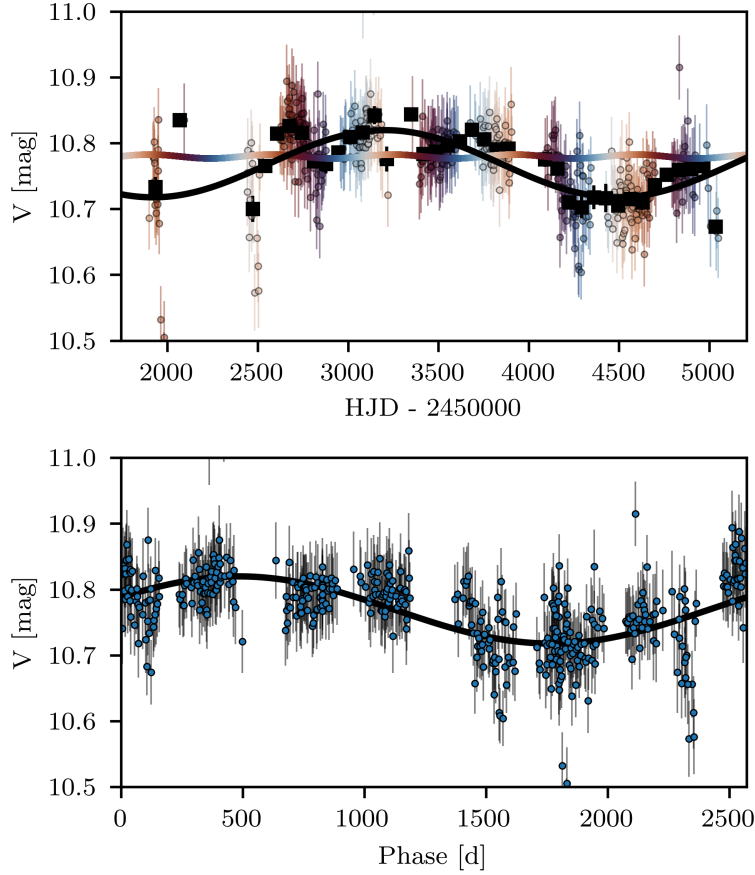


Fig. B.2.: Observed and simulated photometry for NGC 4349 No. 127. Top: V magnitudes extracted from ASAS-3 plotted against time (colored dots). The color-coding is the same as in Fig. 4.4 and refers to the RV period. We also plot binned means (black rectangles) as well as the photometric variability predicted by the $l = 1, m = 1$ oscillation model (continuous multi-colored line). We further overplot a sinusoidal fit with period 2571 d in black. Bottom: ASAS-3 V magnitudes phase-folded to the 2571 d period.

In Fig. B.3 (top), we plot the GLS periodogram of the ASAS-3 data, labeling the four most significant peaks in units of days. Delgado Mena et al. (2018) discuss the same data set and argue that the peak at 338 d is close to the first harmonic ($P/2$) of the RV period or could be linked to the rotation period of the star. However, we find that the most significant peak at 2592 d provides a much more convincing fit to the ASAS-3 data set, which we plot in black in the top panel of Fig. B.2. The sinusoidal fit has an amplitude of 0.05 mag and a period of 2571 d. The discrepancy to the 2592 d period found in the GLS periodogram stems from the sampling of the periodogram. We show a phase-folded plot of the ASAS-3 data in the bottom panel of Fig. B.2.

In the middle panel of Fig. B.3, we show the GLS periodogram of the residuals after removing the fit with period 2571 d. The bottom panel further shows the periodogram

of the window function computed as a Lomb-Scargle (LS) periodogram, as suggested by VanderPlas (2018). The formerly second strongest peak at 430 d coincides with the alias of the 2592 d signal and the strong yearly period present in the window function. It is therefore much reduced in significance by removing the long-period signal.

The interesting 338 d period also changes significantly by removing the fit with period 2571 d. It is reduced in significance and shifted to 361 d, coinciding quite closely with the yearly period. The two neighboring peaks at 248 d and 532 d are furthermore close to the alias period of the yearly period and the 950 d period present in the window function. We therefore argue that the 338 d signal discussed by Delgado Mena et al. (2018) is likely not real and instead an artifact of the window function, as well as its neighboring peaks.

The origin of the fourth peak at 1160 d present in the original GLS periodogram is less certain. While it is close to the first harmonic of the long-period signal, it is not entirely suppressed by removing the 2571 d fit. It is, however, shifted closer to the 950 d peak present in the window function and could therefore potentially be explained as another windowing artifact.

For the 2592 d peak, there is no obvious peak present in the window function. It is also unlikely to be caused by the typical rise of the periodogram power of the window function at periods longer than the observing window. We therefore argue that the 2592 d signal is the only signal that cannot be explained by the window function. Whether this signal is of instrumental or stellar origin is uncertain. If it is real, it seems unlikely to be related to the non-radial oscillation discussed in Sect. 4.4.

It could, in principle, be related to the rotation period of the star. However, given the radius of the star, this would lead to a rotation velocity of $v_{\text{rot}} \sim 0.75 \text{ km s}^{-1}$, considerably lower than most estimates in the literature (see Table 4.1), but consistent with the estimate by Carlberg et al. (2016). We note that the presented simulation of a $l = 1, m = 1$ oscillation mode also requires a somewhat lower rotation velocity to reproduce the variations of the line shape indicators, but caution to use this value to determine the actual rotation velocity of the star.

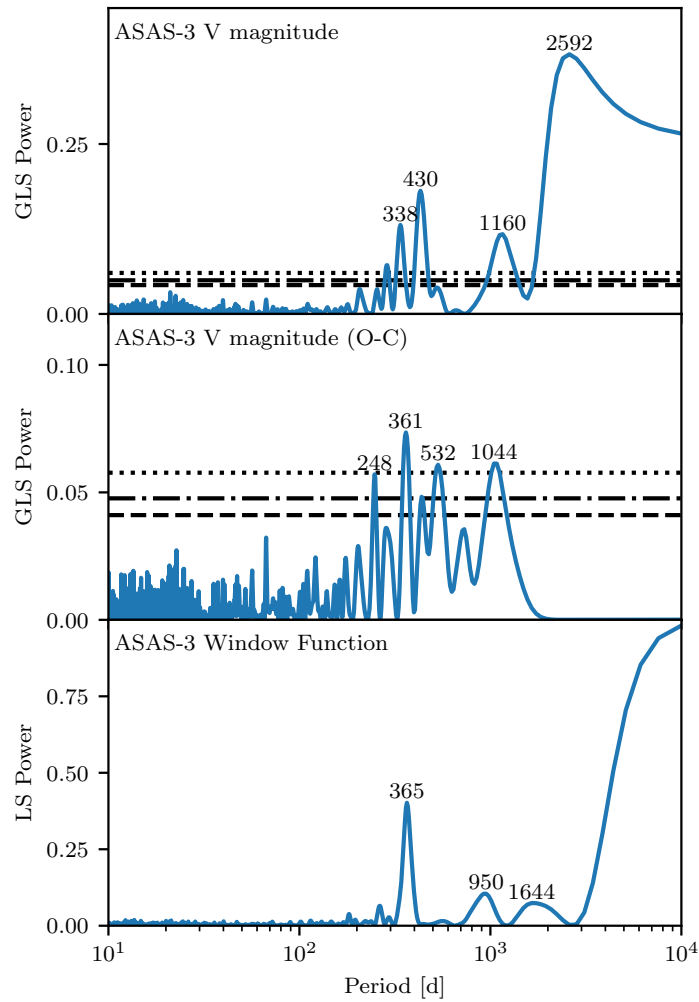


Fig. B.3.: GLS periodogram analysis of the ASAS-3 V-band photometry. Top: GLS periodogram of the original photometry. The FAP levels of 5% (dashed), 1% (dash-dotted), and 0.1% (dotted) were computed via bootstrapping with 10 000 reshuffles and are plotted as horizontal lines. The periods of the four most prominent peaks are given in units of days. Middle: GLS periodogram of the residual photometry after removing the 2571 d fit. Bottom: LS periodogram of the window function.

B.3 Oscillation modes with $m = l$

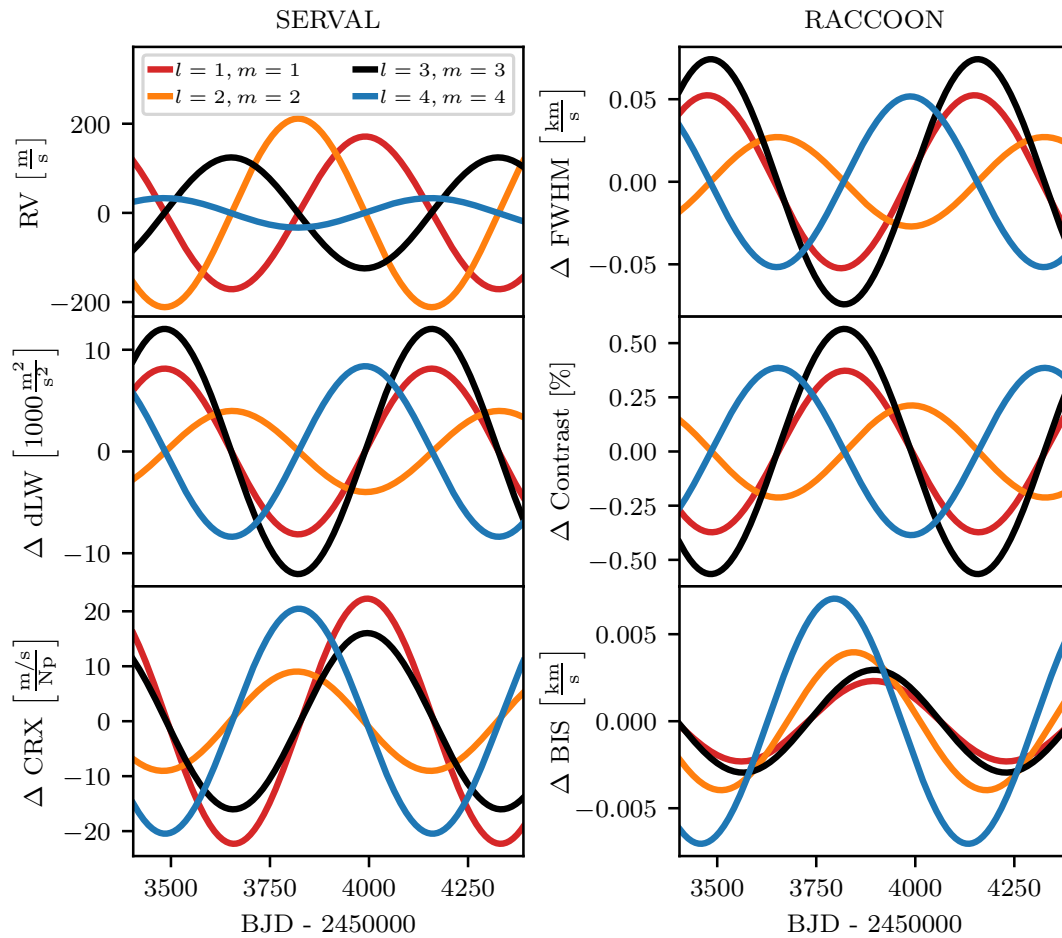


Fig. B.4.: RVs and activity indicators for oscillation modes with $m = l$ plotted against time at inclination angle $i = 45^\circ$. Sinusoids are predicted for all observables and were fitted to the time series. Different amplitudes and phase relations are predicted and can be useful for mode identification. The dLW variations were rescaled with a common factor of 0.1.

B.4 Oscillation modes with $m = -l$

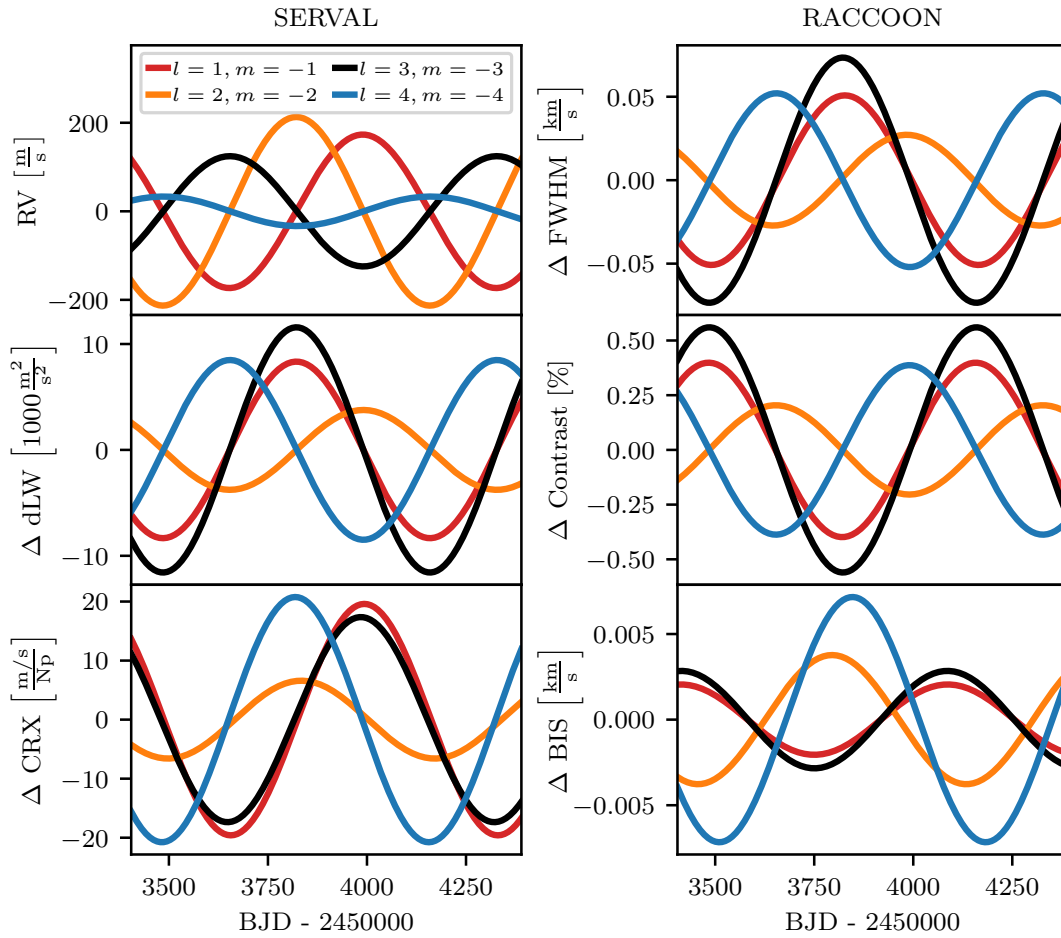


Fig. B.5.: RVs and activity indicators for oscillation modes with $m = -l$ plotted against time at inclination angle $i = 45^\circ$. Sinusoids are predicted for all observables and were fitted to the time series. Different amplitudes and phase relations are predicted and can be useful for mode identification. The dLW variations were rescaled with a common factor of 0.1.

B.5 HARPS data set

Tab. B.1.: SERVAL and RACCOON reduction results.

BJD SERVAL	RV SERVAL $\frac{\text{m}}{\text{s}}$	RV RACCOON $\frac{\text{m}}{\text{s}}$	CRX SERVAL $\frac{\text{m/s}}{\text{km}}$	dLW SERVAL $\frac{\text{Å}}{1000 \frac{\text{m}^2}{\text{s}^2}}$	H α SERVAL	FWHM RACCOON $\frac{\text{km}}{\text{s}}$	Contrast RACCOON %	BIS RACCOON $\frac{\text{km}}{\text{s}}$
2453449.783796	127.1 ± 1.9	-11528.8 ± 6.8	-7.5 ± 14.8	19.9 ± 1.7	0.4091 ± 0.0017	9.205 ± 0.019	49.777 ± 0.077	0.076 ± 0.016
2453460.836163	71.1 ± 2.8	-11578.2 ± 8.8	55.8 ± 20.9	18.6 ± 2.6	0.4169 ± 0.0022	9.228 ± 0.022	48.757 ± 0.087	0.095 ± 0.021
2453469.790637	60.0 ± 2.4	-11598.1 ± 6.0	15.4 ± 18.1	5.0 ± 1.8	0.4056 ± 0.0015	9.157 ± 0.016	49.700 ± 0.065	0.059 ± 0.014
2453499.578838	-24.5 ± 3.4	-11688.5 ± 10.8	8.6 ± 26.9	14.6 ± 4.1	0.4180 ± 0.0027	9.168 ± 0.020	48.874 ± 0.078	0.043 ± 0.025
2453500.641879	-11.3 ± 9.1	-11654.9 ± 19.4	36.6 ± 71.7	19.5 ± 6.3	0.4058 ± 0.0051	9.215 ± 0.020	48.047 ± 0.076	0.066 ± 0.044
2453521.584883	-101.3 ± 2.7	-11754.8 ± 7.7	-18.4 ± 20.4	10.9 ± 2.3	0.4080 ± 0.0019	9.184 ± 0.018	48.917 ± 0.070	0.069 ± 0.018
2453787.795108	-37.8 ± 2.0	-11698.1 ± 6.2	-6.9 ± 15.5	-20.4 ± 1.9	0.4042 ± 0.0016	9.015 ± 0.016	50.623 ± 0.067	0.059 ± 0.014
2453812.758975	-28.2 ± 2.3	-11687.3 ± 7.3	-28.3 ± 17.2	-17.7 ± 2.1	0.4077 ± 0.0019	9.027 ± 0.016	50.444 ± 0.066	0.052 ± 0.017
2453833.703149	-37.9 ± 2.0	-11624.7 ± 5.5	-13.6 ± 15.4	-15.0 ± 1.6	0.3778 ± 0.0014	9.069 ± 0.014	50.372 ± 0.057	0.055 ± 0.013
2453862.612919	62.3 ± 2.1	-11594.8 ± 5.7	38.2 ± 14.9	-14.3 ± 1.7	0.4094 ± 0.0015	9.062 ± 0.020	50.258 ± 0.082	0.079 ± 0.013
2453883.589922	105.1 ± 1.8	-11550.8 ± 5.0	15.2 ± 13.7	-14.1 ± 1.4	0.4096 ± 0.0013	9.060 ± 0.018	50.306 ± 0.073	0.074 ± 0.012
2453922.499565	126.4 ± 4.4	-11532.0 ± 10.3	-42.2 ± 34.2	1.5 ± 2.8	0.4213 ± 0.0027	9.158 ± 0.019	49.554 ± 0.075	0.076 ± 0.024
2453950.476290	173.6 ± 3.3	-11476.0 ± 7.7	43.5 ± 24.5	-2.2 ± 2.2	0.4101 ± 0.0020	9.163 ± 0.019	49.765 ± 0.075	0.062 ± 0.018
2454117.846012	129.3 ± 4.8	-11514.1 ± 9.7	13.6 ± 37.6	4.3 ± 2.9	0.4131 ± 0.0026	9.149 ± 0.013	49.463 ± 0.053	0.043 ± 0.023
2454137.806299	73.9 ± 2.0	-11582.4 ± 5.7	-22.1 ± 14.5	6.5 ± 1.6	0.4061 ± 0.0014	9.191 ± 0.018	49.416 ± 0.072	0.073 ± 0.013
2454169.723975	-0.8 ± 1.5	-11653.4 ± 5.0	6.5 ± 11.5	0.4 ± 1.3	0.4059 ± 0.0013	9.178 ± 0.017	49.463 ± 0.068	0.061 ± 0.012
2454194.779612	-33.6 ± 2.1	-11691.2 ± 6.1	-14.2 ± 15.7	6.9 ± 1.9	0.4022 ± 0.0016	9.207 ± 0.016	49.253 ± 0.063	0.053 ± 0.014
2454202.725871	-84.7 ± 1.9	-11738.0 ± 5.4	18.0 ± 14.1	7.1 ± 1.7	0.3959 ± 0.0014	9.184 ± 0.017	49.591 ± 0.067	0.059 ± 0.013
2454225.659919	-97.7 ± 3.2	-11765.4 ± 9.3	-8.9 ± 24.6	23.7 ± 2.4	0.4036 ± 0.0024	9.258 ± 0.016	48.711 ± 0.062	0.050 ± 0.022
2454228.669709	-91.7 ± 2.3	-11754.5 ± 7.1	-16.1 ± 17.7	14.7 ± 2.3	0.3981 ± 0.0018	9.224 ± 0.017	49.240 ± 0.068	0.057 ± 0.017
2454233.617177	-110.1 ± 2.7	-11763.3 ± 8.1	0.6 ± 20.8	16.6 ± 1.9	0.4038 ± 0.0021	9.229 ± 0.018	49.053 ± 0.070	0.063 ± 0.019
2454258.558537	-199.0 ± 2.6	-11853.6 ± 6.7	-7.3 ± 19.5	12.4 ± 1.9	0.3976 ± 0.0017	9.209 ± 0.024	49.347 ± 0.095	0.101 ± 0.016
2454293.529869	-234.3 ± 1.9	-11889.5 ± 5.3	-30.9 ± 14.3	-3.4 ± 1.5	0.3939 ± 0.0013	9.077 ± 0.020	49.832 ± 0.080	0.068 ± 0.013
2454299.561525	-155.5 ± 3.9	-11807.7 ± 10.0	9.3 ± 30.2	10.8 ± 2.5	0.4008 ± 0.0026	9.125 ± 0.017	49.289 ± 0.068	0.050 ± 0.023
2454319.474304	-193.8 ± 3.8	-11843.4 ± 9.6	-15.5 ± 29.7	6.7 ± 3.2	0.4044 ± 0.0025	9.132 ± 0.016	49.377 ± 0.064	0.034 ± 0.022
2454323.471811	(-205.4 ± 4.0)	(-11866.9 ± 9.3)	(28.5 ± 32.0)	(96.6 ± 2.7)	(0.4059 ± 0.0024)	(9.114 ± 0.018)	(49.211 ± 0.071)	(0.063 ± 0.022)
2454342.475808	-197.1 ± 2.4	-11851.7 ± 5.8	-16.2 ± 18.0	1.9 ± 2.0	0.3862 ± 0.0015	9.122 ± 0.022	49.853 ± 0.088	0.074 ± 0.014
2454349.472032	(-182.2 ± 2.7)	(-11839.4 ± 6.5)	(-13.1 ± 21.6)	(96.4 ± 2.0)	(0.3943 ± 0.0016)	(9.130 ± 0.018)	(49.691 ± 0.072)	(0.070 ± 0.015)
2454481.828543	-30.1 ± 2.6	-11686.1 ± 6.3	3.9 ± 19.8	-10.6 ± 2.3	0.4058 ± 0.0017	9.033 ± 0.021	50.538 ± 0.087	0.067 ± 0.015
2454486.799252	-13.5 ± 3.2	-11668.1 ± 7.8	40.2 ± 24.0	-3.3 ± 2.7	0.4031 ± 0.0021	9.046 ± 0.019	50.143 ± 0.079	0.087 ± 0.018
2454523.803657	128.6 ± 3.2	-11527.4 ± 8.2	21.7 ± 24.6	-3.8 ± 2.8	0.4079 ± 0.0023	9.055 ± 0.022	50.172 ± 0.092	0.088 ± 0.019
2454528.781976	138.0 ± 2.6	-11513.1 ± 6.6	48.7 ± 18.9	-13.0 ± 2.1	0.4015 ± 0.0018	9.039 ± 0.022	50.619 ± 0.092	0.095 ± 0.016
2454553.728094	139.7 ± 2.6	-11518.1 ± 6.6	26.7 ± 19.7	-2.6 ± 1.9	0.4007 ± 0.0018	9.065 ± 0.017	50.135 ± 0.072	0.075 ± 0.016
2454557.719757	159.6 ± 3.7	-11498.1 ± 8.3	-10.5 ± 29.2	-0.3 ± 2.3	0.4016 ± 0.0022	9.074 ± 0.020	50.041 ± 0.080	0.074 ± 0.020
2454567.682293	182.6 ± 3.3	-11469.1 ± 7.5	18.3 ± 25.2	-6.4 ± 2.7	0.4010 ± 0.0020	9.098 ± 0.019	50.259 ± 0.079	0.070 ± 0.018
2454616.605073	227.1 ± 2.4	-11432.9 ± 7.0	27.1 ± 17.8	-16.4 ± 2.1	0.4084 ± 0.0019	9.042 ± 0.021	50.575 ± 0.087	0.075 ± 0.017
2454620.562075	232.3 ± 3.3	-11422.1 ± 10.5	21.1 ± 25.2	4.3 ± 3.5	0.4089 ± 0.0029	9.101 ± 0.016	49.615 ± 0.066	0.041 ± 0.025
2454643.591867	265.9 ± 3.0	-11386.3 ± 8.7	5.3 ± 23.9	-7.3 ± 2.8	0.4205 ± 0.0024	9.101 ± 0.016	50.188 ± 0.064	0.053 ± 0.021
2454878.816129	-40.1 ± 2.4	-11689.7 ± 5.7	-4.9 ± 17.9	8.7 ± 2.0	0.3961 ± 0.0015	9.188 ± 0.015	49.303 ± 0.059	0.050 ± 0.014
2454884.801300	-50.1 ± 2.6	-11707.4 ± 7.1	-9.2 ± 20.3	10.1 ± 2.4	0.4053 ± 0.0019	9.185 ± 0.018	49.328 ± 0.070	0.065 ± 0.017
2454915.766283	-152.5 ± 2.6	-11806.1 ± 6.7	-19.5 ± 19.6	11.1 ± 2.1	0.4050 ± 0.0018	9.196 ± 0.016	49.445 ± 0.065	0.061 ± 0.016
2454937.689290	-209.4 ± 2.3	-11871.2 ± 5.7	-21.6 ± 17.3	5.0 ± 1.7	0.4005 ± 0.0015	9.135 ± 0.019	49.632 ± 0.075	0.071 ± 0.014
2454939.703414	-235.8 ± 3.5	-11889.2 ± 8.0	-0.1 ± 27.5	7.2 ± 2.3	0.3985 ± 0.0021	9.123 ± 0.022	49.375 ± 0.088	0.087 ± 0.019
2454951.726105	-242.7 ± 3.0	-11893.8 ± 7.3	-9.8 ± 23.2	5.7 ± 2.2	0.4081 ± 0.0020	9.107 ± 0.018	49.507 ± 0.071	0.071 ± 0.017
2454993.574110	-286.1 ± 2.6	-11942.3 ± 6.1	-53.2 ± 18.9	-4.4 ± 1.6	0.4007 ± 0.0016	9.074 ± 0.017	50.021 ± 0.068	0.046 ± 0.015
2455036.504252	-250.8 ± 2.6	-11902.9 ± 6.8	-18.8 ± 20.2	-7.7 ± 2.2	0.3867 ± 0.0018	9.077 ± 0.018	50.097 ± 0.075	0.068 ± 0.016
2458117.826166	-0.0 ± 1.7							
2458156.839829	-61.2 ± 1.5							
2458198.769910	-89.5 ± 1.4							
2458257.676477	-246.1 ± 2.0							
2458488.854995	-236.5 ± 1.7							
2458540.848497	-103.5 ± 1.3							
2458849.842858	(384.7 ± 144.7)							
2458852.845746	-94.3 ± 2.0							
2458887.866178	-111.3 ± 2.2							
2459229.836282	-180.0 ± 1.7							
2459411.520342	118.9 ± 3.0							
2459647.867594	-314.6 ± 2.1							

Notes. The spectra taken before and after the HARPS fiber change are separated by the horizontal line. Data points discarded due to outliers in the dLW (before 2015) or RV (after 2015) are given in parentheses.

Appendix to Chapter 5

C.1 Priors used for the Keplerian modeling

Tab. C.1.: Priors used for the Keplerian models in Sect. 5.4.1.

HIP	P (d)	K (m s^{-1})	e	ω (deg)	M_0 (deg)	σ_{jit} (m s^{-1})	RV_{off} (m s^{-1})
Default	$\mathcal{U}(100, 2000)$	$\mathcal{U}(1, 1000)$	$\mathcal{U}(0, 0.9)$	$\mathcal{U}(0, 540)$	$\mathcal{U}(0, 540)$	$\mathcal{U}(0, 300)$	$\mathcal{U}(-5000, 5000)$
46390	$\mathcal{U}(100, 1000)$						
47959							$\mathcal{U}(-50000, 50000)$
64823	$\mathcal{U}(100, 5000)$						
75458 b	$\mathcal{U}(100, 5000)$						$\mathcal{U}(-30000, 30000)$
75458 c	$\mathcal{U}(100, 50000)$						$\mathcal{U}(-30000, 30000)$
88048 b	$\mathcal{U}(100, 5000)$						
88048 c	$\mathcal{U}(100, 5000)$						
89826	$\mathcal{U}(100, 5000)$						

Notes. We give the default priors, as well as deviations from it for particular stars. \mathcal{U} denotes the uniform distribution.

Tab. C.2.: Priors used for the modeling of HIP 64823 in Sect. 5.6.

Parameter	Unit	2P	1P+GP
P_b	(d)	$\mathcal{U}(300, 500)$	$\mathcal{U}(100, 5000)$
K_b	(m s^{-1})	$\mathcal{U}(1, 1000)$	$\mathcal{U}(1, 1000)$
e_b		$\mathcal{U}(0, 0.7)$	$\mathcal{U}(0, 0.9)$
ω_b	(deg)	$\mathcal{U}(0, 540)$	$\mathcal{U}(0, 540)$
$M_{0,b}$	(deg)	$\mathcal{U}(0, 540)$	$\mathcal{U}(0, 540)$
P_c	(d)	$\mathcal{U}(100, 5000)$	
K_c	(m s^{-1})	$\mathcal{U}(1, 1000)$	
e_c		$\mathcal{U}(0, 0.9)$	
ω_c	(deg)	$\mathcal{U}(0, 540)$	
$M_{0,c}$	(deg)	$\mathcal{U}(0, 540)$	
σ_{jit}	(m s^{-1})	$\mathcal{U}(0, 300)$	$\mathcal{U}(0, 300)$
RV_{off}	(m s^{-1})	$\mathcal{U}(-5000, 5000)$	$\mathcal{U}(-5000, 5000)$
B_{GP}	($(\text{m s}^{-1})^2$)		$\mathcal{U}(100, 10000)$
L_{GP}	(d)		$\mathcal{U}(450, 10000)$
P_{GP}	(d)		$\mathcal{U}(10, 800)$
C_{GP}			$\mathcal{U}(0, 1)$

Notes. \mathcal{U} denotes the uniform distribution.

C.2 Corner plot of the joint 1P+GP model for HIP 64823

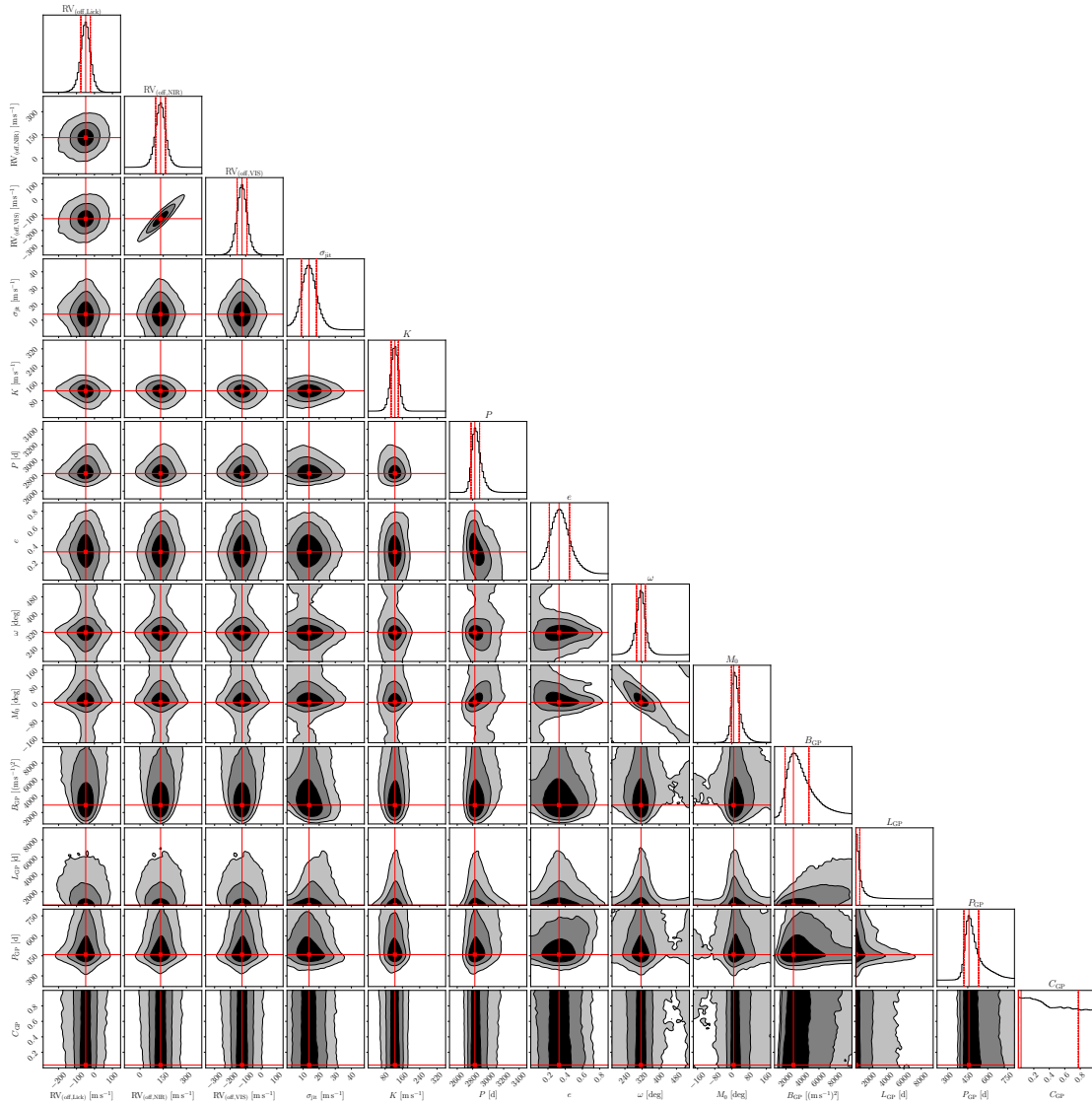


Fig. C.1.: Corner plot of the posterior samples of the joint 1P+GP model for HIP 64823. The mode of each parameter, marked as the continuous, red line, was adopted as the best fitting parameter in Table 5.4. The red dashed lines mark the interval that contains 68% of the posterior samples. We note that the posteriors of the planet model are well constrained, while the posteriors of the GP model (especially the factor C) are relatively broad and thus allow for a wide range of models.

Colophon

This thesis was typeset with $\text{\LaTeX} 2_{\epsilon}$. It uses the *Clean Thesis* style developed by Ricardo Langner. The design of the *Clean Thesis* style is inspired by user guide documents from Apple Inc.

Download the *Clean Thesis* style at <http://cleanthesis.der-ric.de/>.